TECHNICAL NOTE

D-1240

NASA SCOUT ST-1 FLIGHT-TEST RESULTS AND ANALYSES,

LAUNCH OPERATIONS, AND TEST VEHICLE DESCRIPTION

Compiled by Robert J. Mayhue

Langley Research Center
Langley Station, Hampton, Va.

NATIONAL AERONAUTICS AND SPACE ADMINISTRATION

WASHINGTON   June 1962

L
1
9
2
4

L
1
9
2
4

TABLE OF CONTENTS

L
1
9
2
4

L
1
9
2
4

L
1
9
2
4

v1

L
1
9
2
4

LIST OF TABLES

LIST OF FIGURES

L
1
9
2
4

L
1
9
2
4

L
1
9
2
4

NATIONAL AERONAUTICS AND SPACE ADMINISTRATION

TECHNICAL NOTE D-1240

NASA SCOUT ST-1 FLIGHT-TEST RESULTS AND ANALYSES,

LAUNCH OPERATIONS, AND TEST VEHICLE DESCRIPTION

Compiled by Robert J. Mayhue

SUMMARY

The first of a series of flight tests for the development of the four-stage, solid-propellant Scout vehicle was conducted at the NASA Wallops Station under the direction of the Langley Research Center. Vehicle designation for the test was NASA Scout ST-1. Performance characteristics of the vehicle and components were recorded during a high-altitude probe mission.

Flight-simulation studies are presented and show that the accuracy of the guidance system during the flight was within control-system design specifications. The control system functioned normally during the flight with the exception of an overpowering of the reaction-control roll jets near burnout of the third-stage rocket motor. The resulting roll displacement of the vehicle is shown to have caused the monitor tracking radar which had been erroneously tracking a radar beacon in the vehicle on a side lobe to reorient to the major lobe of the receiving antenna. This tracking switch falsely indicated a violent turning maneuver on the monitor plot board and resulted in a hold-fire decision for the fourth-stage rocket motor. Although data for the final thrusting and coast phase of the flight were not obtained, the majority of the test objectives were achieved.

In-flight thrust misalinement angles for the second- and third-stage rocket motors derived from control-system error data and for the first-stage motor determined from flight-simulation studies are presented. All rocket-motor thrust misalinement angles were well within the tolerances used for control-system design. Rocket-motor flight performance is presented, and velocity increments attained from the first three stages substantiated the predicted nominal performance. Operation of the rocket motors was satisfactory with the exception of high-level vibrations which were encountered during third-stage motor burning. Rolling moments which overpowered the reaction-control jets are also attributed to the burning characteristics of the third-stage motor.

A discussion of the premature loss of the third-stage heat shield is given and shows that the heat-shield latching mechanism failed from

pressure loads as the vehicle entered the transonic speed range.
Although venting was provided to relieve the high negative pressures
known to exist on the heat shield at these speeds, a field modification
of the wiring tunnel had the same effect as opening the inside of the
heat shield to ambient pressures. Consequently, the latching mechanism
failed from pressure loads which were of about the same magnitude as the
latching-mechanism yield loads.

Skin temperatures were recorded at several locations on the vehicle
and were generally in good agreement with theoretical values. Aerody-
namic heating presented no problem during the flight since the maximum
temperatures recorded during the flight were only about half the design
values because of the high-launch-angle trajectory.

Environmental vibrations recorded in the vicinity of the guidance
package showed that no significant continuous amplitude levels above
the general instrumentation noise level were present during first- and
second-stage burning. Large vibration amplitudes were recorded during
third-stage burning which coincided with the large roll disturbance
experienced by the vehicle near burnout of the third-stage motor.

INTRODUCTION

In order to fulfill the requirement for a highly reliable and
economical vehicle to perform orbital, vertical-probe, and reentry
missions involving small research payloads, the Langley Research Center
has conceived and developed a four-stage solid-fuel launch vehicle
designated as the Scout. The vehicle (and support equipment) was
designed and constructed under contract by Chance Vought Aircraft, Inc.,
and is capable of performing reentry and high-altitude probe flights
with payload weights up to 300 pounds, and orbital flights with payloads
up to 150 pounds.

The Langley Research Center is conducting a series of flight tests
to determine the performance of the Scout vehicle and components. The
initial flight test was performed at NASA Wallops Station on July 1,
1960. Vehicle designation for this test was Scout ST-1, and the specific
purposes established for the test were as follows:

1. To corroborate design concepts of the system by performing a
   high-altitude probe mission

2. To obtain measurements of flight environmental conditions and
   vehicle performance characteristics

3. To gain operational experience with the vehicle and support
   equipment

In order to provide a reference summary of the initial developmental flight test, this report presents a background description of the ST-1 test vehicle, the methods and procedures used for launch, and a detailed account of the results and analyses of the measured data obtained during the flight.

SYMBOLS

a_N normal acceleration, g units

a_X longitudinal acceleration, g units

a_Y transverse acceleration, g units

C_D drag coefficient, $\dfrac{\text{Drag}}{q_\infty S}$

C_p pressure coefficient, $\dfrac{p_l - p_\infty}{q_\infty}$

d displacement of control jets, in.

F thrust, lb

I total impulse, lb-sec

I_{sp} specific impulse, $\dfrac{\text{lb-sec}}{\text{lb}}$

I_X, I_Y, I_Z moments of inertia of vehicle about X-, Y-, and Z-axis, respectively, slug-ft^2

K_θ control-system position gain, deg/deg

$K_{\dot\theta}$ control-system rate gain, deg/deg/sec

k gyro transfer function

M control moment, ft-lb

P_c motor chamber pressure, psia

P_N nitrogen tank pressure, psig

p_l local static pressure, lb/sq ft

p_∞ free-stream static pressure, lb/sq ft

q_∞ free-stream dynamic pressure, lb/sq ft

r   radial offset, in.

S   vehicle reference area, sq ft

T   temperature, $^\circ F$ or $^\circ R$

t   time, sec

t_b propellant web burning time, sec

t_f total propellant burning time, sec

V   velocity, ft/sec

W_f expended motor weight, lb

W_m loaded motor weight, weight of entire motor including ignition
          system less external wiring and power supply, lb

W_p propellant weight, total weight of motor propellant less
          ignition-system propellant, lb

w_h consumed hydrogen-peroxide weight, lb

X,Y,Z   rectangular coordinate axis system of vehicle (see fig. 46)

x,y,z   coordinate measured parallel to X-, Y-, and Z-axis,
          respectively

α angle of attack, deg

γ flight-path angle, deg

δ control-surface angular deflection, deg

ϵ displacement error, deg

ζ misalinement angle of roll control jet, deg

η	fin tilt angle, deg
θ	pitch attitude angle, deg
θ_P	pitch-program reference attitude angle, deg
κ	misalinement angle of control jet due to flow angularity, deg
Λ	maximum rocket-motor thrust misalinement angle at ignition, deg
λ	geometric rocket-motor thrust misalinement angle, deg
ξ	structural damping ratio
ρ	density of air, slugs/cu ft
τ	equivalent constant rocket-motor thrust misalinement angle, deg
φ	roll attitude angle, deg
ψ	yaw attitude angle, deg
$\Delta\theta_C, \Delta\varphi_C, \Delta\psi_C$	attitude angle errors due to conical motion of gyro input axes (see eqs. (1)), minutes of arc
$\Delta\theta_K, \Delta\varphi_K, \Delta\psi_K$	attitude angle errors due to cross-coupling of gyro axes (see eqs. (2)), minutes of arc
Ω	pitch and yaw control-jet misalinement angle, deg

Subscripts:

A	altitude conditions
aft	aft of payload center of gravity
fwd	forward of payload center of gravity
g	geometric
i	at ignition
p,q,r	roll, pitch, and yaw, respectively

SL   sea-level conditions

v   vacuum conditions

A dot over a quantity denotes differentiation with respect to time.

VEHICLE DESCRIPTION

General Arrangement

The ST-1 test vehicle, shown in the launching position in figure 1, consisted of the following major structure and rocket-motor assemblies:

Stage	Assembly
1	Base section A Algol-IB rocket motor Transition B-lower
2	Transition B-upper Castor-IE5 rocket motor[a] Transition C-lower
3	Transition C-upper Antares-IA1 rocket motor[b] Transition D Third-stage heat shield
4	Altair-IA5S rocket motor[c] Payload assembly Fourth-stage heat shield Payload heat shield

[a]Designated by manufacturer as the XM-33E5 rocket motor.

[b]Designated by manufacturer as the X-254A1 rocket motor.

[c]Designated by manufacturer as the X-248A5S rocket motor.

The first stage was aerodynamically stable and was controlled by a combination of aerodynamic and jet-vane controls. The second and third stages were controlled by hydrogen-peroxide reaction jets, while the fourth stage was spin stabilized. Stage connection and separation were

accomplished by means of aluminum blowout diaphragms which were installed at the separation plane of each stage. Prior to ignition of the stage rocket motor, the diaphragm served to transfer loads across the separation joint. Upon ignition, separation of the preceding stage occurred as the diaphragm failed from rocket-motor blast pressures.

A drawing of the vehicle showing the general arrangement of major assemblies and components is presented in figure 2(a). Photographs of the assemblies are included in figures 2(b) to 2(k).

<h2 style="text-align:center">Structure Assemblies</h2>

Base section A.- The base section A formed the aft portion of the first stage and is shown in figure 2(b). This section included four cruciform fins and jet vanes, the first-stage hydraulic control system, and the first-stage telemeter equipment and antenna. The base section was attached to the aft bolting ring of the Algol motor and housed the motor nozzle and two aft launch fittings. Launch and checkout umbilical connections were provided in the terminal plate of the two wiring tunnels. The airframe of base section A was constructed of a semimonocoque steel and aluminum shell supported with steel rings, longerons, and a bulkhead at the nozzle exit.

The four cruciform fins, with letter designations as shown in figure 2(a), were of steel rib and spar construction with a steel skin and were attached to flanges on the base-section shell. The fin planform had a 45° sweptback leading edge and a straight trailing edge. The fin streamwise cross section was a 4° half-angle wedge with a 0.25-inch leading-edge radius. A fin-tip control surface and a jet vane were mounted on each fin on the same axis at opposite ends of the control shaft and were hydraulically operated by guidance-system commands. The control-shaft bearing was protected from the exhaust of the Algol rocket motor by steel plates coated with ablative materials.

Transition B.- The transition structure between the first-stage and second-stage motors was designated as transition B and contained the second-stage reaction-control system, a separation blowout diaphragm, and the safe-arm unit of the first-stage destruct system. Photographs of transition B are presented in figures 2(c) to 2(e). The structure was formed of two monocoque sections with the Castor motor nozzle used as the primary load-carrying member. The aft portion of the transition, designated as B-lower, was a steel monocoque structure with steel attachment rings at each end. The forward attachment ring of the B-lower section formed the separation joint between the Castor motor nozzle and the section by means of an aluminum blowout diaphragm. The forward portion of the transition section, designated as B-upper, consisted of split

halves of a glass-fiber laminated outer shell reinforced with internal aluminum frames. The B-upper section housed the second-stage reaction-control jets, the control-system hydrogen-peroxide (H_2O_2) and nitrogen (N_2) tanks, and associated control-system hardware and plumbing.

Transition C.- Figures 2(f) and 2(g) show transition section C, which was a two-piece section joining the second-stage Castor motor to the third-stage Antares motor through an aluminum blowout diaphragm. The structure was monocoque with all structural loads carried in the glass-fiber laminated outer shell. The aft portion of this transition section, designated as C-lower, contained the safe-arm unit of the second-stage destruct system and the destruct-system receivers and antennas. The forward part of the transition (C-upper) housed the components of the third-stage control system, including the reaction-control jets and the hydrogen-peroxide and nitrogen tanks.

Transition D.- Figures 2(h) and 2(i) show the transition D section, which formed the transition structure from the third-stage Antares motor to the fourth-stage Altair motor and contained the guidance package, radar beacon and antenna, guidance telemeter equipment and antennas, and the fourth-stage spin-up mechanism. The transition was made of two sections which separated at the spin-table blowout diaphragm. The aft portion of the transition, designated as D-lower, was a steel structure supported by longerons and end rings. The forward ring provided the support structure for the spin bearings and blowout diaphragm. The forward part of the transition section (D-upper) was located above the spin-bearing assembly and was a magnesium structure which served to transmit loads from the spin-bearing assembly to the Altair motor case.

Payload.- The payload assembly, which carried flight-test instrumentation and telemeter equipment, as well as experimental instrumentation which included radiation counters and magnetic and solar aspect sensors, consisted of the structure and components located forward of the fourth-stage Altair motor. This assembly is shown in figure 2(j) and included the payload collar, payload instrumentation, and payload telemeter equipment. The payload collar was an aluminum ring which was attached to the forward ring studs of the Altair motor. Three equally spaced telemeter antennas extended from the payload collar, and payload instrumentation and telemeter equipment were installed on a rack attached to the payload collar. A glass-fiber laminated cover was provided to shield the instrumentation and telemeter equipment.

Heat Shields

Third-stage heat shield.- The Antares motor was protected from aerodynamic heating during the initial phases of the flight by a split

glass-fiber laminated heat shield. Ejection of this heat shield at ignition and pullaway of the third stage was accomplished by lanyards attached to the second-stage Castor motor.

Fourth-stage heat shield.- The fourth-stage heat shield, shown in figure 2(k), was a stainless-steel structure which extended from the aft end of the payload collar to the spin bearing in transition D. The structure was formed in two units which were locked during flight by a spring-loaded cam mechanism. This locking mechanism was released upon ejection of the payload heat shield. Some of the ejection energy of the payload heat shield was imparted to the fourth-stage heat shield by means of connecting lanyards.

Payload heat shield.- The payload assembly was protected from aerodynamic heating by a heat shield which was formed in two units and attached to shear pins on the payload collar (fig. 2(k)). The heat shield was a semimonocoque structure with an outer shell fabricated from spun and wrapped pieces of René 41 material. Separation of the payload heat shield was accomplished by a ballistic actuator installed in the upper end of the payload assembly.

<div align="center">Guidance and Control System</div>

Guidance and control of the vehicle was provided by a three-axis, body-mounted gyro reference system in combination with a three-axis control system. A schematic diagram showing the relationship of major guidance- and control-system components is presented in figure 3.

Specifications established for guidance- and control-system design required that the system be capable of holding the longitudinal axis of the vehicle to within 2° of the programed pitch and yaw attitudes during firing of the first three rocket motors. In addition, the system was required to be capable of orienting the longitudinal axis of the final two stages to within 0.5° of the programed angle.

Guidance system.- Guidance was confined to the pitch plane, with the yaw and roll orientations maintained at the reference attitudes established at launch. Guidance in the pitch plane was referred to the time and attitude at launch, and the vehicle pitch attitude during flight was varied with time in a series of step functions of pitch attitude rate. Reference attitudes for the guidance system were supplied by three body-mounted miniature integrating gyros (designated as MIG's) and a pitch-axis programer. The pitch-axis programer consisted of a d-c power supply and a timer. The power supply provided the pitch-axis MIG with a torquing voltage proportional to programed pitch attitude rates, and the timer introduced the voltage over the desired time

intervals. The relationship between the pitch-axis MIG and the programer is shown schematically in figure 4. A typical timer and programer power circuit for introducing step input to the pitch-axis MIG torque generator is shown in figure 5. The MIG's were housed in the gyro reference package and were installed with the programer (power supply and timer) in transition section D-lower.

Additional functions of the timer were to initiate other in-flight events such as rocket-motor ignition, heat-shield ejection, and application of voltage to the second- and third-stage reaction-control valves. A typical circuit employed for rocket-motor ignition and application of voltage to the reaction-control valves is shown in the schematic diagram of figure 6.

Miniature rate gyros, hereafter referred to as GNAT's, were used in the feedback loop of each control axis to provide damping for stability and to improve vehicle response to commands and disturbances. The GNAT's were located in transition section C-upper, which surrounds the third-stage rocket-motor nozzle. This location was selected in the interest of reducing the structural or body-bending feedback problem caused by an unfavorable phase shift introduced to the rate gyros by the second body-bending mode at the more forward location in the vicinity of the MIG's.

Pitch program.- The pitch-axis MIG was supplied with torquing voltages proportional to programed rates calculated to produce a zero-lift trajectory. A preliminary pitch program to achieve such a trajectory was obtained by approximating the pitch-rate time history associated with the desired controls-locked, no-disturbance, zero-lift trajectory. The approximation of the initial pitch-attitude program was a series of rate step functions which provided the desired pitch-attitude time history for the flight. Adjustment of the pitch program was required in order to compensate for inherent control-system lags and was accomplished by either or both of two methods: (a) by modifications of the magnitude of the pitch-rate steps, or (b) by time shifts of the steps. Simulated flight trajectories were digitally programed to check the accuracy of the pitch program and to make final adjustments. No attempt was made to adjust the program to account for winds.

First-stage control system.- Control forces during the first-stage motor burning period were provided by a combination of jet vanes immersed in the rocket-motor exhaust and aerodynamic fin-tip control surfaces. During the first-stage coast period, the fin-tip control surfaces alone provided the control forces. The jet-vane control-force and drag characteristics are presented in figure 7. A block diagram of the first-stage control system showing servo and body-bending network dynamics is shown in figure 8(a).

The fin-tip control surfaces were operated by hydraulic servo actuators, and the four sets of fin-tip control surfaces and jet vanes operated independently in pairs for three-axis control. Yaw and roll control was shared by the upper and lower pairs of surfaces (on fins A and C, respectively) which moved simultaneously in the same direction for yaw control and in opposite directions for roll control. Pitch control was provided by the right and left fin-tip control surfaces (on fins D and B, respectively).

Second-stage control system.- Control during second-stage flight was provided by hydrogen-peroxide reaction jets operating as an "on-off" system. (See block diagram of fig. 8(b).) Three-axis control was provided by eight jets (a pitch-up, pitch-down, yaw-right and yaw-left jet, and four roll control jets). Arrangement of the reaction jet motors and nominal thrust levels of the motors are presented in figure 9, with control-force directions given letter designations as indicated. Dual thrust levels were employed in the second-stage to provide a high initial control force at Castor ignition in order to assure "capture" under possible adverse conditions arising from thrust misalinement, aerodynamic instability, and initial attitude error existing at the time of ignition. The term "capture" refers to the relinquishing of control by the systems of one stage and the assumption of control by the systems of the succeeding stage. After capture was effected, the initial thrust levels were reduced approximately 20 percent to provide an additional fuel margin for the remaining burning and coast phases. The high thrust level was realized through a temporary overpressurization of the regulated nitrogen supply by means of an auxiliary nitrogen supply (located in the toroid) and a high-pressure regulator. A schematic diagram of the second-stage reaction motors and associated plumbing is presented in figure 10.

Third-stage control system.- Control during third-stage flight was provided by a hydrogen-peroxide reaction-jet system with two thrust levels in order to conserve the fuel supply during long third-stage coast periods. The arrangement and nominal thrust levels of the third-stage reaction-jet motors are shown in figure 9. Three-axis control was provided by ten jets (large pitch-up and pitch-down jets, with high thrust level; small pitch-up and pitch-down jets with low thrust level; yaw-right and yaw-left jets; and four roll control jets). Letter designations indicating control-force directions are shown for each jet in figure 9.

An acceleration switch was used to detect the end of Antares tail-off, at which time the pitch-jet thrust level was lowered, the pitch and yaw dead bands were reduced, and the yaw and roll control was combined in the roll jets. (The term "tail-off" refers to the period of motor

burning from web burnout to final burnout.) Third-stage hydrogen-
peroxide plumbing was similar to that of the second stage and is shown
in the schematic diagram of figure 11.

Fourth-stage control.- The fourth stage received its spatial orien-
tation from the control exerted on the vehicle by the first three stages.
Stabilization of the fourth stage was effected from a spin rate of
approximately 160 rpm. Spin-up of the fourth stage was developed by
three small rocket motors, each having a total impulse of 40 lb-sec.
These motors were mounted tangentially 120° apart in the skirt of the
fourth stage.

Rocket Motors

First-stage Algol rocket motor.- A drawing showing external dimen-
sions of the Algol-IB motor is presented in figure 12. Qualification
static tests were conducted at temperatures of 90°, 70°, 50°, and 30° F.
The Algol motor used for the flight test was the B6 motor, which was
qualified for firing over a temperature range of 70° to 90° F. Nominal
performance values for the Algol motor are tabulated in column 1
(representative) and column 2 (nominal) of table I. The representative
data in column 1 was used for preflight trajectory calculations, and
the nominal data in column 2 was used for the postflight trajectory
calculations. Time histories of the nominal chamber pressure and sea-
level thrust for the Algol motor are presented in figure 13. The
nominal thrust time history, corrected for the ST-1 preflight tra-
jectory, is shown in figure 14.

Second-stage Castor rocket motor.- The Castor-IE5 rocket motor
developed for the Scout vehicle was essentially a Thiokol XM33 motor.
New developments in hardware for the Scout application were an SAE 4130
steel nozzle, a new pyrogen igniter utilizing a plastic case, and a
propellant to suit requirements of the Scout booster system. The XM33
propellant core was used with no modification. The XM33 motor case was
used with no change in wall thickness. The case was constructed of
SAE 4130 steel with a 0.110-inch wall thickness. External dimensions of
the Castor-IE5 motor used for the flight test are presented in figure 15.

The Castor was qualified for firing over a temperature range from
20° to 100° F. Preflight representative and postflight nominal perform-
ance values are presented in columns 1 and 2 of table II, and time his-
tories of nominal chamber pressure and vacuum thrust are shown in
figure 16.

Third-stage Antares rocket motor.- The Antares-IA1 motor was
developed for use as the third-stage propulsion system for the Scout

vehicle. The chamber was a filament-wound glass-fiber reinforced epoxy resin structure and incorporated integrally wound forward and aft adapters of high-strength aluminum. The forward adapter served as a resonance suppressor-igniter support and the aft adapter served as a nozzle attachment fitting. The nominal wall thickness of the case was 0.100 inch. For maximum strength-to-weight ratio, the ends of the case were wound as ellipsoidal domes. A drawing showing external dimensions of the Antares motor used for the flight test is presented as figure 17.

The Antares motor was qualified for firing over a temperature range from 50° to 100° F. Representative and nominal performance values are presented in columns 1 and 2 of table III, and time histories of the nominal chamber pressure and vacuum thrust are presented in figure 18.

Fourth-stage Altair rocket motor.- The Altair-IA5S motor, developed for the Scout vehicle, had a case fabricated from filament-wound glass-fiber reinforced epoxy resin. The ends were wound as hemispherical domes. The case had a wall thickness of 0.055 inch. Glass-fiber shoulders, called doublers, were wound in the forward and aft ends of the chamber, and 24 studs were uniformly spaced in the face of each doubler. External dimensions of the Altair motor used for the flight test are shown in figure 19.

The Altair motor was qualified for firing over a temperature range from 50° to 100° F. Representative and nominal performance values for the Altair motor are shown in columns 1 and 2 of table IV, and time histories of the nominal chamber pressure and vacuum thrust are presented in figure 20.

Ignition System and Destruct Pyrotechnics

The ignition and destruct systems were two separate and independent circuits. For reliability, each system was dual in itself, and each employed a three-wire series-parallel circuit with one wire common to each half of the dual system.

Ignition system.- The ignition system contained two 37-volt battery power supplies to provide current for ignition, and the programer timer which supplied the signal for initiation. Since the timer contacts were not heavy enough to pass the current required for some ignition functions, a squib relay, located in transition D, was used. A schematic diagram of the complete onboard ignition system is shown in figure 21. A schematic diagram of the first-stage ignition system is shown in figure 22.

An interlock was incorporated in the ignition circuit to insure that the circuit could not become operative because of a malfunction of the timer prior to lift-off. At lift-off, the programer timer was started by removing voltage from a holding relay, and the squib switches were placed in the circuit so that a signal from the timer could send a firing signal to them. The ignition circuit was mechanically and electrically shorted by arming bars until the final countdown. During the countdown, the bars were placed in the armed position to complete the circuit.

The first-stage Algol igniter consisted of a double-basket assembly containing Alclo pellets and black powder, which were initiated by four squibs, two wired in parallel on each side of the circuit. The first-stage motor was ignited through the base umbilical cable by using a 28-volt external battery power supply for each side of the parallel circuit.

A standard pyrogen unit with initiators was used for ignition of the second-stage Castor motor. A pressure switch, mounted on the motor, armed the third- and fourth-stage motors at burnout of the second-stage motor. This switch was locked open prior to the flight, and the buildup in pressure of the second-stage Castor motor released the locking pin. Near the end of chamber-pressure decay, the switch closed to arm the third and fourth stages.

The ignition system of the third-stage Antares motor and the ejection mechanism for the payload heat shield were wired in parallel. The Antares motor igniter consisted of a basket assembly containing boron-potassium-nitrate pellets which were initiated by four 1.3-second delay squibs. These delay squibs allowed ejection of the payload heat shield to be completed before the third-stage motor ignited.

The ignition systems for the fourth-stage Altair motor and spin rockets were wired in parallel. The Altair motor igniter consisted of a two-basket assembly incorporating boron-potassium-nitrate pellets with propellant boost strips which were initiated by four squibs with an 1.8-second delay. This delay was incorporated in order to allow the spin motors to develop the required spin rate for stabilization of the fourth stage prior to ignition of the fourth-stage Altair motor. A dual ignition system was used for the spin motors and contained a special three-wire squib which had two bridge wires and three lead wires.

Destruct pyrotechnics.- The destruct system was designed to provide a reliable dual system for the destruction of the vehicle in the event of erratic flight or large trajectory deviations during the thrusting and coast phases of the first and second stages. In addition, a ground command no-fire unit was placed in the ignition circuit to prevent ignition of the fourth-stage motor and spin rockets in case of a deviation from course after third-stage ignition.

The destruct pyrotechnics consisted basically of a dual-explosive linear shaped charge mounted longitudinally along the length of the first- and second-stage motors. The charge consisted of a 3/8-inch-diameter aluminum tube having an 0.028-inch wall thickness. The tube was formed in a V-shaped groove with a 60° angle for the vee and was loaded with a charge of 1.1 grams per inch. Two safe-arm units, located in transitions B and C, were used on each stage for initiation of the charge.

Vehicle Instrumentation

Standard instrument systems with a broad background of proven flight reliability were used to measure and monitor performance of the vehicle. Four telemeter systems were utilized and consisted of a first-stage FM/AM telemeter installed in base A, a third-stage FM/FM telemeter located in transition D, and two separate telemeters (FM/AM and FM/FM) installed in the payload. Two radar beacons and command systems were included in the instrumentation. An S-band radar beacon located in transition D assisted Wallops Station S-band radar in obtaining tracking to fourth-stage ignition. A high-power C-band beacon located in the payload was operated by Wallops Station C-band radar to obtain trajectory data as far beyond fourth-stage burnout as possible. A radio-frequency command system and associated circuitry for command-destruct of the first or second stage was located in transition C. A second command system, located in transition C-upper, was a "no-fire" system with the capability of preventing ignition of the fourth-stage rocket motor. A summary of the instrument systems installed in the vehicle is presented in figure 23.

Telemeter systems.- Descriptions of all the channels of the four telemeter systems are presented in tables V to VIII. A drawing showing approximate locations of the telemeter components in the vehicle is presented in figure 24. Coordinates of the linear accelerometers installed in base A and of the linear accelerometers and rate gyros installed in the payload are given in table IX.

The first-stage telemeter was an FM/AM system which transmitted 1.7 watts of radio-frequency power at 225.7 megacycles. A block diagram of this system is shown in figure 25. Primary measurements included hydraulic-control-system performance, Algol motor chamber pressures, tail-fin skin temperatures, servo-compartment temperatures, and local linear accelerations of the vehicle. Frequency-modulated subcarrier oscillators (designated as S.C. oscillators) in the 100- to 200-kilocycle frequency range were linearly mixed in a modulator which amplitude modulates the carrier of a crystal-controlled transmitter. The pressure, acceleration, and fin-position sensors were variable-reluctance transducers designed to modulate the subcarrier oscillators directly. Special

design oscillators were used for thermocouple and thermistor measurements. In each case, the maximum deviation of the subcarrier oscillators was ±1,500 cps and allowed a channel frequency response of 300 cps for a modulated index of 5.

The third-stage telemeter (guidance telemeter) was a standard IRIG (Inter-Range Instrumentation Group of the Range Commanders), 18-channel, FM/FM system which radiated 12 watts of radio-frequency power at 259.7 megacycles. This telemeter, shown in the block diagram of figure 26, was developed from commercial components which were adopted for monitoring performance of the guidance package in transition D and for monitoring the second- and third-stage reaction-control systems. In order to obtain as much data as possible from the 18-channel system, FM/FM submultiplexing was used to measure the gyro rate and displacement error signals where two subcarrier channels were used to perform the required measurements in the three control planes. Another saving of subcarrier channels was realized by using the same oscillator for telemetering both second- and third-stage rocket-motor chamber (or headcap) pressures, and by using the same four oscillators for monitoring similar reaction-control motors in both the second and third stages. This technique was possible since the second-stage measurements occur prior to the third-stage measurements. Identical sets of transducers were installed in each stage to perform the measurements. The majority of sensors used in this system produced high-level voltages and required a minimum of signal conditioning. Amplifiers were required for the low voltage levels produced by thermocouples and vibration sensors. A phase demodulator and amplifier were required to condition each gyro error signal for suitable telemetering.

The block diagrams for the two payload telemeters are shown in figure 27. A five-channel FM/AM telemeter, similar to the first-stage telemeter, radiated 1.7 watts at 244.3 megacycles. Vehicle angular rates, local longitudinal linear accelerations, and payload external temperatures were measured by this system. The other payload telemeter was a 14-channel FM/FM system similar to the third-stage telemeter. This system radiated 8 watts of radio-frequency power at 240.2 megacycles and measured fourth-stage rocket-motor chamber pressures and pay load environmental conditions (temperatures, accelerations, vibrations, and cosmic radiation). Vehicle aspect-sensing devices were also monitored by this system in an attempt to obtain an independent overall measurement of guidance performance.

Telemeter antennas.- Figure 28 presents antenna performance data for the first-stage telemeter. A slot antenna which measured 8 inches by 1/2 inch was used and was installed with the length parallel to the base ring at the bottom of the vehicle. Provisions were made for fine-tuning adjustment after installation of base A over the motor nozzle.

Figure 29 presents antenna performance data for the third-stage telemeter. Three 10-inch-long end-excited spike antennas with 30° sweepback were located 120° apart circumferentially around transition D. The antennas were machined from molybdenum and were housed in a ceramic insulator which prevented voltage breakdown due to high altitude and aerodynamic heating.

Figure 30 presents antenna performance data for the payload telemeters. Two spike antennas, identical to those previously described, were installed 180° apart in the payload collar. A cavity-type diplex device was used which allowed both telemeters to transmit through the same pair of spike antennas.

In all cases, the antenna data presented were obtained from measurements performed on flight antennas installed in flight sections with transmitters operating on internal battery power. For the payload and transition D measurements, third- and fourth-stage empty rocket-motor cases were attached.

Radar- and radio-beacon antennas.- High-gain-exponent horn-type antennas were used for radar beacons in order to obtain a directional pattern off the rear of the vehicle during flight. The S-band antenna radiated power from an S-band radar beacon located in transition D. The horn was constructed to conform with the circular shape of the transition section and was insulated from the external skin of the vehicle. A covering of stainless steel was provided to protect the antenna against aerodynamic heating. Figure 31 presents the performance data for this antenna.

Figure 32 shows the performance data for the C-band horn antenna which radiated power from the C-band radar beacon located in the payload. The design principle for this antenna was the same as that incorporated for the S-band horn antenna. Since the outer edge of the payload collar extended beyond the fourth-stage rocket-motor case, the antenna was installed inside the collar. The antenna radiating end was covered during the initial portion of the flight by the fourth-stage heat shield. Prior to heat-shield ejection, a small stub antenna was used. After ejection, the beacon was transferred to the horn antenna by means of a coaxial switch.

The antenna performance data presented were obtained from flight antennas installed in flight transition sections. Since the third- and fourth-stage rocket motors were wrapped with aluminum tape to enhance the directivity of these antennas, measurements were performed with transition sections attached to empty rocket-motor cases covered with heavy-gage aluminum foil.

A pair of spike antennas were installed in the payload collar to radiate power from a radio beacon used to obtain Doppler velocity data. However, as a result of radio-frequency interference in the command systems, the radio-beacon system was not energized during the flight, and for this reason, radio-beacon data are not presented.

Command systems.- Functional block diagrams for the two command systems are presented in figure 33. The primary command system accomplishes first- and second-stage thrust termination by splitting the cases of the rocket motors. If the command should occur prior to second-stage motor tail-off, the third- and fourth-stage ignition circuits are disabled and firing of these stages is prevented. Two command receivers detect ground-transmitted signals through separate antennas. These signals are routed through a junction box which provides receiver test points and controls the transfer of receivers from external-ground to internal-battery power. The signals operate power relays which apply voltage from pyrotechnic batteries to the igniters. Each stage contains two igniters operated by separate battery supplies as shown in figure 33. Arming is accomplished in flight prior to command destruct, and loss of radio-frequency carrier automatically commands thrust termination. A high degree of reliability was obtained since each receiver was capable of initiating all igniters. Pyrotechnic batteries were charged from the launch complex late in the countdown.

A separate command system was installed in the third stage to prevent fourth-stage ignition up to the instant of programed ignition. Fourth-stage hold-fire signals were routed through a junction box which functioned in the same manner as described for the primary system. The command signals actuate latching relays which open the ignition wires to the fourth-stage motor. An arming relay interlocks the hold-fire relay and requires actuation prior to the ignition hold-fire relay. Each receiver was capable of interrupting ignition by operating separate relays. If ignition hold-fire was commanded by either relay, a telemeter indication was obtained from the third-stage guidance telemeter.

Since the command systems were located in transitions C-lower and C-upper, which were constructed of nonconducting plastic, metal bow-tie antennas were used. Two bow-tie antennas constructed of brass were used for each receiver. Each antenna was 11 inches long, and each pair of antennas were installed 180° apart circumferentially with the length parallel to the longitudinal axis of the vehicle. Figure 34 presents the performance data for four bow-tie antennas used in sets of two for each receiver. These data were obtained with flight antennas installed in flight sections.

Radiation instrumentation.- A radiation sensor installed in the payload consisted of a transistorized Geiger-Müller counter with a

self-contained power supply. The output from the package was d-c voltage ranging from 0 to 5 volts which was fed to a subcarrier oscillator in the telemeter. Full-scale output voltage was obtained with an input of 30,000 counts per minute. The instrument was designed to have a non-linear output to obtain greater sensitivity in the lower counting rates. A photograph showing the inside of the instrument is presented in figure 35.

Vibration instrumentation.- Crystal accelerometers were installed in transition D and the payload to obtain environmental vibration measurements during third- and fourth-stage motor burning. Three crystal accelerometers (see table VI) were mounted on the guidance package in transition D with sensitive axes parallel to the normal, transverse, and longitudinal axes of the vehicle. These accelerometers were attached to the mounting ring of the guidance package at a circumferential location which was at a 60° angle from the vehicle yaw axis. Three other crystal accelerometers (see table VIII) were mounted with sensitive axes parallel to the vehicle axes on the payload telemeter support structure.

LAUNCH OPERATIONS

Flight Plan

The flight plan for the ST-1 test vehicle was established essentially for a probe mission which would permit radar tracking and telemeter acquisition through fourth-stage burnout from the NASA Wallops Station launch site. The flight plan for the test was based on a no-disturbance trajectory computed from six-degree-of-freedom equations of motion over a rotating, spherical earth. Vehicle launch orientation for the computed trajectory was defined by an azimuth heading of 107° from true north and an elevation angle of 85°. Apogee for the flight with a 193-pound payload was predicted to occur at an altitude of 2,020 nautical miles with an impact range of 4,400 nautical miles. A maximum velocity of 22,000 feet per second was expected to occur near fourth-stage burnout. Staging and events programed for the flight are summarized in the following table:

Stage	Event	Nominal time, sec
1	Algol rocket motor thrusting Coast to an altitude of 130,000 feet	0 to 44.2 44.2 to 62.8
2	Castor rocket motor thrusting Coast for 5 seconds	62.8 to 102.8 102.8 to 107.8
3	Ejection of heat shields Antares rocket motor thrusting Coast for 30 seconds Pitch-over program (1 deg/sec for 15 seconds)	107.8 107.8 to 147.8 147.8 to 177.8 152.8 to 167.8
4	Fourth-stage spin-up Altair rocket motor thrusting Coast to splash	177.8 177.8 to 216.6 216.6 to 3,222 (53.7 min)

The programed coast to an altitude of 130,000 feet during first-stage flight was dictated by control requirements of the aerodynamically unstable combination of the second, third, and fourth stages. In addition, aerodynamic heating during second-stage thrusting is alleviated at the higher altitudes. A 5-second coast was programed during second-stage flight to insure burnout of the Castor motor before ignition of the third-stage Antares motor. The final 30-second coast period during third-stage flight included a pitch-over program to test the operation of the third-stage control jets.

Range Facilities

Scout launcher-tower.- The launcher-tower for the Scout vehicle provides the facilities for erection, servicing, and launching of the vehicle and is shown in the photographs of figures 1 and 36. The tower is a structural steel open framework erected on concentric rails set in a concrete launch pad. The launcher is an integral part of the tower and contains provisions for positioning the vehicle to the desired launch elevation angle. The entire launcher-tower can be rotated for control of launching azimuth.

The tower is provided with erection and servicing facilities which include an elevator, an A-shaped frame with winches and hoist for upper-stage assembly, and nine working levels having extension work platforms which close around the vehicle at the payload and transition assembly levels. Deluge showers are installed at three working levels to afford immediate first aid to personnel during operations involving the use of hydrogen peroxide. An intercommunications system with jack-boxes at all working levels permits coordination and direction of operations. Electrical installations provide outlets for power, floodlights for night operations, and aircraft warning lights. A

transparent Lucite covering is available to enclose the vehicle after erection from the first platform level upward. The enclosure is supplied with air which is thermostatically controlled.

All operating units on the tower are hydraulically powered. The elevation position and umbilical ejection systems are controlled from the blockhouse, whereas individual controls are installed in the tower for all other operating units.

Data acquisition system.- The locations of Wallops Station range facilities are shown in figure 37. Tracking radars, telemetry, and tracking cameras were utilized to gather data during the test. Three tracking radars used to obtain trajectory data included the RCA AN/FPS-16, the Reeves Mod. II SCR-584, and the SCR-584. Additional tracking data were supplied by the Millstone Hill experimental radar of the M.I.T. Lincoln Laboratory at Westford, Massachusetts.

Velocity data during the initial portion of the flight were supplied by a model 10A Doppler Velocimeter, and photographic coverage was obtained from fixed cameras and from tracking cameras located at the stations shown in figure 37.

Wallops Station telemeter receivers were used to record data from all four telemeter transmitters installed in the vehicle. In addition, real-time readout on several performance channels was obtained for "quick-look" data from a Goddard Space Flight Center telemeter trailer. A backup for this station was provided by a Wallops Station sea-range telemeter trailer.

Flight Safety

As described previously, a command-destruct system was incorporated in the vehicle which provided a destruct ability such that the vehicle could be destroyed if the first- and second-stage flight became erratic. In addition, a command "no-fire" system was used for withholding ignition of the fourth-stage rocket motor if third-stage flight became erratic. In order to destruct the first or second stages, shaped charges are ignited which rupture the rocket-motor case and terminate thrusting of the motor. At the same time, the circuit to a decaying pressure switch on the second-stage motor is broken and firing of the subsequent stages is prevented.

Wallops Station tracking radars (RCA AN/FPS-16, Reeves Mod. II SCR-584, and SCR-584) were used for flight safety. Each radar displayed its output on plot boards in the azimuth (ground) plane and in the elevation (vertical) plane. The azimuth tracks of the plot boards were

laid off with azimuth limits to the north and south of the desired
nominal azimuth track. Equally spaced destruct lines for each stage
(up through the end of third-stage coasting flight) were plotted parallel
to the northern and southern azimuth limit lines so that at any time the
vehicle crossed a destruct line, thrust could be terminated or withheld.
The elevation plot of each radar was laid off similarly.

For first-stage flight, the northern azimuth limit was a line just
south of Assateague Island and the southern limit was determined by
limiting the first-stage impact to north of the free aircraft corridor
into the Norfolk, Va., area. These azimuth limits were 067° true and
144° true from the Scout launcher-tower. For second-stage flight, the
determination of the azimuth limits were based on erratic motion during
third-stage flight, since the third stage did not have destruct capa-
bility. The second-stage azimuth limits for allowing the third-stage
to fire were $\pm 20^\circ$ from the nominal trajectory. Similarly, the flight
path and attitude of the third stage just prior to fourth-stage ignition
established a safe limit for allowing the fourth stage to fire. The
third-stage azimuth limits for allowing ignition of the fourth-stage
motor were $\pm 8^\circ$ from the nominal trajectory.

The elevation destruct lines were held at 90° elevation until the
flight-path angle fell below 80°. Thereafter, the upper vertical
destruct line was held 10° above the nominal flight-path angle. Calcu-
lations showed that pitch-down did not present a range safety problem
for any of the stages.

In order to detect tumbling, especially during the third-stage coast
period, a real-time telemetry system measuring vehicle angular rates and
longitudinal acceleration was displayed.

As a backup to the tracking radars, four sky screens were used to
view the vehicle from lift-off until it was out of sight. Direct com-
munications with the operator of each sky screen were maintained so that
command destruct could be initiated if the vehicle crossed any of the
sky-screen limits. The sky screens were positioned at the locations
shown in figure 37. One sky screen was oriented along each first-stage
azimuth limit; one was placed 90° to the flight path; and one was posi-
tioned in line with the coastline.

Preflight Measurements and Calibrations

Vehicle alinement.- Geometric alinement of the vehicle was verified
by inspection of all components prior to assembly. The concentricity
and perpendicularity of each control mounting surface was measured and
ascertained to be within the established tolerances.

After erection on the launcher-tower, the entire vehicle was surveyed with theodolites. Reference marks placed on the top and bottom of each motor in the pitch and yaw planes were used to measure offsets from the plane defined by the upper and lower reference marks on the first-stage Algol motor. Positive values of offset measurements in the following table indicate misalinements toward the tower side of the vehicle in the pitch plane, and positive values in the yaw plane indicate offsets to the left of the yaw axis (viewed from the tower side):

Reference mark	Body station, in.	Offset, in., from -	
		Pitch plane	Yaw plane
Low mark, Castor	438	-0.0625	0.0625
High mark, Castor	253	-.1250	.0625
High mark, Antares	131	-.1250	.1250
Mark on payload collar	36	-.1250	.1250

Rocket-motor alinement.- Measurements were made on each rocket motor to establish the extent of nozzle misalinement and radial center-of-gravity offset in order to obtain a maximum geometric thrust misalinement angle representative of ignition conditions (exclusive of any effects present from burning such as nozzle erosion or gas swirl). The rocket-motor alinement measurements obtained are defined in the following sketch:
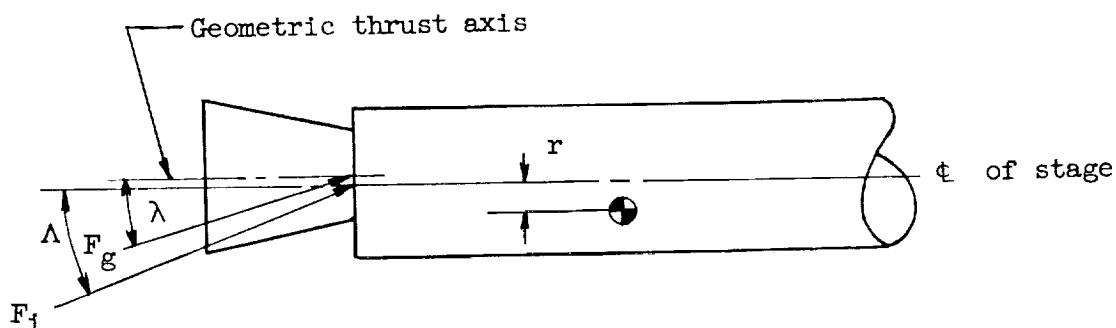
The symbol λ denotes the geometric thrust misalinement angle with the assumption that the geometric thrust axis passes through the centroids of the cross-sectional plane areas at the motor throat and exit. Radial center-of-gravity offset with respect to the center line of each stage is designated as r, and the maximum geometric thrust misalinement angle at ignition is designated as Λ.

The geometric alinement measurements for each rocket motor are listed in the following table:

Rocket motor	r, in.	λ, deg	Λ, deg
Algol	[a]0.250	0.006	0.054
Castor	.108	.008	.049
Antares	.020	.024	.043
Altair	.010	.0095	.036

[a]Assumed value.

It was not possible to obtain the radial center-of-gravity offset of the Algol motor with the facilities available; therefore, a value of 0.250 inch was assumed. It should be noted that precise orientation of the rocket-motor alinement measurements with respect to the pitch and yaw planes was not determined. The alinement data given here represent maximum values, and it is assumed that deviations were in the same plane and were additive.

Fin alinement.- Inclinometer measurements were taken at several stations along one chord line of each of the first-stage fins to determine the effective tilt angle of each fin in the pitch and yaw planes. A typical fin measurement is illustrated in the following sketch:
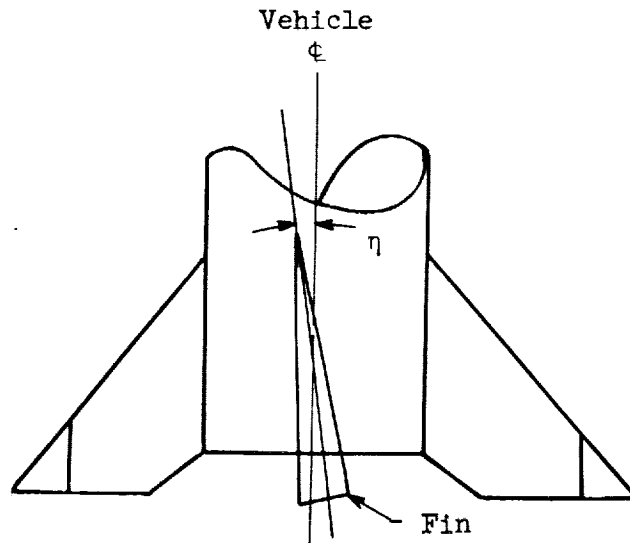
The tilt angle is designated as η and was measured with respect to the vehicle center line. Direction of the tilt angle for each fin is indicated by the direction the vehicle would move as the result of the

misalinement of that fin alone. The tilt angle for each fin, and the effect of this angle on the motion of the vehicle, is presented in the following table:

Fin	η, deg	Effect of tilt angle
A	0.200	Yaw left
B	.016	Pitch up
C	.042	Yaw right
D	.025	Pitch up

With the exception of an apparent deviation in fin A, which was later attributed to the measurement of a local bump in the surface, all values were nominal.

Control-jet alinement.- Angles and displacements as shown in the following sketch were measured to determine the extent of second- and third-stage control-jet misalinements:

Second stage   Third stage
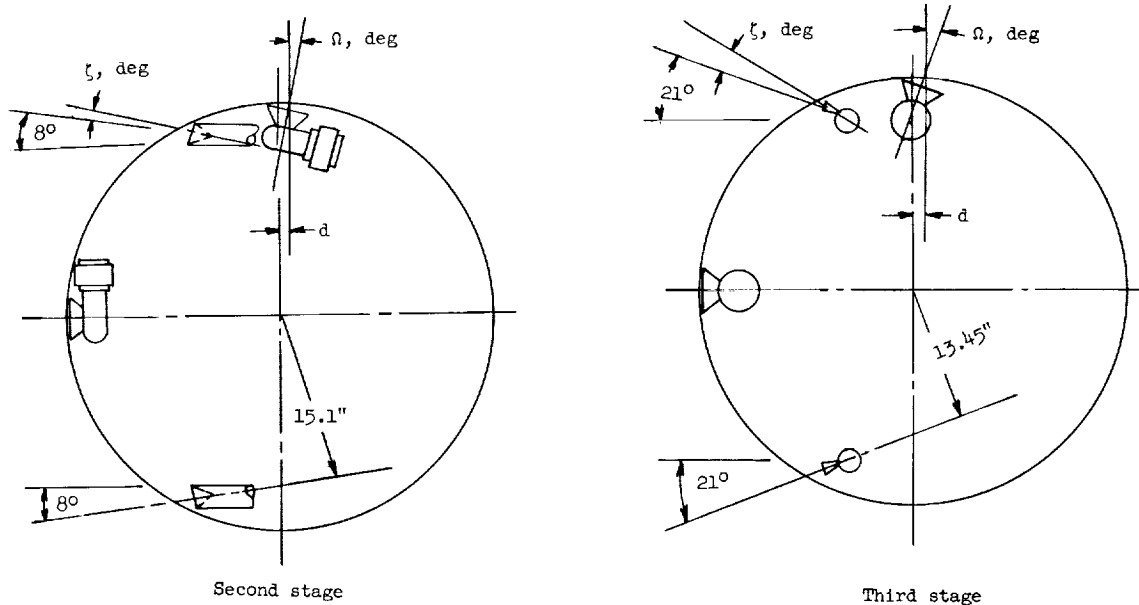
The misalinement angle and displacement of the yaw and pitch control jets are designated as Ω and d, respectively. The misalinement angle of the roll-control jets is designated ζ. All angles and displacements are positive as shown. The results of these measurements obtained on the second- and third-stage control jets are tabulated as follows:

Jet motor	Second stage			Third stage		
	Ω, deg	d, in.	ζ, deg	Ω, deg	d, in.	ζ, deg
Pitch up	0.985	0	---	0.067	0	---
Pitch down	1.163	0	---	-.029	0	---
Yaw right	.925	0	---	.019	0	---
Yaw left	.825	0	---	.029	0	---
Roll, upper left	-----	---	0	-----	---	0
Roll, upper right	-----	---	0	-----	---	0
Roll, lower left	-----	---	0	-----	---	0
Roll, lower right	-----	---	0	-----	---	0

It should be noted that the second-stage pitch and yaw control jets were deliberately offset in the same direction by approximately 1°, whereas the other misalinements were nominal. The reason for the offset was a flow angularity inherent in the design. The flow angularity produced rolling moments which were recorded during operation of the section on a specially instrumented test stand. Side forces acting at the throat of the nozzle were correlated with the corresponding amount of flow angularity, and the results are plotted in figure 38. These data were used as a basis for establishing an intentional clockwise cant angle of 1.1° for the second-stage pitch and yaw jets so that the resultant thrust vector would pass through the vehicle center line.

Vehicle mass properties.- Nominal time histories of the vehicle moments of inertia, center-of-gravity locations, and corresponding control and thrust disturbance moment arms are presented in figure 39 for the first three stages of flight. These data are based on both estimated and measured mass properties of the rocket motors, transition sections, and components. Actual measurements obtained included the mass properties of the third and fourth stages, and the weights and center-of-gravity locations of the transition sections and second-stage Castor motor. A lack of sufficiently large and complex weighing and swinging facilities precluded actual measurement of the mass properties of the first-stage Algol motor. A weight breakdown by major assemblies and components is presented in table X, and a summary of the vehicle mass properties based on nominal flight events is given in the following table:

Flight event	Nominal time, sec	Approximate vehicle weight, lb	Center-of-gravity station, in.	I_Z or I_Y, slug/ft^2	I_X, slug/ft^2
Launch	0	36,842	539.0	337,648	1,393
First-stage burnout	44.2	17,743	413.0	194,948	473
Second-stage ignition	62.8	13,208	296.0	36,678	386
Second-stage burnout	102.8	5,658	242.0	24,500	174
Third-stage ignition	107.8	3,510	140.5	1,474	90
Third-stage burnout	147.8	1,388	110.3	860	40
Fourth-stage ignition	177.8	726	62.4	62	7
Fourth-stage burnout	216.6	262	54.5	23	3

Guidance- and control-system checkout and calibration.- Performance of the guidance- and control-system components as an integrated system was verified before the flight on four different occasions during the preflight checkout phase. Preliminary systems checks were conducted prior to the final qualitative checkout of the control system during the final countdown. The preliminary systems checkouts were used to verify quantitatively the specified performance of the guidance and control system, to permit vehicle telemetry calibration, and generally to assure that all components and associated wiring were satisfactory.

The first preliminary checkout consisted of "flying" the guidance and third-stage control system in conjunction with telemetry on a three-axis inertial frame mounted on an air bearing. The second preliminary checkout was a systems check which was conducted in an assembly building with all guidance and control components installed in the flight-section structures, which had been assembled on empty rocket-motor cases and electrically interconnected by interstage wiring harnesses. A third preliminary systems checkout was performed after erection of the complete vehicle, including live rocket motors, on the launcher-tower prior to the start of the actual countdown. This checkout provided assurance that the final preflight operation of the guidance and control system remained satisfactory after the sections were assembled on the flight rocket motors and also verified compatibility between the launcher and block-house wiring complex.

The final qualitative checkout of the control system was made at the launcher-tower just prior to the flight and followed a format that was essentially the same as that for the preliminary systems checkout on the launcher-tower. The intent of the final checkout was to assure that operation of the guidance and control system on the launcher-tower was comparable to the performance exhibited during the preliminary systems checks under more controlled conditions.

Of primary interest in the guidance- and control-system checkout were the position and rate closed-loop gains. These gains were checked in the first stage by a comparison of measured control-surface deflections obtained from varied magnitudes of simulated control-system position and rate error signals. Plots of control-system position and rate gains in pitch, yaw, and roll for the first-stage are presented in figure 40 together with the range of acceptable deviations from nominal, which are indicated by the shaded areas. In addition to gain checks on the first stage, frequency-response checks were performed on each hydraulic fin-position servo to insure that the dynamic performance was in accordance with previously established dynamic operational criteria. The frequency-response criteria and a typical measured response are presented in figure 41(a). The frequency-response criteria shown include the effects of a body-bending network on servo response. The shaded area depicts the region of tolerance considered permissible in terms of measured phase and amplitude values and the circular and square symbols represent a typical measured response. In order to assure position-servo design slewing rates of the position servos which were specified for operation under load, step inputs were applied to the servo under various combinations of control circuitry and a hinge-moment loading of 50 inch-pounds per degree.

Slewing rates were determined for the various servo circuitry and load conditions from a measure of the slope of the initial (linear) portion of the fin deflection curves shown in figure 41(b). A comparison at the slopes indicates the effects of hinge-moment loading were not significant; however, as might be expected, the effect of the body-bending network was apparent and was responsible for deterioration in rise time of the actuator response. With the body-bending network removed, the slewing rate was well above the specified requirement of 150 deg/sec for a 1,000 inch-pound hinge-moment load.

Phasing and gain checks were conducted on the second- and third-stage control systems with simulated guidance rate and position error signals. Results of the gain checks are plotted in figure 42 in terms of dead bands and switching slopes, with nominal specified dead bands shown as shaded areas. The switching slopes show some switching hysteresis in the differences exhibited by the measured points designated "out" and "back."

Operational tests were conducted on the programer during systems checks to verify the proper time sequence of events to be initiated during the flight, including the sequence of events for the pitch program. The schedule of in-flight events initiated by the programer is given in table XI. The integrity of the pitch program, as indicated from the total pitch angle for the flight, was checked on the launcher-tower. This check was carried out with the inertial reference package mounted on the Griswold servo dividing head, so that the pitch

displacement error could be essentially maintained at zero by manually operating the Griswold servo dividing head as the pitch MIG was being torqued through the required angle. The position of the first-stage pitch fins was monitored to assure a minimum error at all times during the check.

A calibration was conducted on the second- and third-stage control systems to correlate hydrogen peroxide consumed with nitrogen main-tank pressure decay while the vehicle was on the launcher-tower. This calibration served to ascertain the amount of hydrogen peroxide that would be used in the jet-burp check (short pulses to each jet motor in order to warm up catalyst beds) performed just prior to launch and to establish a reference for obtaining a quick estimate of hydrogen peroxide consumed during the flight from a review of the telemetered nitrogen-pressure time history. The calibration also provided another source for correlation of hydrogen-peroxide consumption with data obtained from cycling analyses. The results of the preflight hydrogen-peroxide fuel calibration test are presented in figure 43. The calibration curves of figure 43 were established on the basis of one set of initial main- and toroid-tank pressure conditions. These curves were adjusted for preflight conditions existing at launch by following the procedure illustrated in the following sketch:
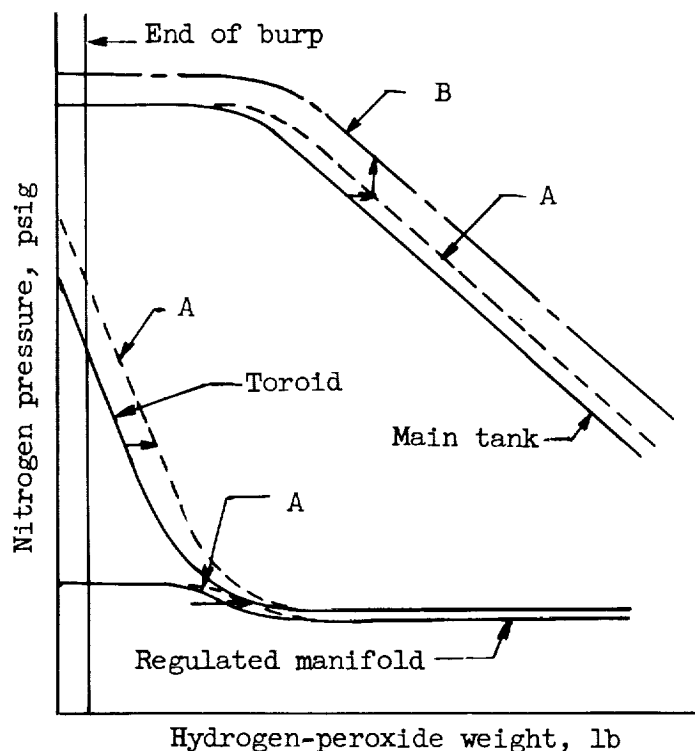
For the second stage, all curves (solid lines in sketch) were displaced to the left or right (A curves) by an amount necessary to set the initial toroid pressure to launch pressure after the pressurization squib was blown. Next, the main-tank pressure curve was moved down or up (to curve B) as required to agree with the main-tank pressure at the time of launch. Since the third stage did not include auxiliary pressurization, the nitrogen-pressure curve was shifted up or down as necessary to coincide with the pressure at the time of launch.

Figure 44 exhibits typical responses of all the control jets in the second and third stages when activated by a short pulse at sea-level conditions. The steps in the valve signal trace indicate opening or closing of the hydrogen-peroxide solenoid valves (lower level) and the buildup in motor chamber pressure (upper level). The responses shown are characteristic of the results obtained from motors that have hot catalyst beds from previous pulses and are, in general, faster than typical cold-motor starts. Hot-motor starts were assured by programing a 200-millisecond pulse to each motor approximately 5 minutes before the flight.

Control-system monitored data.- As each operation of the countdown progressed, control-system parameters considered to be critical were continuously monitored until just before launch time. Of particular interest during this period were data pertinent to the second- and third-stage hydrogen-peroxide systems after their servicing for flight at a approximately minus 8 hours. Time histories of second- and third-stage nitrogen line temperatures and main-tank pressures, and hydrogen-peroxide supply-tank temperatures were recorded and are plotted in figure 45. During the countdown, nitrogen pressures were monitored closely to detect the presence of system leaks, and hydrogen-peroxide supply-tank temperature records were observed for possible upward trends which might indicate spontaneous decomposition of the hydrogen-peroxide supply.

In order to assure satisfactory operation of the guidance system during flight, specifically where position gains and inertial reference were concerned, gyro (MIG) block heater cycling data were obtained during the last 2 hours preceding launch. Since it was possible for high-temperature ambient conditions surrounding the guidance package prior to launch to reduce block heater cycling to the extent that in-flight aerodynamic heating could become critical (heater stop cycling in the off position), cooling air was supplied to transition D-lower until guidance umbilicals were pulled. Figure 45 presents a representative but not complete actual time history of the variation of the MIG gyro heater duty cycle. The reduction in duty cycle as the time of launch neared was attributed to heating from guidance and control components and the telemetry package. Telemetry was turned on somewhat later than guidance and resulted in the rather fast temperature rise of

the telemeter compartment temperature shown on the same plot with gyro block heater duty cycling time history.

Other quantities monitored, but not presented here, were MIG and GNAT motor current and gimbal position indications, 37- and 28-volt power-supply voltage and current, and 400-cps power supply.

Control-system preflight malfunctions.- After erection and assembly of the ST-1 vehicle on the launcher-tower, subsequent system checkouts and several operational countdowns conducted prior to the firing revealed numerous component malfunctions. In two instances, these malfunctions were of such nature that the firing was aborted in the final moments of countdown. The more significant component failures experienced are listed, in the chronological order of their occurrence, as follows:

1. Several hydrogen-peroxide motor chamber-pressure switches and a relay box, both used in telemetering to signify second-stage control-jet operation, were found to be defective.

2. A program event output relay in one timer and prelaunch monitoring circuitry in another failed.

3. An inverter was replaced because of damage caused by a cracked insulating washer and shorted diode.

4. A pitch MIG gyro was replaced because of an open spin-motor winding.

5. A modulator board in the first-stage servo amplifier was replaced in order to provide a greater range of trim adjustment for the first-stage control surfaces.

DATA REDUCTION AND ANALYSIS

Radar Data Reduction

Trajectory data presented for the flight test are based mainly on the results obtained from the RCA AN/FPS-16 tracking radar. Altitude, range, and velocity of the vehicle were derived from FPS-16 raw data which were recorded numerically and used in conjunction with an IBM 650 digital computer programed for an oblate earth. All reduced radar data were converted to the launch-site reference. It should be noted that the vehicle surface range represents the distance over an arc length from the launch site to a projection of the vehicle position on the surface of the earth. Data furnished by supporting radar units were reduced similarly for comparative purposes. Velocities obtained from

both the FPS-16 and SCR-584 radars were corrected for prevailing winds as measured by rawinsonde instrumentation. Free-stream dynamic pressure and Mach number were calculated up to an altitude of approximately 93,000 feet by using atmospheric data furnished by rawinsonde. For altitudes greater than 93,000 feet, the ICAO standard atmosphere was assumed and used directly, since measured atmospheric data at the higher altitudes were not obtained during this test. It is interesting to note that a comparison between rawinsonde and standard atmospheric data from sea level to 93,000 feet showed fairly good agreement.

Telemeter Data Reduction

Figure 46 shows the sign convention used to designate positive directions for the telemeter measurements of vehicle linear accelerations, angular velocities, and control-surface deflections. Unless positive directions or direction of vehicle motions are specified for the telemeter measurements of these quantities, the sign convention shown in figure 46 applies.

Trajectory Computations

All computations used for trajectory analyses were made with an IBM 7090 electronic data processing system programed for a six-degree-of-freedom, rotating, spherical-earth trajectory. In all cases, the flight results which are based on an oblate earth are compared directly with the calculated trajectories, since the differences between an oblate- and spherical-earth trajectory for these ranges are negligible. Results from the following two calculated trajectories were used for comparison with flight results:

1. Preflight calculated trajectory: This calculation was used to establish the flight plan for the test and used only the information that was available before the flight (no winds, no thrust misalinements, and predicted nominal motor performance). Comparison of the preflight trajectory with the measured trajectory represents an overall accuracy of the system.

2. Postflight calculated trajectory: This calculation was based on measured flight data which included winds, actual rocket-motor performance, and thrust misalinements. The wind profiles used in this calculation are compared with those measured 1 hour after the time of flight in figure 47. The thrust-time variations used are compared with flight measurements in figure 48. Comparison of the postflight calculated trajectory with flight data and with preflight calculated data was used in an attempt to estimate the effects of the variables which were changed.

A simulation study was made in order to obtain estimates of the disturbances that might have acted on the vehicle during the early portion of its trajectory. It was assumed that the two predominant disturbances acting on the vehicle during the first-stage thrusting period were winds and thrust misalinement. Since wind measurements were obtained near the time of flight, the thrust misalinement was the primary unknown. However, on a controlled test vehicle during first-stage burning, the control-surface deflections themselves should provide an indication of the magnitude and direction of the thrust misalinement. Of obvious importance to the determination of thrust misalinement from the control-surface deflections is a reasonably accurate knowledge of the control-surface effectiveness. The effectiveness coefficients of the jet vanes and aerodynamic control surfaces have been determined through static tests of the rocket motors, wind-tunnel tests, and theoretical estimates.

It should be noted that the attempt here was not to correlate calculated time histories point for point with flight data, but merely to obtain a reasonable estimate of thrust misalinement relative to the design value. Therefore, certain assumptions were made to simplify the calculations. These assumptions were as follows: All control-system parameters were nominal values and remained constant during the flight; the launch conditions and programed pitch rates were as specified; the winds used in the calculations were the horizontal winds measured near the time of flight. The wind-velocity profile used in the program up to an altitude of 6,000 feet (about the first 14.5 seconds of flight) is presented in figure 47(a). The wind-velocity profile for altitudes above 6,000 feet was obtained by joining the magnitude of the wind velocity (48 ft/sec) at 6,000 feet (balloon data) to the rawinsonde wind data shown in figure 47(b). An average wind azimuth of 260° from north was selected for the flight simulation.

Vibration Data Analysis

Preliminary analysis of the vibration data consisted of an analysis of the variation of frequency with amplitude from the data obtained from the normal-vibration accelerometer mounted on the guidance package for the time during third-stage burning. This analysis was performed on a Davis wave analyzer using 2-second tape loops for a frequency range of 0 to 4,000 cps with a filter nominal bandwidth of 20 cps and the average linear mode of operation. To examine amplitudes further at various frequency ranges, oscillograph records of the rectified signals were made. The resulting record was a trace of the envelope of the wave amplitude. These records were made by using various bandpass filters and low-pass filters. Calibrations for all records were obtained from channel frequency deviations at the playback station. A more detailed analysis of

the variation of frequency with amplitude for the guidance-package vibrations in the normal plane was performed at the Pacific Missile Range by using 1-second intervals for a frequency range of 0 to 4,200 cps and the average linear mode of operation for the wave analyzer. The filters used in this analysis had a nominal bandwidth of 5 cps.

Accuracy

Telemeter measurements.- Tables V to VIII present accuracies of the measurements recorded by telemeter instrumentation in terms of both the predicted and the flight accuracy. Accuracy deviations from the expected normal ranges are discussed in detail in conjunction with the sections of the text describing component flight performance.

Radar-tracking accuracy.- Slant-range measurements of the RCA AN/FPS-16 main tracking radar were accurate to within ±5 yards at maximum range with an angular error of ±0.1 mil (rms). The SCR-584 radar measurements were accurate to within ±15 yards or ±0.1 percent of the measured range. Reduction of raw radar data involved a smoothing process which introduced additional errors. Smoothing of the radar data, however, was limited to within 50 to 60 feet of the measured slant range, and to within 0.1° for angular measurements.

Guidance-telemetry calibration accuracies.- The telemeter system was capable of measuring the error voltage from the rate and displacement gyros (channels 13A to 14C, table VI) to within ±2 percent. In order to minimize additional errors introduced during the process of relating the gyro signals to actual vehicle rates and displacements, a high degree of calibration accuracy for these channels was required. The guidance rate and displacement gyros were calibrated in the field on rate and displacement tables with the gyros connected to the vehicle wiring through jumper cables.

As a result of the calibration data obtained on the rate gyros, measurements obtained from these instruments were subject to ±5 percent error. The rate table used in the calibration did not maintain a constant rate and, consequently, the voltage output from the table varied and an average reading had to be taken. An additional calibration error was introduced at zero rate as the result of a small amount of noise voltage which gave slightly different sensitivity (measured in volts/deg/sec) in the positive and negative directions.

In order to calibrate the displacement gyro, the guidance package which contained the gyros was given highly accurate incremental displacements. The corresponding displacement signals were obtained from the output of the buffer amplifier in the guidance package, and rate

voltage from the rate gyro was added along with the displacement-gyro signals to the input of the buffer amplifier. As a result of mixing the rate and displacement signals, a decrease of the full voltage range for the $\pm 5°$ displacement range was required in order to allow for any additional voltage from the rate gyro. This lower sensitivity decreased the resolution. The displacement gyros were temperature stabilized at 180° F to within $\pm 1°$, and the damping-fluid temperature could have varied from 179° F to 181° F. The sensitivities (in volts per degree) were different for each temperature and could have varied as much as 5 to 10 percent. In order to minimize this source of error, five sets of readings were taken over a long enough period to allow for the temperature variation, and from these readings an average value of sensitivity was obtained. An additional source of error in the displacement measurements was introduced by the use of rate voltages in the extraction of displacement data. As a result of these various sources of errors, the gyro displacement measurements were subject to from ± 5 to ± 8 percent error.

The accuracies quoted for the gyro rate and gyro displacement measurements take into account the scatter of the gyro voltage that was exhibited as the zero crossover point was approached on the calibration curves. This scatter was due to the inherent design of the gyro pickoff and to random 400-cycle voltage pickup and noise. Actually, the accuracies improved for values above or below zero.

FLIGHT-TEST RESULTS

Flight Description

Figure 49 shows the vehicle in flight shortly after lift-off from the launcher. The tracking-radar plot boards which were monitored during the flight are presented in figure 50. All monitored data indicated that the flight was proceeding normally until a sudden shift in azimuth heading was observed on the FPS-16 radar plot board near the end of third-stage motor burning (fig. 50(a)). The FPS-16 plot board indicated that the vehicle had experienced a violent turning maneuver and had crossed the previously determined destruct lines in the azimuth and elevation planes. Consequently, ignition of the fourth-stage motor was withheld in the interest of flight safety.

Data acquisition.- Radar tracking data were obtained from Wallops Station up to apogee of the flight, which occurred at an altitude of approximately 750 nautical miles. The FPS-16 radar tracked the C-band beacon signal from launch until loss of the signal near apogee. The Reeves Mod. II SCR-584 radar was unable to lock on the S-band radar beacon, and no data were received from this facility. (See fig. 50(b).)

The SCR-584 radar acquired the vehicle immediately after launch
(fig. 50(c)) and skin tracked the vehicle to a slant range of approximately 264,000 feet before losing track. The Millstone Hill experimental
radar of the M.I.T. Lincoln Laboratory at Westford, Massachusetts,
acquired the target at 220 seconds after launch and tracked until the
vehicle went below the radar horizon.

CW Doppler velocimeter tracking was lost after 23 seconds when the
vehicle went into a cloud bank which obscured the remaining part of the
trajectory from the manual trackers.

Atmospheric data (free-stream density, pressure, and temperature)
were recorded by rawinsonde instrumentation prior to launch and are presented as a function of altitude in figure 51. The variation of vehicle
altitude with time through third-stage burnout is shown in figure 52.
Time histories of the free-stream Mach number and dynamic pressure are
presented in figure 53. The variation of free-stream Reynolds number
per foot with Mach number for the initial portion of the flight (prior
to third-stage ignition) is given in figure 54. The Reynolds number is
based on CW Dopper velocimeter and rawinsonde data up to a Mach number
of approximately 1.75. In order to extend the Reynolds number range
beyond this Mach number, an ICAO standard atmosphere was assumed in conjunction with FPS-16 radar data.

Telemeter data acquisition was good, with no interference being
observed on any telemeter station. Telemeter receiving station number 1
tracked the first stage to splash at approximately 360 seconds, and
telemeter stations number 2 and 3 tracked the third and fourth stages
for approximately 1,340 seconds before losing the signal.

First-stage flight events.- The first-stage flight had several
events worth noting. Of minor importance was the fact that the timer
was started about a quarter of a second later than planned as the result
of lag induced in the pullout of the flyaway plug which started the
timer. First-stage flight proceeded normally until about 16 seconds
after launch, at which time the third-stage heat shield came off, probably because of high negative pressures induced on the forward area of
the heat shield by flow phenomena associated with the approach of sonic
speed on the shoulder of the transition section just in front of the
shield. The loss of the third-stage heat shield had no apparent effect
on the remainder of the flight. The only other unusual event during
first-stage motor burning was the emergence of two different objects
from the smoke trail within the last quarter of the burning period.
Sequence photographs of one object are presented in figure 55. It is
speculated that these objects may have been pieces of aluminum oxide
which condensed on a jet vane or the nozzle wall and subsequently broke
loose. All other aspects of the first-stage flight were as expected,

and the control requirements were never large enough to require more than half the limit control deflection.

Second-stage flight events.- The flight of the second stage was completely normal as far as is known. No unusual events associated with any of the working components were observed. However, a totally unexpected phenomena connected with the strength of the telemeter signals occurred during this phase of the flight. The signal strength was attenuated when the vehicle passed through the D layer, but recovered completely each time a hydrogen-peroxide jet control motor fired. This phenomena is discussed further in the section entitled "Vehicle Instrumentation Flight Performance."

Third-stage flight events.- The third-stage flight contained several significant departures from preflight predictions. Telemeter data indicated that one pitch-program step failed to appear just prior to third-stage ignition. Since the difference between steps at this time was very small, no influence on the flight could be expected. The cause of the failure (whether in the timer or in the programer) is not known. Simultaneous events occurred as programed. The vehicle contained a "g" switch which was to activate the change from the high to the low thrust level of the pitch control jets at third-stage burnout in order to protect against the overpowering of the small jets in the event that afterburning of serious magnitude occurred. Unfortunately, in spite of static test results to the contrary, the motor vibrations caused chattering in this switch with the result that the high and low controls were constantly being switched in and out during the motor burning.

At 109.8 seconds from take-off an extremely high but nearly instantaneous roll rate appeared on both the rate and rate-plus-displacement channels. No explanation for this event has been found.

Perhaps the most unusual and significant event of the flight occurred at 136 seconds from take-off. The Antares motor generated a rolling moment of sufficient magnitude to overcome the roll motors. This event occurred during a time of increasing motor vibration and caused a shift in roll reference by about 210°. Just prior to motor burnout the vibration ceased, the roll impulse ceased, and the control system regained command at a new roll reference. The rolling of the vehicle caused the FPS-16 radar, which had been tracking the C-band radar beacon in the vehicle, to reorient from a side lobe to the main lobe of the receiving antenna. As a result of this tracking switch, the azimuth plot board appeared to register a violent turning maneuver and the elevation plot board presented a dip down. Although both tracks recovered, the signal for hold fire of the fourth stage had been given (151.3 seconds) and could not be countermanded. Operation during the coast period was normal. The low-thrust-level pitch jets came on and at

the command of the programer rotated the vehicle 15° as planned. As
the fourth stage did not fire, the third and fourth stages continued on
together until splash.

Ignition-system flight characteristics.- The first stage was ground
fired, and no delay in ignition was observed. The planned trajectory
required ignition of the second-stage motor at 62.84 seconds. Motor
chamber pressure indicated that actual second-stage ignition occurred at
62.7 seconds. The timer setting for heat-shield ejection and third-
stage motor ignition was 107.84 seconds. Delay squibs incorporated in
the third-stage motor ignition circuit were used to provide an ignition
delay of 1.3 seconds (nominal). Actual heat-shield separation was
detected at 107.8 seconds, and motor chamber-pressure data showed that
third-stage motor ignition occurred at 109 seconds.

Trajectory Analysis

The overall characteristics of the flight can be seen by referring
to figures 56 to 63. The major differences between the planned values
and actual flight results were due to withholding ignition of the fourth-
stage motor.

Trajectory comparisons.- Comparison of the measured trajectory with
preflight and postflight calculated trajectories is presented in fig-
ure 56 for the total flight. The preflight calculated trajectory for
this comparison was based on a final coast of the combined burned-out
third stage and the loaded fourth stage. It is interesting to note that
the difference between the peak altitudes of the measured and preflight
calculated trajectories is an indication of how precisely the injection
altitude of an orbit might be held. The variations of altitude with
range are plotted to a larger scale in figures 57 and 58. The total
thrusting flight and the effect of the radar tracking switch on the
measured trajectory in the elevation plane only are shown in figure 57.
The radar data obtained before this switch are apparently unaffected by
the side-lobe tracking as can be seen by the good agreement between the
SCR-584 and FPS-16 radar measurements in figure 58. It is obvious from
these comparisons that the actual flight path lay appreciably above the
calculated.

Since this was an attitude-controlled system, the actual space
track was not controlled and the comparison between the measured and cal-
culated flight paths is not too significant. More useful is the compari-
son between the measured and calculated flight-path angle as a function
of time as shown in figure 59. Good agreement is shown between the
radar data after 15 seconds. Radar measurements prior to this time are
considered to be unreliable. The difference between the measured and
preflight calculated data apparently began very early in the first stage.

This difference decreased with time even though the second- and third-stage thrust misalinements were such as to cause a continual pitch-up (on the edge of the 0.8° dead band) during the burning of these stages. The difference between the actual and preflight calculated flight-path angle of about 1.5° near the end of third-stage thrusting is within control-system requirements.

The accuracy of the calculated vehicle track in the azimuth plane is shown in figures 60 and 61. With erroneous radar side-lobe tracking neglected, the angular difference between the measured and predicted trajectories is about 0.8°, which is well within predicted tolerances. Figures 62 and 63 present the measured and calculated velocity time histories through third-stage burnout and through second-stage ignition, respectively. The differences noted are within the variations expected of the rocket motors. A comparison of the velocity decrements during first-stage coast indicates the accuracy of the drag estimates in this Mach number range.

Comparisons of the calculated trajectory in which disturbances were included (postflight) with the preflight calculated trajectory and with the measured trajectory, presented in figures 57 to 61, indicate that a maximum of only about 25 percent of the various differences between these trajectories noted, especially during first-stage burning, can be explained by disturbances such as variations in motor performance, thrust misalinement, and winds. Reasons for the remaining differences could not be determined from the postflight calculations with measured disturbances.

Effect of possible gyro uncaging error.- In an effort to explain the remaining differences between the measured and calculated trajectories, the possibility of a gyro uncaging error was considered. Trajectories were calculated on the IBM 7090 electronic data processing system with the assumption that the gyro had become uncaged at an angle other than the planned launch angle of 85°. While postflight measurements showed no evidence of error in uncage angle and while it was felt that there was little chance that the other components in the gyro alinement system were in error, these possibilities could not be ruled out completely. From the comparisons of figures 64 and 65, it appears that an initial shift in launch angle to 86.3° would result in good agreement between the calculated and measured trajectories and flight-path angles except during the latter part of third-stage flight. The discrepancies during this period may be important enough to raise some question about the hypothesis of the higher uncaging angle. In addition, the pitch control deflections for the 86.3° calculation deviate from the flight and the 85° calculation after about 13 seconds (fig. 65).

First-stage flight simulation.- As previously discussed, an effort was made to determine the extent of thrust misalinement that might have

acted on the vehicle during the first-stage burning period. With known wind disturbances, an indication of the magnitude and direction of first-stage thrust misalinement was provided by a simulation study of the measured control-surface deflections. The calculated and measured control-surface deflections for pitch and yaw are presented in figure 66. Results are presented for the first 20 seconds of flight since the telemeter data became erratic and questionable after this time. In the calculated time histories for both the pitch and yaw control-surface deflections, the disturbances assumed were the wind profile of figure 47 with no thrust misalinement in one case, and the time histories for winds plus a 0.14° thrust misalinement angle in the other case. The thrust misalinement angle as used here is the angle between the thrust vector and the vehicle longitudinal axis. The design value for maximum thrust misalinement angle was 0.25°. The magnitude and direction of the thrust misalinement angle used for these calculations was determined by calculating a flight trajectory corrected for winds and comparing the resulting control deflections ("winds only" curve) with flight time histories. The differences noted in both the pitch and yaw planes, particularly over the period from 10 seconds to 20 seconds, seemed to indicate the possibility of addition in-flight torques caused by thrust misalinement. Also, in order to shift the calculated curves in the proper direction for better agreement, the misalinement torques had to be in a direction to cause the vehicle to pitch down and yaw left. Based on prior knowledge of the amount of control-surface deflection required to counter various amounts of thrust misalinement, a thrust misalinement angle of 0.1° was estimated for both the pitch and yaw planes, which amounted to a resultant misalinement angle of 0.14° acting in a plane 45° to the xy-plane of the vehicle. The calculated time histories of pitch and yaw control-surface deflections for this misalinement angle and winds are also shown in figure 66. In general, the correlation obtained between the calculated and flight data appears to be considerably better after about 6 seconds than prior to that time. The poor correlation near lift-off is to be expected since ground winds and gusts near the ground and high-angle-of-attack data necessary to properly define the vehicle response to such disturbances have not been included in the calculation. The agreement is considered good enough to conclude with some confidence that the thrust misalinement angle during first-stage burning was somewhat less than the design value of 0.25°.

The vehicle angular rates calculated in pitch and yaw and including the effect of winds and a 0.14° thrust misalinement were also compared with flight data, and these results are shown in figure 67. Although the flight time histories appear somewhat more oscillatory than the calculated results (particularly the yaw rates), the average magnitudes agree reasonably well. The relative smoothness of the calculated time histories might be attributed to the smoothing of the wind data in figure 47.

Guidance- and Control-System Flight Performance

A preliminary insight to guidance- and control-system performance is provided by the measured data presented in figures 68 to 90. Time histories of the measured accelerations recorded by linear accelerometers in the payload and base A section are presented in figures 68 and 69, and rate-gyro data from payload instrumentation are shown in figure 70.

Guidance commands, system errors, and control deflections about each vehicle axis (obtained from telemetry) illustrate the manner in which the vehicle responded to pitch-program commands and to disturbances generated by winds, thrust misalinement, stage separation, and aerodynamic moments. Particular attention should be directed to those portions of the records characterized by perturbations in attitude or control deflection, and by extensive second- and third-stage control-jet action. Typical examples are the perturbations associated with the capture maneuver of the second and third stages and the loss of third-stage roll reference due to disturbances introduced by the Antares rocket motor.

First-stage control-system flight results.- During the period of flight when it was possible to compare the telemetered results with expected system performance, the first-stage control system appeared to function normally. No disturbances were experienced which could be considered a threat to the attitude reference of the vehicle, and control-deflection requirements were about half of the limit control deflections. Attitude displacement errors did not exceed 2° and rates did not exceed 2 deg/sec. The wind and gust conditions present at the time of launch were within design values.

Guidance rate-gyro data are verified by the rate-gyro data from payload instrumentation (fig. 71). The steady-state differences noted are within the accuracy of the payload rate-gyro data. Just prior to first-stage coast, the roll channel presented in figure 71(c) shows some differences which are attributed to acceleration effects on the payload rate gyro.

The time history of control-surface deflections in the pitch plane, figure 71(a), indicates that the left and right surfaces began drifting in opposite directions after approximately 22 seconds. This information, however, is not substantiated by corresponding error data in the pitch plane, or by control-surface deflections calculated from the six-degree-of-freedom flight simulation. Also, the curve for roll displacement error, figure 71(c), does not indicate the presence of opposing control-surface deflections in the pitch plane. Postflight heating tests performed on a similar telemetry position sensor revealed that an in-flight temperature profile such as shown in figure 72 (measured in vicinity of a vane) could cause apparent drifts of the order of ±3°. A similar inconsistency between control-surface deflections and system errors is

observed in the yaw plane (fig. 71(b)). Consequently, control-surface deflection data after 22 seconds are considered to be questionable, and the control system is presumed to have been free of any drift and to have performed normally. Although the vehicle was pitching down at average rates which corresponded to the pitch-program rate command, the vehicle maintained a displacement error in the pitch-up direction during the entire first-stage thrust and coast phases. This system "droop" or lag is a characteristic of the system in the presence of external disturbances such as winds or thrust misalinement.

From the indications of yaw rates, roll rates, and displacement error signals in figures 71(b) and 71(c), the disturbances are observed to have been nominal. For convenience, the yaw and roll control-surface deflections are isolated in figure 73 by presenting the average sum (for yaw) and difference (for roll) of the upper and lower surface deflections.

Normal-acceleration data taken from accelerometers located in base A and in the payload during first-stage flight were resolved to the vehicle center of gravity and then combined with vehicle weights, dynamic pressure, and wind-tunnel measurements of lift-curve slope to obtain a time history of angle of attack (fig. 74). This method for extracting angle-of-attack data is justified since it can be shown that the major portion of the vehicle total normal acceleration is due to vehicle aerodynamic lift, and that the contribution from other possible effects such as thrust misalinement and control lift are negligible. Since angle of attack derived from this source is proportional to normal acceleration, its accuracy is determined by the resolution of the accelerometers. The best accuracy occurred near maximum dynamic pressure (t = 34 seconds) where the resolution of angle of attack was of the order of 50 percent of the value shown. It can be seen in figure 74 that for the range of flight angle-of-attack data presented, the agreement with angle of attack obtained from two postflight six-degree-of-freedom simulated trajectories which included the effects of measured winds is generally good.

As an index of the airframe structural loads, the product of dynamic pressure and angle of attack is also presented in figure 74. It can be seen that the peak value of $q_\infty \alpha$ was approximately -6,000 lb-deg/sq ft or approximately one half of the design peak value of ±12,000 lb-deg/sq ft.

Second-stage control-system flight results.- Attitude displacement errors, attitude rates, and jet-operation time histories are presented in figure 75. These data describe second-stage control-system performance and vehicle dynamics during thrusting of the Castor rocket motor.

Initial conditions: The initial conditions for the second-stage control-system flight results are defined as attitude displacement errors and rates and angle of attack existing just prior to the time of Castor

ignition. In view of the aerodynamic instability of the second-stage configuration and the possibility of a 1/4° thrust misalinement associated with the Castor motor, initial tolerances of 3° of attitude displacement error and angle of attack as well as 3 deg/sec of attitude rate were selected as design values. From figure 75 it is apparent that pitch-plane initial conditions (0.3° pitch-up displacement error and 0.5 deg/sec pitch-down rate) were well within the design values. The angles of attack due to tail wind was estimated from other flight data (see fig. 74) to be approximately -1° which, when combined with pitch-up displacement error, increases capture-maneuver control requirements. The capture maneuver defines vehicle motion during the period in which control of the vehicle is relinquished by one stage and assumed by the succeeding stage. In the yaw and roll planes (figs. 75(b) and 75(c)), initial-condition values were less of a problem during the capture maneuver than these observed in the pitch plane.

Disturbances: Results of a disturbing-force analysis made on the second stage are presented in the time histories of figure 76. An average pitch-up disturbance of approximately 120 pounds was found to be acting on the vehicle during Castor burning. Of this total disturbance, approximately one-fourth of the unbalance was caused by the wiring tunnels. This average disturbance of 120 pounds was equivalent to a constant thrust misalinement angle component in the pitch plane of 0.11° (pitch-up). In the yaw plane, the disturbing force varied considerably between ignition and start of tail-off. The yaw disturbance covered a range of about 10 to 55 pounds (yaw left), which represented an equivalent average thrust misalinement angle component in yaw of 0.06°. The pitch and yaw components were resolved into an effective thrust misalinement angle of 0.125°, acting 31° off the vertical plane in the pitch-up and yaw-left direction. The major disturbances in the roll plane occurred at ignition where, with a roll-jet moment arm of 1.33 feet, a 56-pound disturbance lasted for 0.2 second and a 16-pound disturbance occurred shortly thereafter. These disturbances were followed by a relatively constant value of 5 pounds for the remaining interval of Castor burning. After the start of Castor tail-off, the disturbing forces and moments in all three planes decreased proportionally with the decrease in Castor thrust level. This proportional decrease confirmed the assumption that Castor thrust misalinement was the major source of the disturbing forces.

Capture maneuver and control-system evaluation: The capture maneuver in the second stage covers a period of time from Castor ignition (after first-stage separation) until the vehicle attitude is stabilized within each set of displacement and rate dead bands. The length and the magnitude of the capture transient are a direct indication of the severity of the combined disturbances acting on the vehicle at ignition and those arising from initial conditions consisting of

Castor thrust misalinement forces, aerodynamic instability, and unknown disturbances associated with first-stage separation.

Phase-plane plots illustrating the pitch-plane capture maneuver are presented in figure 77(a). The pitch-program rates are small compared with other rates involved and were neglected in the phase plane. Time histories of control-jet operation and the attitude displacement error and pitch rate are included to provide a time reference. The pitch-plane capture maneuver started within the position and rate dead bands at ignition and, after two overshoots in rate, returned to a limit cycle on the pitch-up side of the dead band. An acceleration resulting from the ignition pitch-up disturbance was contained by the pitch-down jet after a rate of 3.5 deg/sec had developed. The vehicle was then accelerated in a pitch-down direction to a maximum rate of 3 deg/sec until attitude rates were again within dead-band limits and corrective jet action ceased. Thrust misalinement and the absence of an opposing jet force almost immediately accelerated the vehicle in the pitch-up direction until pitch-up dead-band limits were exceeded. Shortly thereafter a limit cycle was established with rates remaining on the pitch-up side of the dead band. Although the entire time history is not shown in figure 77(a), this condition continued in the pitch plane until the start of Castor tail-off. Dead-band and switching-slope values were generally in accord with levels established during preflight checks (fig. 42).

Disturbing-force analyses indicated that there was probably a thrust misalinement component present in the yaw plane at Castor ignition, though of lesser magnitude than the pitch component. Since a more favorable initial angle-of-attack condition existed in the yaw plane than in the pitch plane, the capture maneuver in yaw was correspondingly small.

The roll-plane capture maneuver is shown on the phase-plane plot and attitude rate and displacement error time histories of figure 77(b). At ignition, a severe roll-left disturbance was experienced and checked, after which the vehicle was accelerated in the opposite direction by the roll-right jet correction after a 2 deg/sec overshoot. As the vehicle was moved by the roll-right jets, there was a distinct increase in the acceleration at t = 64.25 seconds. This time coincides with the turn-off time of the pitch-down jet and indicates a possible misalinement coupling with roll. The disturbance does not appear to be undirectional as in the pitch plane, since after the second overshoot of 2.75 deg/sec the opposing jet combination (roll left) is required to bring the vehicle back into dead-band limits. Although not as pronounced as in pitch, there was a limit cycle in roll, which is indicative of a predominantly roll-right disturbance. Preflight dead-band values appeared to hold true in flight. However, it would seem from indications in the phase-plane plot that the switching slope may have decreased slightly from the original value of 2.5.

There are several aspects of the time-history presentation of guidance- and control-system performance in figure 75 which should be pointed out at this time. The jet cycling frequency as reflected in the rate channel was higher in pitch than in yaw, an observation logically suggesting a higher level of disturbance in pitch than in yaw. Also, after the start of Castor tail-off, the system rate and error signals and hence jet activity in all control planes decreased and became random as might be expected.

In general, the second-stage control system capture-maneuver conditions were nominal, and performance in pitch, yaw, and roll was very satisfactory throughout the operating period of the second-stage flight.

Third-stage control-system flight results.- Third-stage control-system performance is illustrated by the time histories of attitude rates, displacement errors, and control-jet operation presented in figures 78 and 79.

Initial conditions: The original design initial conditions as defined for the second stage were also applied to the third-stage control system; that is, 3^0 of attitude displacement error and angle of attack, as well as 3 deg/sec of attitude rate. At the attitude conditions existing at third-stage ignition, angle of attack was not a point of consideration. Pitch and yaw initial conditions of attitude displacement error shown in figure 78(a) and (b) were of the order of 0.2^0 pitch down and 0.2^0 yaw left, respectively, which were very modest compared with the allowable design values. Altitude rate initial conditions in pitch and yaw were 0.3 deg/sec pitch down and 0.4 deg/sec yaw right, which again were nominal compared with design values. Roll initial conditions shown in figure 78(c) were somewhat higher than those in pitch and yaw, with a 2^0 roll-left (CCW) displacement error and a 2 deg/sec roll-left (CCW) rate. Minor disturbances in position and rate are evident in all planes over the period from t = 108 seconds until the third-stage ignition at t = 109.2 seconds. These disturbances were apparently caused by the fact that the signal for Antares ignition and the third-stage valve-on signals occurred simultaneously at t = 107.8 seconds. However, actual ignition was delayed by a squib until t = 109.2 seconds. During the interim of 1.4 seconds, both second- and third-stage control jets were operating and opposing one another, as evidenced by the nature of the rates associated with pitch and yaw compared with those in roll. (See fig. 78.)

Disturbances: The same type of analysis was made on third-stage rate gyro (guidance) and reaction-control jet telemetery time histories as was carried out on the second stage in order to obtain magnitudes and directions of disturbances acting on the third stage during Antares thrusting. Results of the analysis are presented in the time-history curves of figure 80. Pitch-up disturbances averaging about 10 pounds acted on the vehicle during Antares burning. Several disturbances of

relatively large impulse were also observed just before tail-off. The 10-pound pitch-up force was equivalent to a constant thrust misalinement angle component in pitch of 0.04°. Yaw disturbances for the same time averaged approximately 8 pounds, although these disturbances varied from approximately 2 to 10 pounds and exhibited a large impulse after ignition. The equivalent constant thrust misalinement angle component was 0.03°. A resultant effective thrust misalinement angle was computed to be 0.05°, acting nearly halfway between the pitch-down and yaw-left directions. In roll, there was one large impulse (0.06-second duration) of 126 ft-lb at ignition and two rather substantial roll-right moments of 20 ft-lb each, which occurred just before tail-off. Other than the impulse and moments just described, it is apparent from figure 78(c) that there were no other disturbances of significance present in the roll plane during third-stage thrusting.

Capture maneuver: The capture maneuver was accompanied by unexpectedly high vibration levels. These vibrations, in combination with large disturbances associated with Antares burning, were responsible for the loss of roll reference immediately after ignition, which, in turn, apparently caused coupling between the pitch and yaw modes. An acceleration-sensitive switch was used in the third-stage control system to reduce pitch jet thrust levels, reduce pitch and yaw dead bands, and to transfer roll and yaw control to the roll jets after burnout. This switch proved to be sensitive to these high vibration levels even though preflight checks had indicated otherwise. The vibration levels at ignition (and frequently thereafter) were sufficient to trigger the acceleration switch and thus switch the controls to coasting conditions. This condition resulted in lower corrective thrust levels and tighter dead bands than normally intended for use during Antares thrusting. The first 6 seconds of time history after third-stage ignition in all three control planes of figure 78 clearly demonstrate the effects of interaction of the three control modes. Large roll rates and displacement errors were permitted to build up unchecked by the roll jets until the roll MIG was saturated by roll-right displacement error. This saturation caused a loss of roll reference for 4 seconds because the roll error signal was overridden by the yaw error and the roll jets were used for yaw control. It is doubtful that the small roll jets functioning correctly could have stemmed the roll disturbance. During the same period of time, almost simultaneous pitch-down and yaw-left motions were ineffectively opposed by the small pitch-up jets and by the yaw-jet combination of upper- and lower-right roll jets, respectively. It is evident that the control system did not return the vehicle attitude to within dead-band limits, but that the disturbance and vibration level subsided enough to permit proper operation of the acceleration switch and control system. Proper control operation was reestablished at about t = 112.5 seconds, after which recovery in all control modes was initiated. Pitch and yaw displacement errors and rates were brought within dead-band values by about t = 116 seconds. However, decay of the roll

transient was not complete until t = 130 seconds. The relatively
quick recovery in pitch and yaw resulted from the combination of higher
jet thrust levels and a concurrent reduction in the disturbing forces
which had induced severe vehicle rolling.

System evaluation: As a means for ascertaining control performance
of the third stage, the vehicle motions were studied in the phase plane.
The first point of interest considered is the recovery from a pitch-up
disturbance presented in figure 81(a) which shows the effects of the
chattering acceleration switch which effectively reduced the pitch dead
band and pitch jet thrust level. The rate time history prior to the
disturbance illustrates the manner in which the large pitch jets main-
tained the attitude displacement errors and rates within their respective
dead bands. With the advent of a disturbance and a chattering accelera-
tion switch, the reduced thrust level was not adequate and the rates and
displacement errors grew, being checked only momentarily as the large
jets switched in and out. After a peak pitch-up displacement error of
about 2° and rate of about 2 deg/sec, the disturbance was finally checked
by a series of substantially long, large pitch-down jet pulses. The dead
band, during this period, varied between burn and coast control condi-
tions with total spreads of 0.46° to 1.6° so the flight dead band is
between the two. This condition is apparent in the phase-plane plot of
figure 81(a). Effects of the chattering acceleration switch just before
entry into a transient caused by a yaw disturbance are exhibited in a
different way in figure 81(b). From t = 111.8 to 112.6 seconds, yaw
correction was furnished by upper- and lower-right roll jets, which have
only one-tenth of the corrective force available from one of the large
yaw jets.

Consequently, the displacement error started to decay only after
the large yaw-right jet was activated. Large yaw-jet activation appeared
to be consistent with preflight dead-band width with one exception. This
exception occurred in connection with a combined large yaw-right rate,
and a small yaw displacement error, which changed from 1° yaw left
(t = 114 seconds) to 0.8° yaw right (t = 115 seconds). Since the error
combination was clearly outside of the dead band, yaw-left jet operation
should have continued but did not. (See fig. 81(b).) There was no
apparent reason for the lapse in valve signal other than a momentary
control-system malfunction since immediately afterward normal jet opera-
tion was resumed. It was apparent that the disturbance which caused the
transient was moving the vehicle in the yaw-left direction since the yaw-
right acceleration remained at a fairly substantial value even during
"off" times of the corrective yaw-left jet pulses.

Control response to another yaw disturbance is depicted in fig-
ure 81(c) and again, as in the case previously described, shows the
effect of the chattering acceleration switch. Momentarily, at
t = 140.5 seconds, yaw-right correction was supplied by the upper- and

lower-right roll jets with little success. Even for some time after the large yaw-right jet was applied, the displacement error continued to build up, and was reduced only slightly before the upper end of the dead band was entered, an event which turned off the yaw-right jet. The displacement errors and rates then returned to the vicinity of the origin along one side of the dead band. Yaw-jet action appeared to be erratic during the time period of figure 81(c) (139 seconds to 145 seconds), particularly after the onset of the disturbance, where the error clearly indicated that a jet should have been operating in two instances between t = 139 and 140.5 seconds, but was not. There was no apparent reason for the failure of the yaw jets to operate as required by the error signal.

A final phase-plane and time-history plot for a disturbance during third-stage burning is presented in figure 81(d) for the final decaying oscillations of the roll transient which developed shortly after ignition of the Antares motor. A slight malfunction of the acceleration switch apparently had little effect on the ability of the system to damp out the oscillation effectively. It is difficult to determine accurately roll dead band and switching slopes because of the intermittent change in the yaw control mode; however, in most instances, the total dead-band width appeared to agree fairly well with preflight values while the switching slope seemed to bend to the left or exhibit a more shallow slope in comparison with preflight measurements.

The final point of interest during third-stage thrusting is referenced to the time history of figure 78. At approximately t = 137 seconds, the Antares motor entered a period of exceptionally rough burning which lasted for $4\frac{1}{2}$ seconds and included a high level of vibration. The primary disturbing force was experienced in roll, while pitch and yaw disturbances followed as coupled effects. The vehicle reached a peak clockwise roll rate of about 40 deg/sec during this time and saturated the roll position MIG for $9\frac{1}{2}$ seconds, with a loss of reference in the roll-right direction. Full roll corrective moment was applied against the disturbance without success. Meanwhile, vibration effects on the acceleration switch momentarily reduced the pitch-down jet thrust level, and a pitch-up rate was allowed to develop. The combination of pitching motion and vehicle rolling coupled the pitch disturbance into the yaw plane and a large yaw rate followed. At t = 140.8 seconds, the acceleration switch ceased chattering and normal pitch and yaw thrust levels were reestablished and pitch and yaw displacement errors and rates were reduced. Roll correction continued after Antares burnout, and the roll transient was finally damped out during coast, at about t = 155 seconds (fig. 79(c)).

The jet time histories of figure 78 confirm the findings of thrust misalinements and disturbances discussed previously. The pitch-jet time

history in figure 78(a) shows that during Antares burning the pitch-down jets were used almost exclusively until burnout, a fact which indicates that a constant disturbance is acting in the pitch-up direction. In the yaw plane, the disturbing force acted in the yaw-left direction, as shown by the almost constant usage of yaw-right jets (fig. 78(b)). It will be recalled that yaw right was provided, unintentionally, with the appropriate combination of roll jets. Roll-left jet activity indicated that primarily roll disturbances tended to roll the vehicle in the clockwise direction (fig. 78(c)).

Third-stage coast: About the only vehicle motion and control activity during the third-stage coast period was in connection with the damping of yaw and roll transients resulting from disturbances during Antares burning and the final pitch-program step from t = 148.838 to 163.838 seconds. (See fig. 79.)

Figure 82 presents the phase-plane plot together with displacement-error and rate time histories that illustrate the final decay dynamics of the roll transient initiated during the rough burning period shortly before Antares tail-off. This time period is of interest since it exhibits control-system performance during third-stage coast when no thrust misalinement is acting on the vehicle. It can be seen in figure 79 that while roll correction was being applied, yaw correction was intermittently employed in the normal mixing mode. Under coast conditions, it is apparent that the roll jets were adequate for stabilizing the vehicle in both yaw and roll. Roll dead band is not well defined at large displacement errors and rates on the phase plane (fig. 82) because of the yaw-roll mixing. However, once the phase-plane responses are in the vicinity of the origin, it is apparent that preflight dead-band limits were good in flight.

From the pitch time history of figure 79(a), it may be observed that during third-stage coast the vehicle maintained an average constant pitch-down rate which corresponded closely to the final pitch-program step of 1 deg/sec. After about t = 150 seconds until the end of coast, figure 79 shows that there were no disturbances present and hence very little jet activity in any of the three control planes.

Comparison of rocket-motor thrust misalinement with control-system design criteria.- The magnitudes of the thrust misalinement angles obtained from preflight measurements (static) and from flight disturbing-force analyses are summarized and compared with the values specified for control-system design in the following table:

Motor	Static thrust misalinement angle, deg	Flight thrust misalinement angle, deg	Specified thrust misalinement angle for design, deg
Algol	0.054	0.140	0.250
Castor	.049	.125	.250
Antares	.043	.050	.100
Altair	.036	-----	.050

Comparison of the thrust misalinement angles is presented on the basis of magnitude only, since orientation of the misalinements with respect to the pitch and yaw planes was not determined for the static measurements and was not specified for control-system design criteria. It should be noted that the static thrust misalinement angles are maximum geometric values at ignition, with the assumption that deviations were in the same plane and were additive.

An increase in the misalinement angles during flight is to be expected, since additional misalinements due to nozzle erosion and gas swirl may be present during motor burning. As pointed out previously, the thrust misalinement angle listed for the Algol motor was used for a flight simulation study and gave good correlation with measurements of control-surface deflections shortly after lift-off. In all cases, the preflight static and flight thrust misalinement angles were well below the values specified for control-system design.

Guidance pitch program.- The mechanics of establishing a pitch program and the manner in which it is implemented with the programer and timer in the guidance system were described previously. The pitch-program rates and the preflight and telemetered checks of these rates are presented in table XII. The telemetered values are noted to be consistently higher, but these differences are believed to have been caused primarily by an inadequate final recalibration of the pitch torque voltages following a last-minute replacement of the pitch MIG. Timer operation was initiated by first-stage umbilical pull at vehicle lift-off. Initiation of timer operation occurred approximately 0.24 second after first-stage ignition command which corresponds to time zero for telemetry. As a result, a slight discrepancy will be noted between telemetry and timer-programed events. The time durations of the first three pitch-rate steps were obtained as programed. The fourth step was properly initiated but continued unchanged into the fifth step, a result indicating a possible timer lockup or programer malfunction. This event resulted in a slightly larger total program angle than intended. The sixth step was early by 0.348 second but ran the required 15 seconds. The telemetered value of total pitch program angle was 2.6° greater than the originally programed total angle of 43.596°. The difference, however, is within the resolution of the telemetry data.

It was determined after the flight that as a result of a rate-gyro electrical grounding problem during pitch-program adjustment runs, an error existed in the pitch MIG torquing voltages which caused the total program angle to be larger in flight by $1\frac{1}{2}^{\circ}$ more than intended. This error agrees in direction, but not magnitude, with the telemetry indication that the total pitch program angle was 2.6° greater than intended. This indication was within the possible telemetry error.

First-stage flight-path angle.- Calculated values of first-stage flight-path angle are compared with data obtained from SCR-584 and FPS-16 radar measurements in figure 83. The sketch in figure 83 presents the nomenclature used to define the vehicle attitude angles θ and α, flight-path angle γ, and pitch program and error angles θ_p and ϵ_q. In this presentation, for a given time the preflight measured value of pitch-program attitude angle θ_p was combined with the angular pitch position error ϵ_q (fig. 71(a)) to obtain the vehicle attitude angle θ. This angle θ was then added to the angle of attack $-\alpha$ (fig. 74) to obtain the flight-path angle γ. A comparison of results reveals that agreement is fairly good, with radar data generally showing slightly higher values. A higher than normal launch angle could account for the values observed. It is believed unlikely, however, that such an error in launch angle existed.

Guidance gyro error analysis.- A detailed analysis of the digital telemetered data has yielded the values of gyro errors due to two relatively obscure and little-recognized effects; coning and cross coupling between gyro axes (refs. 1 and 2). Coning error is a purely geometric phenomenon which is independent of the manufacturing quality or mechanical operation of the angular sensor (provided the sensor measures body angles). It occurs in a gyro whenever the input axis moves so as to sweep out a net solid angle, as it would if it described a cone. Simple expressions for the errors due to coning effect are

$$\left.\begin{aligned} \Delta\theta_C &= \frac{1}{2}\int_0^t (\dot{\phi}\psi - \dot{\psi}\phi)\,dt \\[2mm] \Delta\psi_C &= \frac{1}{2}\int_0^t (\dot{\phi}\theta - \dot{\theta}\phi)\,dt \\[2mm] \Delta\phi_C &= \frac{1}{2}\int_0^t (\dot{\psi}\theta - \dot{\theta}\psi)\,dt \end{aligned}\right\} \tag{1}$$

where θ, ψ, and ϕ are pitch, yaw, and roll angles about the body axes.

Values of θ, ψ, and φ and their time derivatives at 0.1-second intervals over most of the flight (0.5-second intervals up to 62 seconds after launch) were combined as shown in the coning error equations and integrated to generate the results presented in figure 84.

Kinematic rectification or cross coupling arises from the fact that the gyro input, spin, and output axes are not orthogonal when registering an output. If a gyro with unit transfer function is given a 1° input, the gimbal will rotate 1° and thereby tilt the input axis. Any motion about the original spin axis is coupled into the new input axis by the sine of 1°. Errors of this sort can be expressed as

$$\left. \begin{aligned}
\Delta\theta_K &= k \int_0^t \theta\dot{\psi}\ dt \\[2em]
\Delta\psi_K &= k \int_0^t \psi\dot{\theta}\ dt \\[2em]
\Delta\varphi_K &= k \int_0^t \varphi\dot{\theta}\ dt
\end{aligned} \right\} \qquad (2)$$

where again θ, ψ, and φ are body pitch, yaw, and roll angles and k is the gyro transfer function. Results of the integration of the cross-coupling expressions are shown in figure 85.

Error magnitudes presented in figures 84 and 85 are relatively small during first- and second-stage operation. After the third-stage ignition disturbance, however, the errors reached maximum values of 1.5° in pitch, 1° in yaw, and 0.25° in roll. The greater part of the error during thir third-stage flight developed when the vibration level was high and when roll reference was lost during coupling of vehicle motions. If the static transfer function of the gyro is less than unity, the cross-coupling errors are reduced. The gyro used in the vehicle has a ratio of gimbal angle to input angle of about 0.3. The time histories of figure 84 show that the coning errors increased sharply just after third-stage ignition. This sharp increase can be explained by the small roll disturbance impulse which occurred shortly after ignition and by the simultaneous loss of yaw control for several seconds. Rather large displacements and rates appeared in both roll and yaw during this period which had a large effect on the pitch gyro. The errors became even larger after the unexpected roll disturbance which occurred about 138 seconds after launch.

Several things should be noted about the coning errors presented in figure 84. First, the accuracy of the data is probably not good, partly as the result of combining the rate and position signals for telemetry. Secondly, the data are only given at discrete intervals - every 0.5 second up to 62 seconds and each 0.1 second thereafter. This choice of intervals means that only gross, low-frequency-motion effects on coning could be observed. Since coning due to high-frequency vibrations can cause large gyro drifts under certain circumstances, the most important part may be omitted from these calculations. One area, however, has been observed in sufficient detail; the second- and third-stage limit cycles apparently did not contribute much to the gyro errors.

Hydrogen-peroxide fuel consumption.- Two independent methods were utilized to determine hydrogen-peroxide fuel consumption during operation of the second- and third-stage control systems. One method was based on in-flight nitrogen pressure drop correlated with preflight calibrations of nitrogen pressure decay with hydrogen peroxide consumed. The other method was based on computations which combined measured in-flight jet-on times with design values of jet thrust and peroxide specific impulses that were assumed to deviate from the nominal levels.

Telemetered values of the time variation of pressure in second- and third-stage main-tank nitrogen supplies are presented in figure 86. The values of nitrogen pressure were referred to the calibration curves of figure 43 that had been adjusted to launch pressures, and the resulting peroxide consumption curves obtained are also shown in figure 86. The overall pressure drop depicted for the second stage was not believed to represent a total drop due to operation of the jets from the main-tank supply, but is attributed to a leak in main-tank plumbing or drift in telemetry. The linear pressure decay between $t = 63$ and $t = 90$ seconds was interpreted as the true character of the leak or drift. Usage from the main-tank supply was not thought to have started until $t = 90$ seconds, where depletion of the toroid nitrogen supply is indicated by the data of figure 86(a). The curve for hydrogen-peroxide fuel consumption in the second stage bears out this interpretation, and includes the effect of the leak or drift continuing at the same rate until separation from the third stage at $t = 109.2$ seconds and resulting in a flight consumption of 54 pounds. Nitrogen pressure variation was apparently normal during third-stage operation and indicated the use of 5.5 pounds of hydrogen peroxide.

An analysis made of the pitch, yaw, and roll jet time histories produced a set of total jet-on times for each stage which actually represented the duration of the valve-signal "on" times. Chamber-pressure-switch indications (above 100 psig) could have provided a jet-on indication; however, pressure-switch operation was not consistently evident in telemetry whereas valve signals were. Hydrogen-peroxide fuel consumption was then determined by assuming that the jets delivered nominal thrust

levels with a design specific impulse of 142 lb-sec/lb, by which
reasoning the second and third stages were found to have consumed
37 pounds and 4.6 pounds, respectively.

It is obvious from the foregoing results that the two methods for
determining hydrogen-peroxide fuel consumption are not in agreement;
therefore, as a means of explaining the differences, tables and plots
of fuel consumption have been prepared and presented in figure 87 which
reflect the effects of the following influencing factors:

1. Effect of possible second-stage system toroid-tank leakage during
countdown: Since only the main nitrogen tank pressure was monitored
during the countdown, it was not known exactly what pressure existed in
the toroid after the pressurization squib was blown. It is assumed,
however, that toroid pressure was the same as that of the main tank, and
based on a preflight test, an 1,100-psig drop followed when the squib
was blown, which resulted in an initial toroid pressure before burping of
1,800 psig (reference calibration curves, fig. 43(a)). A difference in
the initial toroid pressure could have altered the apparent hydrogen-
peroxide fuel consumption obtained from the calibration curves by about
8.5 pounds for a 300-psig difference from the assumed value. The plot at
the bottom of figure 87(a) illustrates the effect of a 300-psig change in
initial toroid pressure. A leak, if present, could have reduced the
amount of hydrogen peroxide apparently consumed from 54 to 39 pounds, if
as much as 600 psig were lost from the toroid.

2. Effect of errors resulting from use of valve-signal jet-on times:
There were some indications of possible error associated with the assump-
tion that the duration of valve-signal "on" times were representative of
the actual periods of jet thrusting. Valve signals, as mentioned pre-
viously, were the choice of criteria for designation of jet-on times
rather than chamber-pressure-switch indications, because chamber-pressure-
switch operation was not well enough defined on the telemetry records to
establish an accurate time interval. A comparison was made of jet-on
times read for both valve-signal and pressure-switch indications (jet was
"on" for chamber pressures above 100 psig) during second-stage operation
in pitch and yaw. This comparison revealed that during yaw-jet operation,
the indications were nearly identical. In pitch, however, chamber-
pressure-switch times were 10 to 20 percent longer than times obtained
from valve signals. In this connection, it was noted that during second-
stage operation, the total impulse from jets in pitch and yaw (on the
basis of nominal 600-lb thrust levels and valve-signal jet-on times) were
3,570 and 1,440 lb-sec, respectively. For the same period, the total
disturbance impulses in pitch and yaw were 3,750 and 875 lb-sec, respec-
tively. (See fig. 87(a).) Undoubtedly the pitch jets produced more
impulse than 3,570 lb-sec in order to have neutralized the disturbing
impulse of 3,750 lb-sec. Since the jet-on times for yaw valve signal
and chamber-pressure switch were nearly identical and the relationship

of jet impulse to disturbance impulse was proper, it would seem possible that the pitch jet-on times were in error as a result of the use of valve-signal indications as representative of "on" times. The curve at the bottom of figure 87(a) was computed by using measured valve-signal jet-on times. However, if the times used had been adjusted (10-percent longer), the curve would have been shifted to the right and a higher apparent fuel consumption would have been obtained.

3. Effect of possible thrust-level and specific-impulse deviations from nominal: Differences from the specific-impulse design value of 142 lb-sec/lb could have produced effects in overall hydrogen-peroxide fuel consumption similar to those exhibited from the error in jet-on times. It is apparent that a trade-off exists between the jet-on time and thrust level for a given impulse. Also, degradation in specific impulse could result from the cycling of the jets. However, the frequency of the limit cycle was believed to be low enough to have removed this cycling as a very serious effect.

Figures 87(a) and (b) show the variation of specific impulse with hydrogen-peroxide fuel consumption for the second- and third-stage control systems on the basis of the information displayed in figure 87, the following conclusions are noted:

1. The difference in hydrogen peroxide consumed during second-stage operation as shown by a comparison of the results taken from nitrogen pressure calibration curves and those based upon jet-on times (nominal thrust levels and design specific impulse) is attributable to several factors. A variation in the initial N_2 toroid pressure from the assumed value (see fig. 87(a)) could have produced better agreement between the two methods. Also, deviations from nominal thrust levels and design specific impulse used with measured jet-on times would have had the same effect. Jet-on times were not completely correct, but the effect of longer and shorter "on" times was recognized as resulting in more or less peroxide consumed, respectively, for a given specific impulse. The possible error in jet-on times was not thought to be as significant as the other effects mentioned and is eliminated from further consideration. The region of heaviest shading in figure 87(a) defines an area of agreement for the two methods employed to determine hydrogen-peroxide fuel consumption. If the initial toroid pressure were assumed to be lower than 1,650 psig, that is, if a more severe leak were assumed, then the heavily shaded area would be shifted to the left and the general area of agreement would reflect a relative increase in specific impulse and lower hydrogen-peroxide fuel consumption. Finally, the general region of agreement shown by the heavily shaded area in figure 87(a) is representative of the best degree of resolution of the hydrogen-peroxide fuel consumed that was possible to ascertain from flight records.

2. The explanation for the difference in hydrogen-peroxide fuel consumed by the third stage is similar to that described for the second

56

stage, with the exception that a toroid nitrogen tank was not used. A specific impulse of 125 lb-sec/lb (assuming nominal thrust levels and measured jet-on times) would yield 5.2 pounds of hydrogen-peroxide fuel consumed. (See fig. 87(b).) This value is in good agreement with the results from the nitrogen pressure calibration curve (5.5 pounds). An increase above nominal thrust within the shaded portion of the curve for measured jet-on times would have yielded the same agreement.

It should be noted that hydrogen-peroxide fuel consumption during third-stage coast was very modest (fig. 86(b)).

Jet-on duty cycle and frequency.- Telemetry time histories of hydrogen-peroxide jet operation during the period of second- and third-stage thrusting provided jet-on and jet-off times (obtained from valve signals) from which duty cycle and frequency were determined. Variation of jet duty cycle and frequency with time for the second and third stages has been plotted in figure 88.

Duty cycle and frequency for the second-stage control jets, shown in figure 88(a), generally follow the trend of the disturbing forces during this period of time. (See fig. 76.) Pitch frequencies varied between 0.5 and about 1.75 pulses/sec, but were in the vicinity of 1.5 pulses/sec for the most part. Yaw frequencies ranged from 0.4 to 1.2 pulses/sec but were well below 0.75 pulse/sec generally. Duty cycles varied similarly, with the pitch jets operating at an average of 15 percent, and the yaw jets usually below 7.5 percent. Roll-jet frequencies were as high as 1.3 pulses/sec, but for the most part were between 0.6 and 0.8 pulses/sec. A peak duty cycle of 22.5 percent was observed in roll. However, a duty cycle of 5 percent was representative of the longer period of second-stage operation. As might be expected, pitch, yaw, and roll duty-cycle and frequency variation could be correlated with the variation in severity of the disturbing forces. Also, pitch duty cycle and frequencies were higher than those of yaw by a factor of two, which would be anticipated from the relative magnitude of thrust misalinement acting in each of the two planes.

Because of the difficulties experienced in the third stage with the acceleration switch that permitted mixing of control modes and use of lower level jets inadvertently, correlation of jet duty cycle and frequency with disturbing forces was not as apparent as in the second stage. Generally duty-cycle variations in pitch, yaw, and roll presented in figure 88(b) were indicative of the time periods during which peak disturbances occurred. Frequencies in pitch and yaw were higher than in the second stage and ranged from 2 to 4.5 pulses/sec in pitch and 1 to 2.75 pulses/sec in yaw. Roll frequencies did not exceed 0.7 pulse/sec and were usually much lower than 0.6 pulse/sec.

Body-bending data.- Oscillations observed on the payload normal and transverse accelerometers and in the rate-gyro telemetry traces were found to provide a good source for extraction of frequency and damping data. To a lesser extent, during third-stage operation the hydrogen-peroxide jets pulsed in response to the body-bending frequencies as sensed by the rate gyro. Oscillations identified in the frequency range of the rigid and elastic modes were analyzed, where possible, for damping ratios. Results of the investigation of in-flight structural and aerodynamic airframe characteristics together with pre-flight estimates are presented in figure 89.

First-stage body-bending data: Locations of the payload accelerometers and rate gyros on which oscillations were observed during flight are shown in the sketch at the top of figure 89(a). Just below this sketch are shown typical curves which characterize the calculated first three body-bending-mode shapes at launch and at burnout. Comparison of the calculated and measured time variation of frequencies for rigid and first three body-bending modes in figure 89(a) shows that good agreement was obtained in most cases. It can be seen that rate-gyro data, where available, generally substantiated the accelerometer information. The dynamics of the servo actuator was described by a first-order lag. The time constant of the lag, or servo "break" frequency, is shown as a constant value in figure 89(a). Only limited data were available on the damping qualities of the elastic structure of the first stage.

Second-stage body-bending data: In the second-stage configuration, the pitch and yaw jets at their location near the aft end of the stage were very effective in exciting the body-bending frequencies. The plot of frequency variation with time at the top of figure 89(b) indicates very good agreement of flight and estimated data for the first body-bending mode in the vicinity of second-stage ignition. At burnout, the in-flight frequencies do not quite attain the predicted frequency of 8.6 cps but are relatively close with a value of almost 8 cps. Agreement of estimated and in-flight frequencies for the second body-bending mode was not particularly good compared with that of the first mode. However, it was within 15 percent of the predicted value. Oscillations in second-stage accelerometer records yielded a considerable amount of damping information, which is presented as a time history of damping ratio at the bottom of figure 89(b). The damping ratios are seen to vary from 3.8 percent critical at second-stage ignition to 2.4 percent at third-stage ignition. These values are somewhat higher than the assumed design value of 1 percent.

Third-stage body-bending data: Rather severe accelerations were detected in the payload at the normal and transverse accelerometer positions. As noted at the top of figure 89(c), an acceleration of the order of 3.4g (peak-to-peak) was recorded. This acceleration was probably caused by fourth-stage heat-shield ejection or rough Antares burning

at ignition rather than pulses from the large pitch and yaw jets. The substantial cluster of frequencies from accelerometer and rate-gyro data in the range from 13 to 17.5 cps over the greater part of the thrusting time of the Antares motor are considered to represent third-stage first body-bending frequencies since they are correlated at different locations by different instruments. Calculated preflight estimates established the first bending-mode frequency at 28.9 cps for the ignition case. There is no immediate explanation for the large difference. Damping ratios observed with the frequencies range from 3 percent critical to 2.2 percent and again are higher than initially assumed for the structure.

Vibration analysis of flight data was not within the intended scope of the body-bending analyses or guidance- and control-system performance analyses. However, a short rerun of the third-stage guidance rate-gyro records, for which a higher filter break frequency was used, revealed the presence of vibration. All the flight yaw-rate telemetry data were reduced with the use of an 8-cps filter. A short burst of record obtained with a 45-cps filter is compared with a section of the third-stage record which was reduced with the use of the 8-cps filter, and is shown in figure 90. Frequencies of 20 and 100 cps appeared on the 45-cps trace which were not visible on the 8-cps trace. As might have been expected, there was also a phase lag involved with the use of an 8-cps filter that was not present when the 45-cps filter was used. The phase difference was revealing in that better correlation of jet activity with the resulting accelerations observed on the rate time histories was possible when compensating the 8-cps rate record for the phase lag.

Vehicle Instrumentation Flight Performance

Some interesting results during the thrusting phases of the flight are indicated in the examples of telemeter oscillograph records presented in figures 91 to 95. The channels which deviated from the expected normal during the flight are marked by an asterisk in tables V to VIII. These channels are discussed in this section from an instrumentation viewpoint. In addition, data results not covered in other sections are presented here.

Telemeter flight performance.- The four inductance coils monitoring first-stage control-surface positions are rated for stable operation up to 200° F. As noted previously, control-surface data began a large shift at about t = 22 seconds, although correlation with guidance rate and displacement data indicated that these shifts should not have occurred. Thermocouples located on the bearing housing near the instruments indicated temperatures over 350° F. Postflight temperature tests on similar instruments showed a considerable inductance shift above

300° F. Control-surface deflection data, therefore, are believed to be questionable beyond about 22 seconds after launch.

The events channel in figure 91 shows the occurrence of the premature ejection of the third-stage heat shield at 16 seconds after launch. This event was verified by flight movies. Initiation of command no-fire of the fourth stage at 151.3 seconds is indicated by the events channel in figure 93. A recorder on the ground command transmitter indicated that the command was given at approximately this time. Definite correlation could not be obtained since the transmitter recorder did not have range timing recorded, and only the time that the recorder was started with respect to range timing is known. It is considered reasonably certain, however, that the time of occurrence of fourth-stage no-fire was 151.3 seconds.

The resultant pressure from the second-stage headcap was approximately 30 to 50 psia lower than the nominal Castor motor pressure. Thrust data as obtained from the longitudinal accelerometer in the payload did not show a corresponding decrease from the nominal. This low headcap-pressure reading is considered to be the result of some instrument malfunction, although from an instrumentation viewpoint, no reasonable explanation can be made.

The third-stage headcap-pressure data agreed quite well with nominal except that at tail-off the pressure did not return to zero but to 22 psia. One explanation for this pressure return is a zero shift in the subcarrier oscillator. Another possibility is that the pressure potentiometer became damaged by the high vibration levels during third-stage burnout.

No adverse temperatures were measured inside the telemeter package in transition D or in the payload. All of the heat was created internally by the telemeter components. The maximum temperature measured in the transition D telemeter was 130° F in the vicinity of the amplifier used for the guidance rate and displacement signals and for the signal voltages from the vibrometers. In the payload, all internal temperatures were about 60° F at lift-off. This low temperature was maintained by air cooling supplied to the payload prior to lift-off. After 10 minutes of flight, the maximum temperature near the dc-dc converter reached about 145° F.

Of the three vibration channels, only one, channel 16, which measured transverse vibrations of the guidance package, supplied any data. Most of the higher level vibration occurred at 2,000 cycles or above. The system is designed mainly for vibration in the 10- to 2,000-cycle region for a subcarrier oscillator modulation index of 1.5 or higher. The data above 2,000 cycles are obtainable except that with the increased

bandwidth more noise enters the system. Therefore, for the data in these higher frequencies, ±10 percent accuracy is the best obtainable.

Channels 17 and 18 did not supply any vibration data. The output condenser on the vibrometer amplifier of channel 17 shorted during the final 2 hours of the countdown. Cathode bias voltage from the amplifier was then applied to the channel 17 oscillator and caused it to shift up to within 3,000 cycles of channel 18. This shift placed channel 17 within the band of channel 18. The data from these two channels are, therefore, of no use.

As previously indicated, the data from the yaw-rate, pitch-rate, and roll-rate channels showed close correlation to the guidance rate channels. At third-stage burnout when the vehicle rolled, the payload roll-rate channel was integrated to obtain the total resultant displacement. The guidance roll-rate and roll-displacement channels saturated during this time, so the total displacement could not be obtained. The range of the rate channels in the payload was set so as to obtain the large vehicle rates, whereas the ranges on the guidance rate and displacement channels were set narrow in order to see how close the guidance dead bands were held.

The magnetic aspect sensor on channel 11 showed that the vehicle rolled at the same time indicated by the roll rate and roll displacement channels. These data indicated a total roll displacement of 211°. This value compares quite closely to the roll displacement of 210° obtained from the payload roll-rate gyro.

The magnetic aspect sensor on channel 12 malfunctioned, and no data were obtained from this instrument.

As a result of countdown delays, launching of the vehicle occurred at twilight (7:00 p.m., e.s.t.). Since the horizon detector on channel 13 could not accurately discern the horizon at this time, no absolute attitude information was obtained from this instrument. However, the horizon detector verified that the vehicle experienced a roll displacement near the end of third-stage burning.

Operation of the solar aspect system on channel 14 required the vehicle to be spinning. Since fourth-stage ignition was withheld and the vehicle did not spin up, no data were obtained from this system.

Figure 96 shows the variation of signal strength received with slant range for each of the four telemeter systems. Signal strength calculated by theory is also included in these plots. The theoretical value of signal strength was based on transmitted power, the gain of the sending and receiving antennas, and assumed free-space propagation

loss. With the exception of the base A telemeter (FM/AM), the measured signal strength generally followed the calculated values of signal strength. In the case of the base A telemeter, it is believed that the flame of the first-stage motor caused signal attenuation. The base A antenna was located a few inches above the nozzle ring and was thus highly susceptible to flame attenuation. The initial low signal strength on receiver no. 2 was due to improper directing of the antenna at lift-off.

On the three other telemeters, momentary decreases in signal strength occurred at second-stage and third-stage ignition. These decreases were probably due to momentary flame attenuation. On the transition D and payload telemeters, a decrease of signal strength during second-stage burning can be noted. This attenuation is of a peculiar nature and is described in detail in reference 3. The signal strength during this time fluctuated up and down 20 db. The attenuation disappeared and the signal strength returned to normal each time a yaw or pitch hydrogen-peroxide jet motor fired.

The decrease in signal strength which began at a slant range of about 200 nautical miles, and the rising and falling of signal strength with increasing range, were probably due to attitude changes of the vehicle and consequent antenna pattern reorientation.

The transition D telemeter signal was lost at a slant range of approximately 1,000 nautical miles (about 5 minutes sooner than the payload telemeters). This signal loss was due to loss of battery power caused by over 15 minutes of the battery life being used up prior to launch. The remaining telemeter signals were lost when radio horizon was reached.

Radar-beacon flight performance.- Figure 97 shows received signal strength of the payload C-band beacon plotted against slant range. The signal strength was recorded from the receiver in the FPS-16 C-band range radar which was tracking the beacon during flight. A dashed line shows the theoretical signal strength plotted against slant range, which was obtained from calculations based on radar-beacon power, beacon-antenna gain, free-path attenuation, receiving-antenna gain, and radar-receiver sensitivity.

Several flight events are related in the plot presented in figure 97. Prior to a slant range of approximately 140 nautical miles, the the average signal strength (in decibels) was 25 db or more below the theoretical signal strength. After a slant range of approximately 140 nautical miles, the measured and calculated signal strengths on an average are nearly equal. An investigation of telemetry and trajectory data has established that the FPS-16 C-band range radar was initially

tracking the vehicle on a side lobe of the radar antenna and reoreinted to the major lobe at a slant range of approximately 140 nautical miles. Figure 97 supports this investigation since the major lobe of the receiving antenna has approximately a 28-db gain over the side lobes. Also, the decrease and following increase in signal strength shown indicates the null which would be passed through as the radar reoriented from the side lobe to the major lobe.

Figure 97 also shows the characteristic decrease in signal strength as caused by flame attenuation during second- and third-stage motor ignition.

The RCA AN/FPS-16 radar at Wallops Station has a normal maximum range of 500 nautical miles. In order to track beyond this range, the operator must take the radar out of the automatic tracking mode and reposition the range tracking gate. This operation requires approximately 30 seconds before automatic tracking can be resumed. During the interval the radar would not be precisely on target and a decrease in signal strength would be expected as shown between a slant range of 500 and 600 nautical miles in figure 97. Beyond 600 nautical miles, the signal strength decreased from the calculated. However, this decrease would be expected since the vehicle was approaching apogee and the off-the-rear antenna pattern was becoming unfavorable to Wallops Island.

The S-band beacon appeared to function properly during the flight. Because of ground radar difficulties, the returned beacon signal was not automatically tracked. However, beacon returns were noted on the radar scope beyond slant ranges of 300,000 yards.

Radiation measurements.- The radiation sensor in the payload worked successfully and recorded from launch to t = 1,329 seconds. These data were analyzed and are presented in reference 4.

Command-system flight performance.- The command destruct system was not initiated during the flight, and its performance could not be established. As pointed out previously, the fourth-stage motor command hold-fire system was initiated at 151.3 seconds and performed satisfactorily.

Rocket-Motor Flight Performance

First-stage motor pressure and thrust.- Time histories of measured headcap pressure and flight thrust for the Algol-IB rocket motor used in the ST-1 flight are presented in figure 98. Additional performance data are tabulated in column 6 of table I. The flight pressure integral was 16,845 psia-sec, with a total impulse of 4,246,000 lb-sec. The final burning time of the motor was 43.60 seconds.

In comparison, the total impulse derived from flight data was 0.5 percent lower than the manufacturer's predicted sea-level impulse. Although the flight pressure integral was low and slightly outside the nominal sigma value (one standard deviation), contrary to the value reported in reference 5, it is within the accuracy of the instrumentation used. The accuracy of this measurement is estimated at 3 percent because of the long elapsed time between system calibration and use. The flight web burning time appears normal when compared with the nominal, and the final burning time was only slightly outside the 1-sigma value.

The thrust of the Algol motor during flight was computed from longitudinal accelerometer data, corrected for a constant 10° jet-vane deflection, and from the drag parameter $C_D S$ shown in figure 99 and the weight time history shown in figure 100. The flight impulse computed by this method, however, appeared to be outside the 3-sigma value because of overall instrumentation accuracies.

Second-stage motor pressure and thrust.- The measured headcap pressure and flight thrust time histories for the second-stage Castor-IE5 motor are shown in figure 101. Additional performance data are presented in column 6 of table II. The flight pressure integral for this motor is not presented, since the pressure measured in flight was low. Up to 11 seconds of burning time (75 seconds of flight) the pressure was 25 psia below the nominal. Just after 11 seconds of burning time, a sudden shift in pressure occurred and the pressure was down about 40 psia until web burnout. A sample oscillograph trace of the Castor heading pressure showing this sudden pressure shift is shown in figure 92. Since the accelerometer and velocity data were normal at this time, it is concluded that the initial low pressure and sudden shift were caused by an instrumentation malfunction in the pressure measurement system.

The total impulse of the Castor motor during flight was 1,945,100 lb-sec, with a final burning time of 41.85 seconds. The flight impulse was computed from longitudinal accelerometer data, the drag parameter $C_D S$ shown in figure 102, and the weight time history shown in figure 103. This method of obtaining the total impulse from flight data appears to be applicable, since the resulting value was only 0.85 percent lower than the predicted impulse. Although the flight impulse was higher than the representative value (column 1, table II) from which the preflight trajectory was calculated, it was within the 1-sigma value from the nominal (column 2, table II).

The web burning time of 27.85 seconds was within the 2-sigma value of the nominal and was only 0.78 percent lower than the manufacturer's predicted. The final burning time was also within the 2-sigma value.

64

Third-stage motor pressure and thrust.- The measured headcap pressure and flight thrust time histories for the Antares-IA1 motor used in this test are presented in figure 104. Additional performance data for this motor are tabulated in column 6 of table III. The flight pressure integral is not given, since the pressure trace did not return to zero after burnout but came to rest at 22 psia. The failure of the pressure trace to return to zero after burnout is attributed to a zero shift in the instrumentation. Since valid assumptions could not be made as to when the shift occurred, the Antares motor pressure data is considered to be unreliable.

The total impulse of the Antares during flight was calculated from longitudinal accelerometer data and from the weight time history shown in figure 105. The resulting total flight impulse was 533,100 lb-sec, with a final burning time of 36.93 seconds. This value of total impulse is within both the 2-sigma value and the accuracy of the method of calculation. The flight impulse was within 0.5 percent of the manufacturer's predicted value of 535,890 lb-sec.

The web and total burning times were very short, and the most feasible explanation for these short burning times is in a possible elevated grain temperature prior to launch. The main reasons for this explanation are that the average temperature at Wallops Station for several days prior to launch was 83° F and the high ambient temperature during this time exceeded 90° F. Also, the Antares was enclosed in a sealed work envelope, and while the Castor was also enclosed in the same work envelope, the higher burning-rate sensitivity to temperature of the Antares could have resulted in a decreased burning time which would not have been observed in the Castor. In addition, the nominal data for the Castor are for a temperature of 77° F whereas these data for the Antares are for 70° F.

Velocity data.- In the velocity time history in figure 62, the measured velocity increment during Algol thrusting was 2.1 percent lower than the velocity increment predicted from preflight trajectory calculations utilizing the representative motor data listed in column 1 of table I. The small differences between the representative data used for preflight calculations and the nominal data listed in column 2 of table I do not account for the calculated velocity being higher than the flight velocity.

The Castor velocity increment was 2.2 percent higher than that calculated. Part of this discrepancy is due to the differences between the representative data used for the preflight calculation (column 1 of table II) and the nominal data used for the postflight calculation (column 2 of table II). For both the Algol and Castor motors, the velocity differences are also accountable for, in part, by radar and calculation errors.

The maximum velocity measured during the flight was approximately 15,500 feet per second near the end of Antares motor thrusting with a maximum longitudinal acceleration of approximately 10g at this time. This velocity was 2.8 percent higher than that predicted by using represenatative motor data. The velocity difference between measured and calculated values for the Antares motor may also be attributed in part to radar and calculation errors.

Concluding remarks.- All rocket motors receiving firing current performed satisfactorily. Headcap-pressure potentiometer, accelerometer, and radar velocity data all indicated that the Algol performance was slightly low. However, the variance of all three measured quantities is within instrumentation and calculation accuracy.

Radar velocity data indicated that Castor performance was high when compared with the preflight theoretical velocity that was calculated with representative motor data. With this fact taken into account and the fact that accelerometer data showed total flight impulse to be only 0.61 percent from the nominal, it is concluded that the Castor motor delivered nearly nominal performance.

Although the representative data used to calculate velocity increments for the Antares showed negligible variance from the nominal and manufacturer's predicted data, the flight velocity was high. This high velocity can be explained partly by possible radar and calculation error. However, it is felt that the Antares motor yielded a slightly higher performance than expected.

Aerodynamic Heating

Thermocouples were located in base A, transition D, and payload sections of the vehicle to measure temperatures resulting from aerodynamic heating at critical stations during the boost and coast phases of the flight through ignition of the third-stage motor. Each temperature measurement was commutated at the rate of 6 samples per second for all stations. Time histories of the temperatures measured by various thermocouples (designated as TC followed by an assigned number) are presented and comparisons are made where possible with theoretical temperatures computed by the methods described as follows.

Theoretical methods.- Calculations of the theoretical temperatures, with the exception of the temperature at the base A fin rib, were obtained from a thin-wall solution programed on an IBM 704 electronic data processing machine in conjunction with an elliptical, particle trajectory for a nonrotating earth with a launch elevation angle of 85°. The general method of Dusinberre (ref. 6), also programed on the IBM 704 computer, was used to calculate the temperature for the fin rib, which

required a thick-wall solution. Both programs include losses due to radiation from exposure to air but not losses due to conduction to surrounding components.

For velocities less than 3,000 feet per second, the Sibulkin stagnation-point heat-transfer theory of reference 7 was used to obtain convective heating rates for the hemispherical nose of the vehicle. For velocities above 3,000 feet per second, a modification of the Fay and Riddell stagnation-point theory of reference 8 was used for calculation of the theoretical temperatures. The latter theory includes real-gas effects. Heat-transfer rates for surfaces other than the hemisphere were obtained from Van Driest theory (ref. 9), which is applicable to both flat plates and conical surfaces.

Base A temperatures.- Thermocouples were installed at six locations on the skin of a first-stage fin and at three internal locations including the forward internal rib, the tip actuator bearing, and the jet-vane actuator bearing, as shown in figure 106. The thermocouple installed on the fin leading edge, thermocouple 1, was inoperative and no measurements were obtained for this location.

Time histories of the measured skin temperatures are presented in figure 107. The theoretical turbulent skin-temperature curve, which was calculated for thermocouple station 2, is in very good agreement with the measured temperatures (fig. 107(a)). The reason for the decrease in temperature on the base of the fin, thermocouple 5, from about 34 to 42 seconds is unknown, but may be associated with the Algol motor tail-off which occurred over approximately this time interval. (See fig. 98.) No attempt was made to predict the actuator bearing or trailing-edge temperatures. Comparison of the thick-wall solution for the fin rib with the measured temperatures at this station by thermocouple 6 (fig. 107(b)) shows that the theory is in excellent agreement with the measurement.

Transition D temperatures.- Eleven thermocouples were installed in transition D at the locations shown in figure 108. No data were recorded, however, by thermocouples 2, 4, and 6 during the data portion of the flight. The measurements on the skin (thermocouples 8, 9, 10, and 11) and access door (thermocouple 5) indicate turbulent flow (figs. 109(a) and (b)), whereas the measured temperatures on the conduit fairing (thermocouples 1 and 7) and horn antenna (thermocouple 3) indicate laminar flow (figs. 109(c) and (d)). The difference between the two measurements on the conduit fairing is probably due to the highly conductive material that was used to pot the thermocouple which recorded the lower of the two temperatures. The rapid decrease in the measured temperatures on the horn antenna at about t = 30 seconds (fig. 109(d)) was probably caused by the thermocouple breaking away from the skin. The general shape of

the curve after the break suggests that the thermocouple regained contact with the skin after a short period of time.

Payload heat-shield temperatures.- Skin temperatures were measured on the payload heat shield at the stagnation point and at stations on the hemispherical, conical, and cylindrical surfaces as shown in figure 110. A protective chrome-oxide coating with a nominal thickness of 0.002 to 0.003 inch was applied to the exterior surfaces of the heat shield at construction, and additional coating material was spread by spatula over various unspecified areas where the initial coating had flaked off during the preflight work. Since the thickness of the coating at the thermocouple locations is unknown, comparisons of the measurements with the theoretical predictions made for uncoated skin are useful primarily to show that the skin temperatures were not greater than the design values.

Figure 111(a) shows the temperatures at the stagnation point where the skin coating is believed to have been thin in relation to the skin thickness. This nose-cap section was constructed of 0.125-inch-thick material, but the thickness at the stagnation point may have been reduced somewhat during the spinning process used for fabrication of the section. No thickness measurements of the metal were made before installation of the thermocouples. The measured stagnation-point temperatures agree with the predictions for an uncoated skin as well as can be expected.

Thermocouple 2 on the nose cap was inoperative. Thermocouple 3 was also on the 0.125-inch-thick nose cap, and the temperature measurements (fig. 111(b)) are in good agreement with turbulent predictions for uncoated skin until first-stage burnout when the free-stream Reynolds numbers are becoming very low (see fig. 54).

Temperatures on the conical section (thermocouples 4 and 5) and on the cylindrical section (thermocouple 6) were less than the predicted turbulent temperatures for the uncoated skin as shown in figure 111(c) and (d). It might be expected that the temperatures on these sections would be influenced by the coating (of unknown but possibly appreciable thickness) because of the thinness of the skin, which was 0.04 inch and 0.02 inch on the conical and cylindrical sections, respectively.

Concluding remarks.- In general, the theoretical temperatures are in good agreement with the measured temperatures obtained on the first-stage fin, transition D section, and the nose of the payload heat shield. The maximum temperatures recorded were about half of the design values because of the high-launch-angle trajectory, and showed that aerodynamic heating presented no problem during the flight.

Investigation of Heat-Shield Failure

From the tracking film (see fig. 112) and from a telemetered events switch signal, it was determined that the third-stage heat shield came off prematurely and broke up at about 16 seconds after lift-off. Mach number at this time was approximately 0.90. Wind-tunnel data (figs. 113 and 114) indicate the existence of high negative pressure over the forward end of the heat shield at subsonic speeds, which reach a maximum at a Mach number of 0.90. In order to alleviate the resulting load, six equally spaced 1/4-inch-diameter holes were drilled in the heat shield at the station corresponding to the peak negative pressure coefficient. Calculations indicate that the vent area of the holes was sufficient to maintain the pressure inside the heat shield at less than 0.1 psi above the outside pressure at the location of the holes. (The heat shield had been statically tested to a bursting pressure of 0.4 psi.) However, during the assembly of the vehicle on the launcher, a field modification was made which consisted of sawing 11 slots in the wiring tunnel which extended along the length of the third-stage motor under the heat shield. As can be seen from figure 113, these slots had the effect of opening the inside of the heat shield to essentially ambient pressure, through transition section C and the second-stage wiring tunnel. The area of the saw slots was approximately 10 times that of the six vent holes. There was, in effect, no venting of the inside of the heat shield, and the heat-shield latching mechanism was subjected to the loads arising from the low-pressure region over the forward end of the heat shield. Figure 114 presents the variation of pressure coefficients with body station at a Mach number of 0.9. Integration of the pressure indicates that at the time of failure, the pressure load was approximately equal to the calculated yield load of the heat-shield latching mechanism. It is concluded, therefore, that the heat-shield failure resulted from this load.

Environmental Vibration

First-stage vibrations.- No continuous amplitude levels above the general noise level were discernible on any of the vibration channels during first-stage burning. An analysis of the variation of frequency with amplitude was therefore not performed. Some low-level short-duration vibration was shown by the payload longitudinal linear accelerometer near the end of first-stage burning. Figure 115 shows the times of occurrence and the amplitudes of this recorded oscillation. Frequencies of the oscillations are noted at various times. The response of the payload longitudinal vibration accelerometer at first-stage ignition is presented in figure 116.

Second-stage vibrations.- No continuous amplitude levels above the general noise level were discernible on any of the vibration channels

during second-stage burning. An analysis of the variation of frequency with amplitude was not performed. Figure 117 shows the response of the payload longitudinal linear accelerometer at second-stage ignition.

Third-stage vibrations.- Figure 118 shows the response of the payload longitudinal linear accelerometer at third-stage ignition. The discontinuities in the trace are the result of telemeter signal dropouts.

No useful data were obtained from the vibration channels 17 and 18 in transition D, the normal and longitudinal vibration accelerations, respectively. The reason for the loss of these two channels has been explained previously. Most of the analysis effort was made on the transverse vibration accelerations obtained by the 40-kc channel 16.

From the analysis of the variation of frequency with amplitude, a plot of frequency against time (fig. 119) was made for the transverse vibration acceleration channel. Some low-amplitude data points were used to fill out the curves and show the trends. Investigation of the resonant burning characteristics of the third-stage motor has provided tentative identification of some of the predominant frequency curves shown in figure 119. The solid curves are the calculated frequency curves of the motor cavity acoustical modes of oscillation. The frequency curves obtained from flight data analysis are identified by numerical or letter designations. The predominant frequency curves, sometimes called "sliding tones," are characteristic of the third-stage motor. It has been known that the third-stage motor exhibits the phenomenon known as resonant burning or unstable combustion. This resonant burning creates high-frequency, high-amplitude pressure oscillations about the mean chamber pressure. Numerous investigations and studies have been made of this phenomenon, and tentative identification of the modes of oscillation has been made. In the investigations of Smith and Sprenger (ref. 10), the frequencies observed were primarily those of the tangential modes of oscillation which were identified as pure traveling tangential modes. The question as to how the oscillations are excited has not yet been fully explained, although the explanation given by most investigators is that the oscillation is self-excited (ref. 11). These pressure variations can become very large, in some cases larger in a positive sense than the mean chamber pressure.

Frequency curves 1, 2, 3, 4, and 5 shown in figure 119 appear to be the first five tangential modes of oscillation, respectively. Curves 22 and 32 appear to be a combination of the second and third tangential modes, respectively, with a longitudinal mode. Curves 22 and 32 are not as continuous as curves 1 to 4, but show definite shifts at various times. Because of the particular internal configuration of the motor cavity, it is difficult to calculate the longitudinal mode frequencies. No data examined at present show any continuous frequency data points during the main burning time which would indicate these longitudinal modes. From

other data, the first longitudinal mode at third-stage burnout appears
to be about 300 cps. Curves C and E have not yet been identified. The
analyses indicate that the vibration wave form measured is primarily
mixed quasi-sinusoidals of varying amplitudes or primarily quasi-periodic.

The frequencies obtained in the present data agree closely with the
frequencies obtained from calculations using the methods of reference 10.
The value of the velocity of sound used in the calculations was about
5 percent less than the theoretical value obtained from the motor param-
eters. This value was chosen to show close agreement between the respec-
tive data frequency curves and not necessarily to show exact agreement
with the data in general. Also, the assumption of rigid boundaries used
in deriving the frequency equation is, of course, not strictly correct.
The measured frequencies should, in general, be less than the calculated
frequencies because of the real nonrigid boundaries.

A typical wave-analyzer output plot showing the variation of ampli-
tude with frequency of the transverse vibration accelerations is presented
in figure 120. No predominant frequencies were observed below 900 cps on
the frequency-against-amplitude analysis except for one discontinuous set
between 122.2 and 143.2 seconds. The apparent absence of lower frequen-
cies of significant magnitude may be a peculiarity of this particular
motor. Also, frequencies below 300 cps are difficult to ascertain from
the plots similar to figure 120. An analysis of the variation of fre-
quency with time for the frequency range 0 to 500 cps shows the presence
of several predominant curves during the time period from 126 to 137 sec-
onds which do not show up on the frequency-against-amplitude analyses.
A frequency-against-amplitude wave analysis for an expanded low-frequency
range (0 to 500 cps) was made for this time period by using 1-second tape
loops and a nominal filter bandwidth of 10 cps. This analysis failed to
show any amplitude levels over about 0.5g.

Discernible random vibration was generally less than ±0.5g except
for one frequency range around 2,900 cps at a few time periods, and then
was less than ±1.5g. The latter was probably affected by what appears
to be a signal noise frequency at about 2,900 to 3,000 cps which was
present prior to ignition, continued throughout burning, and was present
after burnout. The general noise level was low. No attempt was made to
obtain power-spectral-density plots.

Amplitudes for the predominant frequency curves of figure 120 are
shown in figures 121 and 122. It should be noted that these amplitudes
are given in ±g. It should be recognized that the amplitudes are aver-
aged over a finite time period during which the amplitude may, and
occasionally does, vary sharply. The decrease in analysis period from
2 seconds to 1 second improved the frequency and amplitude resolution
greatly. The subcarrier amplifier appears to have been overdriven by
the amplifier between 136.2 seconds and 141.1 seconds. This event was

probably caused by the high frequencies combined with large amplitude levels. There were no low-pass frequency filters and no amplitude limiters in the system. The amplitudes shown for this time period are not necessarily accurate, although they should be on the low side. Discernible vibration ends at 143 seconds.

No signal response checks were made for the vibration channels of the telemeter system. Calibrations for the data reduction were obtained by using subcarrier frequency deviations at the playback station. All amplitudes are uncorrected for amplitude dropoff at the higher frequencies above the IRIG rated intelligence frequency of 600 cps for the 40-kilocycle channel measuring transverse vibration accelerations.

To examine further the amplitudes within certain frequency ranges, oscillograph records of the wave amplitude envelope (rectified signal) were made as described in the discussion of data reduction. This envelope trace varied sharply most of the time. Figure 123 is a summary of these curves obtained by using various bandpass filters. The curves shown represent the peak values of this varying trace over a time period of 0.2 second or less. Figure 124 is a summary of similar curves obtained by using various low-pass filters.

The large vibration amplitudes experienced from 136 seconds to 141 seconds coincide with the large roll disturbance experienced by the vehicle. Also the vibration amplitude levels caused an acceleration switch in the control system to chatter throughout most of third-stage burning. The effect of this chatter on the control performance has been discussed previously.

Low-frequency, low-amplitude oscillations were observed on the payload longitudinal linear accelerometer during various time periods during third-stage burning. These oscillations were also indicated by the instrument measuring pitch rate in the payload at the same time intervals and at other time intervals during which the normal linear accelerometer oscillation was insignificant. These oscillations were not apparent on the payload instruments measuring rate of yaw and rate of roll. Correlation of times of occurrence with the erratic operation of the large and small pitch control motors in the third stage was inconclusive. Times of occurrence and frequencies of these oscillations recorded by the payload longitudinal linear accelerometer are tabulated as follows:

L
1
9
2
4

Flight time, sec	Frequency, cps	Amplitude, ±g
111.0	---	0
111.2	114	.49
111.9	112	.54
112.4	---	0
115.1	---	0
115.4	121	.58
116.0	---	0
116.6	---	0
116.8	109	.53
117.1	---	0
117.8	---	0
118.1	114	.7
118.4	115	.76
118.8	---	0
124.0	---	----
125.7	125	----
127.0	129	----
129.3	---	----
131.1	---	----
132.2	[a]136	----
133.2	[a]139	----
133.8	[a]135	----
134.2	---	----

[a]From rate-of-pitch trace.

No continuous amplitude levels above the general noise level were discernible on the three vibration channels in the payload during third-stage burning. This general noise level was about ±6g as determined from composite signal oscillograph traces.

Analyses of the variation of frequency with amplitude for the complete time period were not performed. Analyses made for several sample time periods indicated nothing significant.

SUMMARY OF RESULTS

Although erroneous radar tracking resulted in the prevention of fourth-stage motor ignition in the interest of range safety, the majority of test objectives established for the initial flight of the Scout vehicle were achieved. Overall results obtained from the flight have shown that the design concepts of the system are sound. In addition, this flight test has led to the discovery and solution of problem areas associated with the early development phases of the vehicle and components. Principal results obtained are summarized as follows:

1. Guidance accuracy for the flight was determined from a comparison of measured and predicted trajectories which indicated that the actual flight-path angle was about 1.5° higher than the value predicted, and that the angular difference in the azimuth track was 0.8°. These angular differences are within control-system design specifications. Flight simulation studies have shown that part of the differences could be attributed to variations in motor performance, thrust misalinement, and winds, especially during first-stage burning. Reasons for the remaining differences could not be detected from simulation studies.

2. Guidance- and control-system flight performance data have demonstrated the capability of the system to perform a probe-type mission. The first- and second-stage controls functioned properly, with control requirements during first-stage flight being about half the limit control deflections. Generally, the third-stage controls functioned normally except for overpowering of the roll jets by an unexpected rolling-moment disturbance near third-stage burnout. This disturbance caused the vehicle to lose roll reference by about 210° and is attributed to the burning characteristics of the third-stage motor.

3. Data acquisition for the flight was satisfactory with the exception of side-lobe tracking from launch to about third-stage burnout by the Wallops Station RCA AN/FPS-16 C-band radar facility. The induced roll displacement of the vehicle near third-stage burnout caused the FPS-16 radar to switch tracking from the side lobe of the receiving antenna to the main lobe. Consequently, the radar monitor plot board indicated a violent turning maneuver which caused the range safety officer to prevent firing of the fourth-stage motor. Although the control system regained command of the vehicle at a new roll reference immediately prior to third-stage burnout and the plot board tracks recovered, the hold-fire signal had been given and the fourth-stage motor therefore did not fire.

4. Second- and third-stage rocket-motor thrust misalinement angles were derived from measured control-system data. The resultant thrust

misalinement angle for the second-stage motor was computed to be 0.125°, acting about 31° off the vertical plane in the pitch-up and yaw-left direction. The third-stage motor resultant thrust misalinement angle was computed to be 0.05°, acting nearly halfway between the pitch-down and yaw-left directions. These values are well within tolerances used for control-system design. The thrust misalinement angle during first-stage burning was concluded from simulation studies to have been less than the design value of 0.25°.

5. In-flight performance of the rocket motors was demonstrated to be satisfactory during the flight, with the exception of high-level vibrations and possible rolling moments induced by the burning characteristics of the third-stage motor. The maximum velocity attained was approximately 15,500 feet per second near the end of third-stage motor burning with a maximum longitudinal acceleration of approximately 10g at this time. Velocity increments from the three stages substantiated predicted nominal performance data within the overall accuracy of the instrumentation and methods of analysis used.

6. Structural integrity of the vehicle was demonstrated during the flight with the exception of the premature loss of the third-stage heat shield as the vehicle entered the transonic speed range. Although venting was provided to relieve the high negative pressure known to exist at the forward end of the heat shield at these speeds, a field modification of the wiring tunnel had the effect of opening the inside of the heat shield to ambient pressures. Consequently, the heat shield latching mechanism failed from pressure loads which were of about the same magnitude as the latching-mechanism yield loads.

7. In general, skin temperatures measured on the first-stage fin, transition D section, and the payload heat shield were in good agreement with theoretical values and indicated that aerodynamic heating presented no problem during the flight. The maximum temperatures recorded during the flight were only about half of the design values because of the high-launch-angle trajectory.

8. Environmental vibration recorded in the vicinity of the guidance package in transition D showed that no significant continuous amplitude levels above the general instrumentation noise level were present during first- and second-stage burning. No continuous amplitude levels above the general noise level were discernible on the three vibration channels in the payload during third-stage burning. Vibration analyses for the third-stage burning period indicated that the vibrations recorded were primarily quasi-periodic with large variations in amplitudes. Large vibration amplitudes coincided with the large roll disturbance experienced by the vehicle near burnout of the third-stage motor. These vibrations caused an acceleration switch to chatter and resulted in a

constant switching in and out of the high and low reaction-jet controls during third-stage burning.

Langley Research Center,
National Aeronautics and Space Administration,
Langley Air Force Base, Va., February 6, 1962.

REFERENCES

1. Goodman, L. E., and Robinson, A. R.: Effect of Finite Rotations on Gyroscopic Sensing Devices. Jour. Appl. Mech., vol. 25, no. 2, June 1958, pp. 210-213.

2. Cannon, R. H., Jr.: Kinematic Drift of Single-Axis Gyroscopes. Paper 57-A-72, ASME, 1957.

3. Sims, Theo E., and Jones, Robert F.: Rocket Exhaust Effects on Radio Frequency Propagation From a Scout Vehicle and Signal Recovery During the Injection of Decomposed Hydrogen Peroxide. NASA TM X-529, 1961.

4. Gurtler, C. A.: Radiation Measurements in the Slot Between the Van Allen Belts to an Altitude of 1415 Kilometers. Jour. Geophys. Res. (Letters to the Editor), vol. 66, no. 9, Sept. 1961, pp. 3050-3054.

5. Smith, R. D., and Thibodaux, J. G., Jr.: Propulsion for the Scout Vehicle. [Preprint] 1461-60, American Rocket Soc., Dec. 1960.

6. Dusinberre, G. M.: Numerical Methods for Transient Heat Flow. Trans. A.S.M.E., vol. 67, no. 8, Nov. 1945, pp. 703-712.

7. Sibulkin, M.: Heat Transfer Near the Forward Stagnation Point of a Body of Revolution. Jour. Aero. Sci. (Readers' Forum), vol. 19, no. 8, Aug. 1952, pp. 570-571.

8. Fay, J. A., and Riddell, F. R.: Theory of Stagnation Point Heat Transfer in Dissociated Air. Jour. Aero. Sci., vol. 25, no. 2, Feb. 1958, pp. 73-85, 121.

9. Van Driest, E. R.: The Problem of Aerodynamic Heating. Aero. Eng. Rev., vol. 15, no. 10, Oct. 1956, pp. 26-41.

10. Smith, R. P., and Sprenger, D. F.: Combustion Instability in Solid-Propellant Rockets. Fourth Symposium (International) on Combustion, The Williams & Wilkins Co. (Baltimore), 1953, pp. 893-906.

11. Geckler, Richard D.: Unsolved Problems in Solid-Propellant Combustion. Fifth Symposium (International) on Combustion, Reinhold Pub. Corp. (New York), 1955, pp. 29-40.

TABLE I.- ALGOL PERFORMANCE DATA

Data item	1 Representative	2 Nominal	3 One standard deviation[a] from nominal	4 Percent of one standard deviation from nominal	5 Manufacturer's predicted for ST-1 motor	6 Flight of ST-1	7 Percent deviation of flight from representative	8 Percent deviation of flight from nominal	9 Percent deviation of flight from predicted
T	70° F	70° F	----------	----	70° F	Not available	----------	----------	----------
W_m	22,636 lb	22,648 lb	53 lb	0.23	22,684 lb	22,684 lb	0.21	0.16	0.00
W_p	19,000 lb	18,998 lb	47 lb	0.25	19,080 lb	19,080 lb	0.42	0.43	0.00
W_f	3,360 lb	3,443 lb	59 lb	1.71	3,397 lb	Not available	----------	Not available	Not available
t_b	35.0 sec	36.06 sec	0.65 sec	1.80	Not available	36.00 sec	2.9	0.11	Not available
t_f	44.0 sec	41.29 sec	1.76 sec	4.26	Not available	43.60 sec	0.91	4.62	Not available
$\int_0^{t_f} P_c\, dt$	Not available	16,980 psia-sec	450 psia-sec	2.65	Not available	16,485 psia-sec	----------	-2.92	Not available
I_{SL}	4,077,311 lb-sec	4,077,800 lb-sec	17,700 lb-sec	0.43	4,083,100 lb-sec	----------	----------	----------	----------
I_A	Not available	4,300,000 lb-sec	18,700 lb-sec	0.43	4,305,500 lb-sec	4,246,000 lb-sec	Not available	-0.37	-0.50

[a] One standard deviation, σ, is computed by the equation: $\sigma = \left(\dfrac{\Sigma D^2}{N}\right)^{1/2}$ where ΣD^2 is the sum of the squares of the deviations from the nominal and N is the number of samples.

TABLE II.- CASTOR PERFORMANCE DATA

Data item	1 Representative	2 Nominal	3 One standard deviation[a] from nominal	4 Percent of one standard deviation from nominal	5 Manufacturer's predicted for ST-1 motor	6 Flight of ST-1	7 Percent deviation of flight from representative	8 Percent deviation of flight from nominal	9 Percent deviation of flight from predicted
T	77° F	77° F	-------------	----	77° F	Not available	----	------------	------------
W_m	8,865 lb	8,845 lb	36 lb	0.41	8,862 lb	8,862 lb	-0.03	0.19	------------
W_p	7,313 lb	7,320 lb	26 lb	0.36	7,327 lb	7,327 lb	0.19	0.10	------------
W_f	1,429 lb	1,390 lb	47 lb	3.38	1,395 lb	Not available	----	Not available	Not available
t_b	27.0 sec	27.20 sec	0.51 sec	1.88	28.07 sec	27.85 sec	3.10	2.39	-0.78
t_f	39.9 sec	39.9 sec	1.1 sec	2.76	Not available	41.85 sec	4.90	4.89	Not available
$\int_0^{t_f} P_c \, dt$	Not available	15,960 psia-sec	130 psia-sec	0.81	16,111 psia-sec	Not available	----	Not available	Not available
I_v	1,938,000 lb-sec	1,957,000 lb-sec	12,940 lb-sec	0.66	1,961,700 lb-sec	1,945,100 lb-sec	0.37	-0.61	-0.85

[a] One standard deviation is computed by the equation: $\sigma = \left(\dfrac{\Sigma D^2}{N}\right)^{1/2}$ where ΣD^2 is the sum of the squares of the deviations from the nominal and N is the number of samples.

I-1924

L-1924

TABLE III.- ANTARES PERFORMANCE DATA

Data item	1 Representative	2 Nominal	3 One standard deviation[a] from nominal	4 Percent of one standard deviation from nominal	5 Manufacturer's predicted for ST-1 motor	6 Flight of ST-1	7 Percent deviation of flight from representative	8 Percent deviation of flight from nominal	9 Percent deviation of flight from predicted
$\bar{T}$	77° F	70° F	-------	----	70° F	Not available	-----	-------	-------
W_m	2,295 lb	2,285 lb	16 lb	0.70	2,300 lb	2,300 lb	0.22	0.66	0
W_p	2,087 lb	2,084 lb	6 lb	0.29	2,092 lb	2,092 lb	0.24	0.38	0
W_f	180 lb	178 lb	7 lb	3.93	182 lb	Not available	-----	Not available	Not available
t_b	36.0 sec	36.80 sec	0.96 sec	2.61	Not available	34.40 sec	-4.4	-6.52	Not available
t_f	40.0 sec	39.7 sec	0.8 sec	2.02	Not available	36.93 sec	-7.5	-6.98	Not available
$\int_0^{t_f} P_c\, dt$	Not available	11,686 psia-sec	51 psia-sec	0.44	Not available	Not available	-----	Not available	Not available
I_v	534,000 lb-sec	534,080 lb-sec	490 lb-sec	0.09	535,890 lb-sec	533,100 lb-sec	-0.17	-0.18	-0.50

[a]One standard deviation is computed by the equation: $\sigma = \left(\dfrac{\Sigma D^2}{N}\right)^{1/2}$ where ΣD^2 is the sum of the squares of the deviations from the nominal and N is the number of samples.

TABLE IV.- ALTAIR PERFORMANCE DATA

Data item	1 Representative	2 Nominal	3 One standard deviation[a] from nominal	4 Percent of one standard deviation from nominal	5 Manufacturer's predicted for ST-1 motor
T	77° F	70° F	----------	----	70° F
W_m	514 lb	515 lb	1 lb	0.19	516 lb
W_p	455 lb	456 lb	1 lb	0.22	456 lb
W_f	52 lb	50 lb	1 lb	2.00	52 lb
t_b	36.6 sec	38.5 sec	1.8 sec	4.72	Not available
t_f	38.6 sec	41.40 sec	1.82 sec	4.40	Not available
$\int_0^{t_f} P_c \, dt$	Not available	8,975 psia-sec	135 psia-sec	1.50	Not available
I_v	116,500 lb-sec	116,840 lb-sec	630 lb-sec	0.54	116,500 lb-sec

[a]One standard deviation is computed by the equation: $\sigma = \left(\dfrac{\Sigma D^2}{N}\right)^{1/2}$ where ΣD^2 is the sum of the squares of the deviations from the nominal and N is the number of samples.

TABLE V.- DESCRIPTION OF BASE A FM/AM TELEMETER CHANNELS

Channel frequency, kc	Measurement	Instrument	Range	Overall accuracy		Description of data
				Predicted	Flight	
110.0	Commutation of 8 skin temperatures	Chromel-alumel thermocouples	Ambient to 800° F	±10° F	±10° F	Five thermocouples measure skin temperatures on fin B Two measure bearing housing temperature, and one measures internal temperature of fin strut
119.5	Servo compartment temperature	Resistance thermometer	0° to 350° F	±3° F	±3° F	Measures local servo compartment temperature
*129.5	Fin position indicator, fin A	Variable-inductance coils	±18°	±2 percent	±5 percent up to 21 sec; not reliable beyond 21 sec	Measures the position of the control fin with respect to the model
*139.5	Fin position indicator, fin D	Variable-inductance coils	±18°	±2 percent	±5 percent up to 21 sec; not reliable beyond 21 sec	Measures the position of the control fin with respect to the model
*150.0	Fin position indicator, fin C	Variable-inductance coils	±18°	±2 percent	±5 percent up to 21 sec; not reliable beyond 21 sec	Measures the position of the control fin with respect to the model
*160.5	Fin position indicator, fin B	Variable-inductance coils	±18°	±2 percent	±5 percent up to 21 sec; not reliable beyond 21 sec	Measures the position of the control fin with respect to the model
170.0	First-stage motor headcap pressure	Variable-inductance pressure cell	0 to 485 psia	±2 percent	±2 percent	Supplies chamber pressure time history of Algol motor.
179.5	Normal static acceleration	Variable-inductance accelerometer	±2g	±2 percent	±2 percent	Measures normal acceleration in base A during first-stage burning and coast.
190.5	Transverse static acceleration	Variable-inductance accelerometer	±2g	±2 percent	±2 percent	Measures transverse acceleration in base A during first-stage burning and coast.
199.5	Hydraulic accumulator pressure	Variable-inductance pressure cell	0 to 3,000 psia	±2 percent	±2 percent	Supply continuous monitor of hydraulic accumulator pressure in base A

*Channel deviated from expected normal.

TABLE VI.- DESCRIPTION OF TRANSITION D FM/FM TELEMETER CHANNELS

Channel number	Measurement	Instrument	Range	Special network	Overall accuracy		Description of data
					Predicted	Flight	
1	Third-stage small-pitch-motor operation	Two valve relay switches; two chamber pressure switches	Switch open or close	Binary coded resistance matrix	±2 percent	±2 percent	Indicates which motor fires; can determine 16 different combinations of switch closures; indicates when voltage is fed to the peroxide valve and when pressure builds up in the motor
*2	Events	Third-stage skin switch; four-command destruct channel no. 7 relay closures, and fourth-stage hold-fire switch closure	Switch open or close; 0 to 32 volts on guidance voltage	Coded resistance circuit	±2 percent	±2 percent	The third-stage skin switch indicates heat-shield ejection; a relay closure of command destruct channel no. 7 indicates the command destruct receivers are captured with radio frequencies from ground transmitter; a ledex relay is used to open the ignition leads to the fourth-stage motor; a contact on this relay was used to indicate on the telemeter when command destruct commanded hold-fire; this channel also continuously monitors the guidance 28-volt power supply.
3	Pitch-program voltage	Voltage for guidance torquer	0 to 5.2 volts	Isolating resistor	±2 percent	±2 percent	Measures voltage being applied to pitch-gyro torquer
4	Second- and third-stage upper-roll-motor operation	Two valve relay switches; and two chamber pressure switches in each stage	Switch open or close	Binary coded resistance matrix in each stage	±2 percent	±2 percent	Indicates which motor fired; can determine 16 different combinations of switch closures; indicates when voltage is fed to the peroxide valve and when pressure builds up in the motor
5	Second- and third-stage lower-roll-motor operation	Two valve relay switches; and two chamber pressure switches in each stage	Switch open or close	Binary coded resistance matrix in each stage	±2 percent	±2 percent	Indicates which motor fired; can determine 16 different combinations of switch closures; indicates when voltage is fed to the peroxide valve and when pressure builds up in the motor
6	Second- and third-stage yaw-motor operation	Two valve relay switches; and two chamber pressure switches in each stage	Switch open or close	Binary coded resistance matrix in each stage	±2 percent	±2 percent	Indicates which motor fired; can determine 16 different combinations of switch closures; indicates when voltage is fed to the peroxide valve and when pressure builds up in the motor
7	Second- and third-stage large-pitch-motor operation	Two valve relay switches; and two chamber pressure switches in each stage	Switch open or close	Binary coded resistance matrix in each stage	±2 percent	±2 percent	Indicates which motor fired; can determine 16 different combinations of switch closures; indicates when voltage is fed to the peroxide valve and when pressure builds up in the motor
8	Second-stage N_2 main-tank pressure	Pressure potentiometer	0 to 3,500 psia	Voltage dropping resistor	±3 percent	±3 percent	Supplies continuous monitor of control-system N_2 pressure
9	Third-stage N_2 main-tank pressure	Pressure potentiometer	0 to 1,500 psia	Voltage dropping resistor	±3 percent	±3 percent	Supplies continuous monitor of control-system N_2 pressure
*10	Second- and third-stage motor headcap pressure	Pressure potentiometer	Second stage - 0 to 600 psia; third stage - 0 to 400 psia	Isolating resistors for feeding both pots to a single channel	±3 percent	±3 percent on third stage; see text for second-stage data	Supplies pressure time history of motor chamber pressure for Castor and Antares motors
*11	Commutation of telemeter 150 volt monitor and 10 compartment temperatures: transition B ambient, transition B N_2, transition C ambient, transition C N_2, four in transition D telemeter compartment, guidance package ambient, guidance gyro block	Thermistors	90° F to 220° F on two guidance temperatures; 30° F to 220° F on remaining temperatures	Voltage dropping resistor and oscillator calibration network	±2° F from 30° to 120° F; ±5° F from 120° F to 220° F; ±2° F from 90° F to 220° F on two guidance temperatures	Same as predicted	Measures temperature during flight in critical areas; monitors 150 volts used to bias binary coded resistance matrices

*Channel deviated from expected normal.

L-1924

TABLE VI.- DESCRIPTION OF TRANSITION D FM/FM TELEMETER CHANNELS - Concluded

Channel number	Measurement	Instrument	Range	Special network	Overall accuracy		Description of data
					Predicted	Flight	
12	Commutation of 11 skin temperatures	Iron-constantan thermocouples	Ambient to 1,000° F	Oscillator calibration network and d-c amplifier	±20° F	±20° F on eight thermocouples; three thermocouples lost	Obtains skin temperature around transition D section
*13A	Guidance roll-displacement error signal	Guidance roll displacement gyro	±5°	400-cycle phase demodulator	±5 percent to ±8 percent	±5 percent to ±8 percent	Measures the 400-cycle error signal from the guidance roll displacement gyro which is proportional to the vehicle roll displacement in degrees
*13B	Guidance pitch-displacement error signal	Guidance pitch displacement gyro	±5°	400-cycle phase demodulator	±5 percent to ±8 percent	±5 percent to ±8 percent	Measures the 400-cycle error signal from the guidance pitch displacement gyro which is proportional to the vehicle pitch displacement in degrees
*13C	Guidance yaw-displacement error signal	Guidance yaw displacement gyro	±5°	400-cycle phase demodulator	±5 percent to ±8 percent	±5 percent to ±8 percent	Measures the 400-cycle error signal from the guidance yaw displacement gyro which is proportional to the vehicle yaw displacement in degrees
*14A	Guidance roll-rate error signal	Guidance roll rate gyro	±20 deg/sec	400-cycle phase demodulator	±5 percent	±5 percent	Measures the 400-cycle error voltage from the guidance roll rate gyro which is proportional to the vehicle roll rate in deg/sec
*14B	Guidance pitch-rate error signal	Guidance pitch rate gyro	±8 deg/sec	400-cycle phase demodulator	±5 percent	±5 percent	Measures the 400-cycle error voltage from the guidance pitch rate gyro which is proportional to the vehicle pitch rate in deg/sec
*14C	Guidance yaw-rate error signal	Guidance yaw rate gyro	±8 deg/sec	400-cycle phase demodulator	±5 percent	±5 percent	Measures the 400-cycle error voltage from the guidance yaw rate gyro which is proportional to the vehicle yaw rate in deg/sec
15	Guidance 400-cycle supply voltage	Guidance inverter	0 to 15 volts; 0 to 450 cycles	Voltage dropping resistor	Voltage ±2 percent; frequency ±0.01 percent	Voltage ±2 percent; frequency ±0.01 percent	Monitors guidance 400-cycle supply voltage and frequency
*16	Vibration in the transverse direction on the guidance package	Crystal accelerometer	±60g peak	----------------	±5 percent	±10 percent	Measures vibration data in the 10- to 2,000-cycle range
*17	Vibration in the normal direction on the guidance package	Crystal accelerometer	±60g peak	----------------	±5 percent	No data	Measures vibration data in the 10- to 2,000-cycle range
*18	Vibration in the longitudinal direction on the guidance package	Crystal accelerometer	±120g peak	----------------	±5 percent	No data	Measures vibration data in the 10- to 2,000-cycle range

*Channel deviated from expected normal.

TABLE VII.- DESCRIPTION OF PAYLOAD FM/AM TELEMETER CHANNELS

Channel frequency, kc	Measurement	Instrument	Range	Special network	Overall accuracy		Description of data
					Predicted	Flight	
119.5	Commutation of six skin temperatures and heat-shield eject switch	Chromel-alumel thermocouples and microswitch	Ambient to 1,400° F	Resistance network for heat-shield eject switch	±20° F	±20° F	Obtains skin temperatures on various points of payload heat shield; indicate when payload heat shield is ejected
*129.5	Longitudinal static acceleration	Variable-inductance accelerometer	-4g to +20g	-----------	±2 percent	±2 percent	Obtains longitudinal acceleration during the firing of each stage; when data are integrated, will obtain velocity of vehicle
*179.5	Yaw rate	Rate gyro	±1 radian/sec	-----------	±2 percent	±2 percent	Measures vehicle rate of displacement in the yaw direction; will supply correlation data for guidance yaw rate data channel 14C transition D FM/FM telemeter
*190.5	Pitch rate	Rate gyro	±1 radian/sec	-----------	±2 percent	±2 percent	Measures vehicle rate of displacement in the pitch direction; will supply correlation data for guidance pitch rate data channel 14B transition D FM/FM telemeter
*199.5	Roll rate	Rate gyro	±1 radian/sec	-----------	±2 percent	±2 percent	Measures the vehicle rate of displacement in the roll direction; will supply correlation data for guidance roll rate data channel 14A transition D FM/FM telemeter

*Channel deviated from expected normal.

L-1924

TABLE VIII.- DESCRIPTION OF PAYLOAD FM/FM TELEMETER CHANNELS

Channel number	Measurement	Instrument	Range	Special network	Overall accuracy		Description of data
					Predicted	Flight	
*5	Radiation	Geiger-Müller counter	0 to 50 milliroentgens/hr	-------------	See ref. 4	See ref. 4	Measure cosmic radiation rate in the altitude range of the vehicle
6	Fourth-stage motor headcap pressure	Pressure potentiometer	0 to 40 psia	Voltage dropping resistor	±3 percent	No data	Obtains a chamber-pressure time history of the Altair motor
7	Normal static acceleration located forward of the c.g.	Linear accelerometer	±10g	Voltage dropping resistor	±4 percent	±4 percent	Obtains static acceleration in the normal direction; along with channels 8, 9, and 10 will indicate translation and irregular motions of the vehicle axes
8	Transverse static acceleration located forward of the c.g.	Linear accelerometer	±10g	Voltage dropping resistor	±4 percent	±4 percent	Same as channel no 7, except in the transverse direction
9	Normal static acceleration located on or near the c.g.	Linear accelerometer	±5g	Voltage dropping resistor	±4 percent	±4 percent	Same as channel no. 7
10	Transverse static acceleration located on or near the c.g.	Linear accelerometer	±5g	Voltage dropping resistor	±4 percent	±4 percent	Same as channel no. 8
*11	The direction of vehicle with respect to earth's magnetic lines of force, sensor mounted perpendicular to vehicle axis	Schonstedt magnetic aspect sensor	±600 milligauss	-------------	±3 percent	±3 percent	By measuring the local earth's magnetic field, the direction of the vehicle with respect to the magnetic lines of force can be obtained; by knowing earth's local magnetic vector at any point, along with data from the other magnetic aspect sensors and radar data, the attitude of the model can be obtained; at spin-up of the fourth stage this channel shows a sine wave from which the spin rate can be found
*12	Same as channel no. 11 except sensor mounted parallel to vehicle axis	Schonstedt magnetic aspect sensor	±600 milligauss	-------------	±3 percent	No data	Same as channel no. 11, except will not indicate any spin data
*13	Attitude of the fourth stage prior to spin-up	Horizon detector	±180° in pitch direction	-------------	±3 percent	No data	Determines attitude of the fourth stage by detecting the earth's horizon prior to fourth-stage spin-up
*14	Attitude of the fourth stage after spin-up	Naval Research Lab. designed solar aspect system	Vehicle attitude	-------------	±3 percent	No data	Determines attitude of the fourth stage by detecting direction of the earth and sun after spin-up
*15	Commutation of seven telemeter compartment temperatures in the payload	Thermistors	30° F to 220° F	Voltage dropping resistor and oscillator calibration network	±2° F from 30° F to 120° F; ±5° F from 120° F to 220° F	Same as predicted	Measures temperature during flight in critical areas in the payload-telemetry package
*16	Vibration in the transverse direction on the main plate of the payload telemeter	Crystal accelerometer	±100g	-------------	±5 percent	No data	Measures vibration data in the 10- to 2,000-cycle range
*17	Same as channel no. 16 except in the normal direction	Crystal accelerometer	±100g	-------------	±5 percent	No data	Measures vibration data in the 10- to 2,000-cycle range
*18	Same as channel no. 16 except in the longitudinal direction	Crystal accelerometer	±120g	-------------	±5 percent	No data	Measures vibration data in the 10- to 2,000-cycle range

*Channel deviated from expected normal.

TABLE IX.- COORDINATES OF GEOMETRIC CENTERS OF

LINEAR ACCELEROMETERS AND RATE GYROS

Vehicle assembly	Instrument	Quantity measured	Body station, x, in.	y, in.	z, in.
Base A	Normal accelerometer	a_N	812.34	0	18.31
	Transverse accelerometer	a_Y	811.18	0	18.31
Payload	Longitudinal accelerometer	a_X	29.18	0	0
	Forward normal accelerometer	$a_{N,fwd}$	24.33	0	0
	Aft normal accelerometer	$a_{N,aft}$	42.09	0	0
	Forward transverse accelerometer	$a_{Y,fwd}$	25.85	0	0
	Aft transverse accelerometer	$a_{Y,aft}$	43.44	0	0
	Rate-of-pitch gyro	$\dot{\theta}$	28.33	-1.45	-2.53
	Rate-of-yaw gyro	$\dot{\psi}$	28.33	0	2.53
	Rate-of-roll gyro	$\dot{\phi}$	28.33	1.42	-2.53

TABLE X.- WEIGHT BREAKDOWN FOR ST-1 TEST VEHICLE

Item	Weight, lb
First stage:	
Transition B-lower	98.2
Hoisting ring	76.6
Algol motor	22,689.0
Base A section	726.0
Nozzle insulation	42.0
Vehicle before first-stage firing	36,842.0
Expended propellant during firing	19,099.0
Vehicle after firing	17,743.0
Second stage:	
Transition C-lower	118.8
Castor motor and nozzle	8,859.2
Nozzle insulation	31.3
Transition B-upper	289.9
H$_2$O$_2$ and N$_2$	193.0
Tunnels, hats, wiring	56.9
Vehicle before second-stage firing	13,208.1
Expended propellant	7,466.0
Expended nozzle insulation	21.3
Expended H$_2$O$_2$	63.0
Vehicle after second-stage firing	5,657.6
Third stage:	
Transition D-lower	688.1
Antares motor and transition C-upper	2,467.0
Tunnels, hats, wiring	26.2
H$_2$O$_2$ and N$_2$	20.0
Vehicle before third-stage firing (without heat shields)	3,510.0
Payload heat shield	31.5
Altair motor heat shield	80.0
Antares motor heat shield	38.0
Vehicle before third-stage firing (with heat shields)	3,659.0
Expended propellant	2,122.0
Vehicle after third-stage firing (without heat shields)	1,388.0
Fourth stage:	
Payload, collar, Altair motor, nozzle	689.0
Skirt and spin motors	13.1
Flare experiment	23.0
Dynamic-balance weight	0.8
Vehicle before fourth-stage firing	725.9
Expended items	464.2
Vehicle after fourth-stage firing	261.7

L-1924

TABLE XI.- IN-FLIGHT EVENTS INITIATED BY PROGRAMER

Time from lift-off, sec	Timer-controlled event
3	Start pitch step no. 1
10	Stop pitch step no. 1 Start pitch step no. 2
30	Stop pitch step no. 2 Start pitch step no. 3
62.838	2nd-stage ignition 2nd-stage poppet valves on Pitch and yaw gain change
80.838	Stop pitch step no. 3 Start pitch step no. 4
105.838	Stop pitch step no. 4 Start pitch step no. 5
107.838	3rd-stage ignition 3rd-stage poppet valves on
148.838	Stop pitch step no. 5 Start pitch step no. 6
163.838	End pitch program
175.838	4th-stage ignition 3rd-stage poppet valves off

TABLE XII.- COMPARISON OF PREFLIGHT AND

TELEMETERED PITCH PROGRAM RATES

Step number	Pitch program			
	Preflight		Telemetered	
	Time, sec	Rate, deg/sec	Time, sec	Rate, deg/sec
---	0 to 3	0	0 to 3.24[a]	0
1	3 to 10	-.9929	3.24 to 10.24	-1.025
2	10 to 30	-.3643	10.24 to 30.26	-.380
3	30 to 80.838	-.1783	30.26 to 81.09	-.193
4	80.838 to 105.838	-.0749	}81.09 to 148.73[b]	-.090
5	105.838 to 148.838	-.0796		
6	148.838 to 163.838	-1.000	148.73 to 163.74	-1.036

[a]Lift-off occurred 0.24 second after zero time.

[b]Step no. 4 continued unchanged into step no. 5.
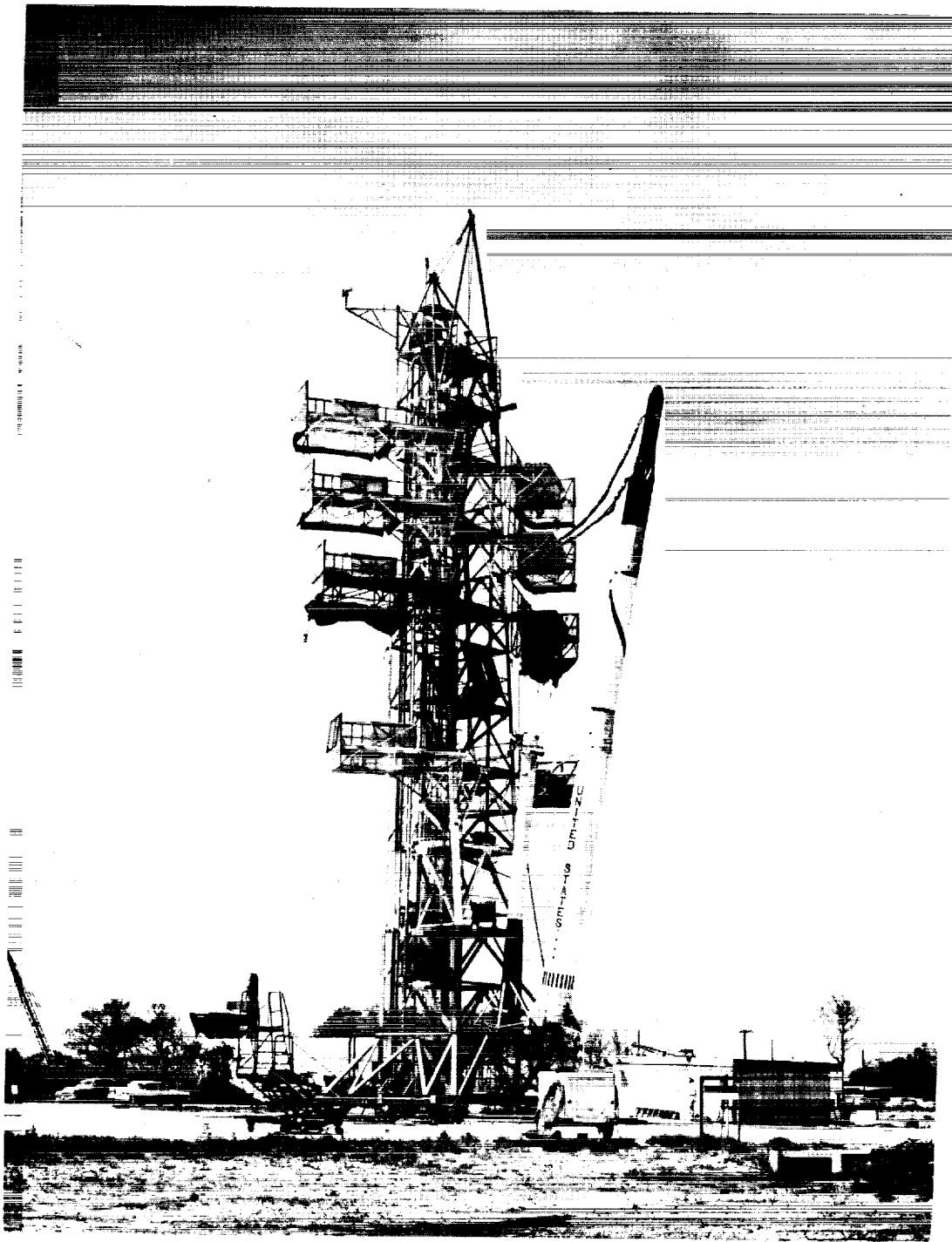
L-1924

L-60-3967

Figure 1.- Scout ST-1 test vehicle in launch position at
NASA Wallops Station.
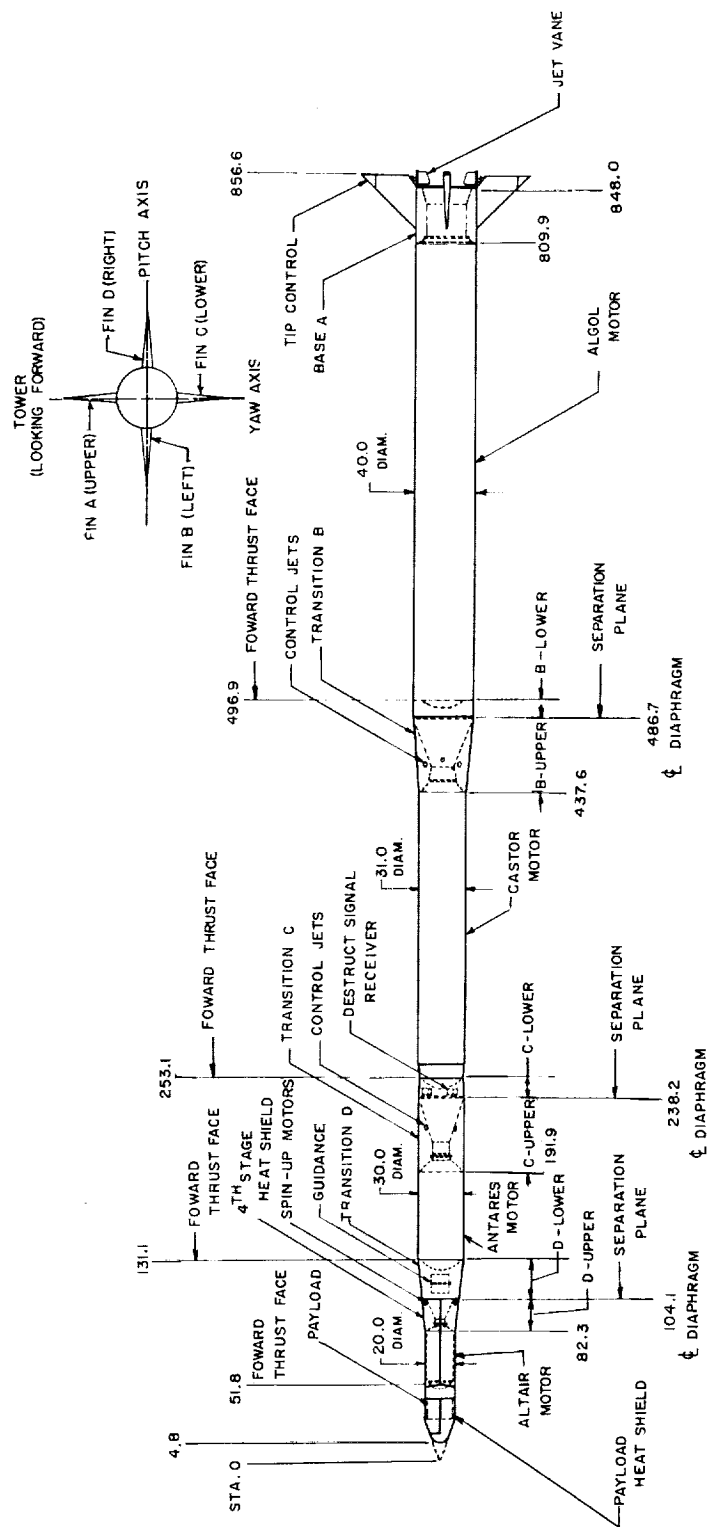
L-1924

(a) General arrangement. All dimensions are in inches.

Figure 2.- General arrangement and major assemblies of ST-1 test vehicle.

L-60-3505

(b) End view of first stage showing base section A.

Figure 2.- Continued.
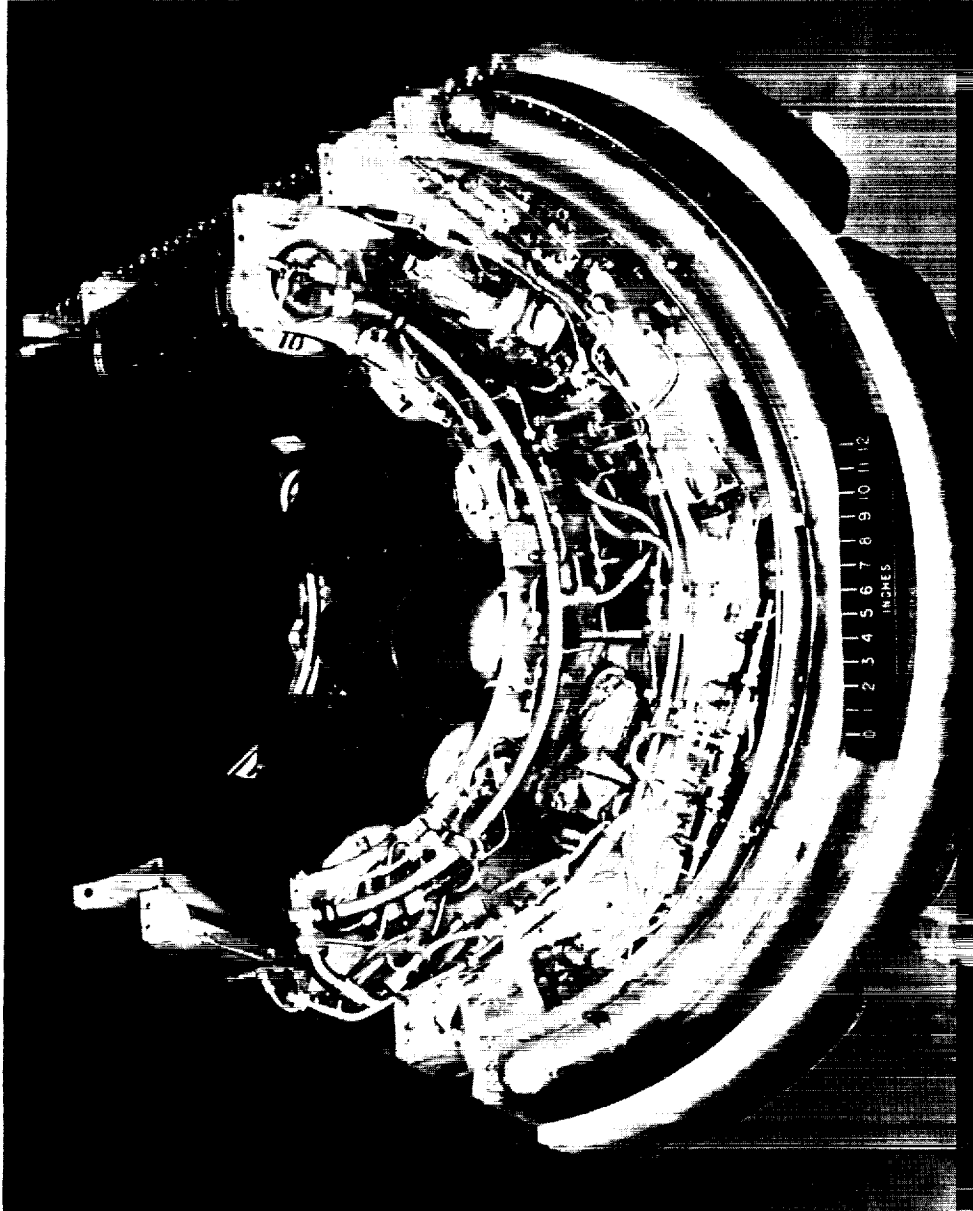
L-1924

L-60-130

(c) Internal view of transition B-upper split fairing showing part of second-stage control-system plumbing.
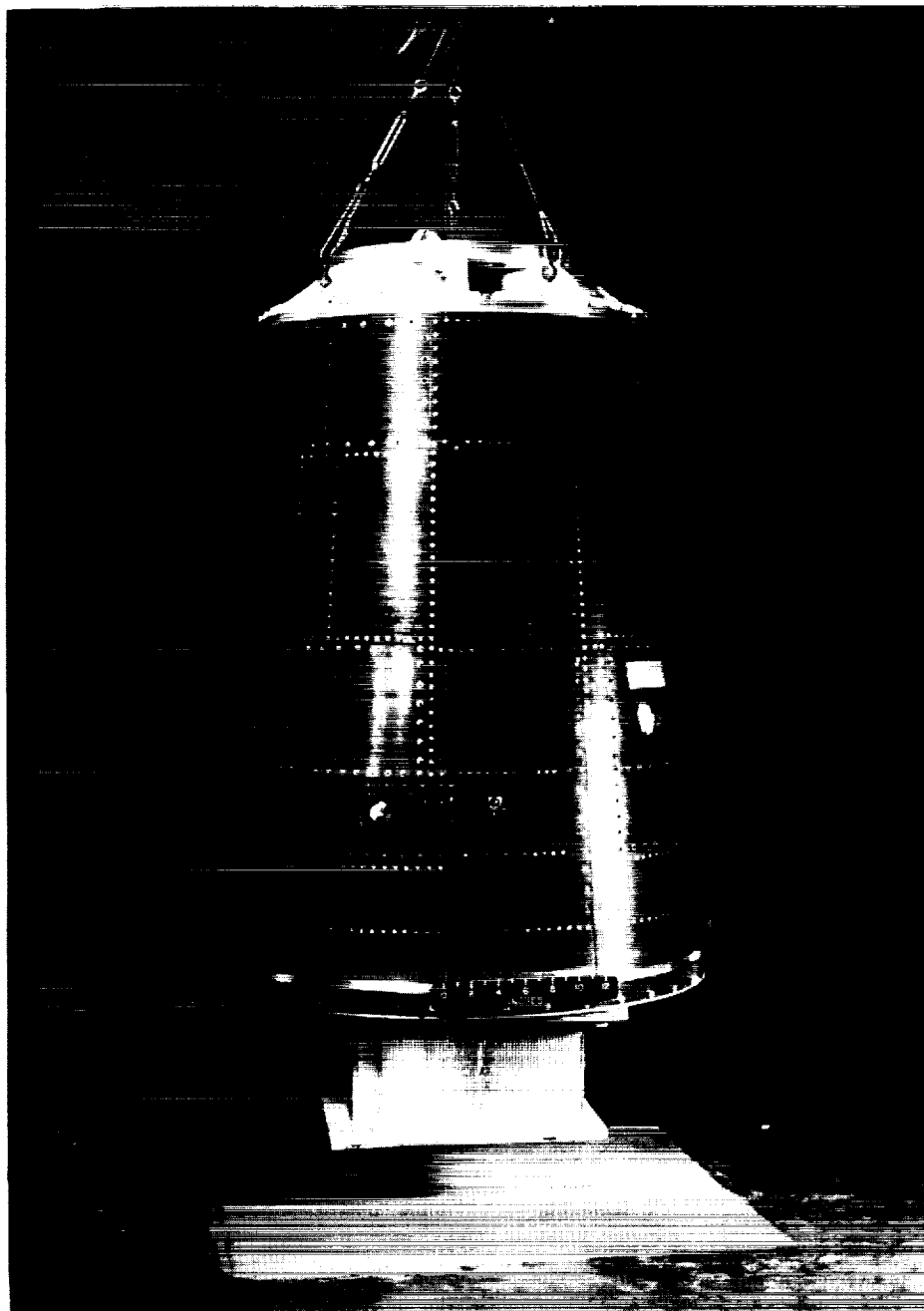
Figure 2.- Continued.

L-60-1895

(d) Transition B-upper assembly.

Figure 2.- Continued.
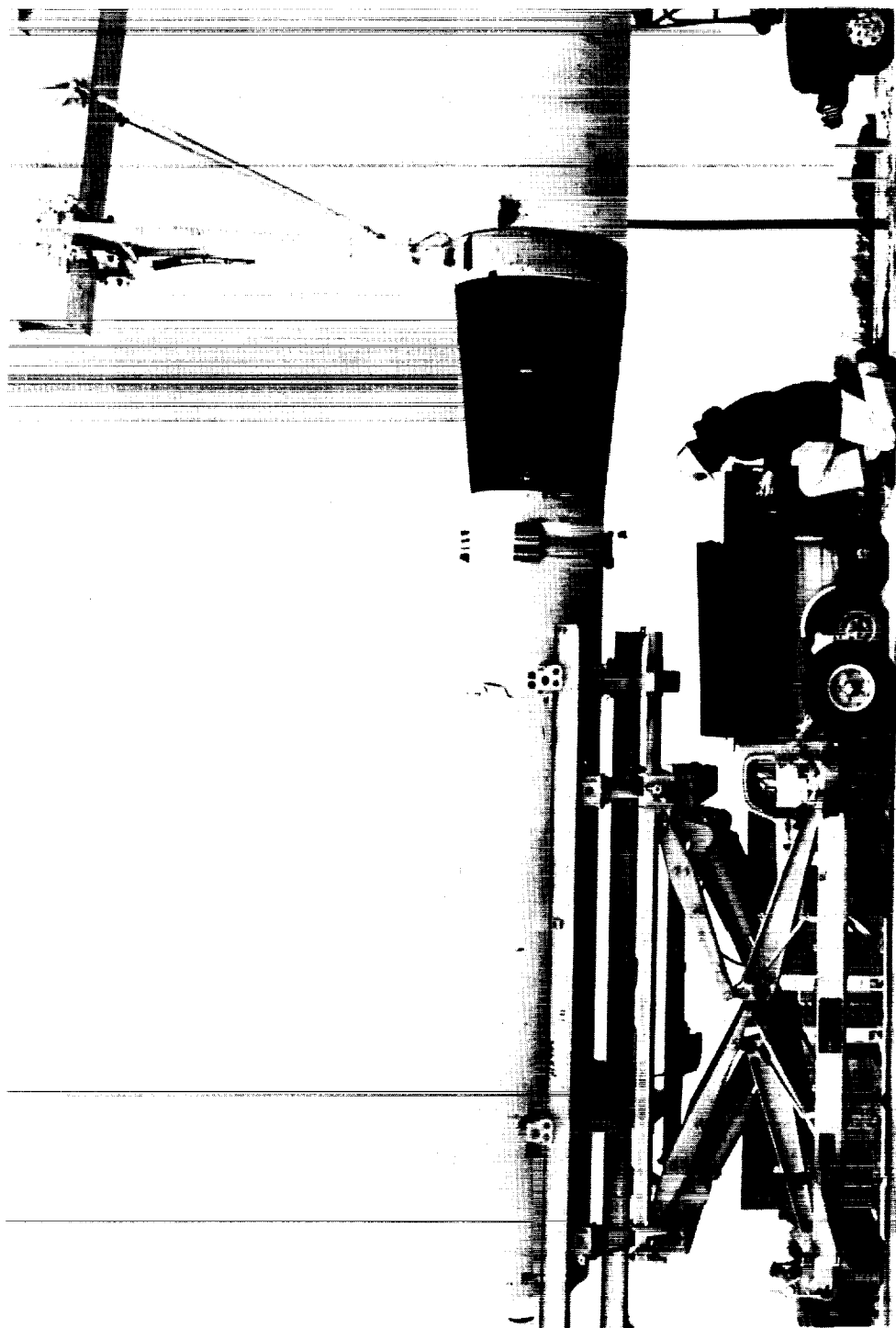
L-1924

(e) Second-stage motor and transition B erected on launcher.

Figure 2.- Continued.
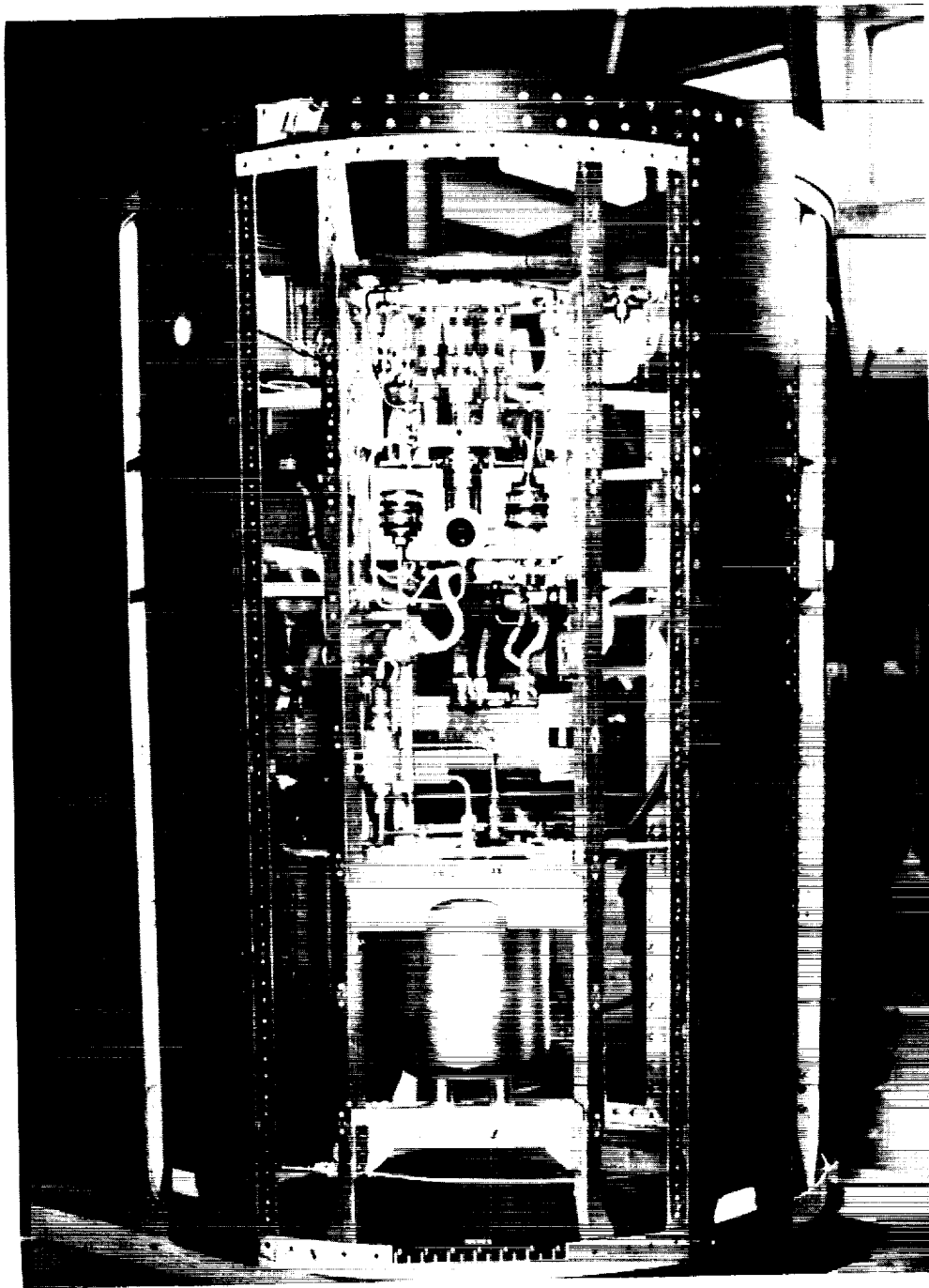
L-60-2026

(f) View of transition C-upper fairing showing part of third-stage
control-system plumbing.

Figure 2.- Continued.
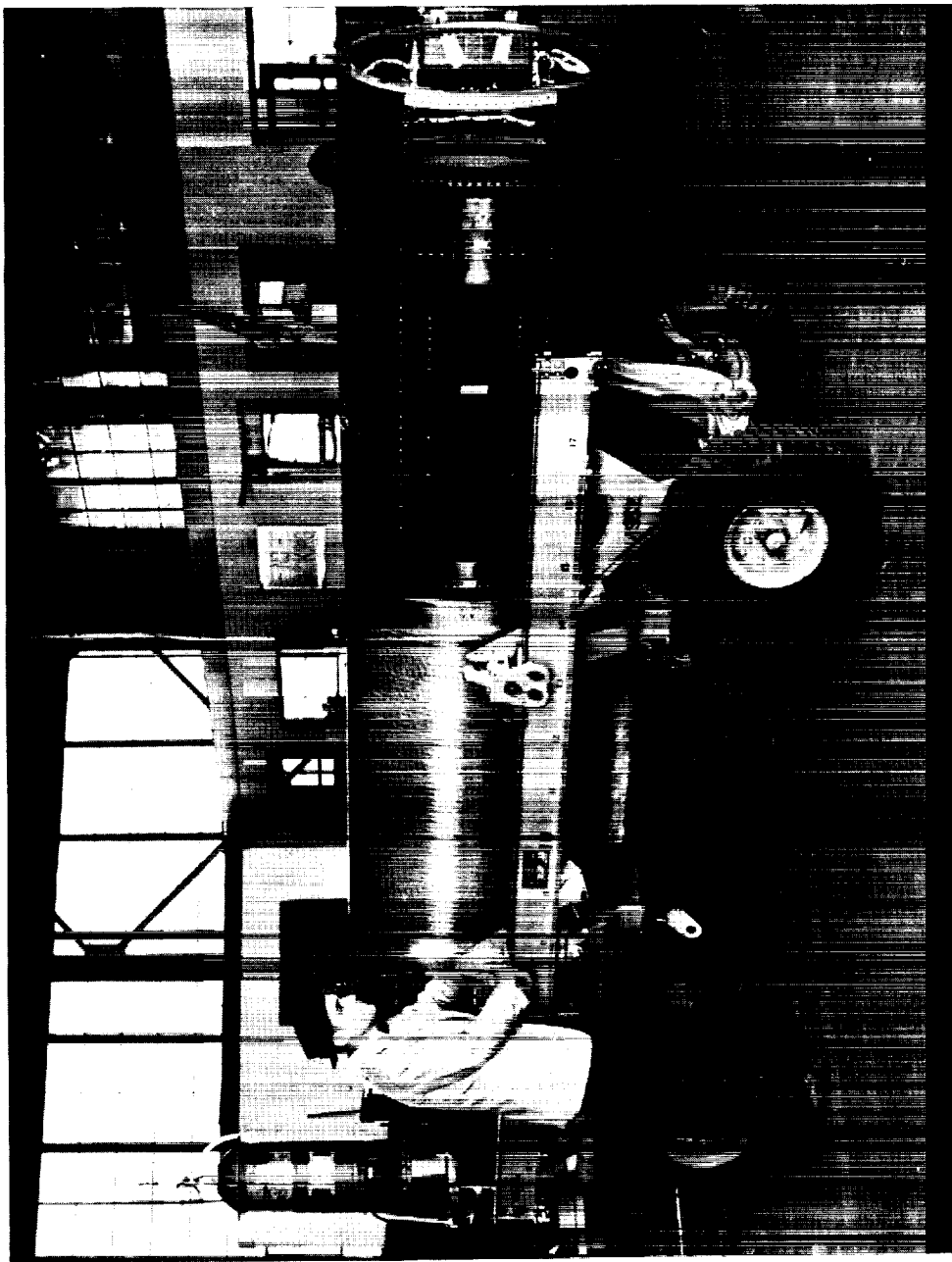
L-1924

L-60-1186

(g) Transition C assembly and third-stage motor.

Figure 2.- Continued.
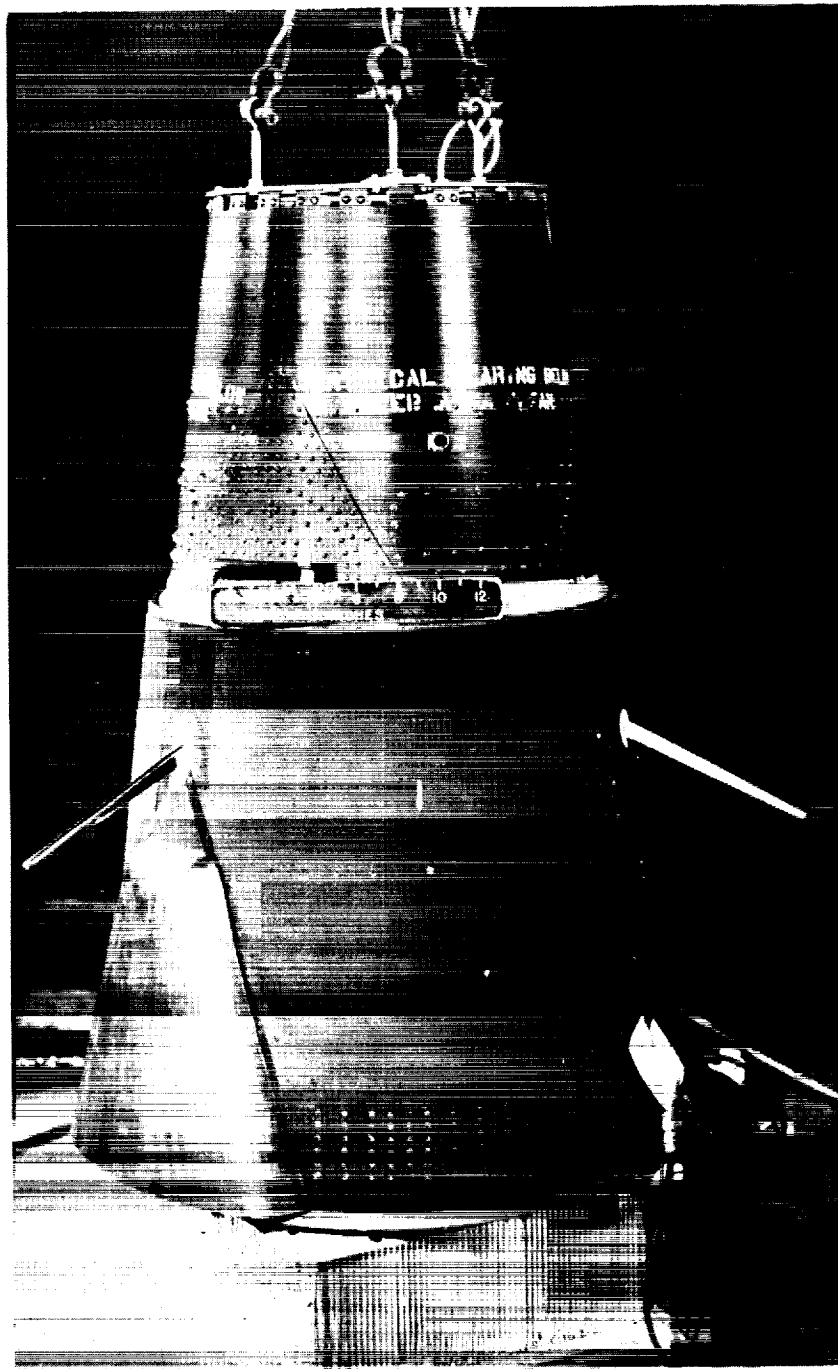
L-60-1539

(h) Transition D-lower fairing and spin-table assembly.

Figure 2.- Continued.
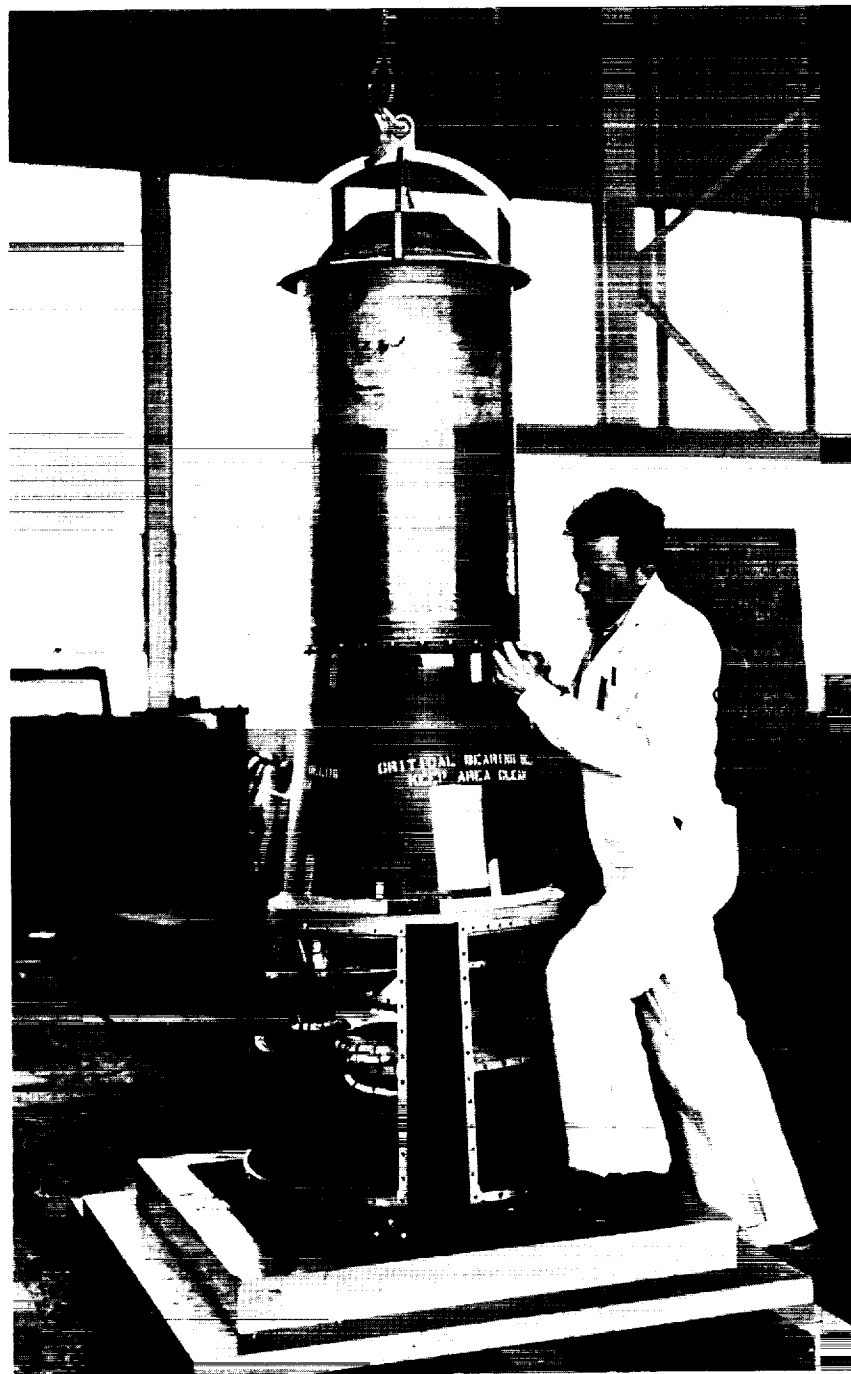
L-1924

L-60-1177

(i) Transition D assembly and fourth-stage motor.

Figure 2.- Continued.
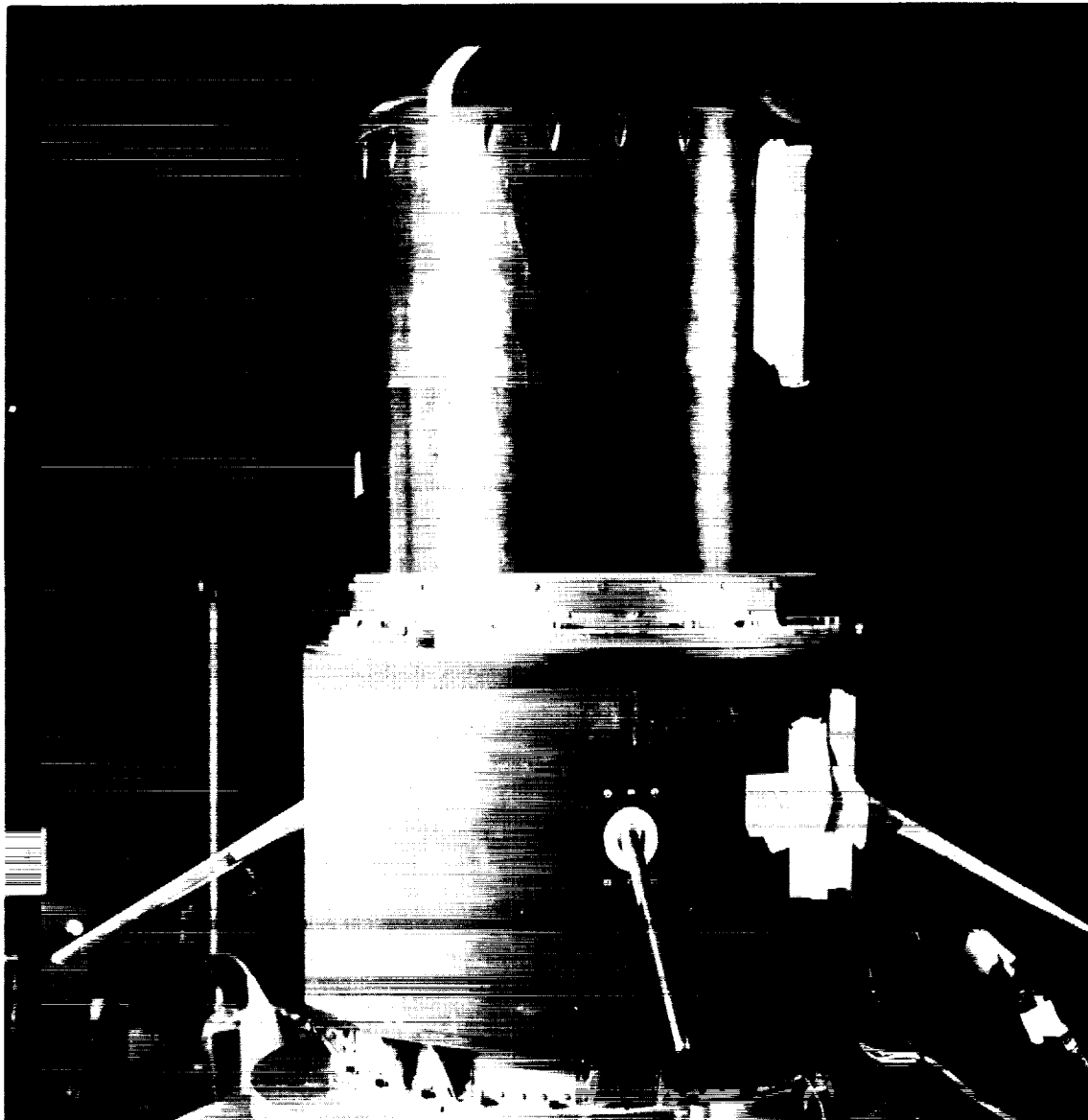
L-60-1545

(j) Payload assembly.

Figure 2.- Continued.
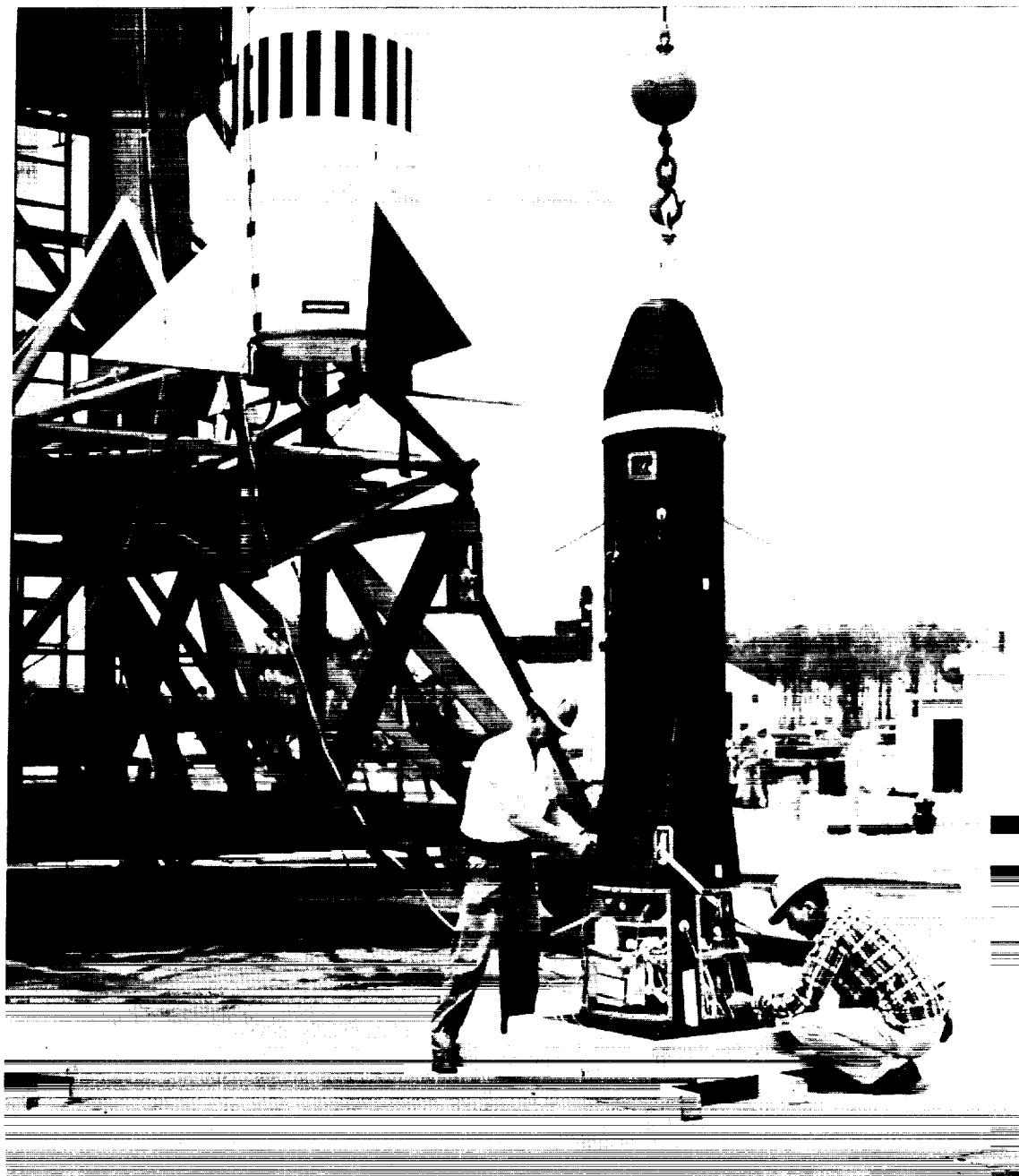
L-60-3951

(k) Transition D and fourth-stage assemblies with heat shields installed.

Figure 2.- Concluded.
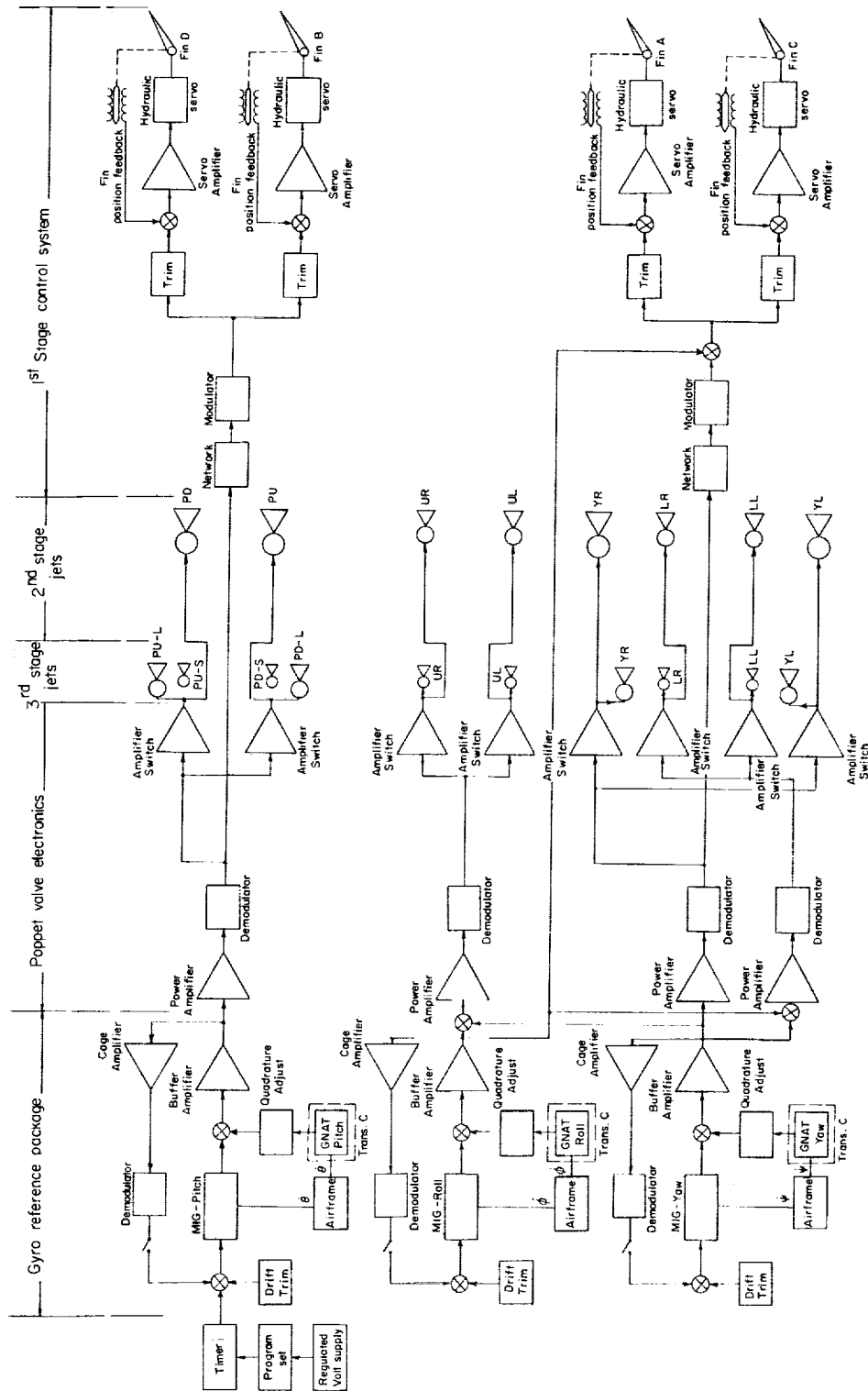
Figure 3.- Schematic diagram of complete guidance and control system.
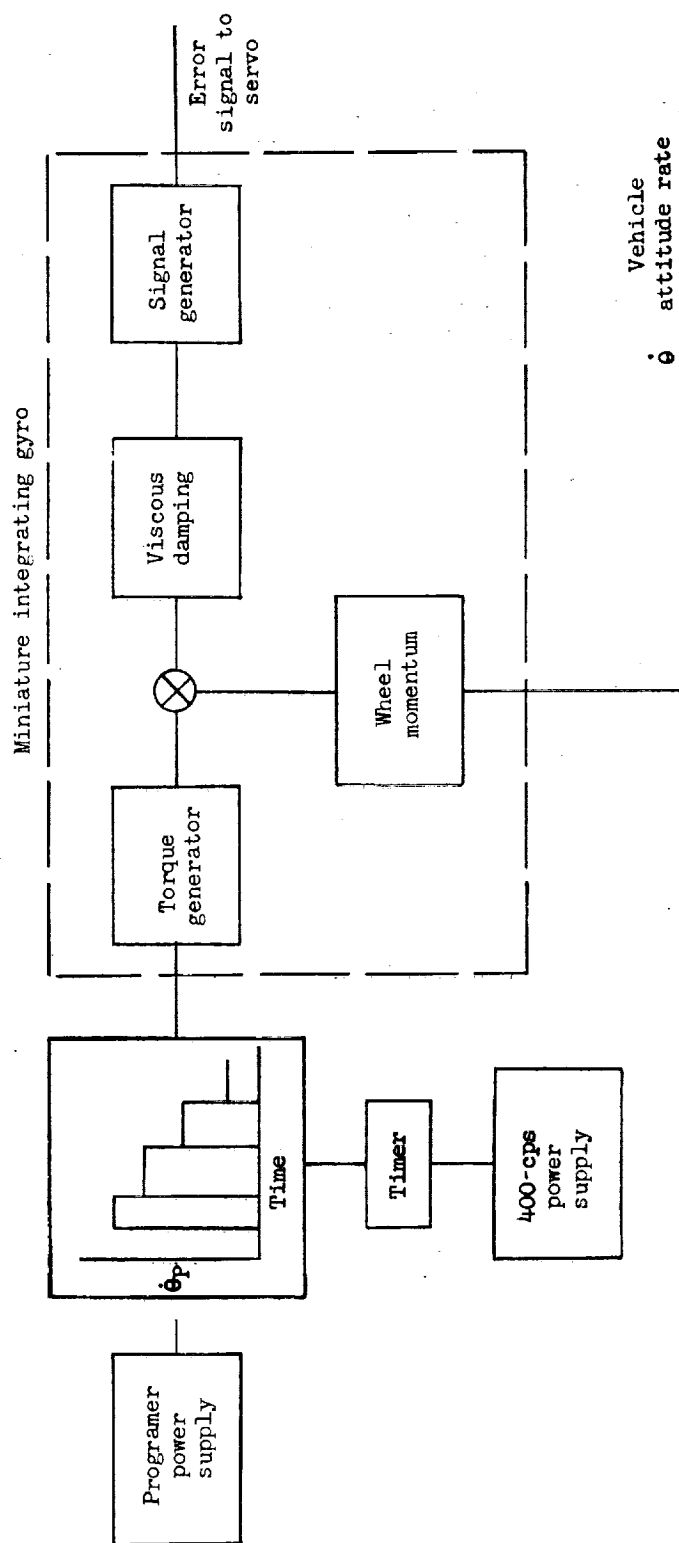
Figure 4.- Schematic diagram of miniature integrating gyro (MIG) and programer.

To preceding lockup and pitch step

Lockup monitor circuit

Programer power supply

Lockup

d-c power supply

Lockup

Pitch step
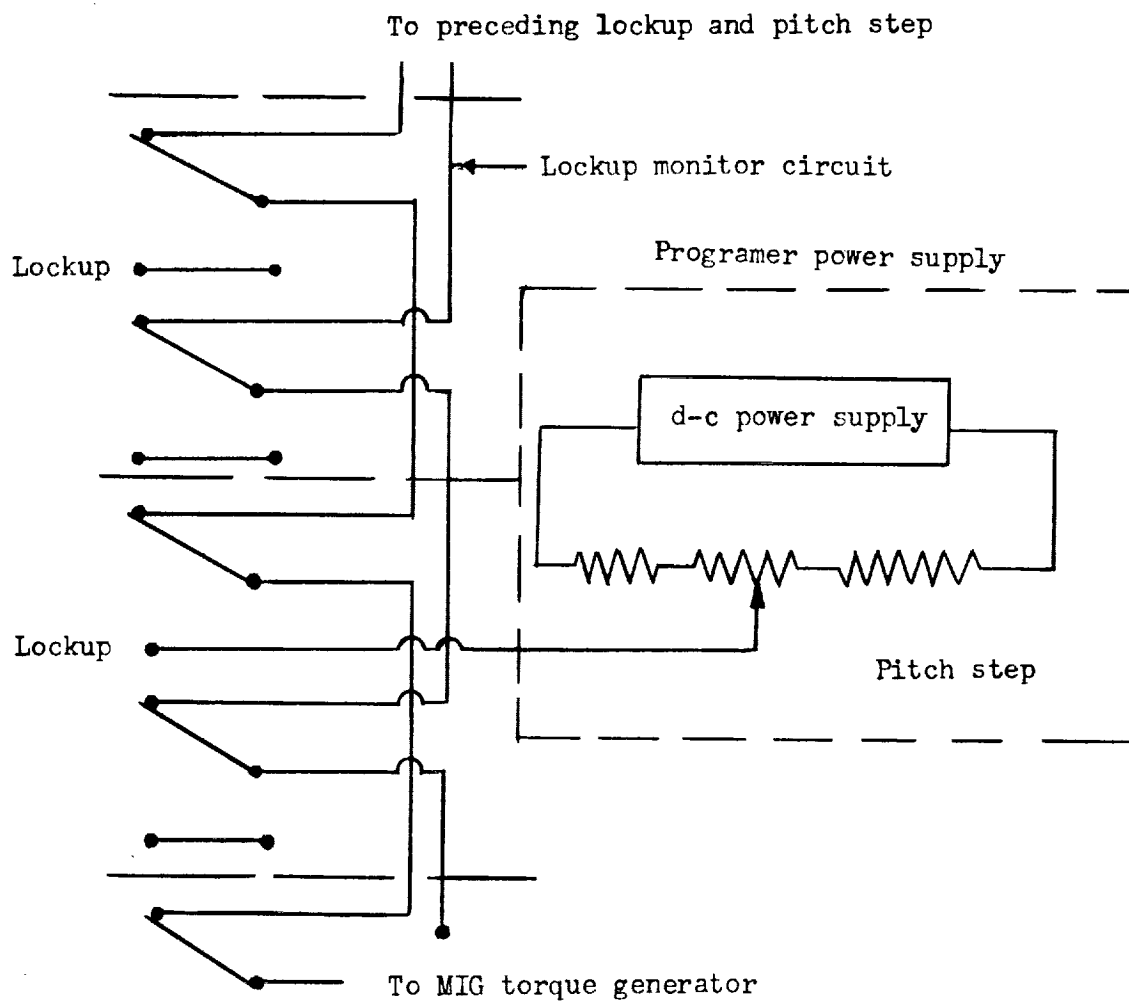
To MIG torque generator

Figure 5.- Typical timer and programer power circuit for introducing
step input to MIG torque generator.
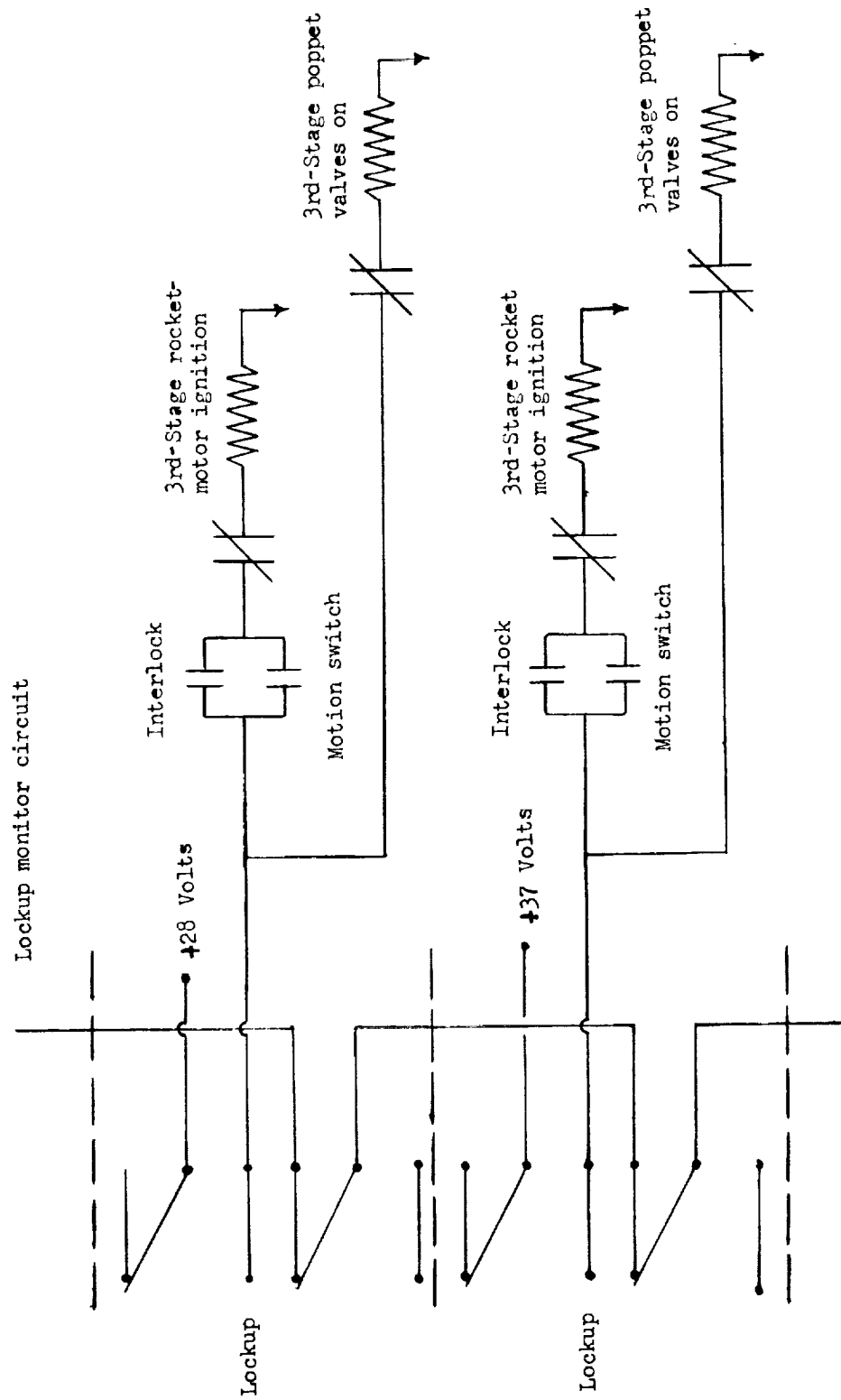
Figure 6.- Timer and associated circuitry for ignition of third-stage engine and application of voltage to third-stage hydrogen-peroxide jet valves.
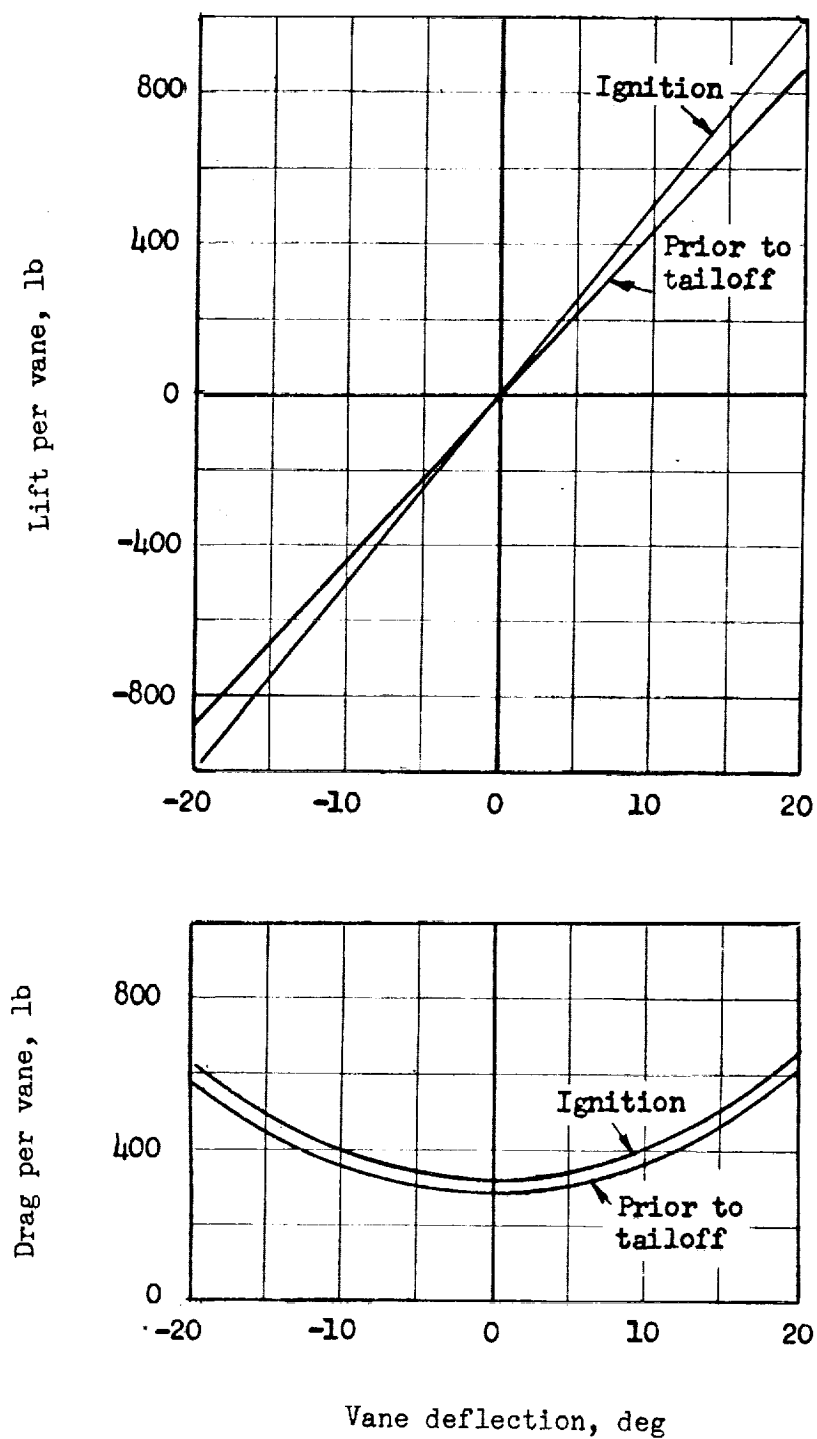
Figure 7.- Variations of jet-vane lift and drag forces with control
deflection. Data obtained during ground tests conducted by
Aerojet-General.

$$\epsilon_q = K_\theta \theta + K_{\dot{\theta}} \dot{\theta}$$
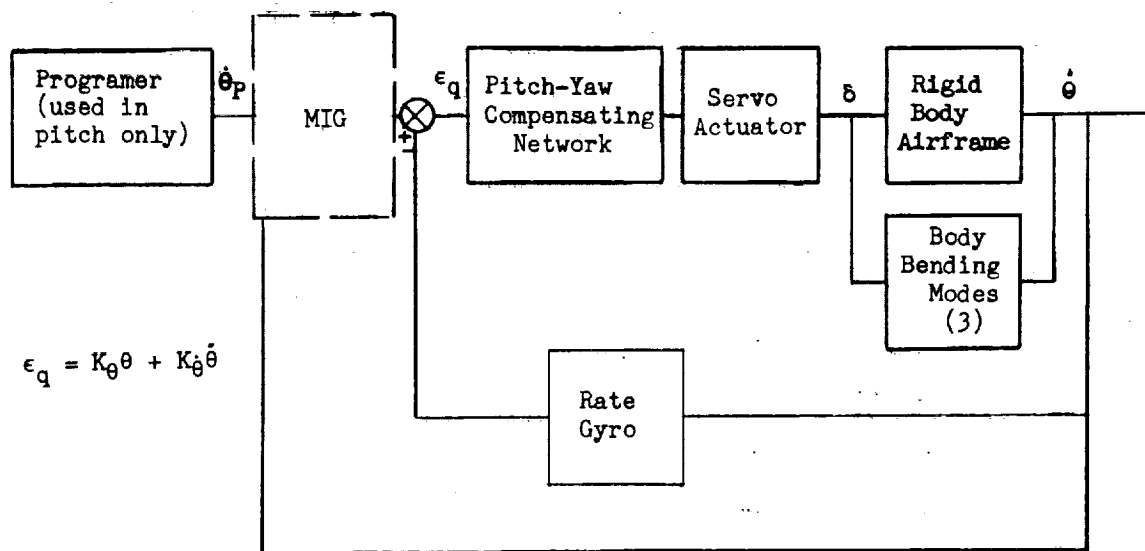
(a) First stage.
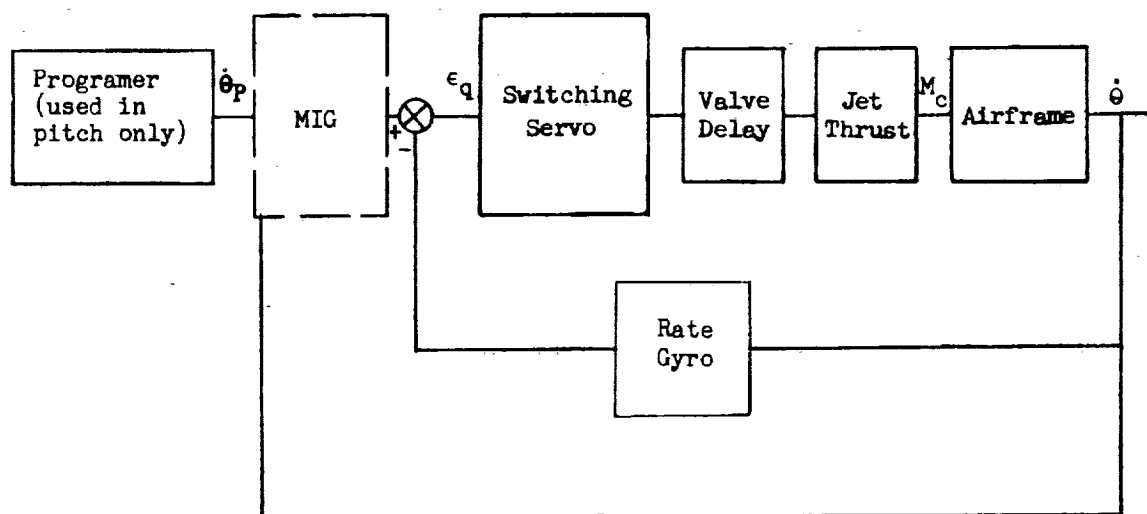
(b) Second and third stages.

Figure 8.- Block diagrams of guidance and control system.

Jet motor	Thrust level*, lb					
	Second stage		Third stage		
	High	Low	Burn	Coast
Pitch	600	475	44	2.2
Yaw	600	475	44	2.2(2)
Roll	24	20	2.2	2.2
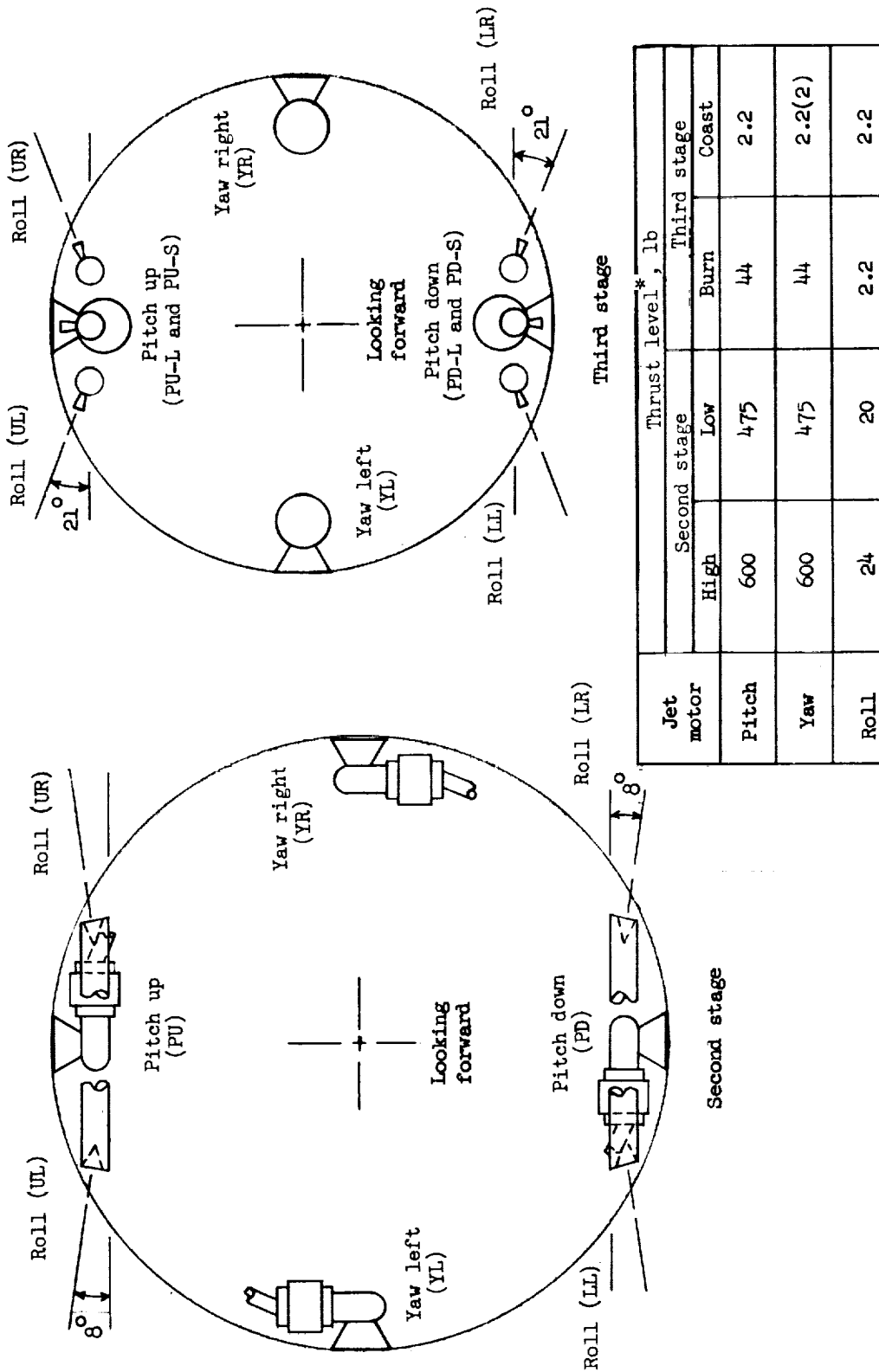
*Nominal values. (See fig. 44 for typical levels.)

Figure 9.- Arrangement and thrust levels of second- and third-stage hydrogen-peroxide jet motors.

L-1924
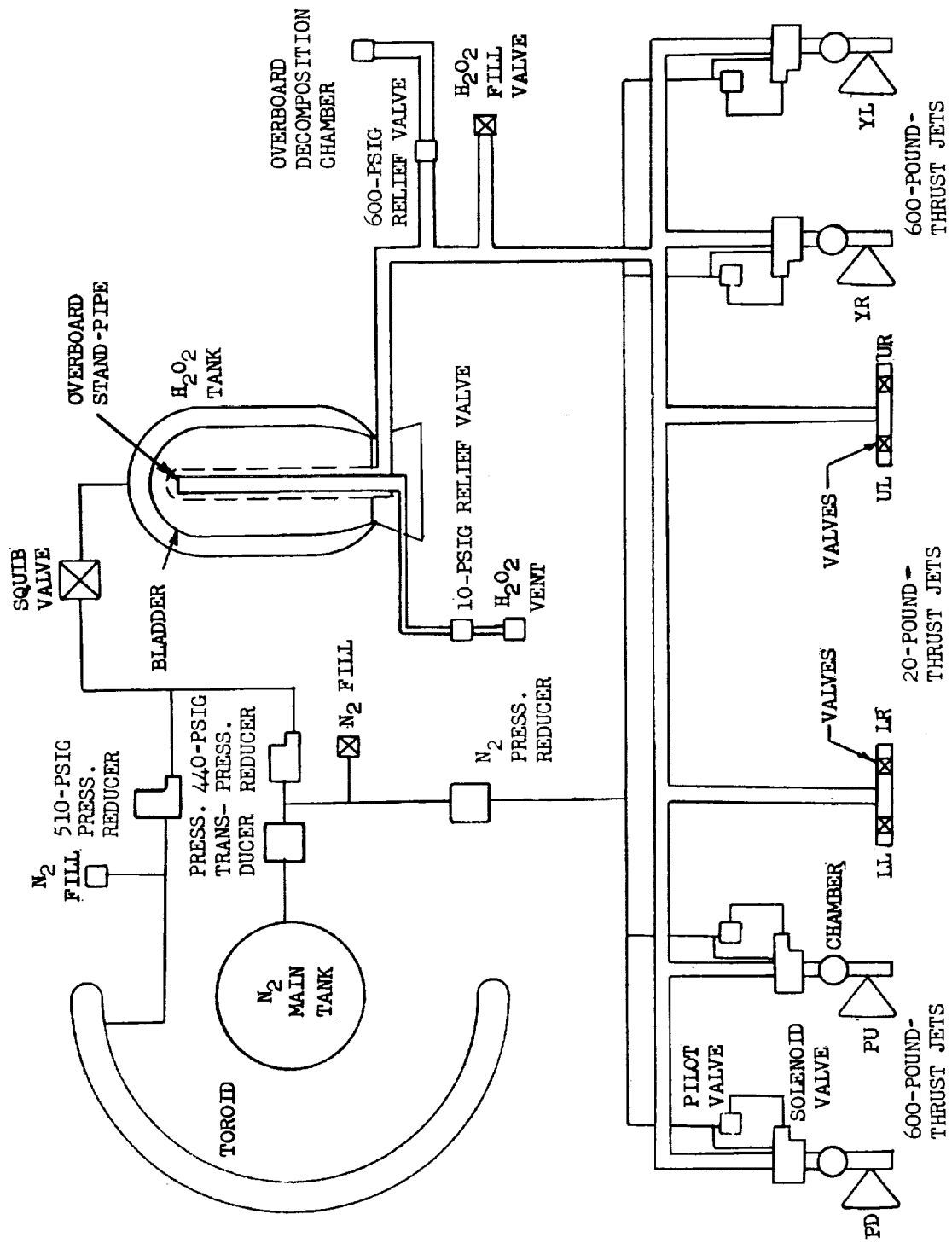
Figure 10.- Schematic diagram of second-stage hydrogen-peroxide jet motors and plumbing.

OVERBOARD
DECOMPOSITION
CHAMBER

H_2O_2
FILL
VALVE

PD-L

PU-L

44-POUND-
THRUST JETS

BLADDER

OVERBOARD
STAND-PIPE

10-PSIG
RELIEF VALVE

H_2O_2
VENT

PU-S   UR

UL

2.2-POUND-
THRUST JETS

SQUIB
VALVE

LR

PD-S

LL

TEMP.
TRANSDUCER

440-PSIG PRESS. REDUCER

CHECK VALVE

N_2 VENT

YR

44-POUND-
THRUST JETS

VALVE
CHAMBER

N_2
TANK

N_2
FILL

600-PSIG
RELIEF VALVE

YL

L-1924
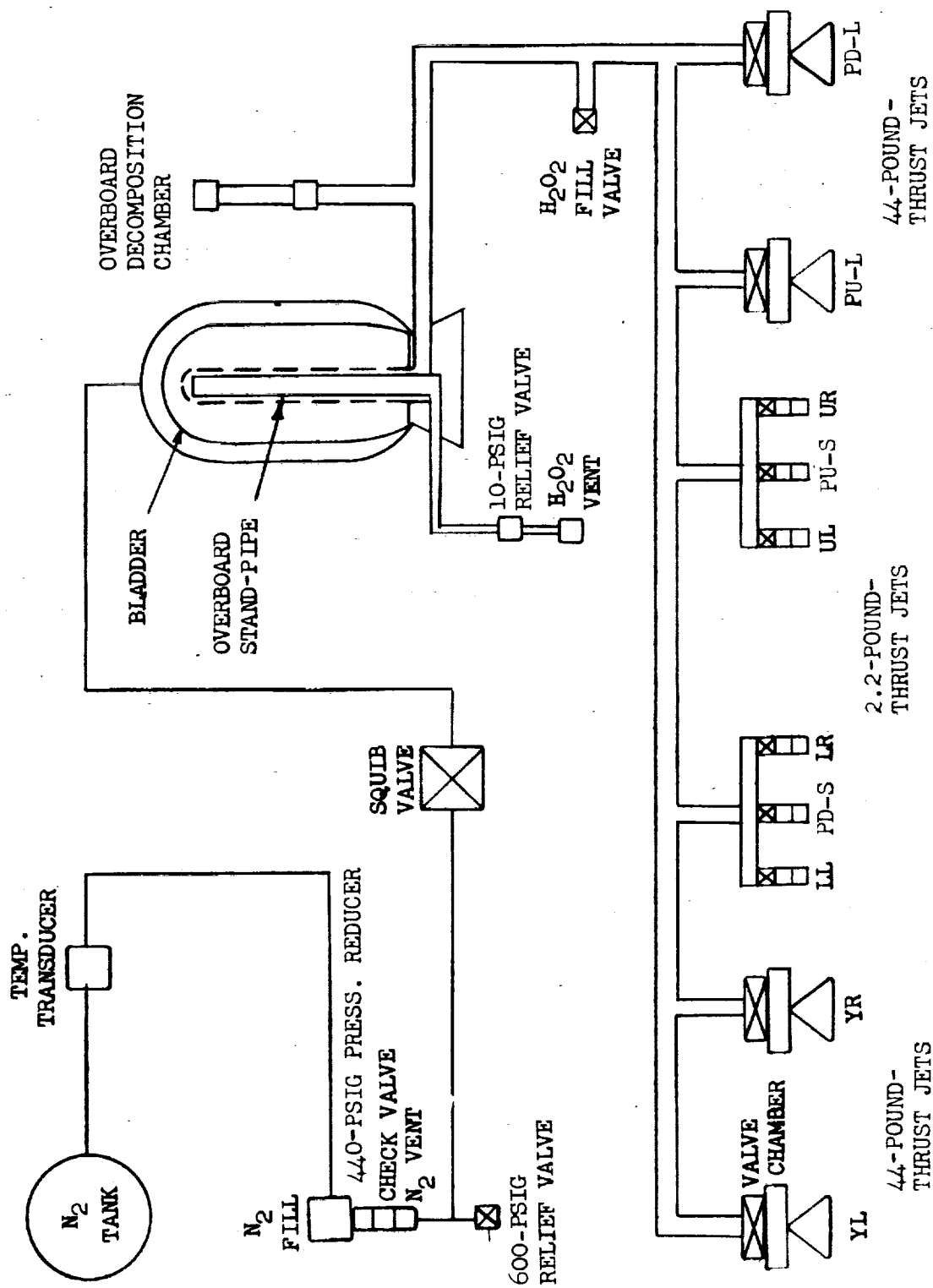
Figure 11.- Schematic diagram of third-stage hydrogen-peroxide jet motors and plumbing.

L-1924
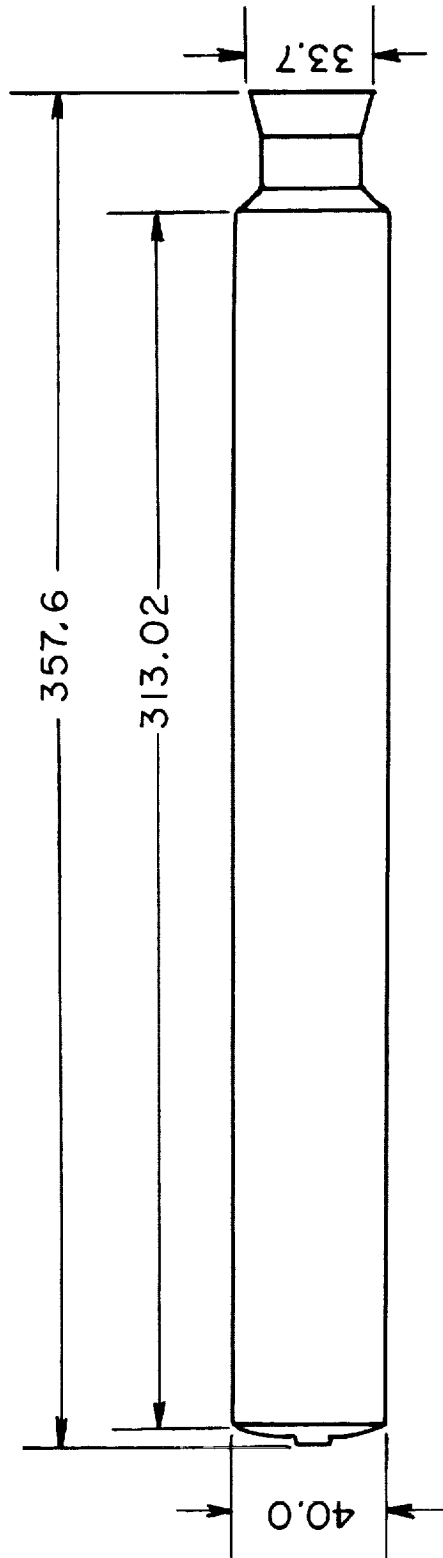
Figure 12.- External view of Algol rocket motor. All dimensions are in inches.

112
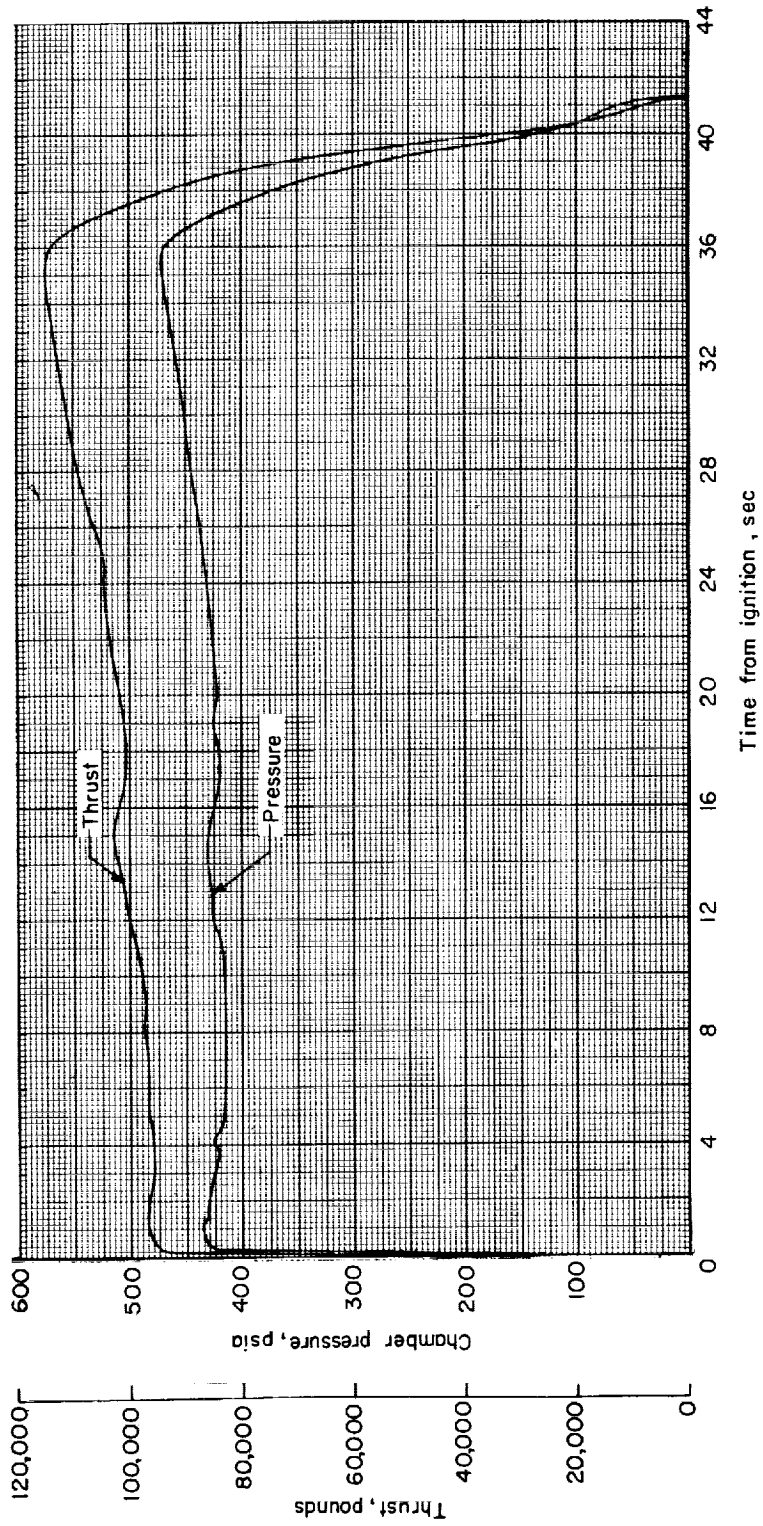
Figure 13.- Time histories of nominal chamber pressure and sea-level thrust of Algol motor.
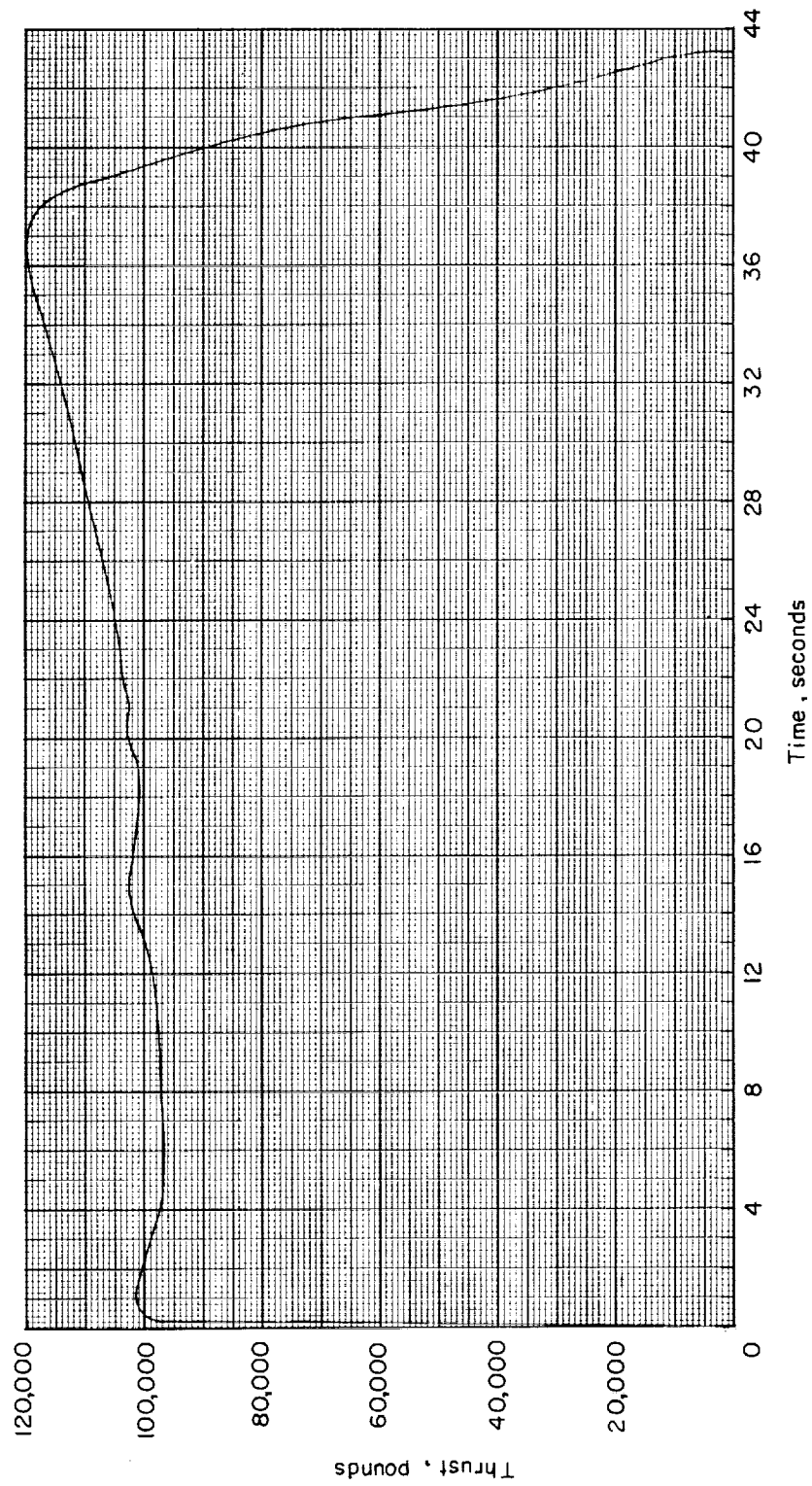
L-1924

Figure 14.- Time history of nominal thrust of Algol motor corrected for preflight trajectory.
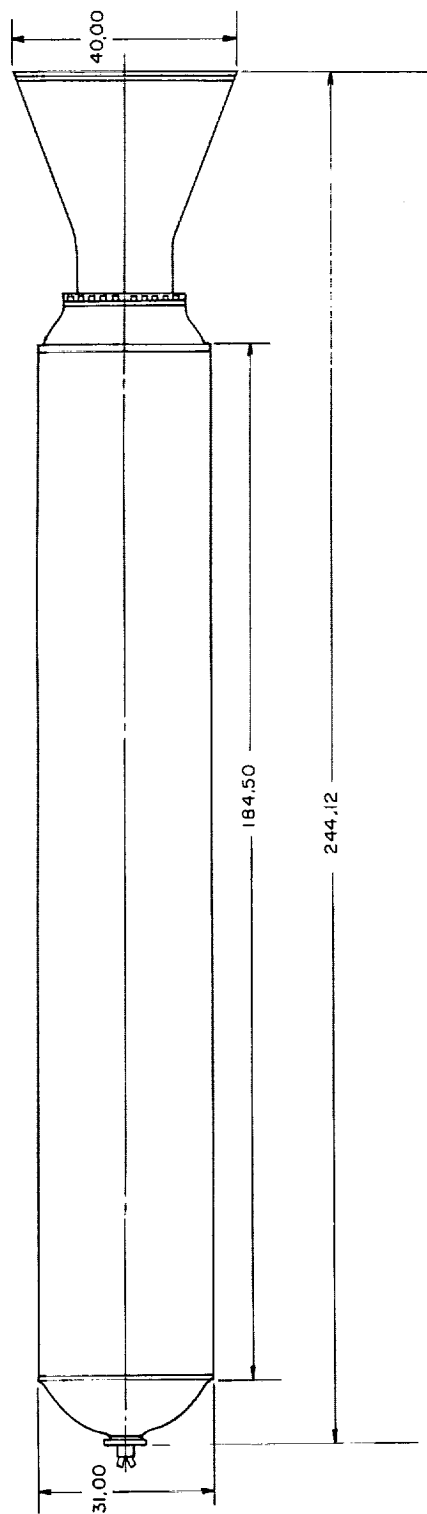
Figure 15.- External view of Castor rocket motor. All dimensions are in inches.

L-1924
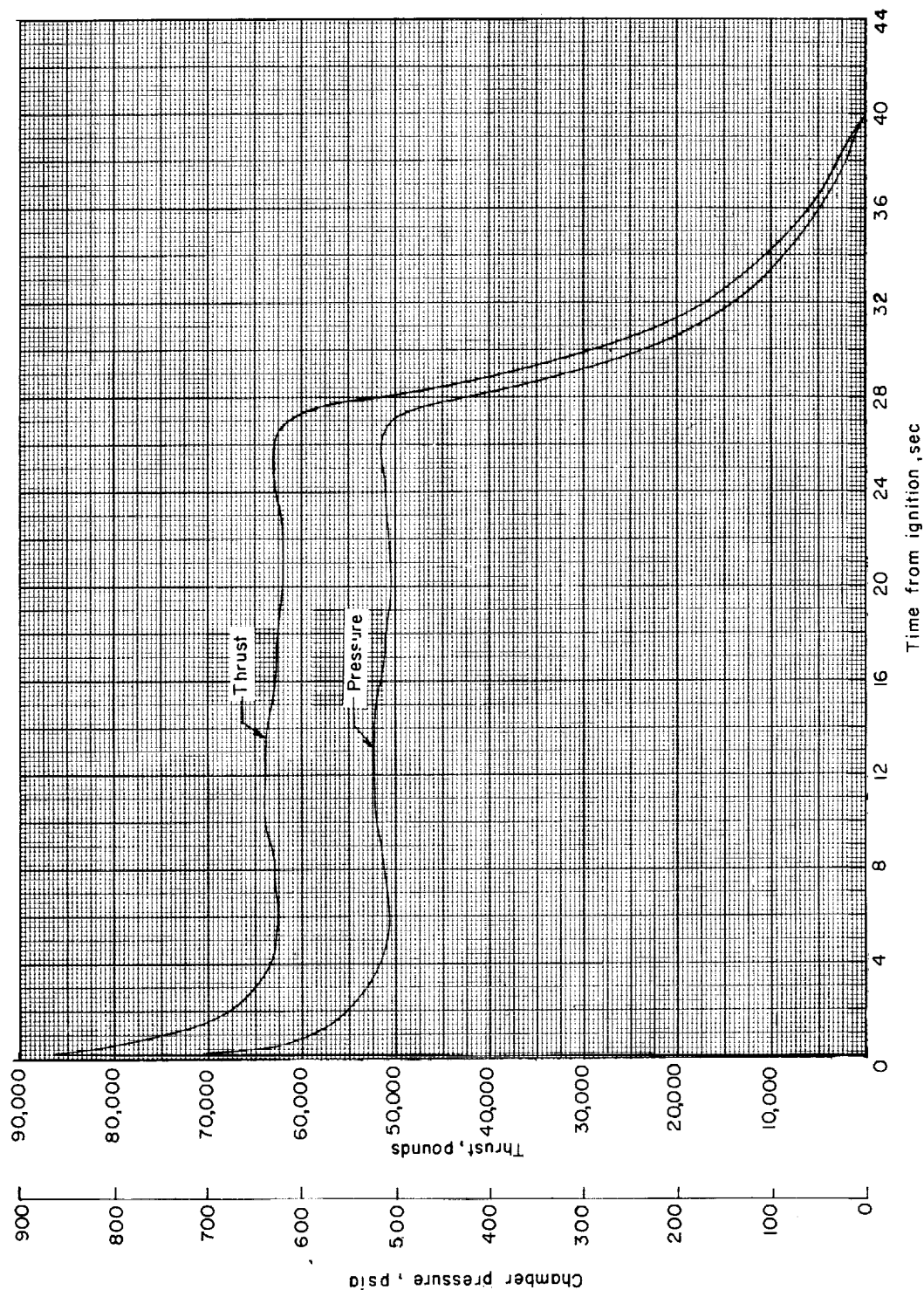
Figure 16.- Time histories of nominal chamber pressure and vacuum thrust of Castor motor.
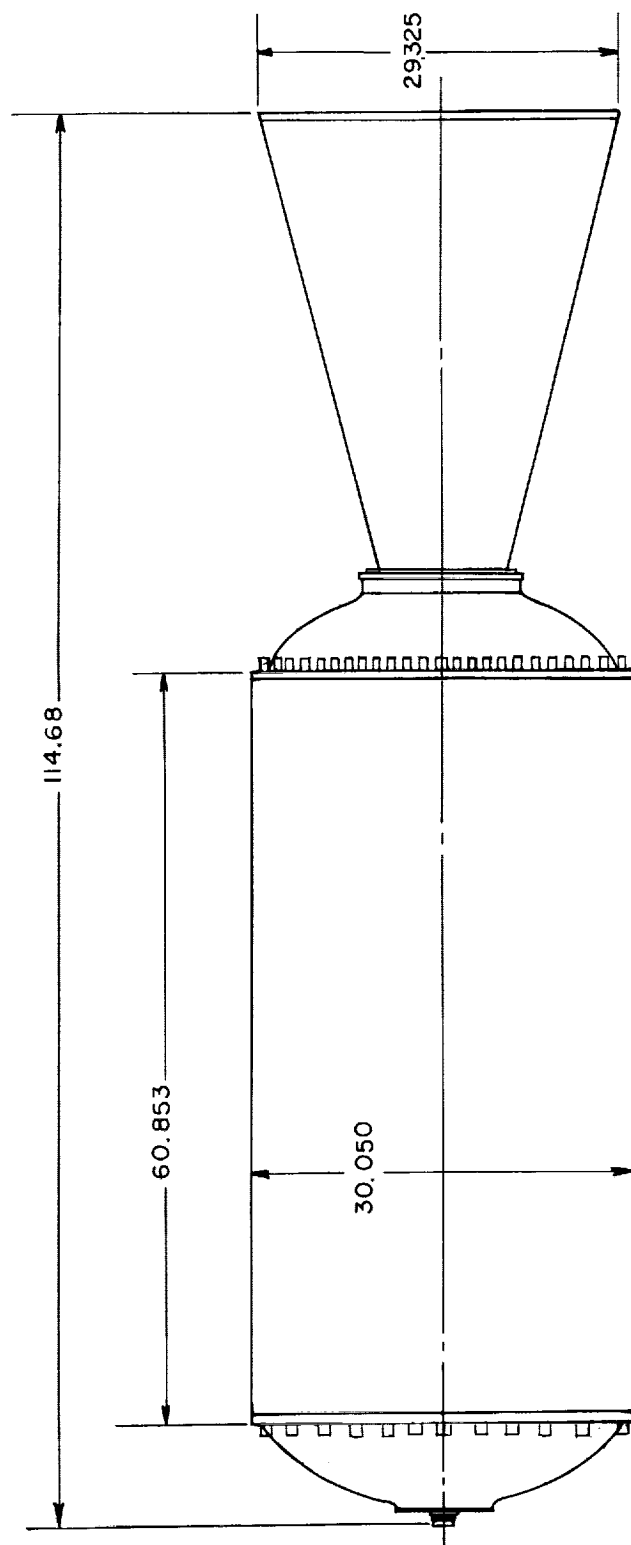
Figure 17.- External view of Antares rocket motor. All dimensions are in inches.
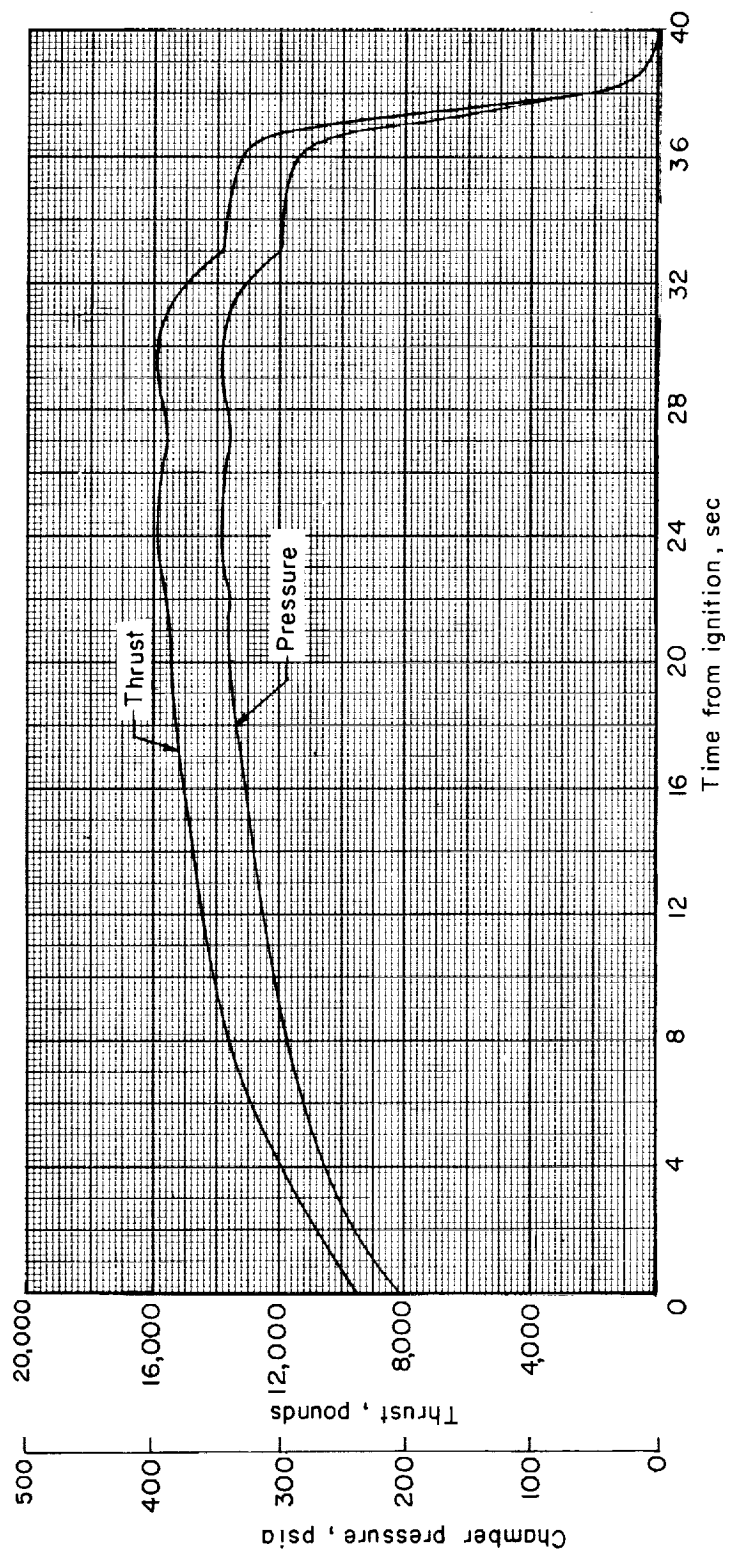
Figure 18.- Time histories of nominal chamber pressure and vacuum thrust of Antares motor.
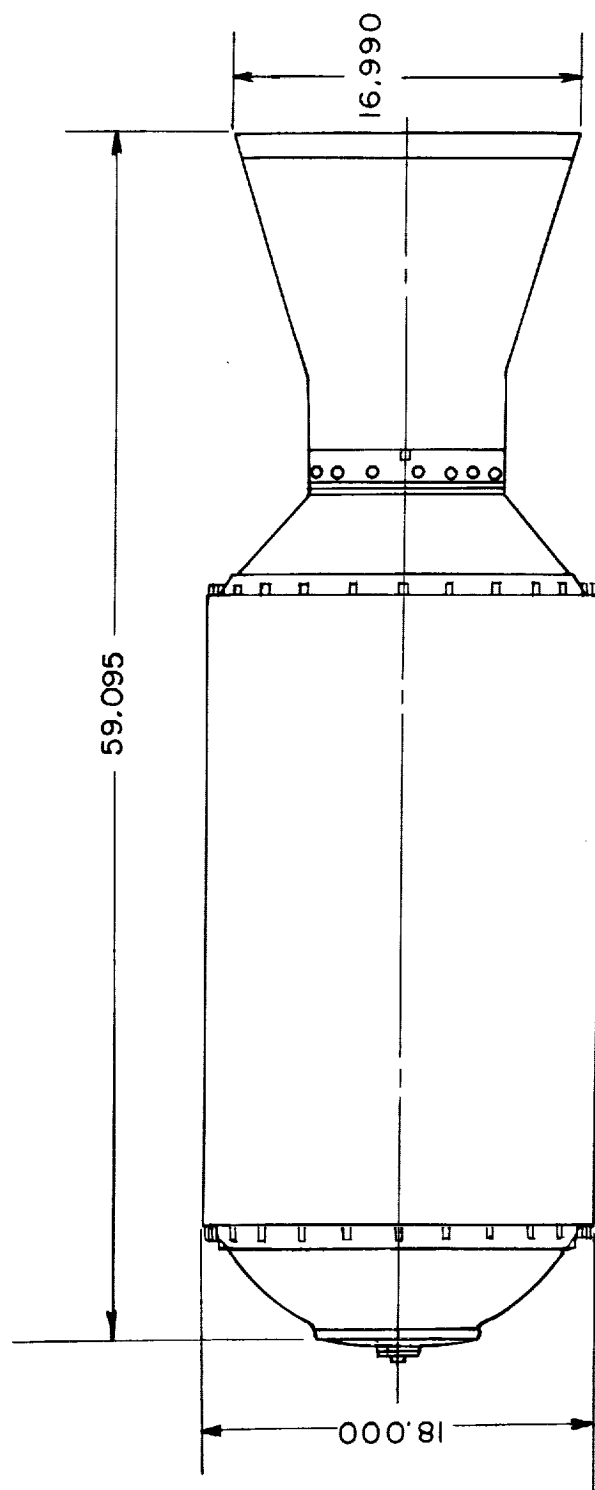
Figure 19.- External view of Altair rocket motor. All dimensions are in inches.

L-1924

L-1924
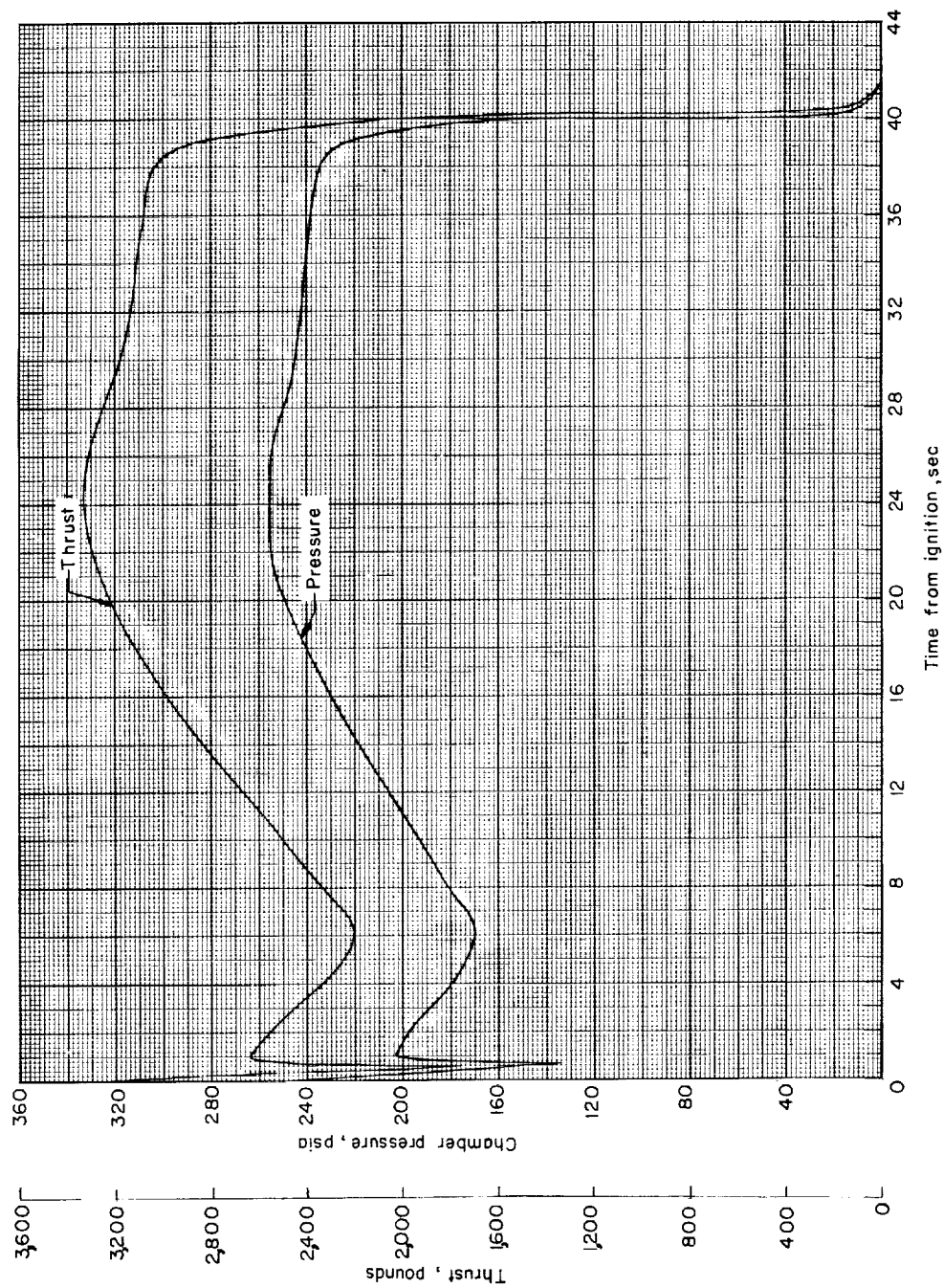
Figure 20.- Time histories of nominal chamber pressure and vacuum thrust of Altair motor.

To ground charging and discharging equipment

28 Volts

28 Volts

Shaped charge

Shaped charge

2nd Stage
ignition

3rd Stage
ignition

Ballistic
actuator igniter

Ballistic
actuator igniter

Nose heat-
shield jettison

No-fire relay contacts

No-fire relay contacts

4th Stage
ignition

Spin-motor
ignition

L-1924

Symbols

⊲▭▷	fuse	⊲▭▷	resistor (fixed)
o—|⊢o	normally open contact	±||⊦	battery
o—⊬o	normally closed contact	o	terminal or stud
(o o)	shorting bar	—ᐱᐯᐱ—	squib
→	plug	•—∅—o	pressure operated switch (normally open)

Figure 21.- Schematic diagram of onboard ignition system.

L-1924

To programer

Fire indicator

Fire indicator
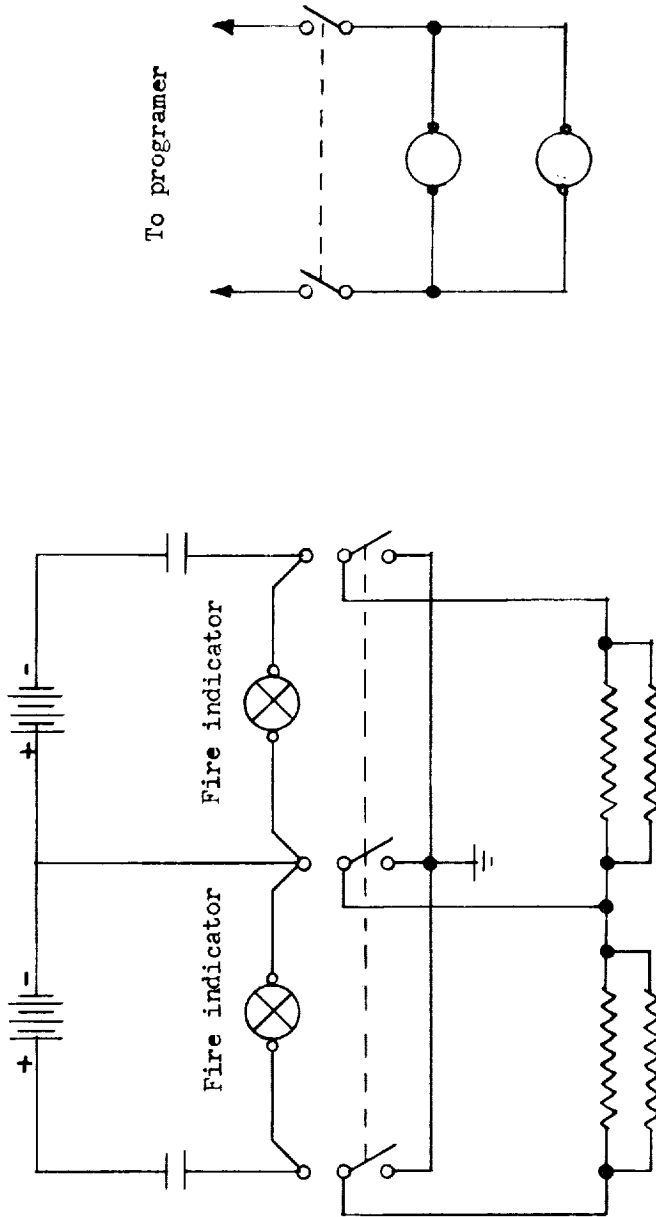
Symbols

battery	normally open contact
indicating light	switch
mechanical linkage	squib
terminal or stud	plug
ground	relay

Figure 22.- Schematic diagram of first-stage ignition system.
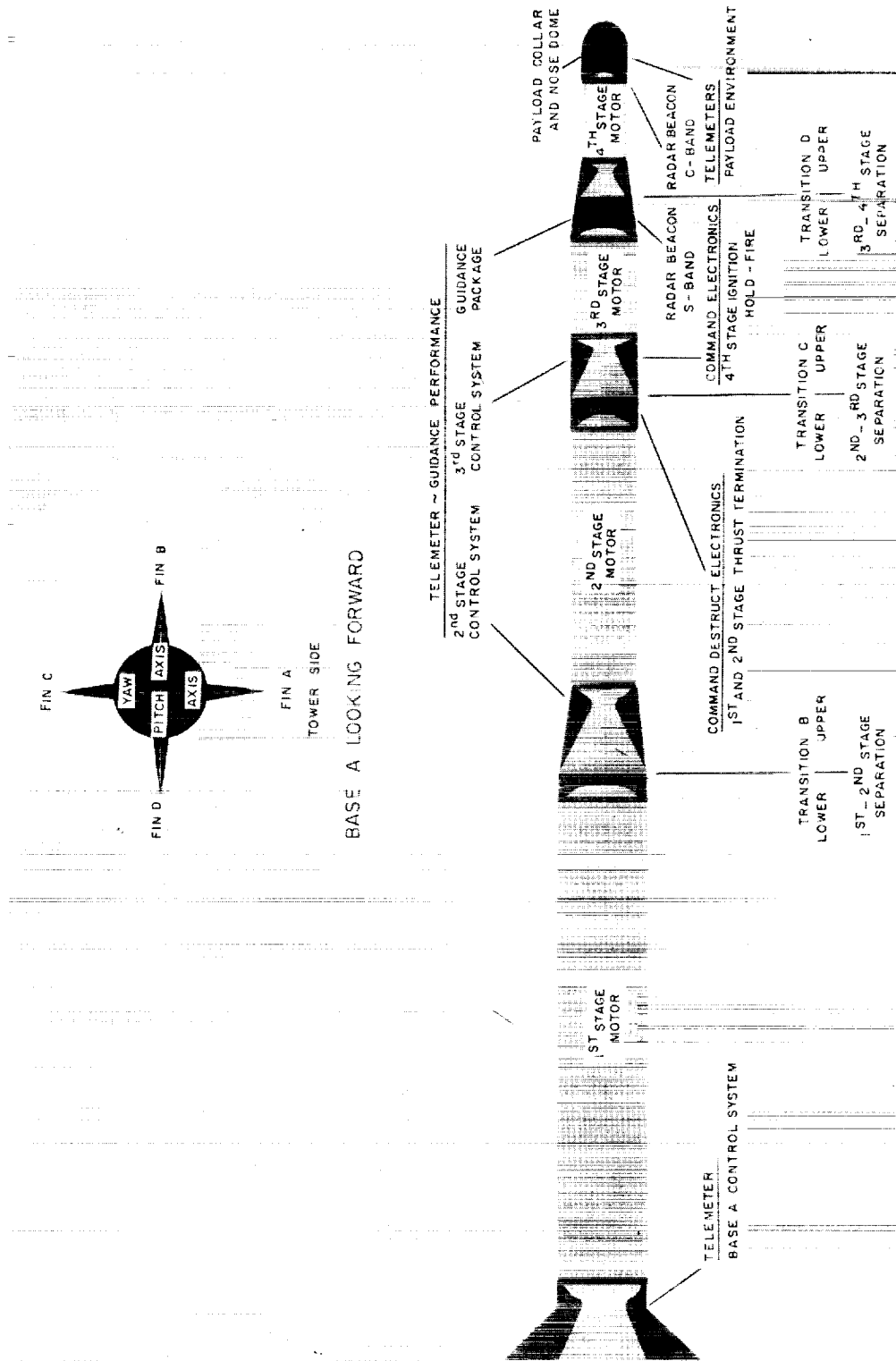
Figure 23.- Summary of instrument systems in Scout ST-1 vehicle.
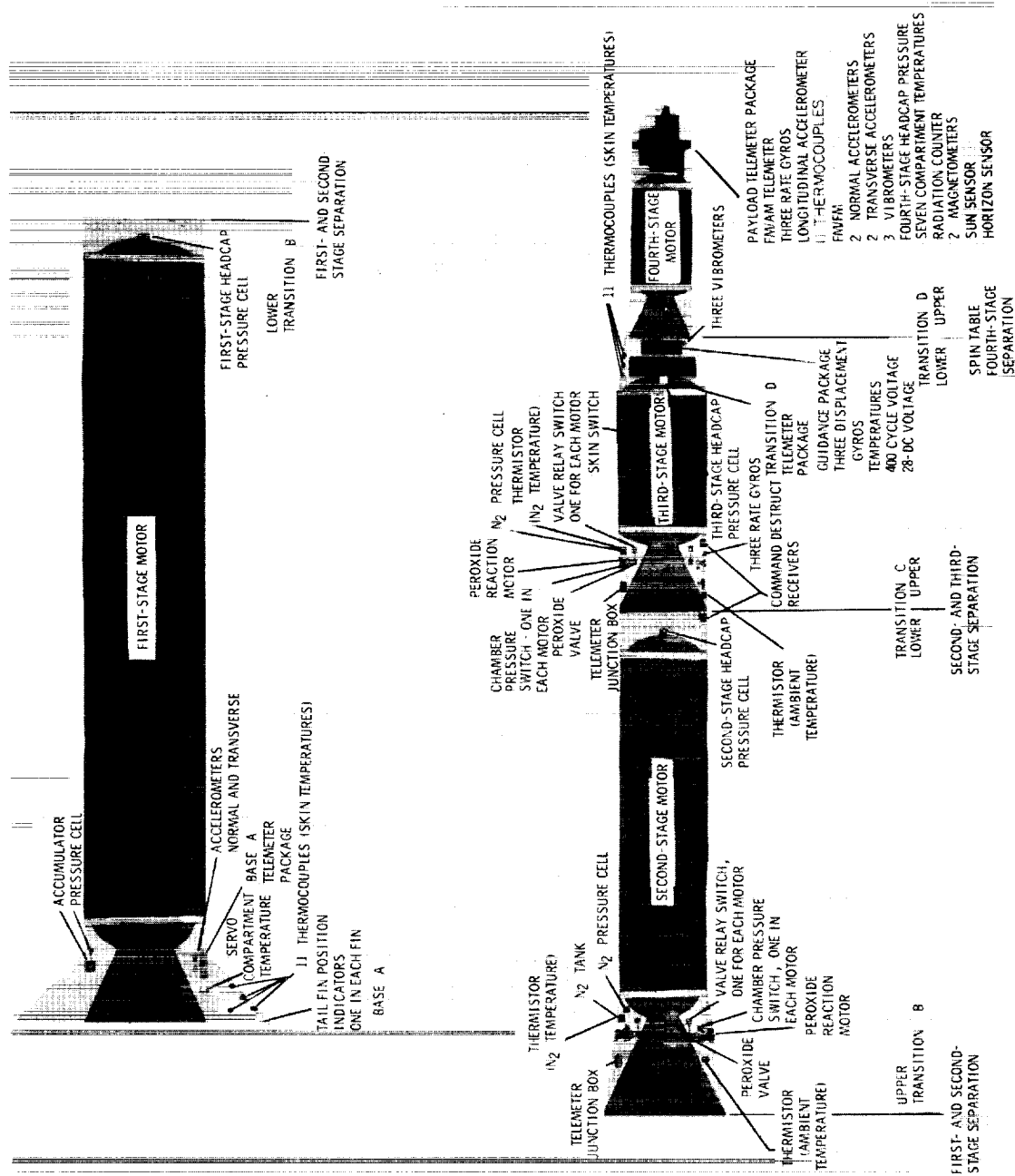
Figure 24.- Location of telemeter components.
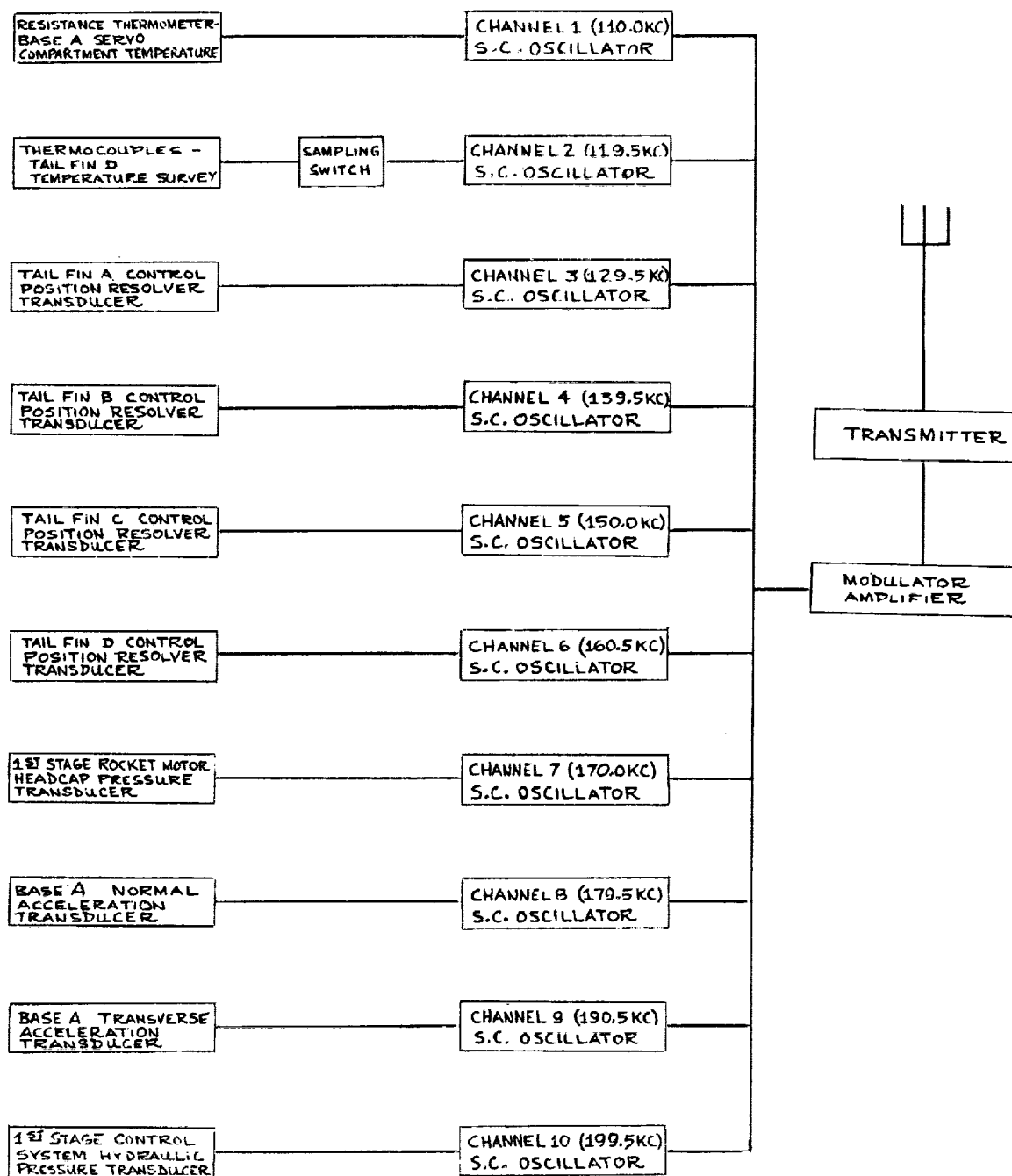
124

Figure 25.- Block diagram of first-stage telemeter.
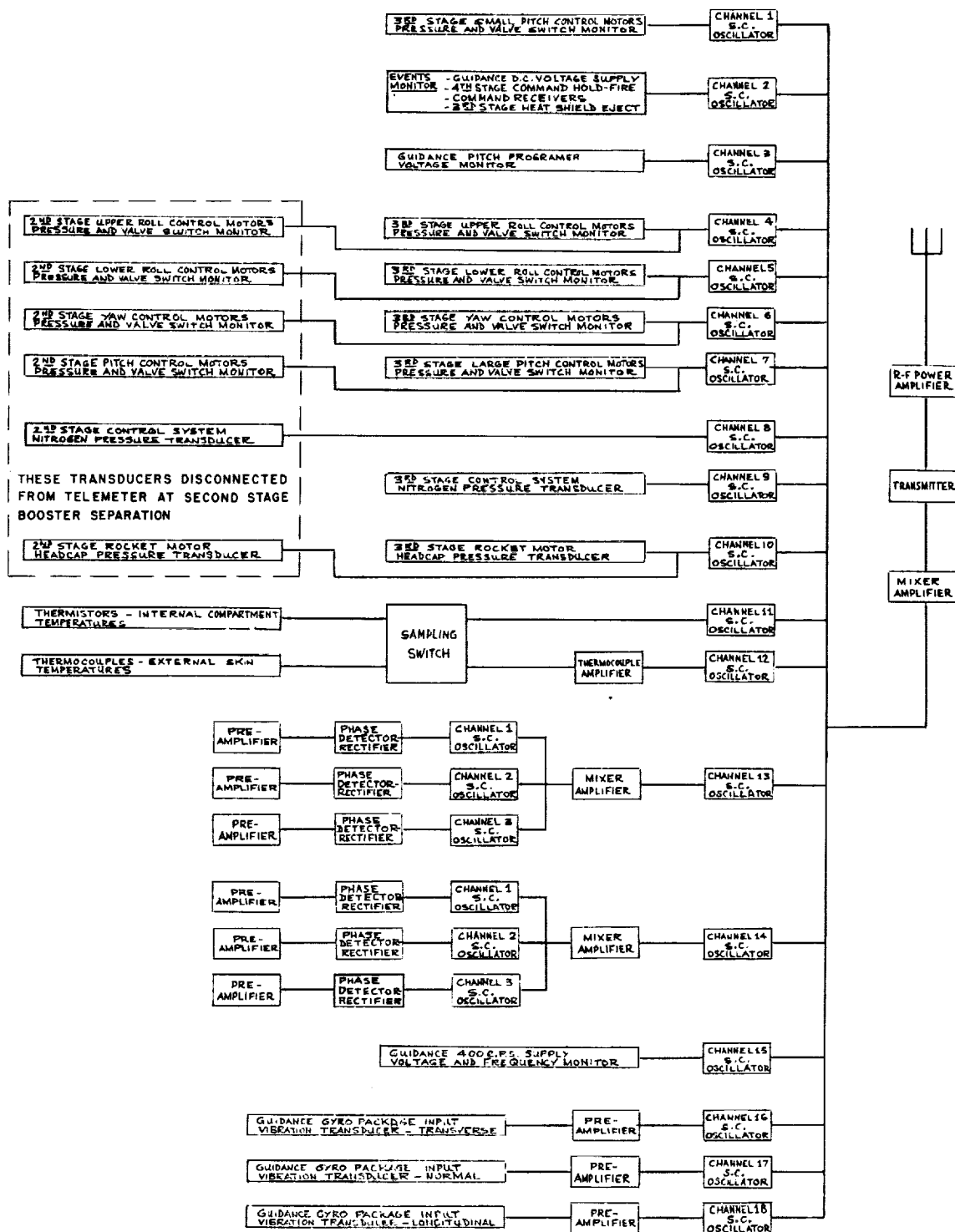
Figure 26.- Block diagram of second- and third-stage telemeters.
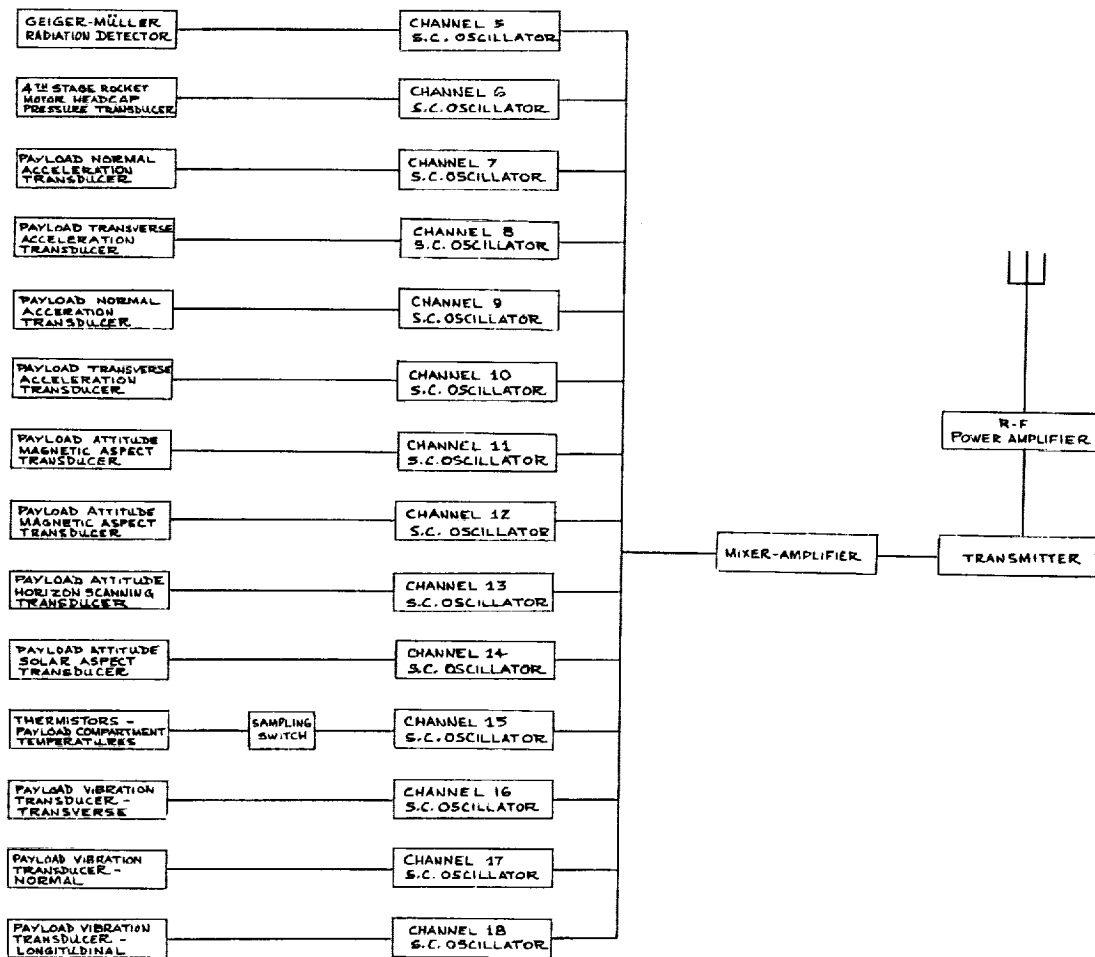
(a) FM-FM telemeter.
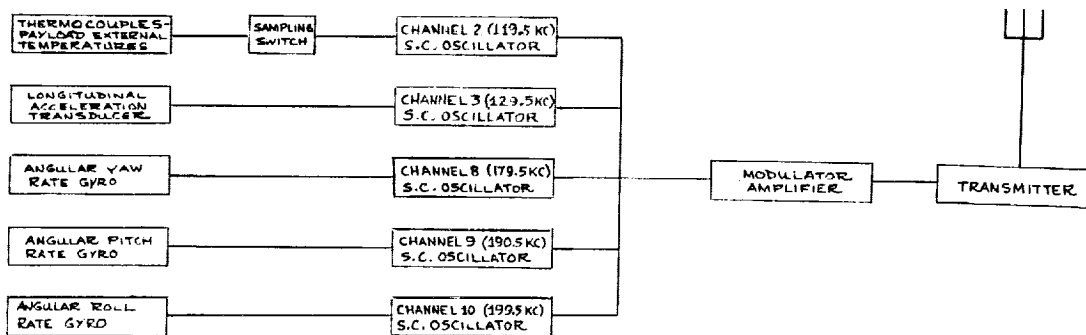
(b) FM-AM telemeter.

Figure 27.- Block diagrams of payload telemeters.

L-1924

EACH PATTERN DRAWN TO SAME
SCALE AND MEASURED AT
225.7 MEGACYCLES
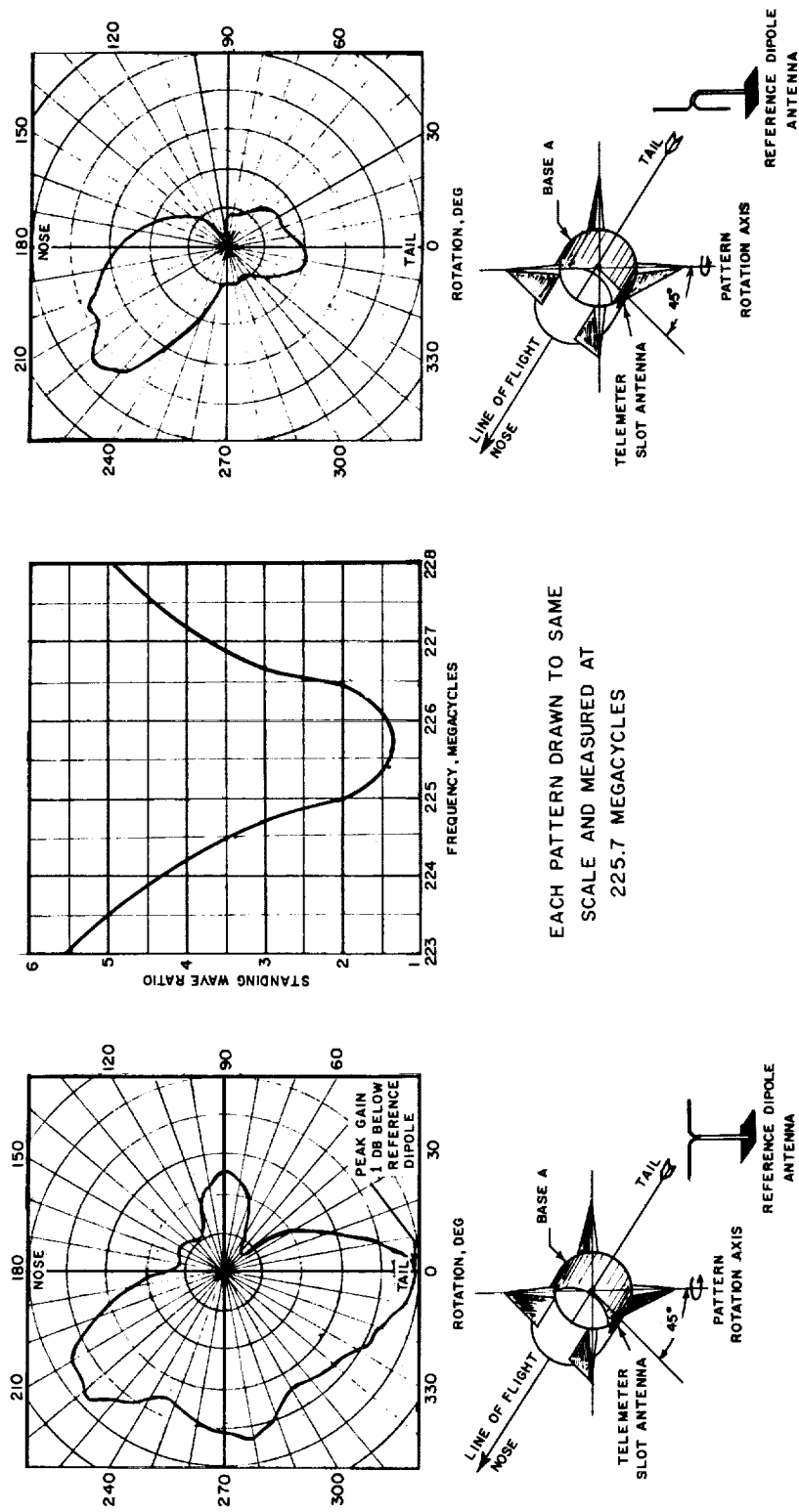
Figure 28.- Performance data for first-stage telemeter antennas.
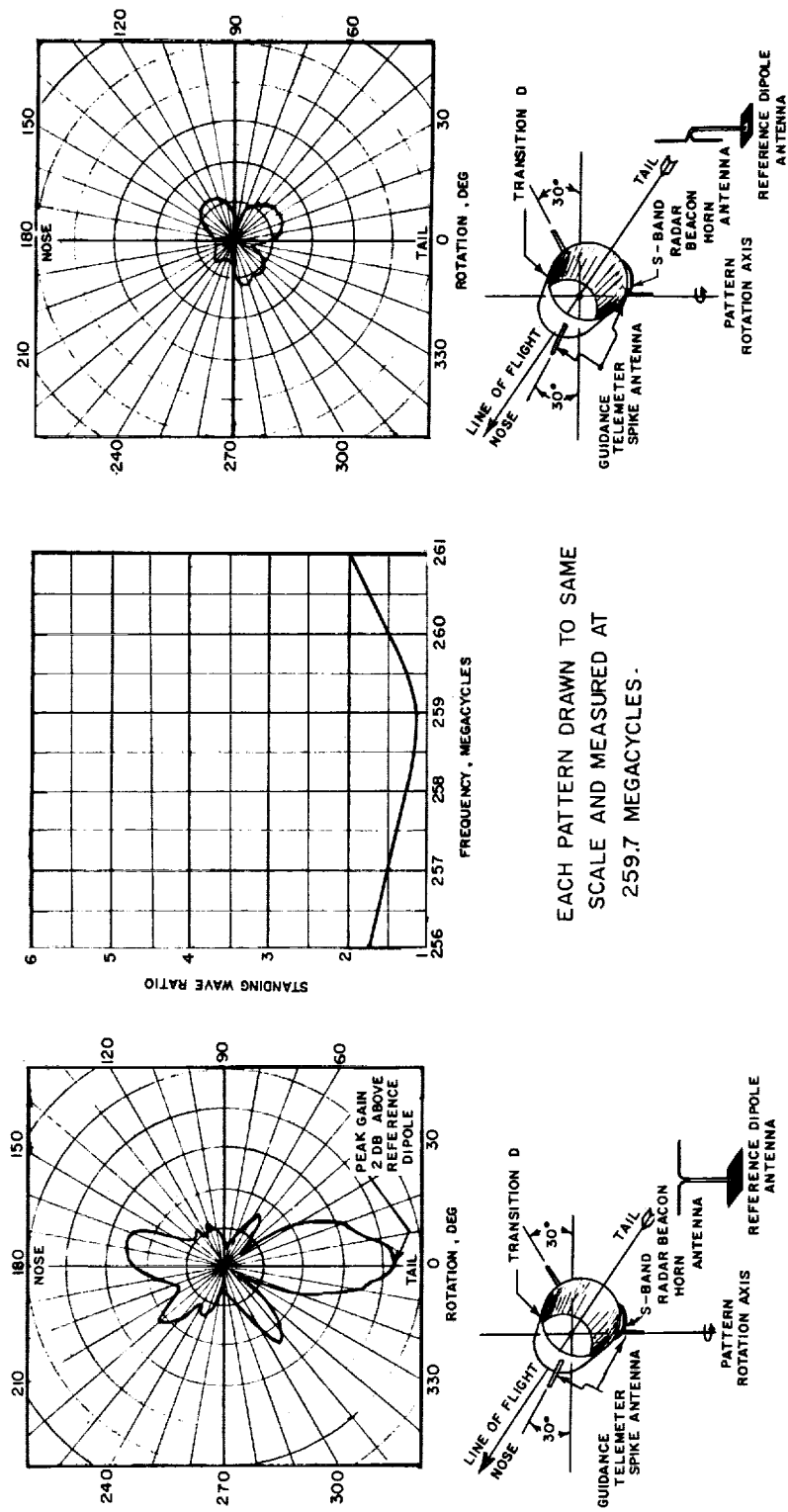
EACH PATTERN DRAWN TO SAME
SCALE AND MEASURED AT
259.7 MEGACYCLES.

Figure 29.- Performance data for third-stage telemeter antennas.

L-1924

L-1924

EACH PATTERN DRAWN TO SAME
SCALE AND MEASURED AT
242.0 MEGACYLES.
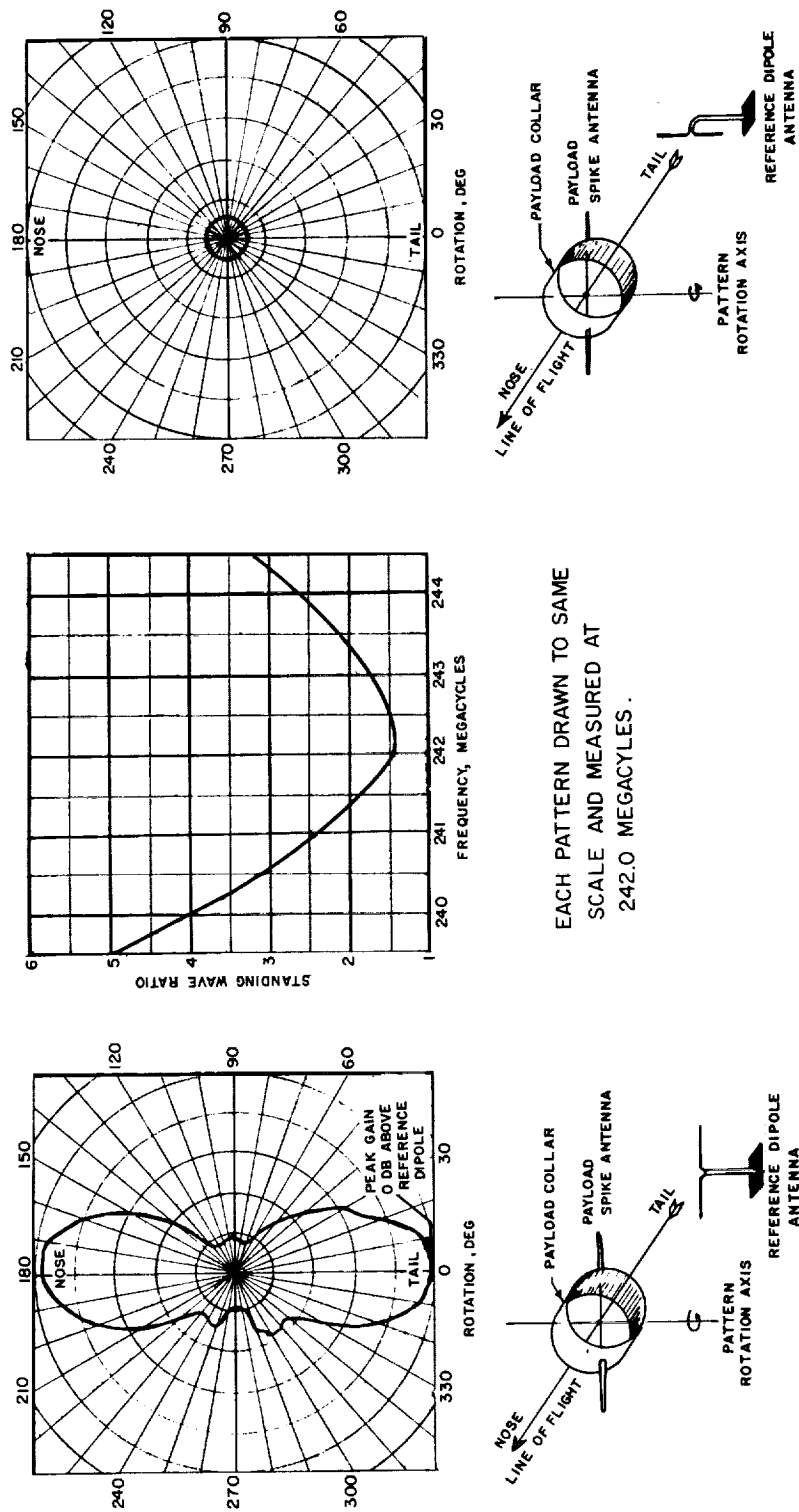
Figure 30.- Performance data for payload telemeter antennas.

130

L-1924

GAIN
6 DB ABOVE
REFERENCE
DIPOLE

PEAK GAIN
11.5 DB ABOVE
REFERENCE
DIPOLE

NOSE

TAIL

ROTATION, DEG

TELEMETER SPIKE ANTENNA

TRANSITION D

TAIL

REFERENCE
HORN
ANTENNA

30°

30°

LINE OF FLIGHT

NOSE

RADAR BEACON
HORN ANTENNA

PATTERN
ROTATION AXIS

FREQUENCY, MEGACYCLES

STANDING WAVE RATIO

EACH PATTERN DRAWN TO SAME
SCALE AND MEASURED AT
2870 MEGACYCLES.
RADAR BEACON RECEIVER
FREQUENCY 2859 MEGACYCLES.
RADAR BEACON TRANSMITTER
FREQUENCY 2880 MEGACYCLES.

NOSE

TAIL

0° ELEVATION

5° ELEVATION

15° ELEVATION

ROTATION, DEG

TRANSITION D

TELEMETER SPIKE ANTENNA

30°

ELEVATION
AXIS

TAIL

REFERENCE
HORN
ANTENNA

LINE OF FLIGHT

NOSE

30°

RADAR BEACON
HORN ANTENNA

PATTERN
ROTATION AXIS

Figure 31.- Performance data for S-band radar beacon antenna.

LI-1964

NOSE

GAIN
9 DB ABOVE
REFERENCE
DIPOLE

PEAK GAIN
17 DB ABOVE
REFERENCE
DIPOLE

TAIL

90

60

120

180

240

270

300

330

30

ROTATION, DEG

TELEMETER SPIKE ANTENNA

PAYLOAD COLLAR

TAIL

45°

NOSE

45°

LINE OF FLIGHT

RADAR BEACON
HORN ANTENNA

PATTERN
ROTATION AXIS

REFERENCE
HORN
ANTENNA

STANDING WAVE RATIO

3.5

3

2.5

2

1.5

5400   5500   5600   5700   5800   5900

FREQUENCY MEGACYCLES

EACH PATTERN DRAWN TO SAME
SCALE AND MEASURED AT
5500 MEGACYCLES.
RADAR BEACON RECEIVER
FREQUENCY 5485 MEGACYCLES.
RADAR BEACON TRANSMITTER
FREQUENCY 5560 MEGACYCLES.

NOSE

0° ELEVATION

5° ELEVATION

15° ELEVATION

TAIL

90

60

120

180

240

270

300

330

30

ROTATION, DEG

TELEMETER SPIKE ANTENNA

PAYLOAD COLLAR

ELEVATION AXIS

TAIL

45°

LINE OF FLIGHT

NOSE

45°

RADAR BEACON
HORN ANTENNA

PATTERN
ROTATION AXIS

REFERENCE
HORN
ANTENNA

Figure 32.- Performance data for C-band radar beacon horn antenna.
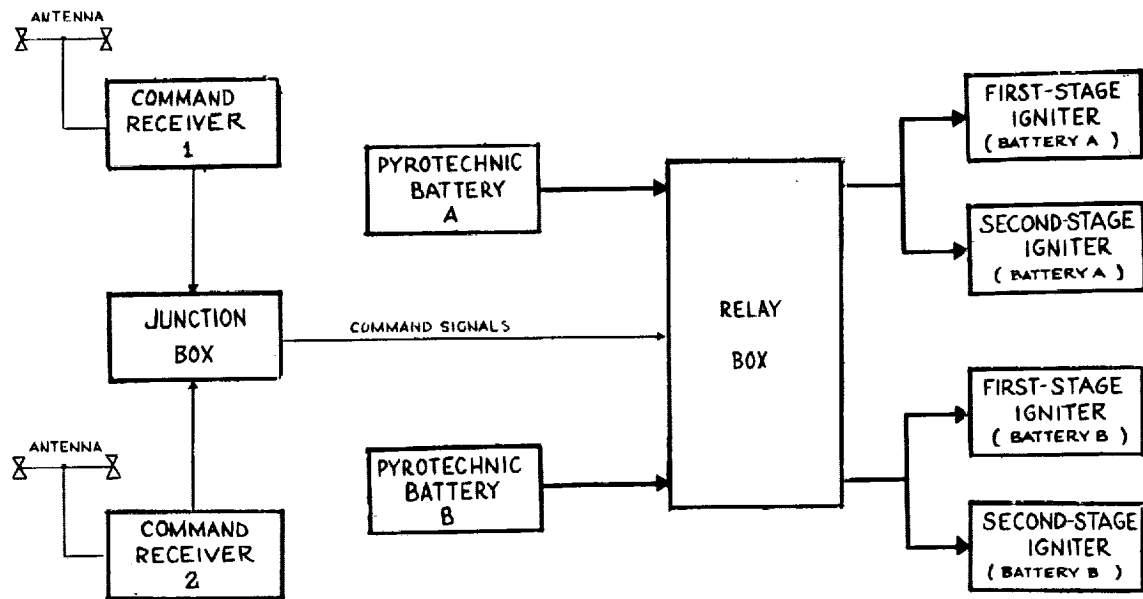
(a) Thrust-termination command system.
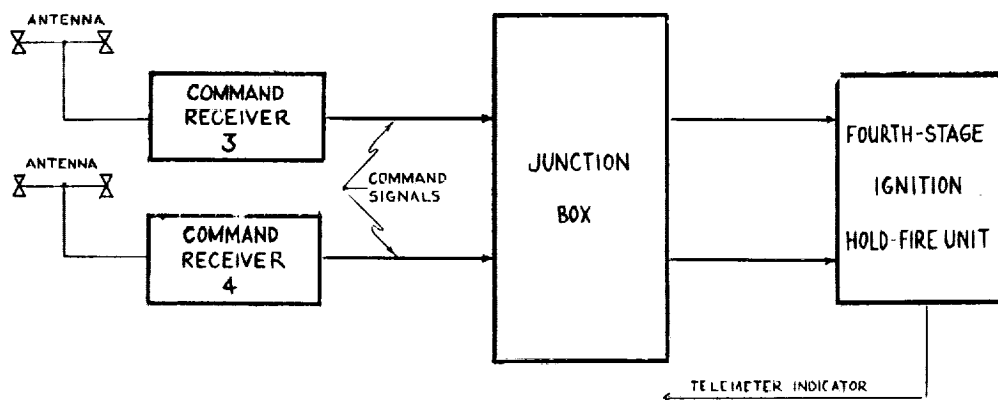
(b) Fourth-stage hold-fire command system.

Figure 33.- Block diagram of command systems.
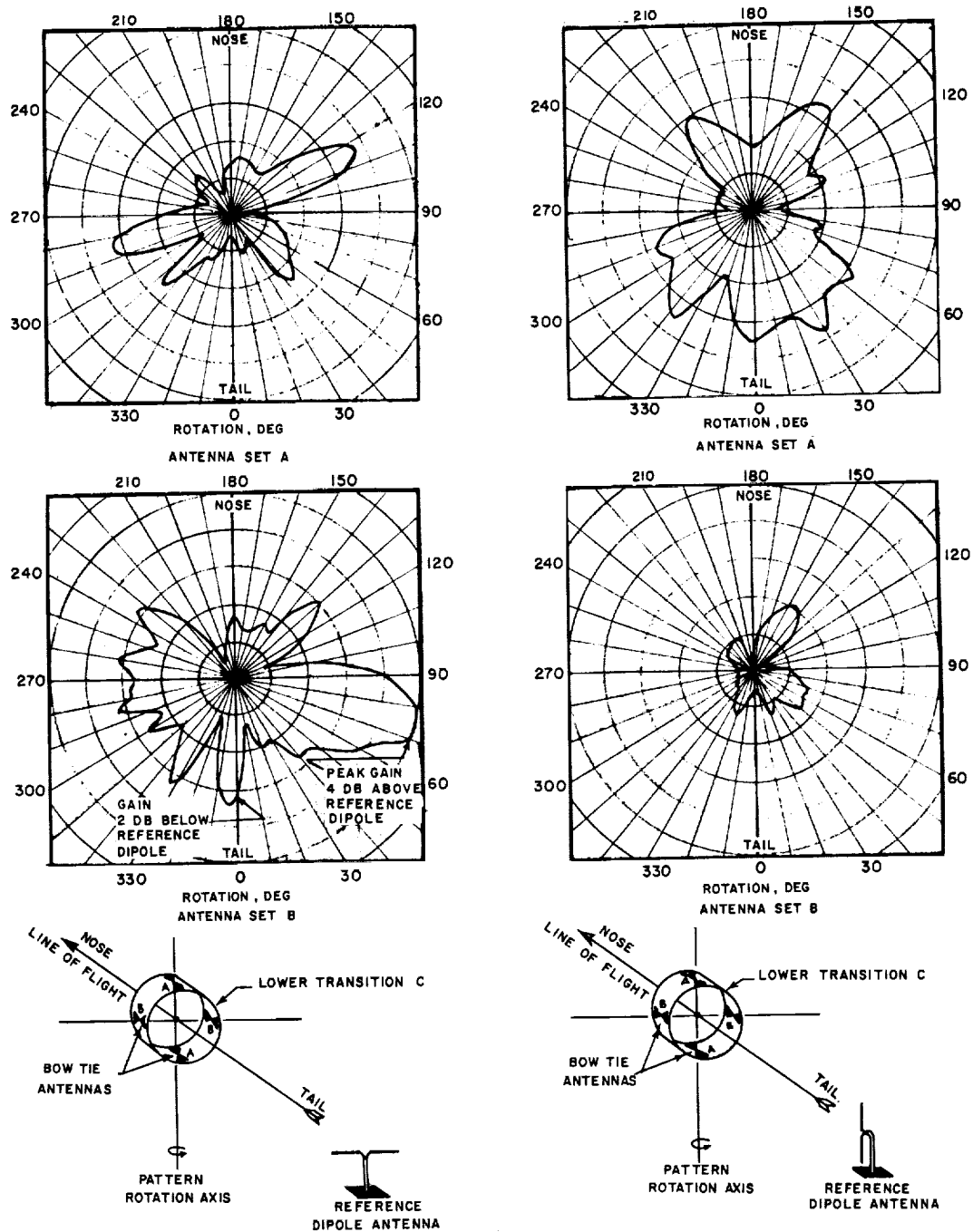
L-1924

EACH PATTERN DRAWN TO SAME SCALE AND MEASURED AT
APPROXIMATELY 400 MEGACYCLES.

Figure 34.- Performance data for command-receiver antennas.
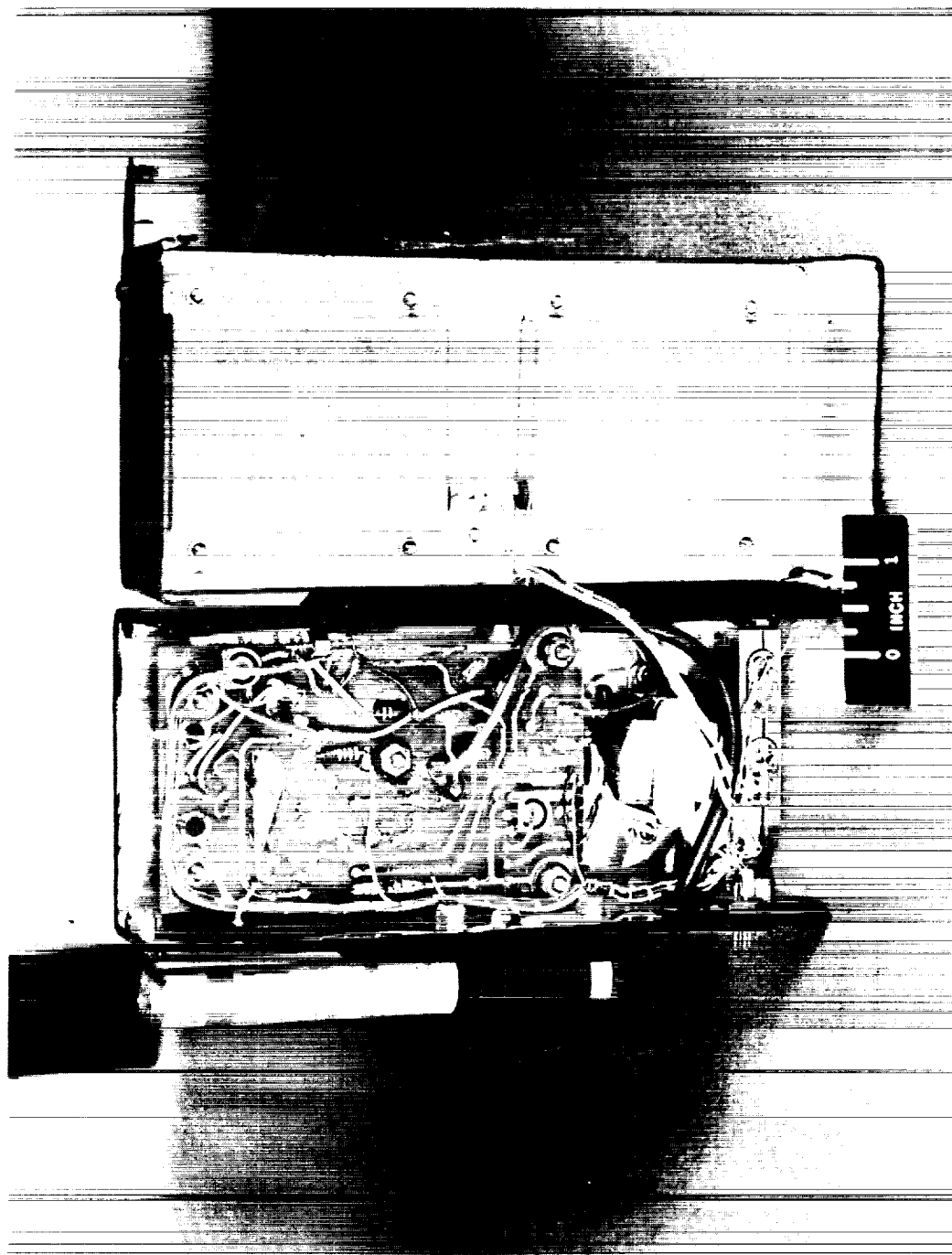
L-61-303

L-1924

Figure 35.- Inside view of radiation sensor.
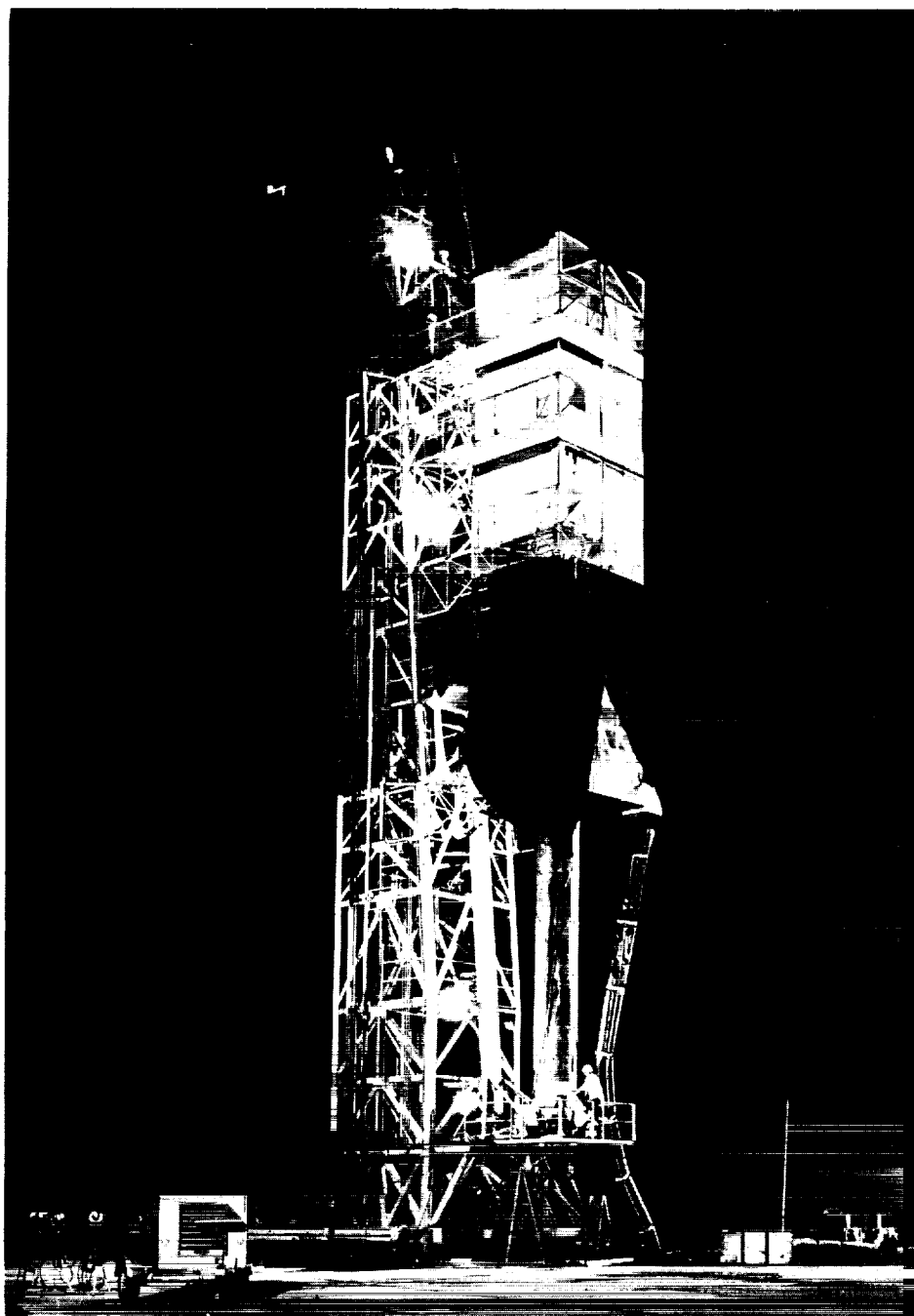
L-60-6490

Figure 36.- Launcher-tower for Scout vehicles at NASA Wallops Station.

L-1924
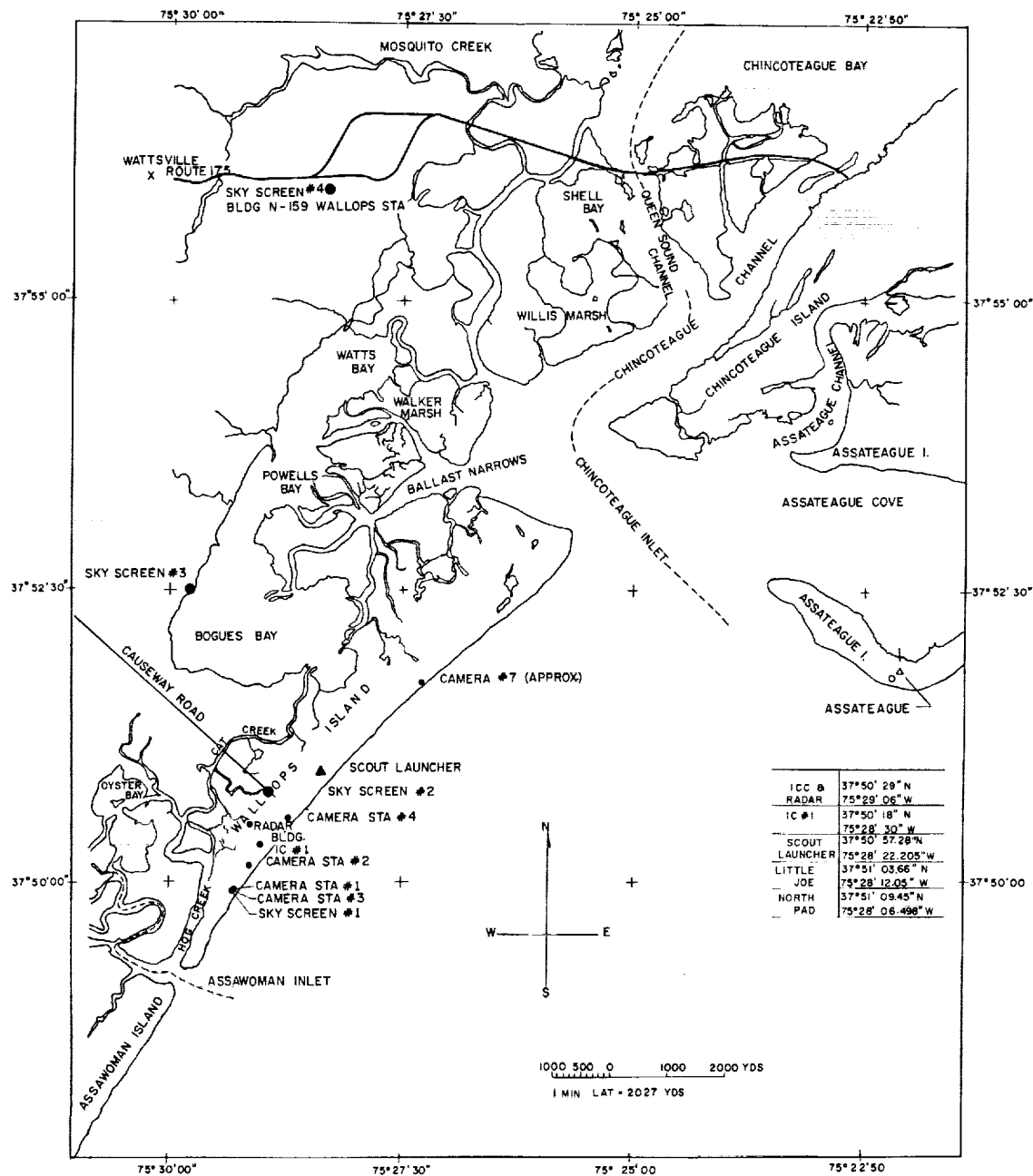
Figure 37.- Locations of Wallops Station range facilities at time of ST-1 flight.

L-1924
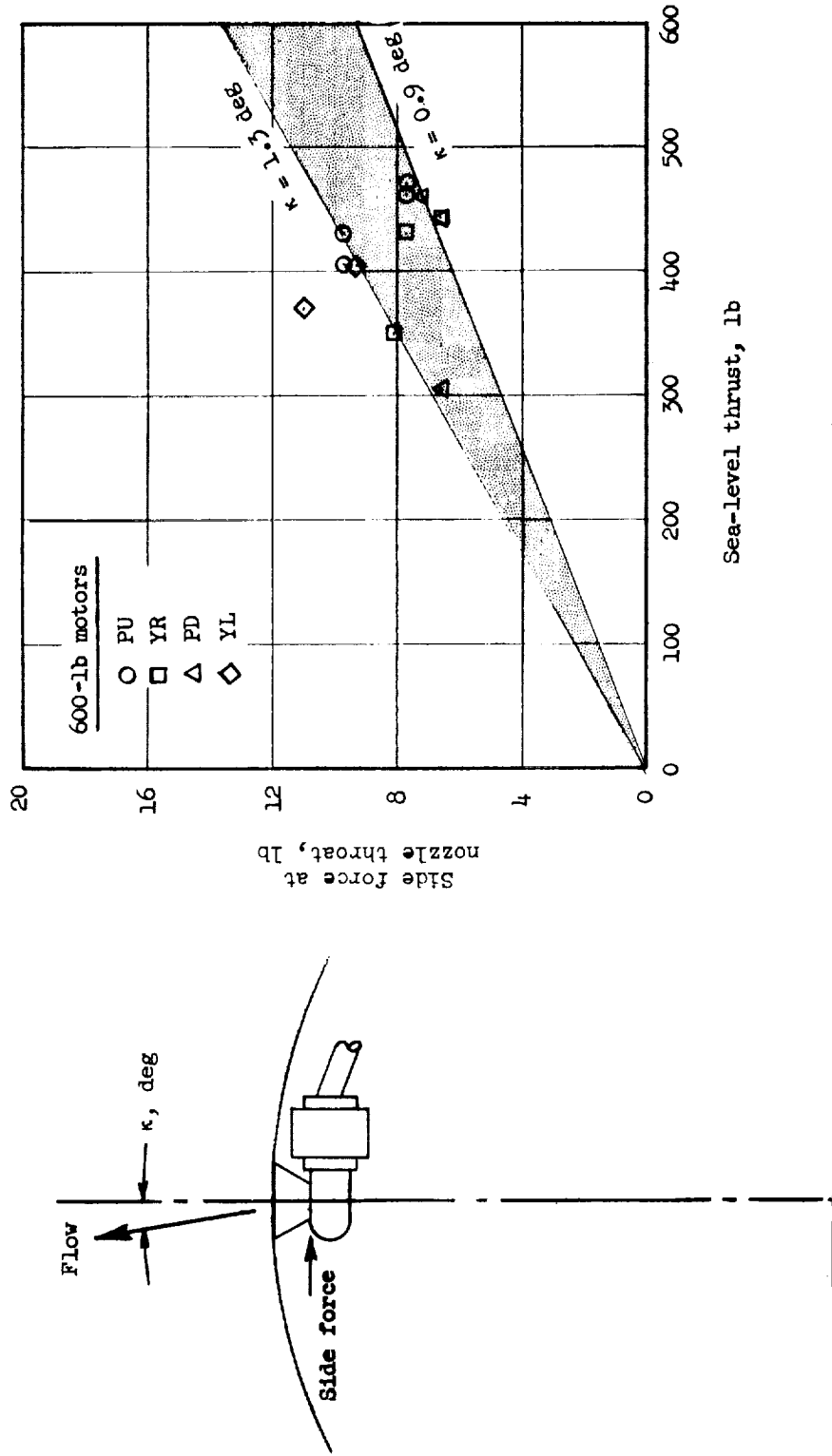
Figure 38.- Variation with sea-level thrust of side force due to flow angularity of second-stage 600-pound-thrust pitch and yaw motors.
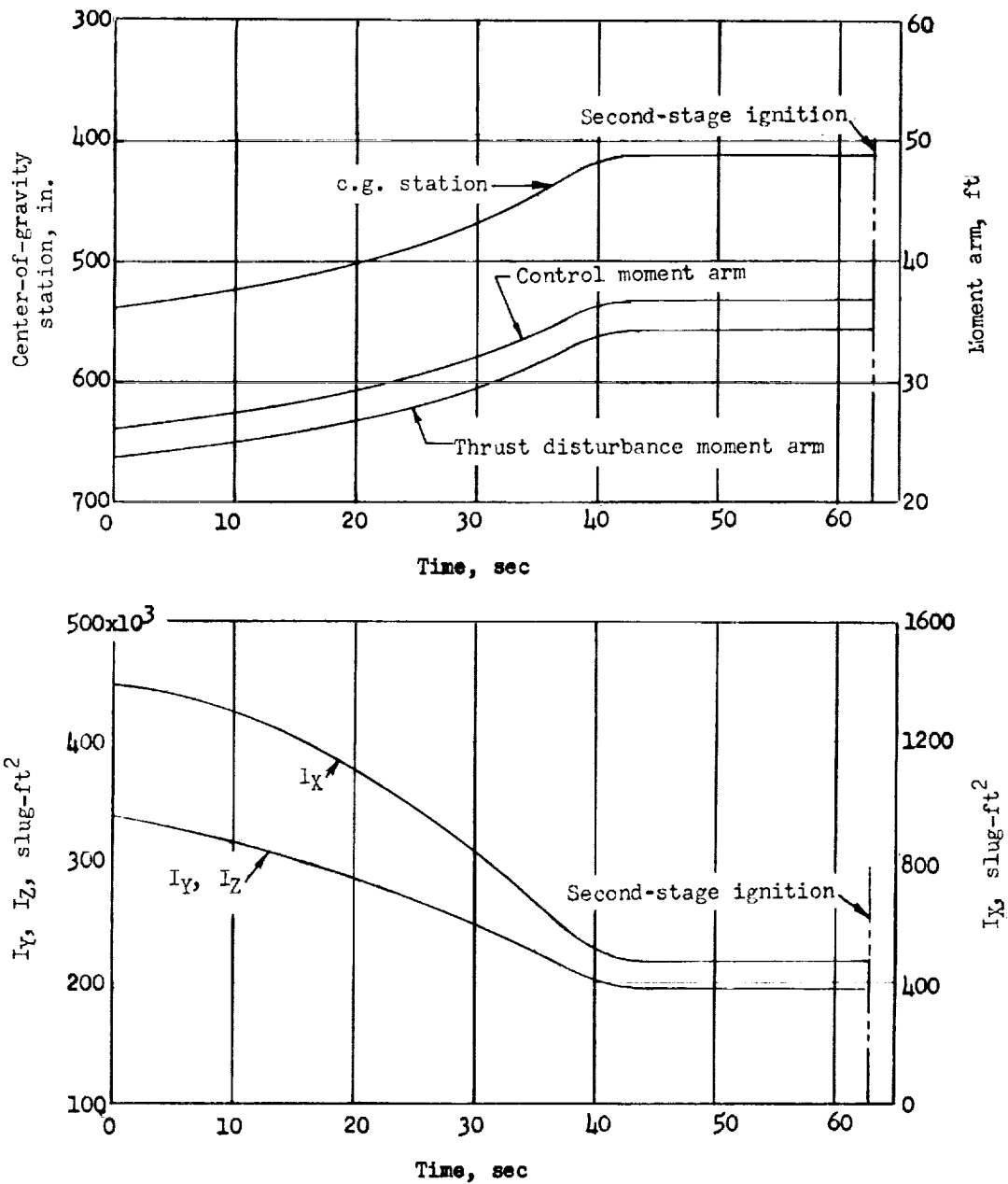
(a) First stage.

Figure 39.- Time variation of vehicle center of gravity, moment of inertia, and control and thrust disturbance moment arms.
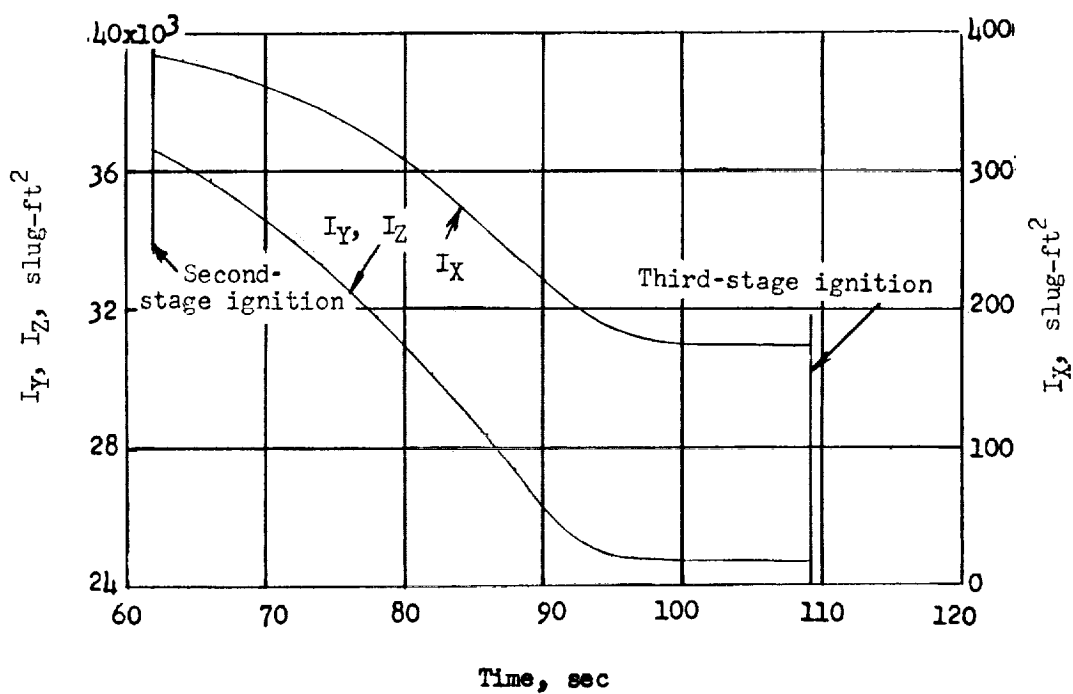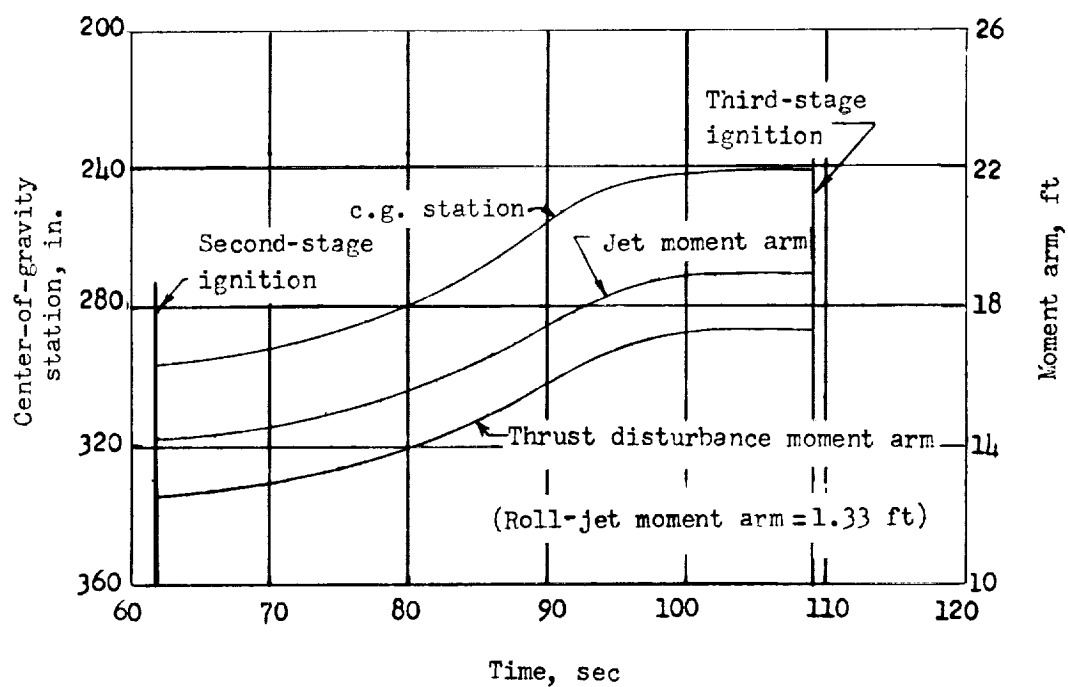
(b) Second stage.

Figure 39.- Continued.
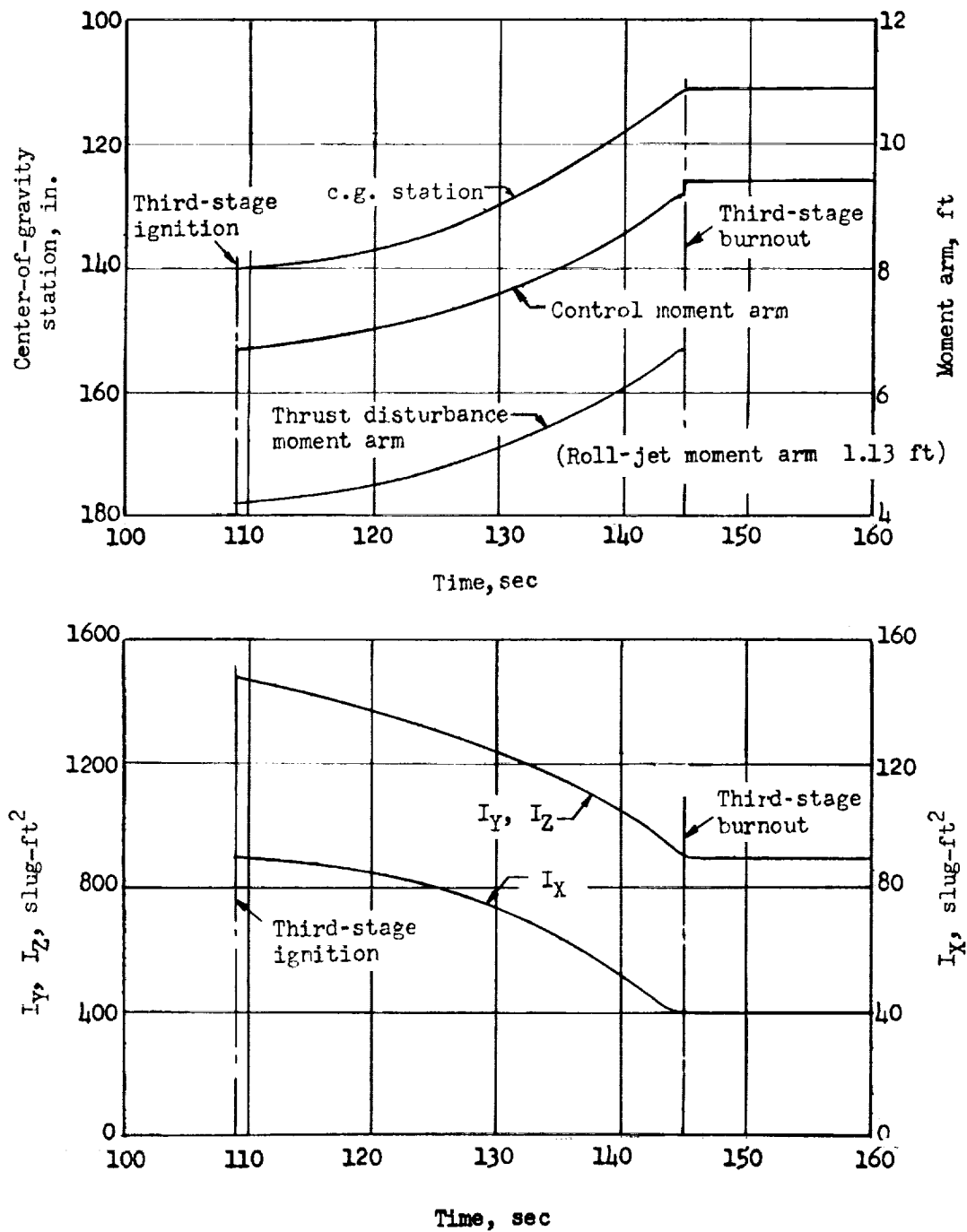
(c) Third stage.

Figure 39.- Concluded.
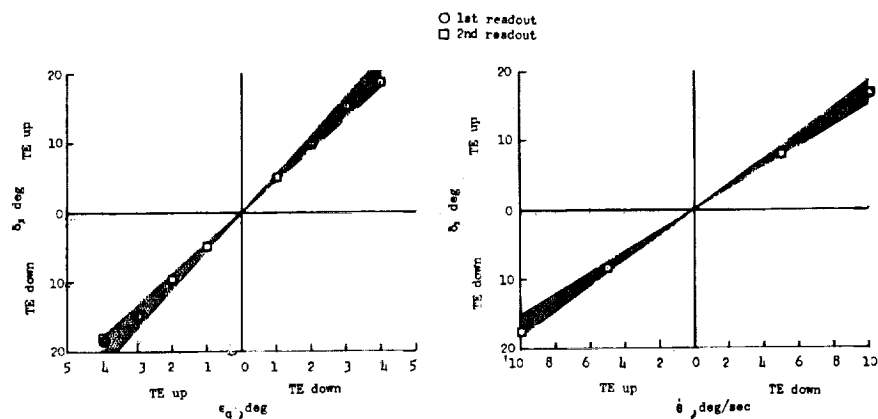
(a) Pitch.
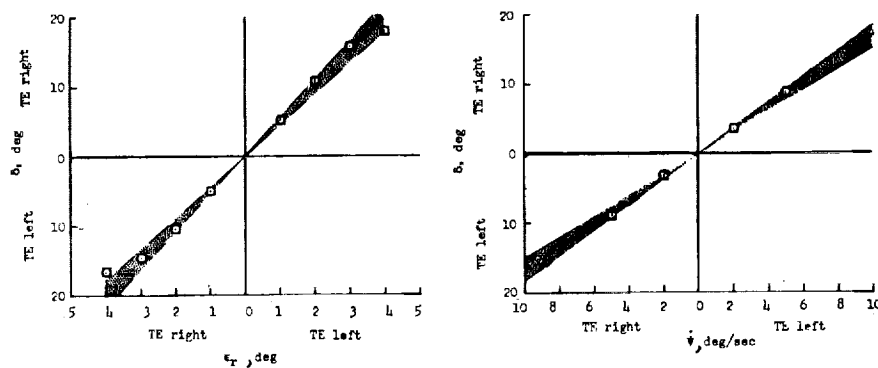
(b) Yaw.
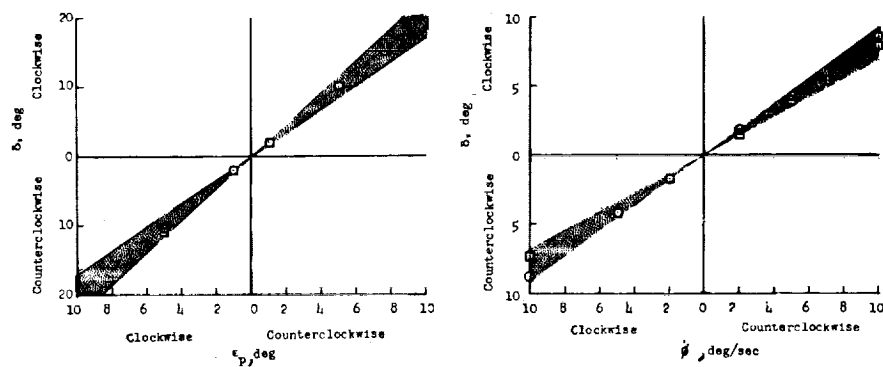
(c) Roll.

Figure 40.- Measured first-stage control-system position and rate gains. The shaded areas indicate ±10 percent of the nominal values.

L-1924
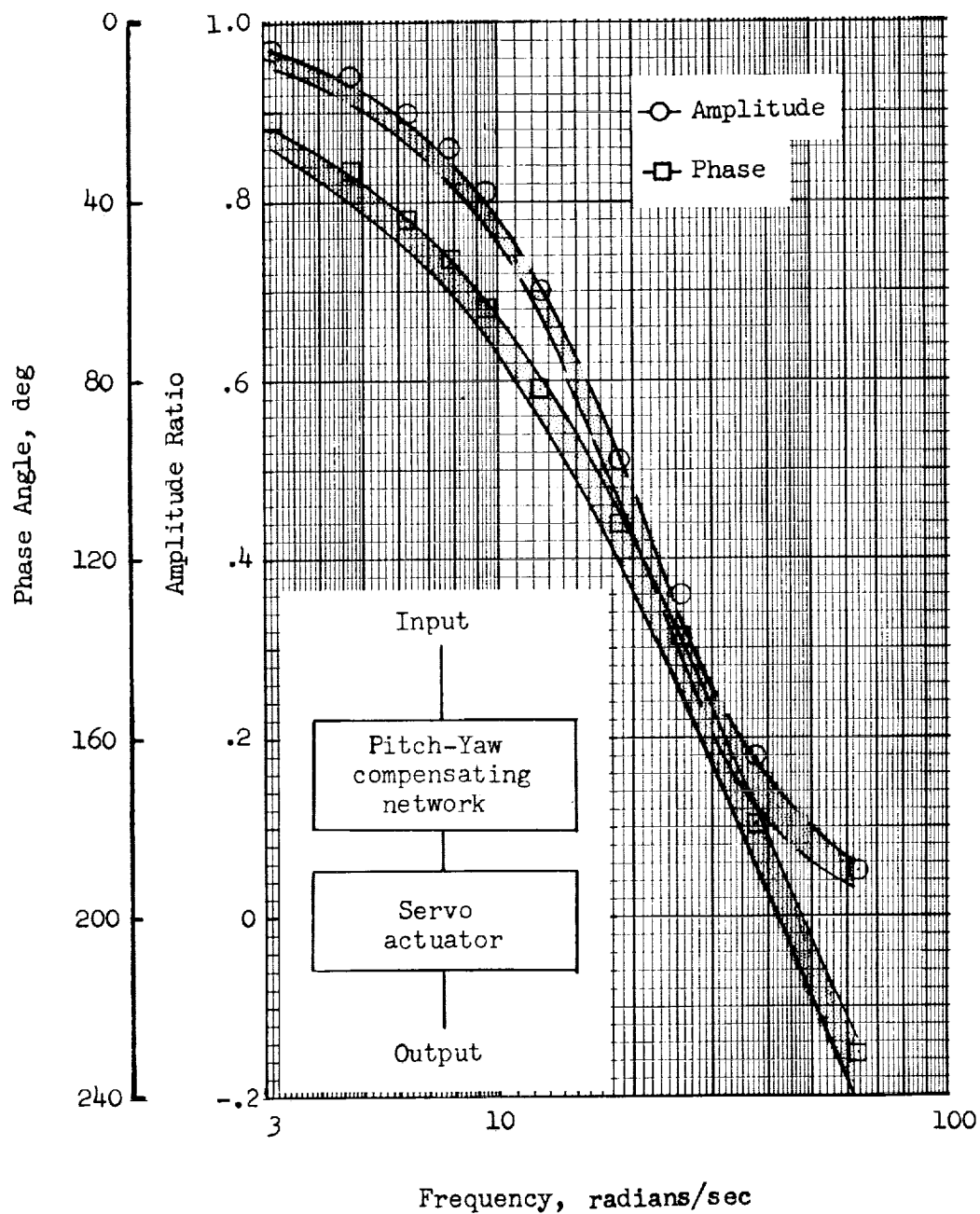
(a) Frequency-response criteria shown with a typical measured response. Tolerance bands are indicated by shaded areas.

Figure 41.- Frequency-response criteria and response to simulated error step inputs and hinge-moment loading for first-stage control system.
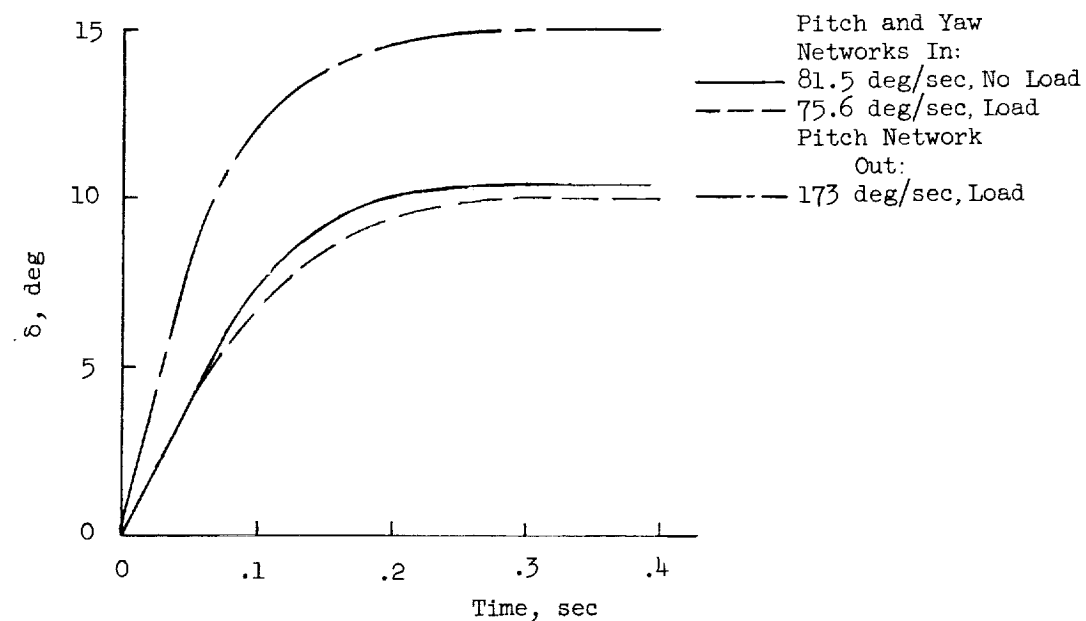
Pitch
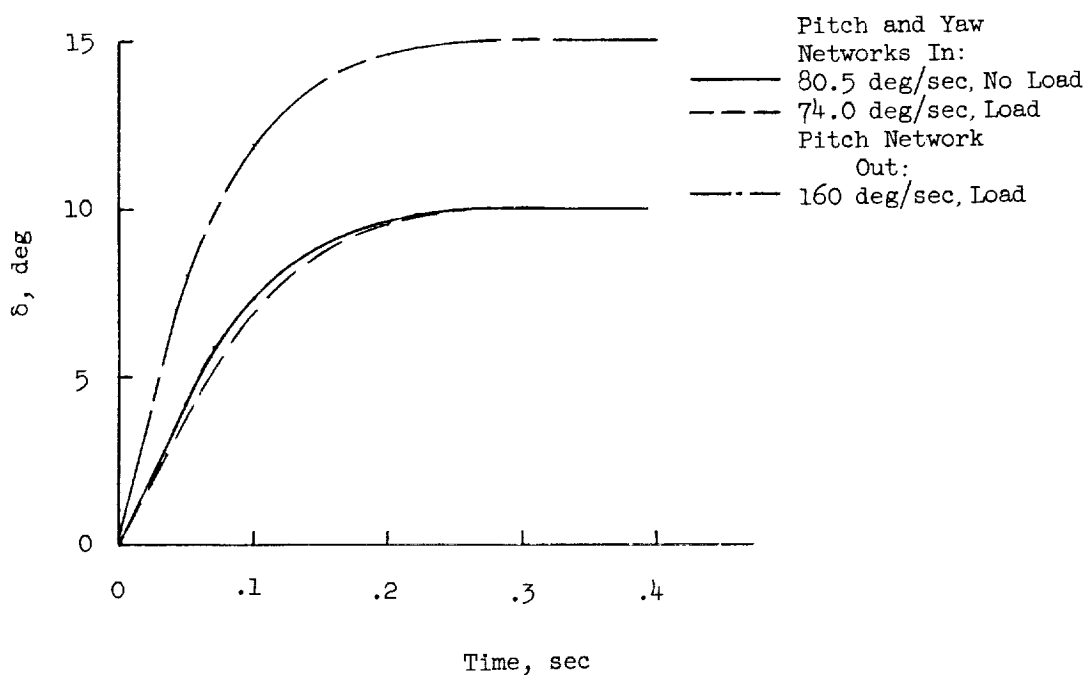
Pitch (pitch and yaw combined)

(b) Response to simulated error step inputs and hinge-moment loading of 50 in-lb/deg.

Figure 41.- Concluded.

L-1924

144
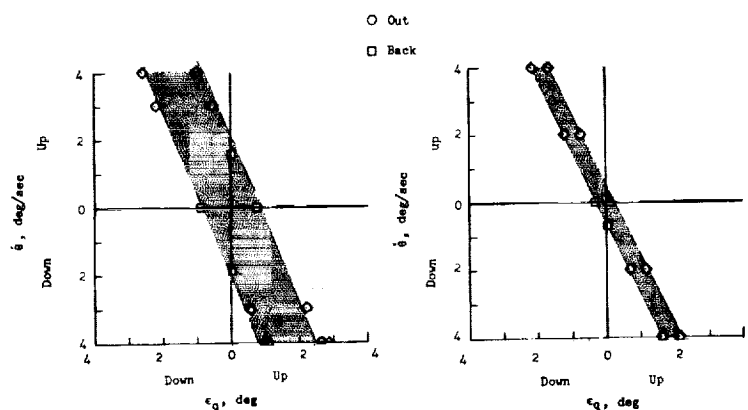
(a) Pitch.
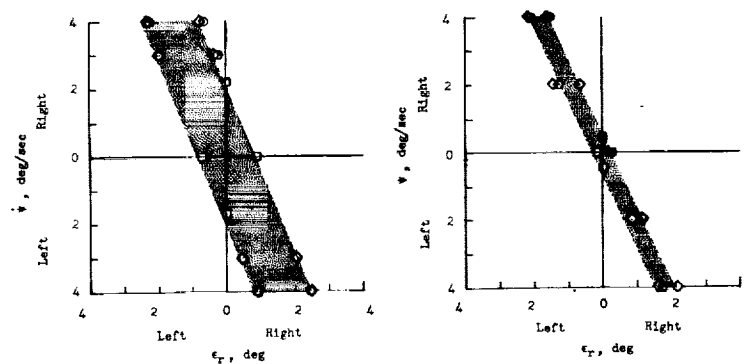
(b) Yaw.
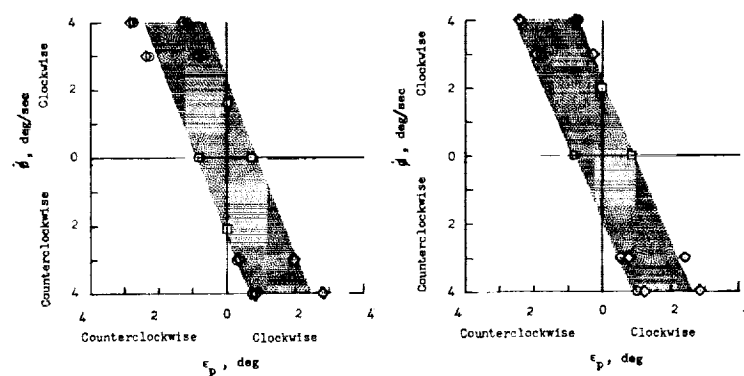
(c) Roll.

Figure 42.- Measured dead-band and switching-slope characteristics of
second- and third-stage control systems. (Shaded area is nominal
dead-band width.)
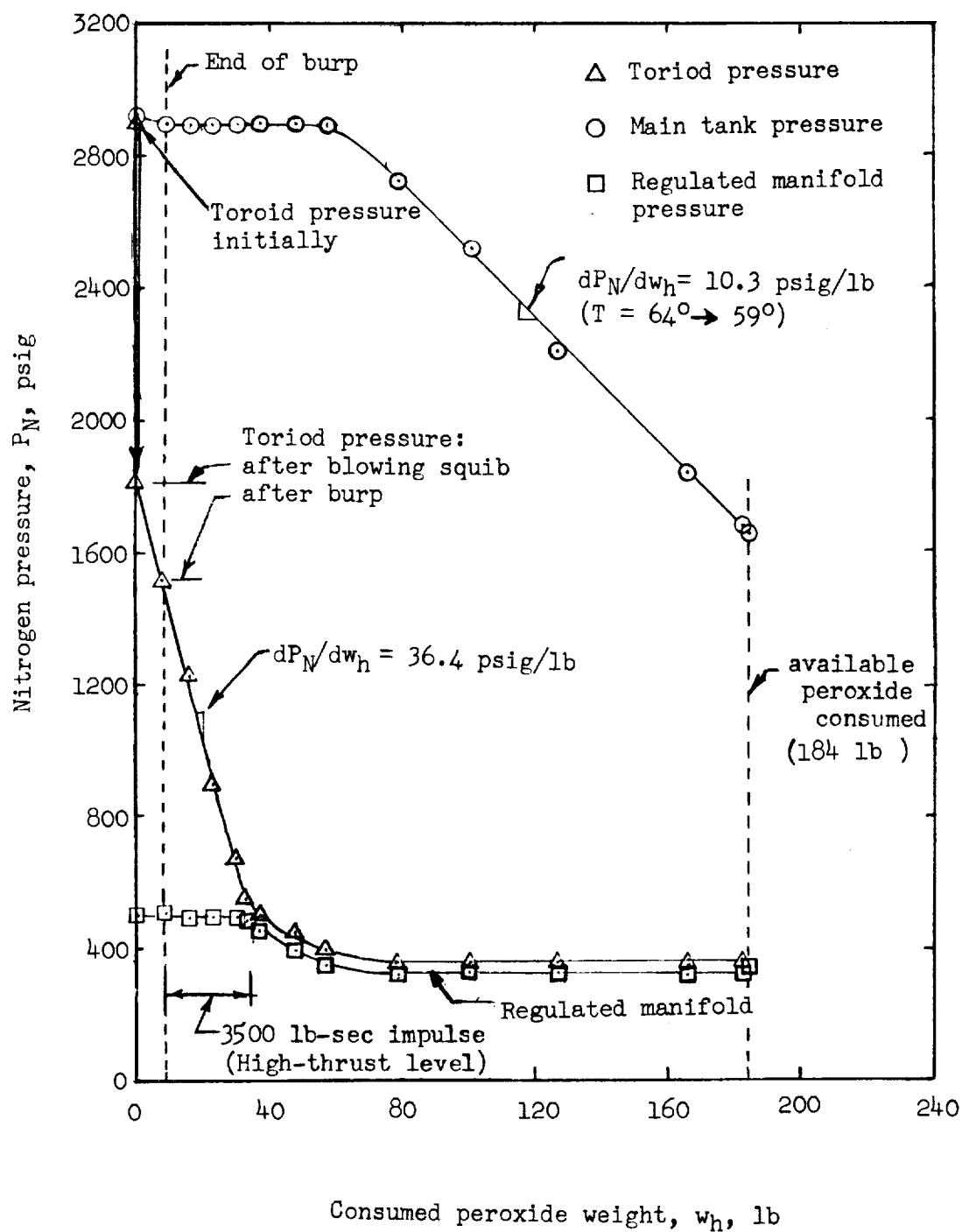
(a) Second stage.

Figure 43.- Preflight hydrogen-peroxide fuel calibration test results.
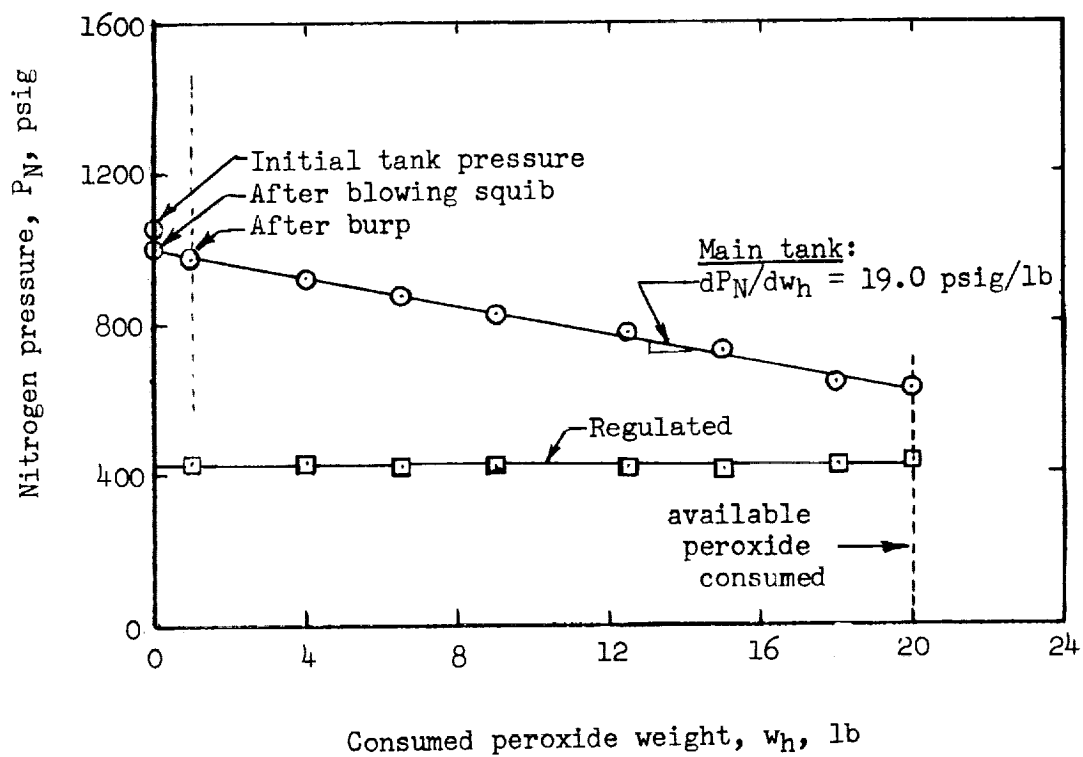
(b) Third stage.

Figure 43.- Concluded.

L-1924

F = 660 lb
P_c= 298 psig

Chamber pressure signal

Valve signal

Pitch up

F = 630 lb
P_c= 285 psig

Pitch down

|←←-.01 sec

F = 656 lb
P_c= 296 psig

Yaw left

F = 602 lb
P_c= 272 psig

Yaw right

F = 22.2 lb
P_c= 198 psig

Roll upper left

F = 23 lb
P_c= 206 psig

Roll upper right

F = 21 lb
P_c= 187 psig

Roll lower left

F = 23.2 lb
P_c= 207 psig

Roll lower right

Time, sec

Time, sec
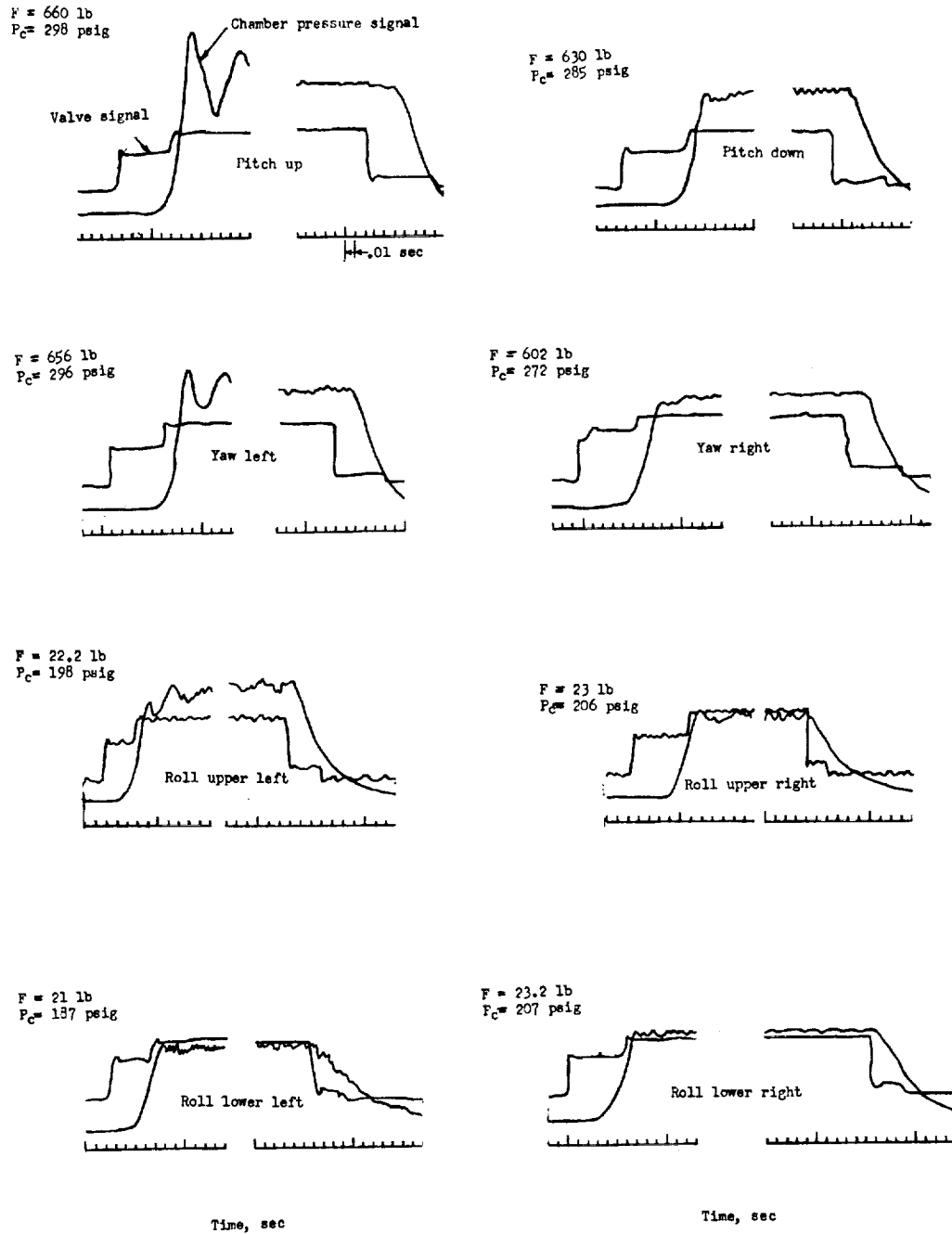
(a) Second stage.

Figure 44.- Typical responses of hydrogen-peroxide jet motors for one jet
operating condition. Smallest time interval shown is 0.01 second.

148
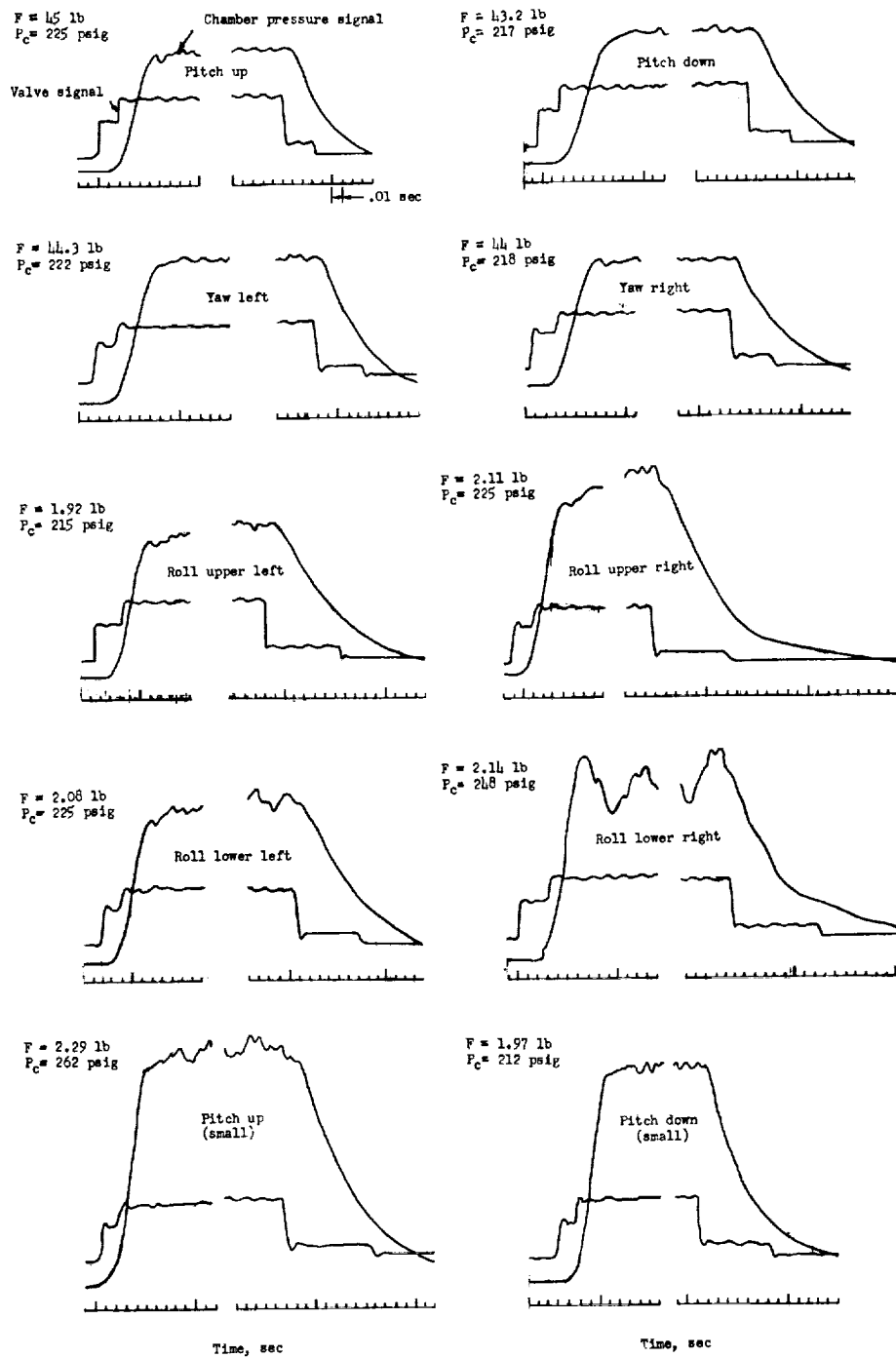
(b) Third stage.

Figure 44.- Concluded.

L-1924
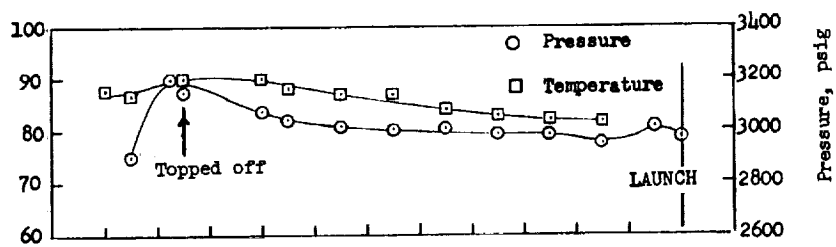
(a) Second-stage nitrogen supply.
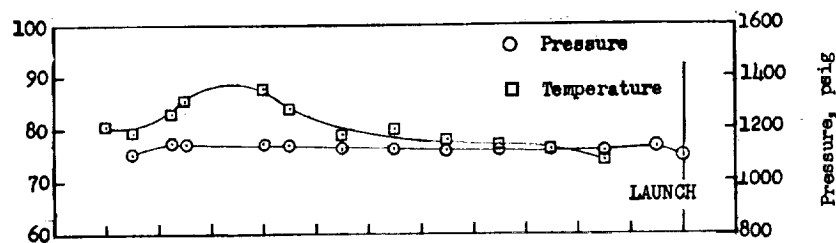
(b) Third-stage nitrogen supply.
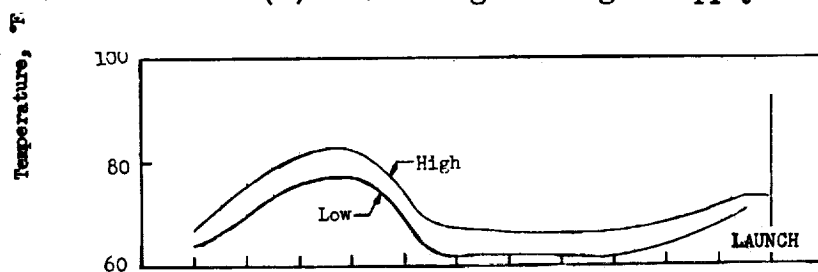
(c) Hydrogen-peroxide temperatures (transitions B and C).

Real time (e.s.t.), hours
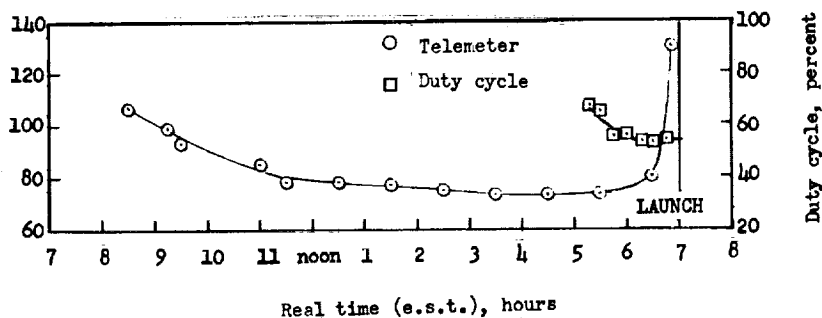
(d) Gyro heater duty cycle and transition D telemeter compartment temperature.

Figure 45.- Monitored data of control system during countdown.
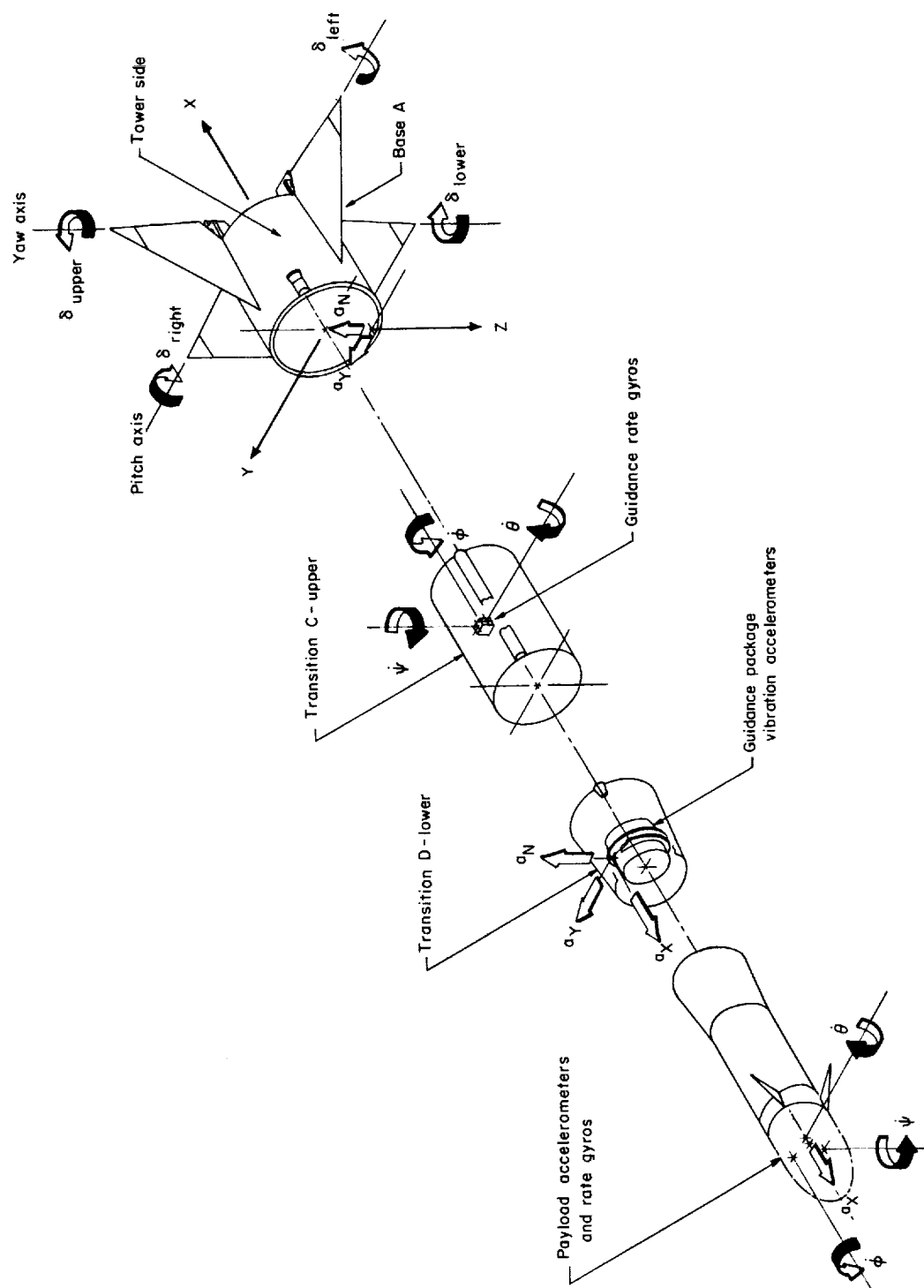
Figure 46.- Sign convention for measured linear accelerations, angular velocities, and fin-tip control-surface deflections. Arrows indicate positive directions.
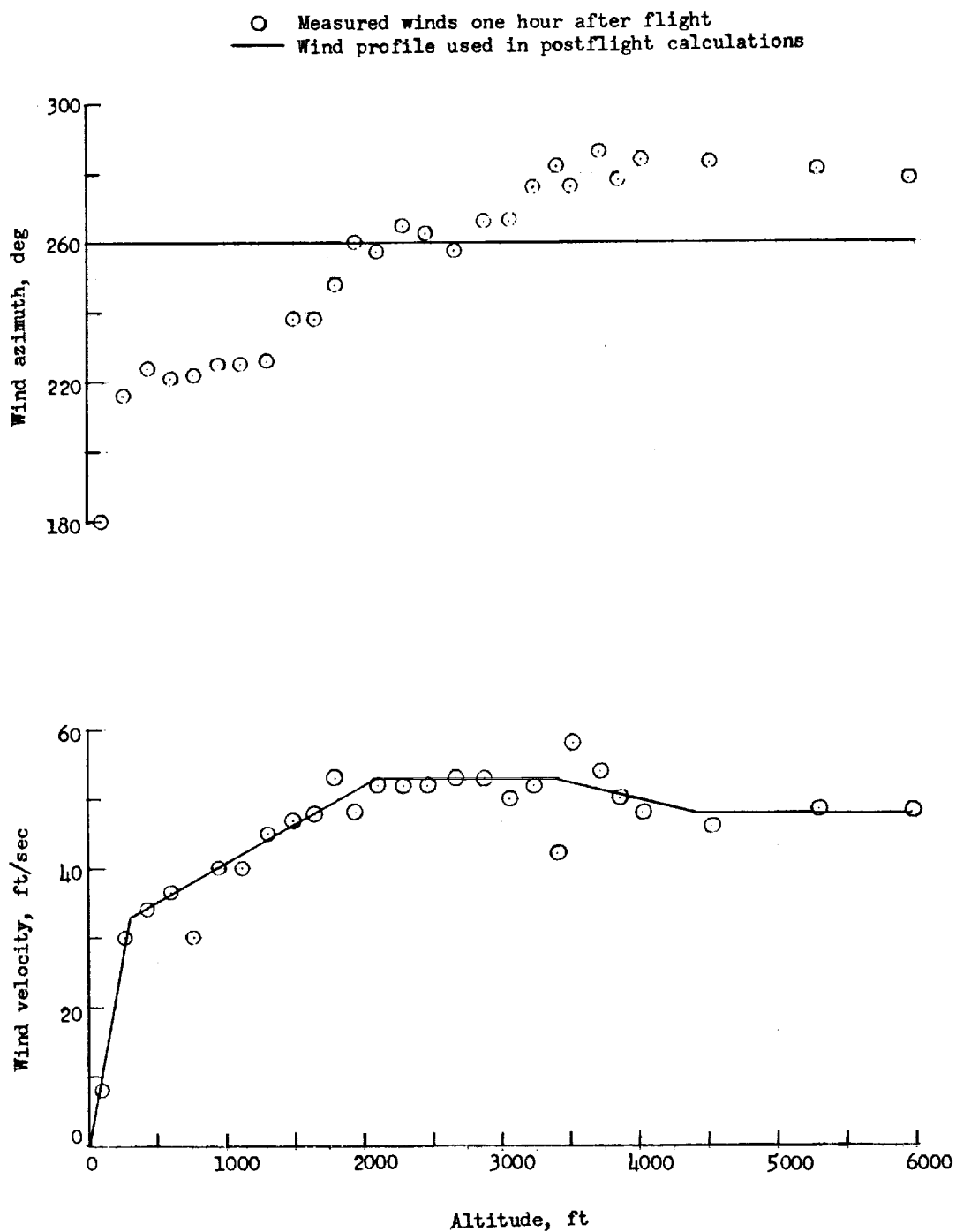
(a) Balloon (radar tracking).

Figure 47.- Wind data used for postflight calculations.

○ Measured winds one hour after flight
—— Wind profile used for postflight calculations
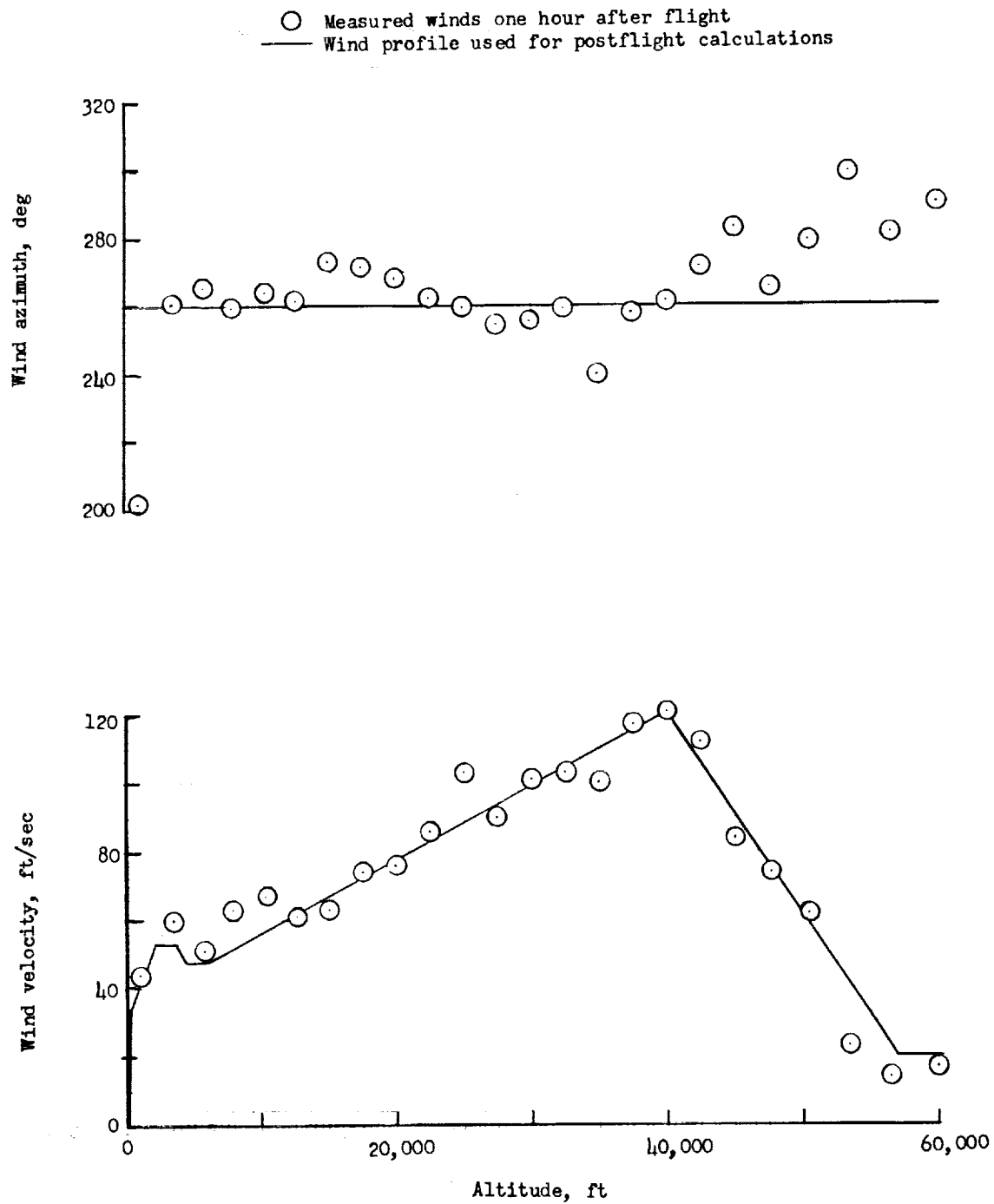
(b) Rawinsonde.

Figure 47.- Concluded.

L-1924

Time from ignition, sec
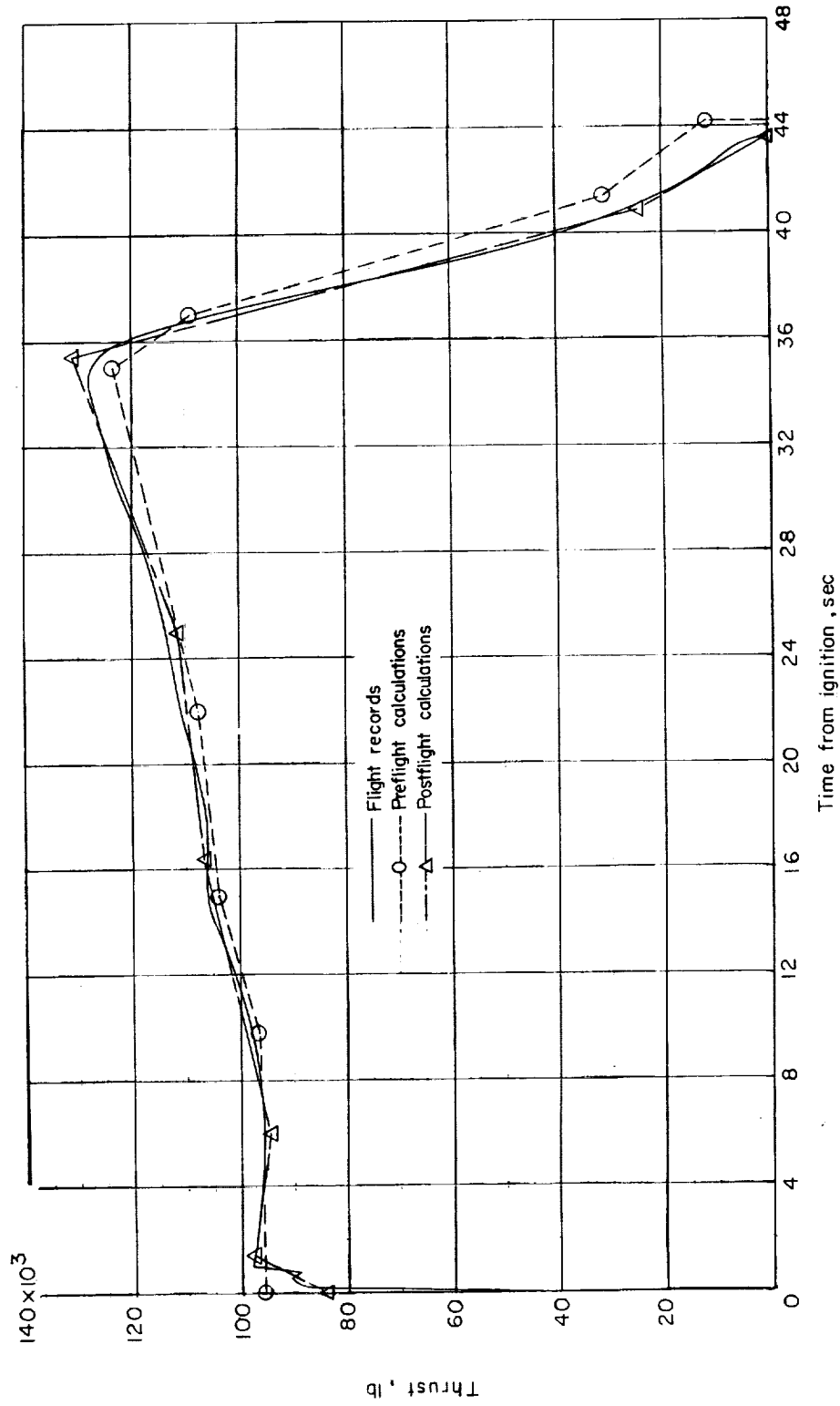
(a) First stage.

Figure 48.- Variation in thrust with time.
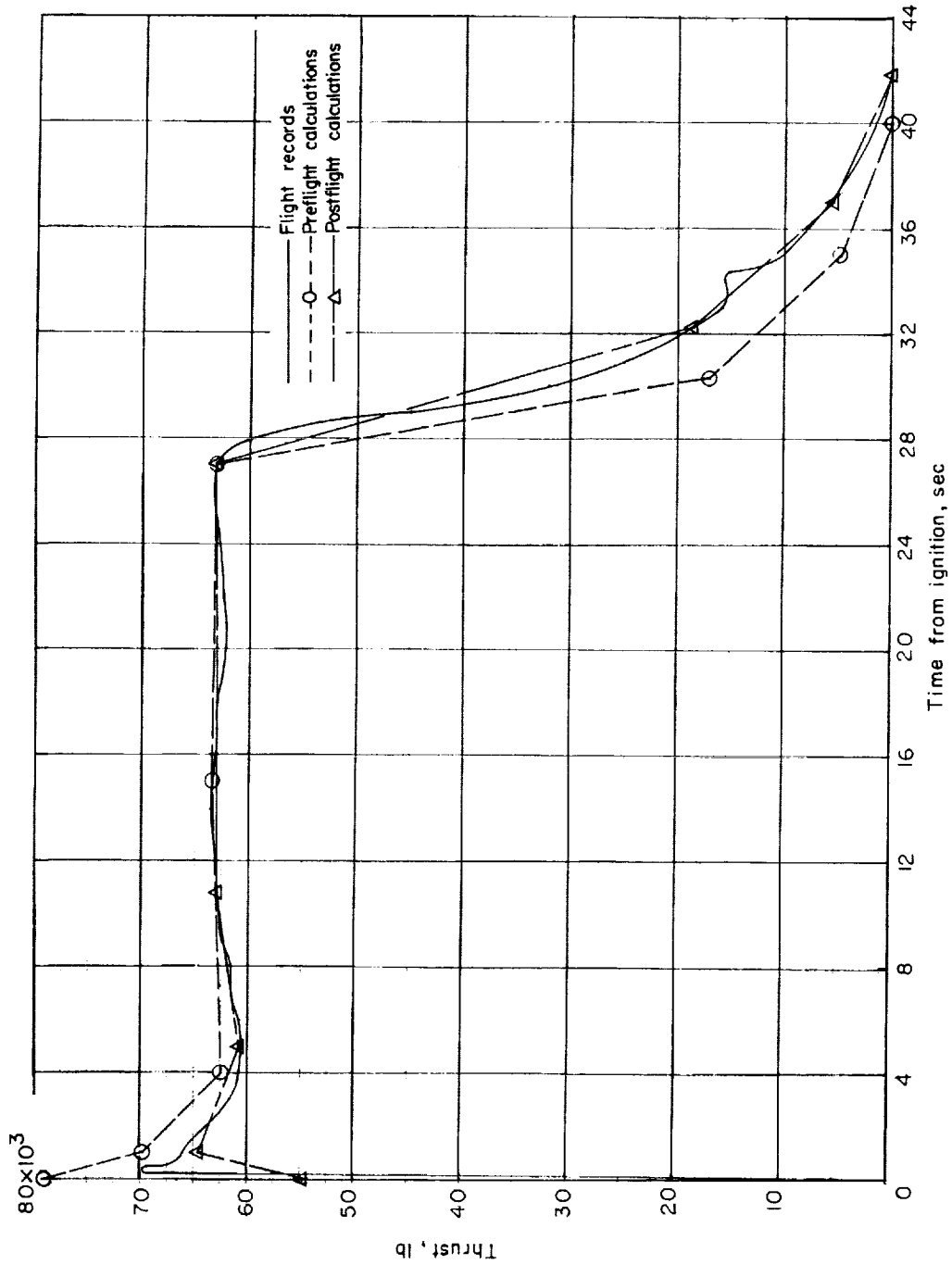
(b) Second stage.

Figure 48.- Continued.
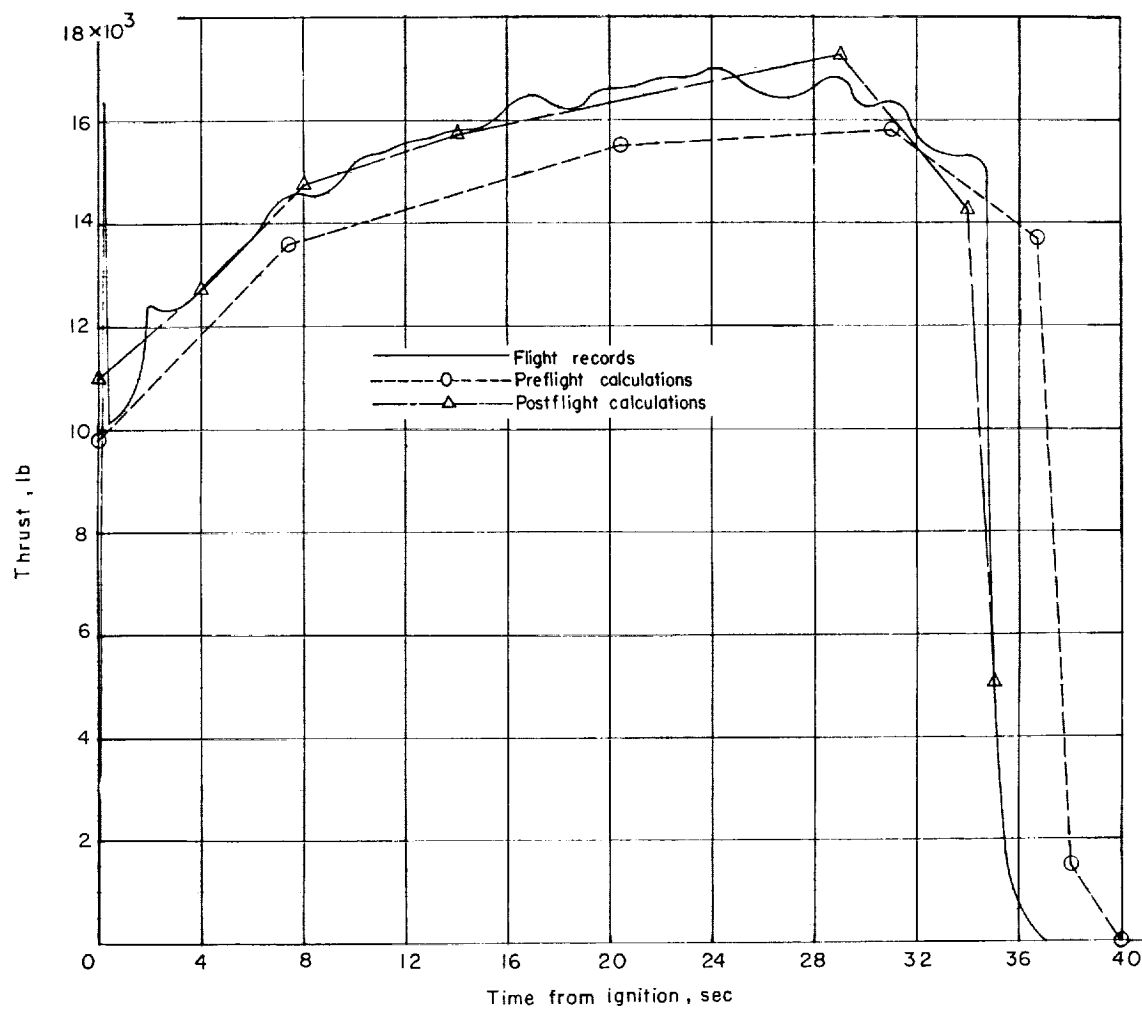
L-1924

(c) Third stage.

Figure 48.- Concluded.
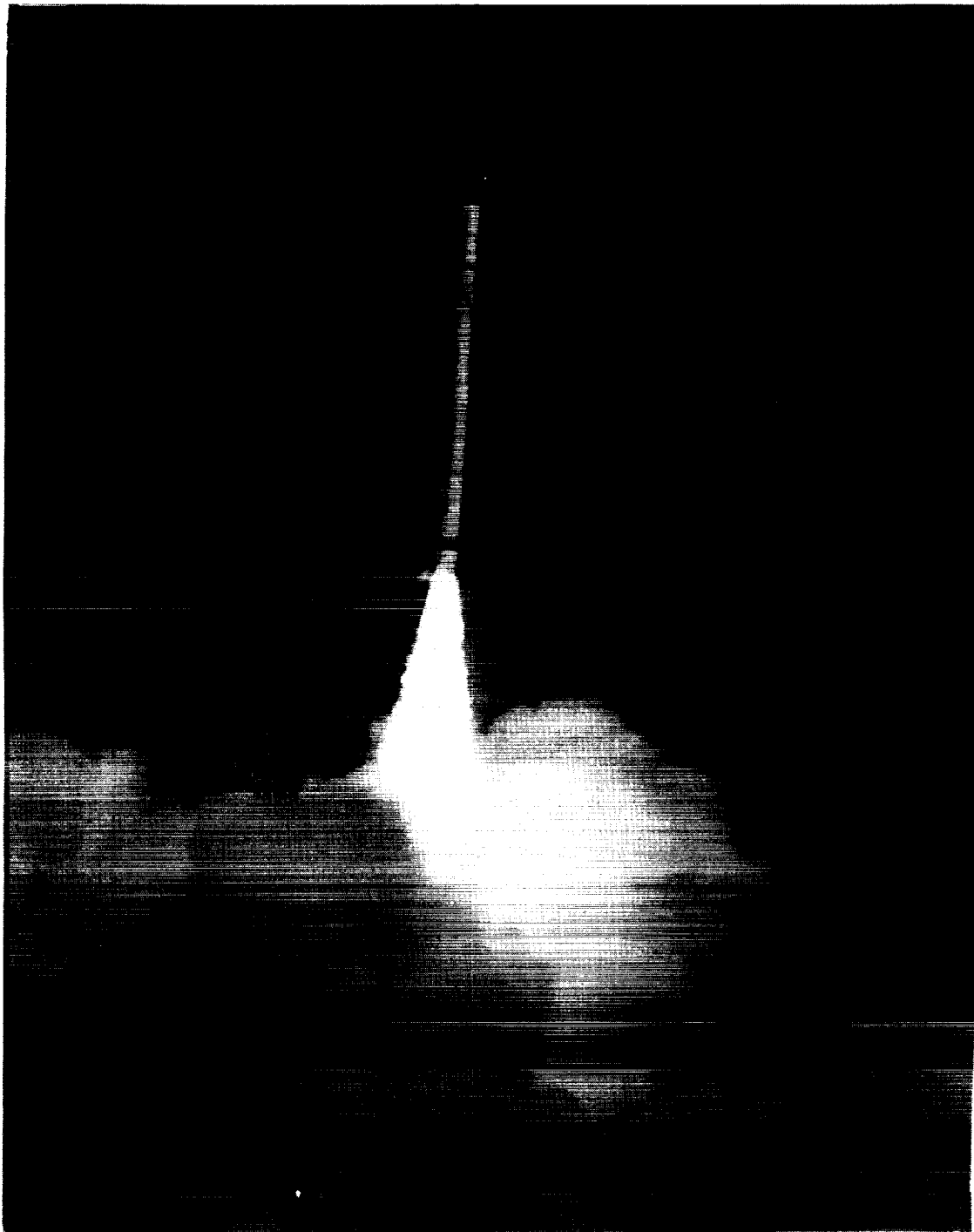
L-1924

L-60-7309

Figure 49.- Launching of Scout ST-1 test vehicle from
NASA Wallops Station.

L-1924

(a) RCA AN/FPS-16 radar.

Figure 50.- Copies of radar plot boards for ST-1 flight test.

158
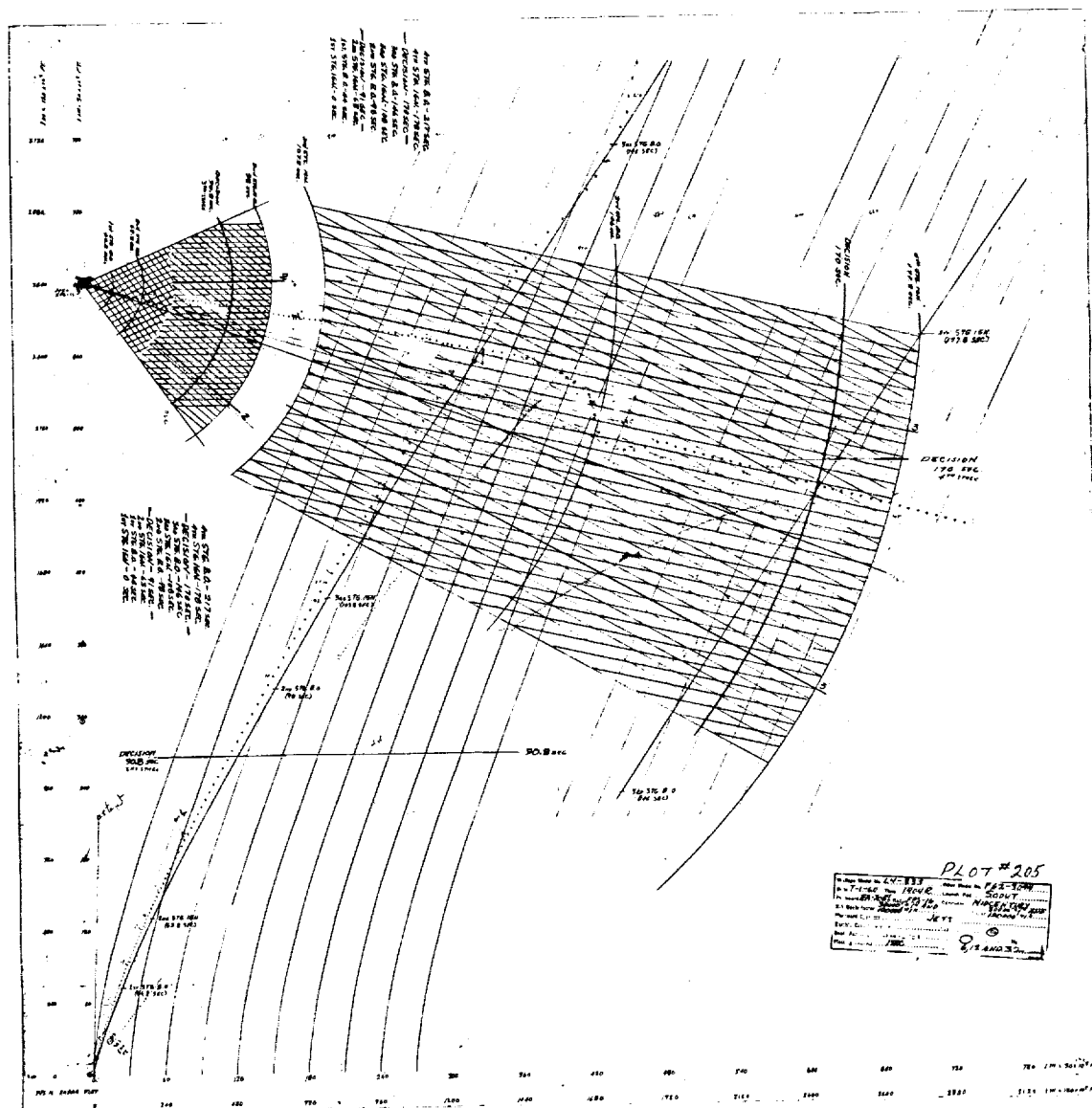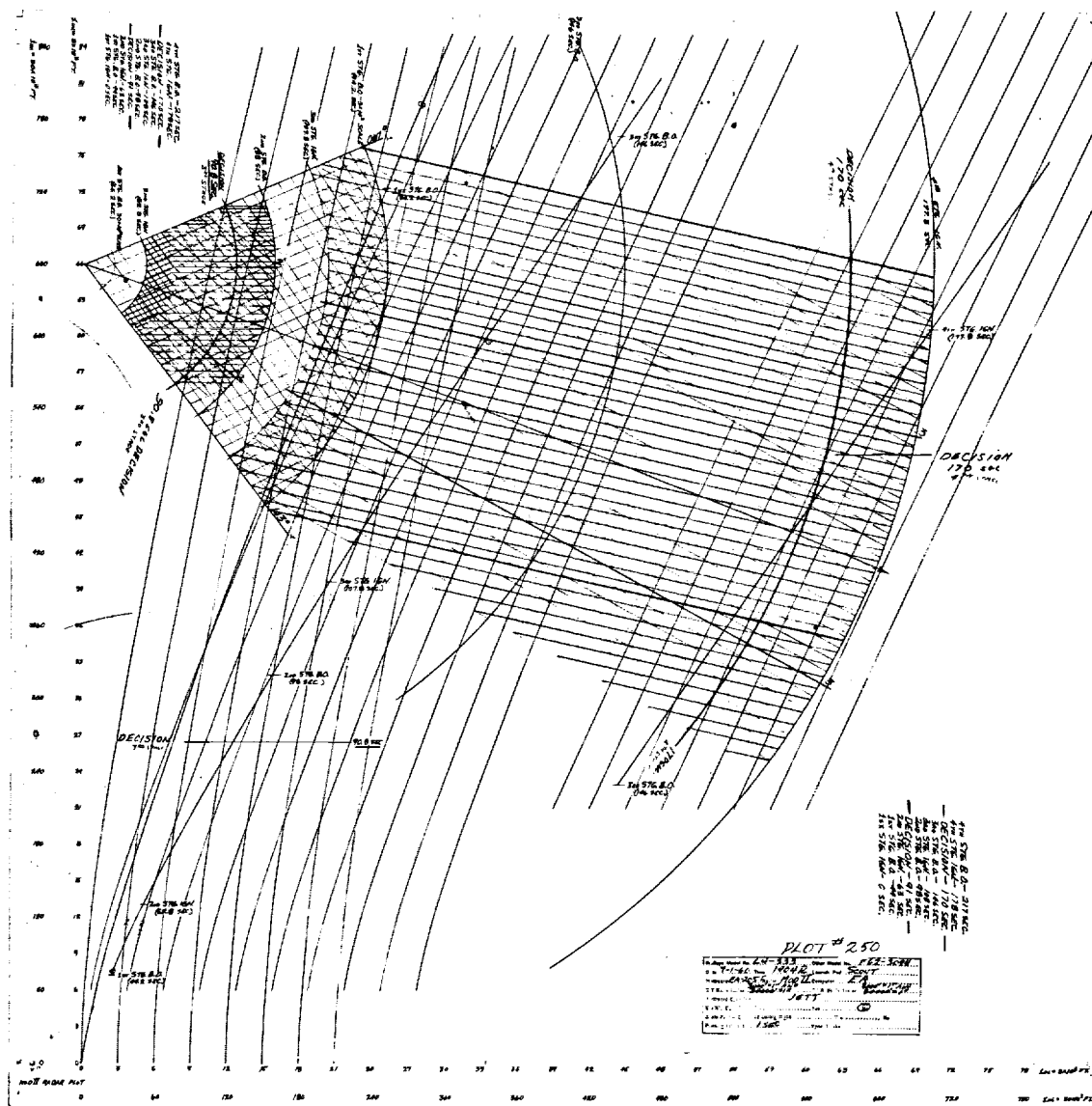
(b) Reeves Mod. II SCR-584 radar.

Figure 50.- Continued.

L-1924

(c) SCR-584 radar.

Figure 50.- Concluded.

160
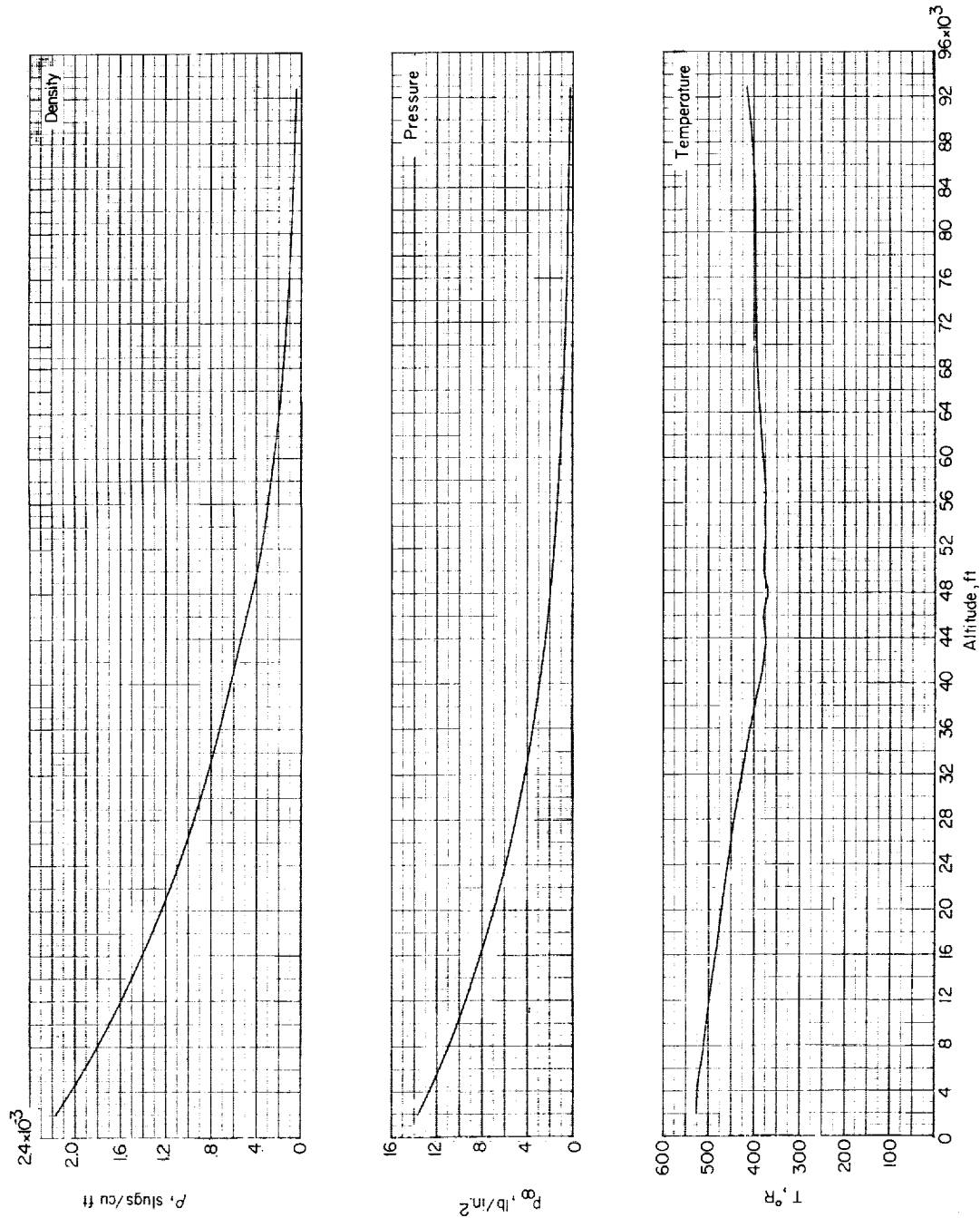
Figure 51.- Variation of free-stream density, pressure, and temperature with altitude. Recorded by rawinsonde instrumentation prior to launch.
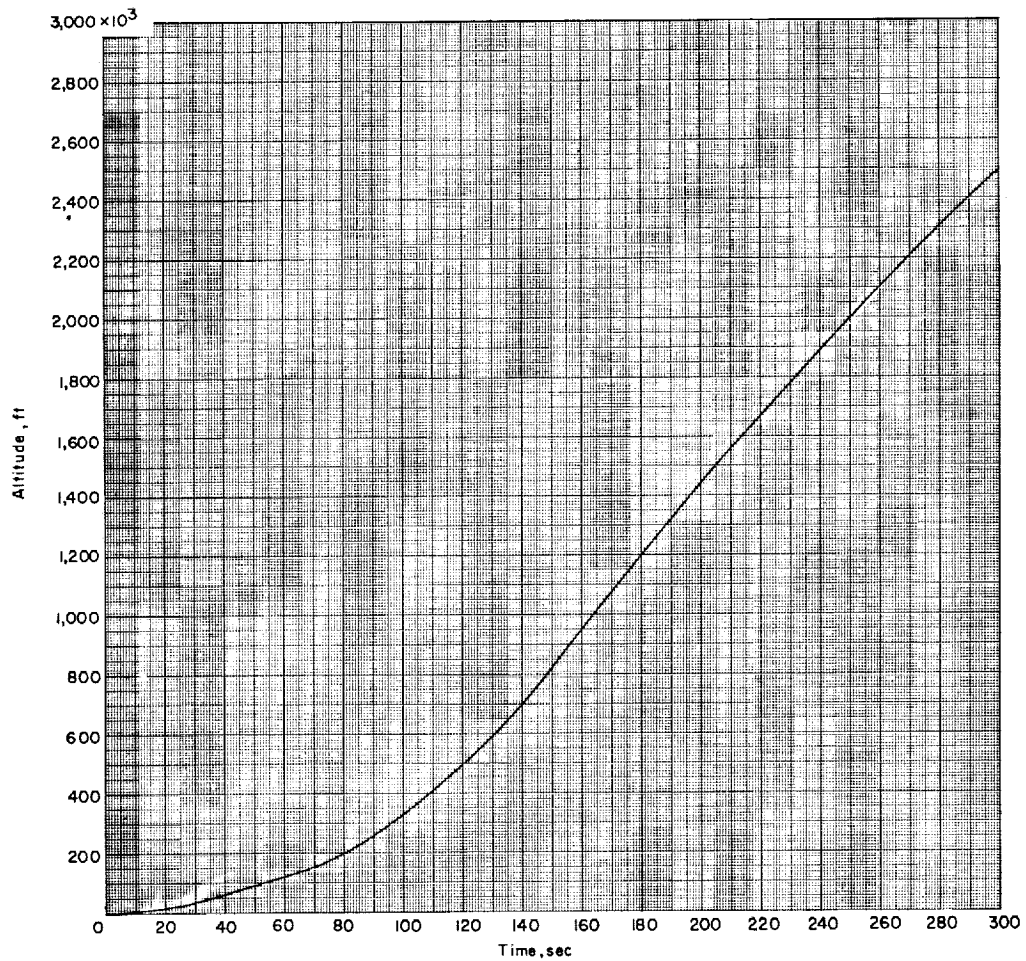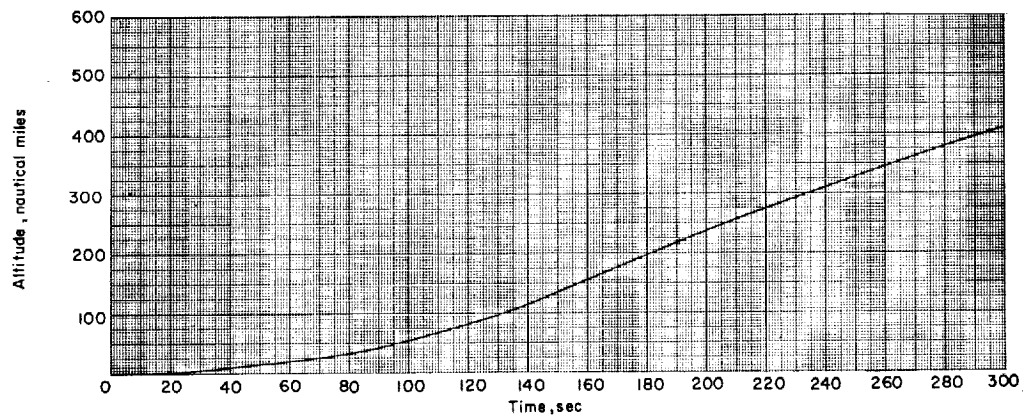
Figure 52.- Variation of vehicle altitude with time through
third-stage burnout.
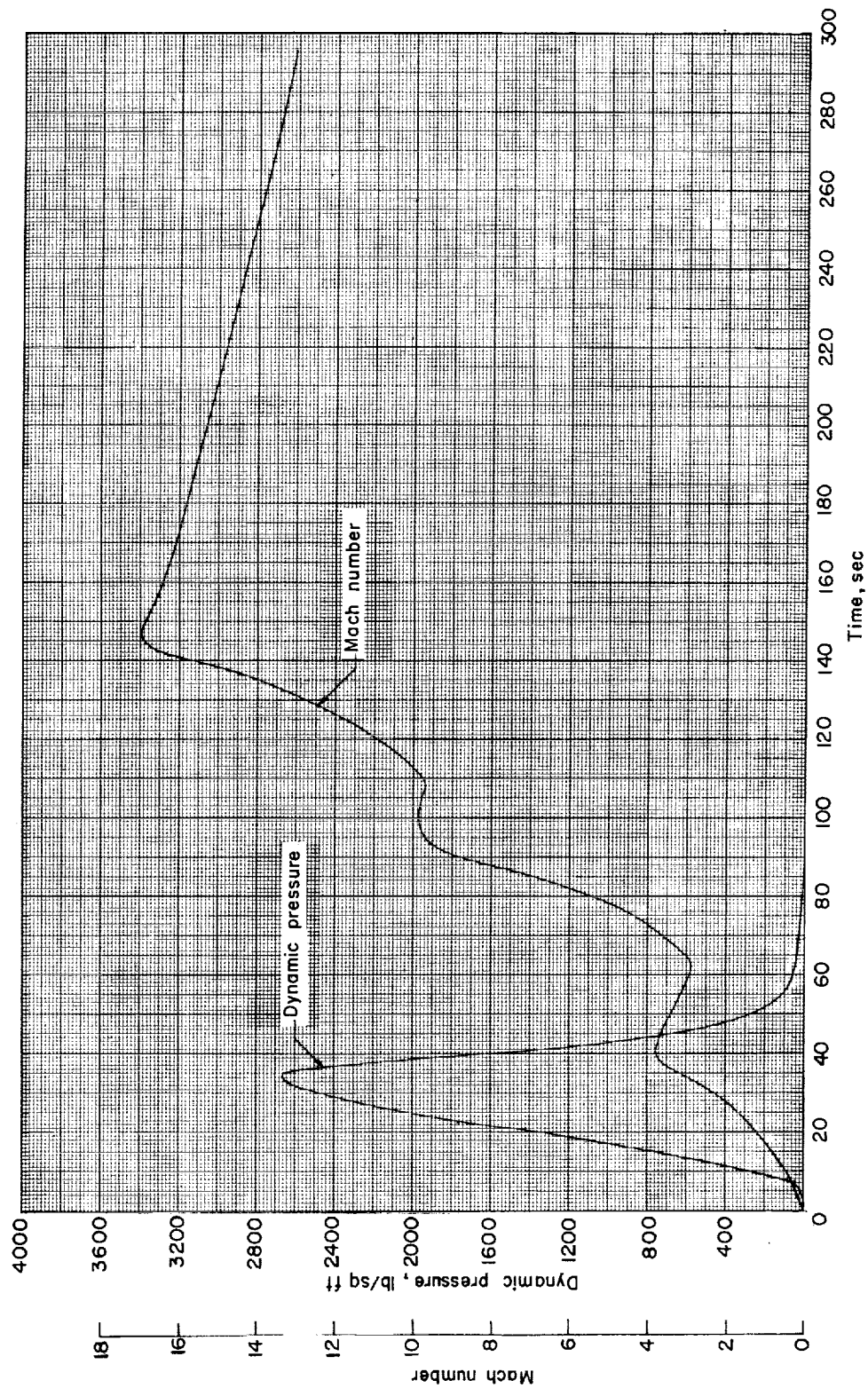
Figure 53.- Variation of free-stream Mach number and dynamic pressure with time.

L-1924
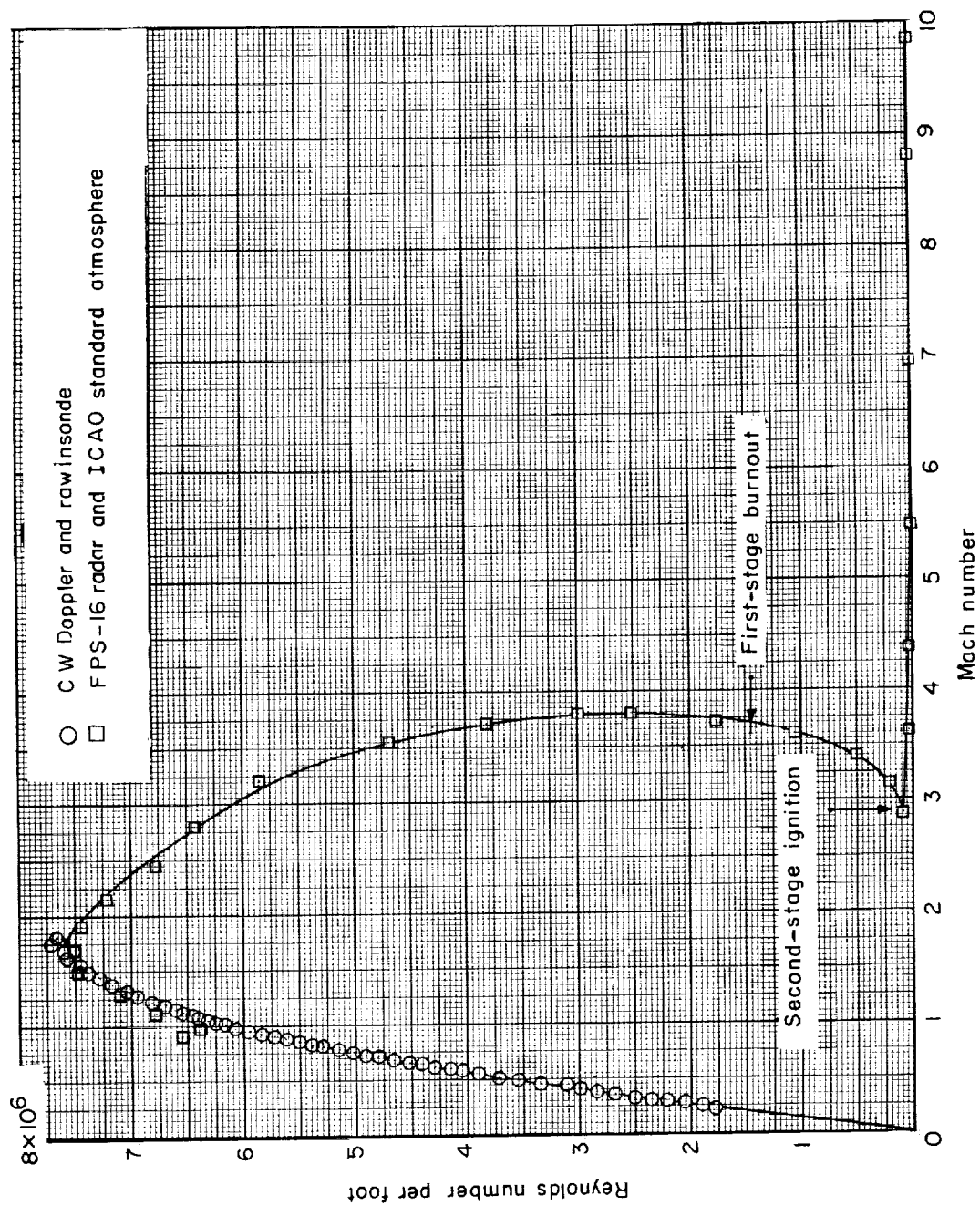
Figure 54.- Variation of Reynolds number per foot with free-stream Mach number.

164
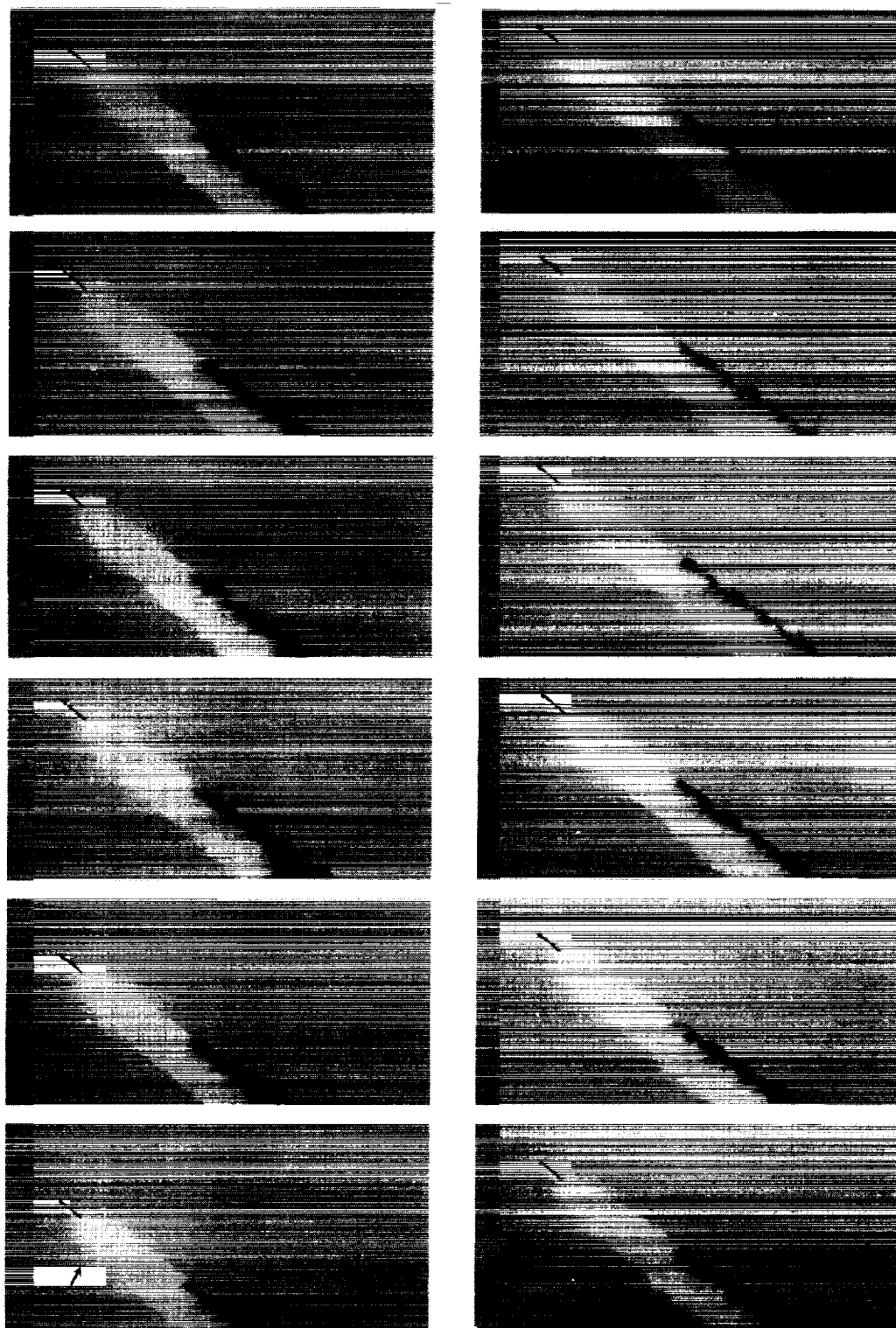
Figure 55.- Photo sequence of particle emerging from exhaust of first-stage rocket motor.

L-61-35

L-1924
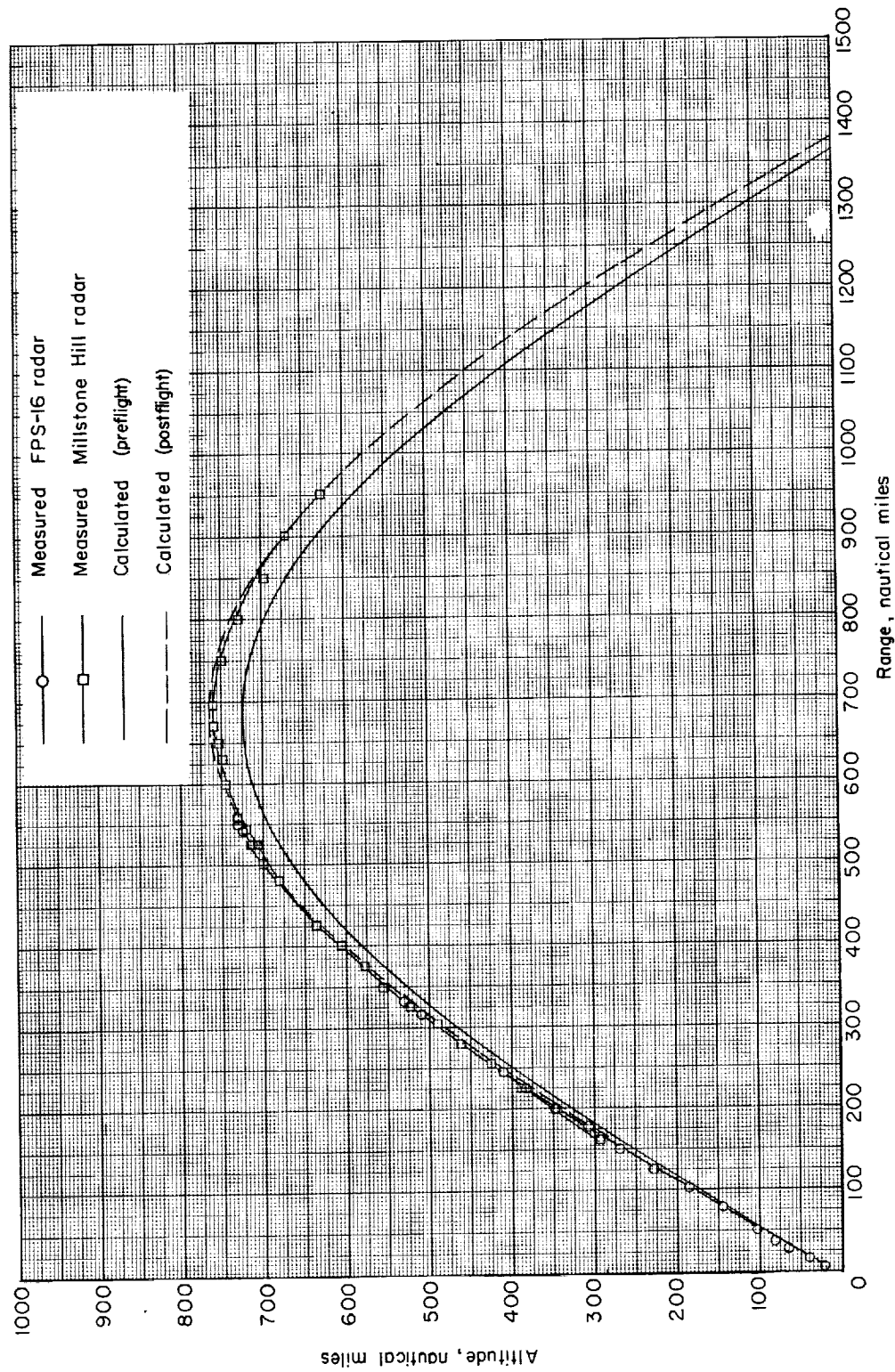
Figure 56.- Variation of vehicle altitude with range from launch to splash.
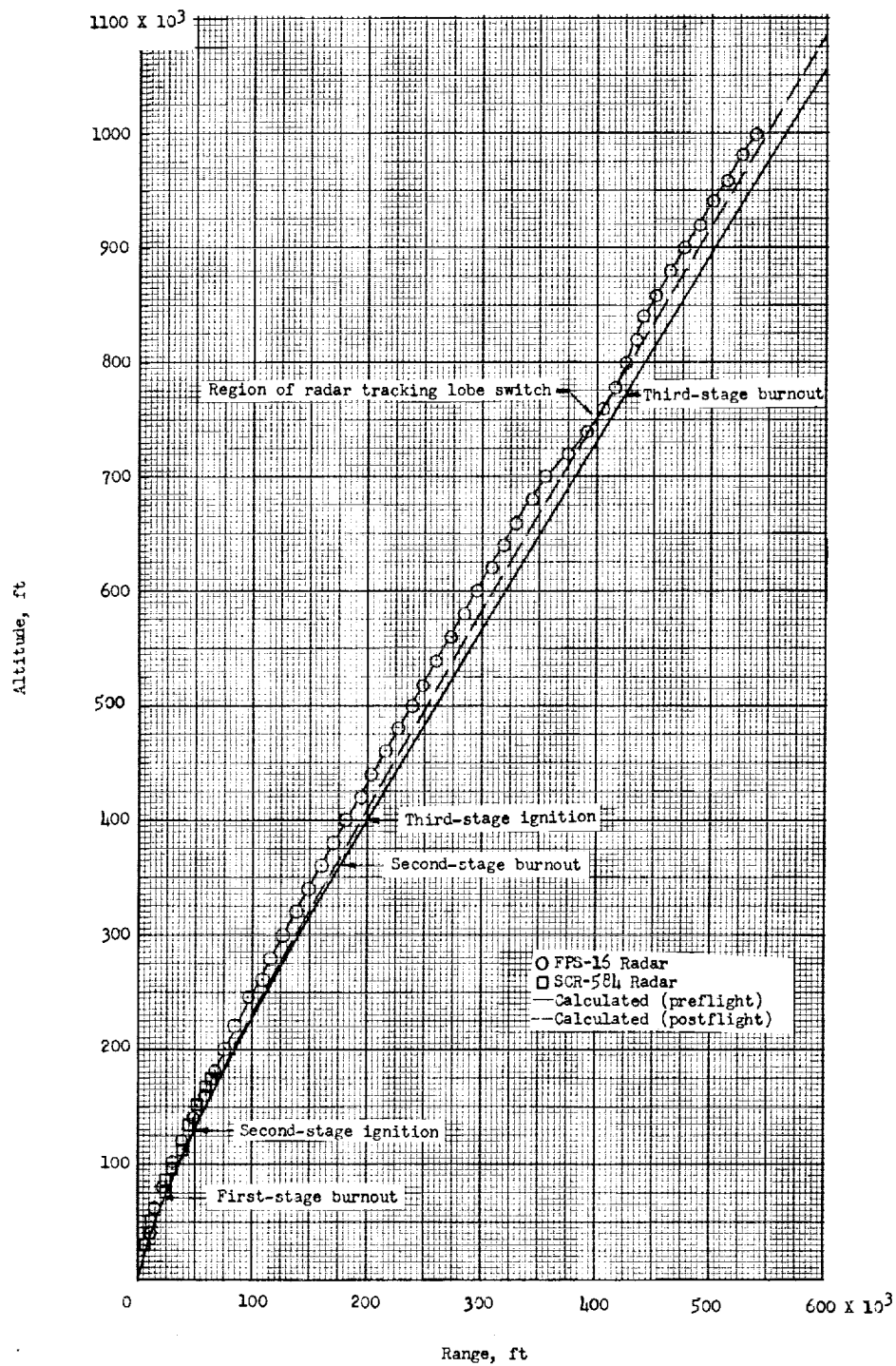
Figure 57.- Variation of altitude with range through third-stage burnout. Calculated and measured data.
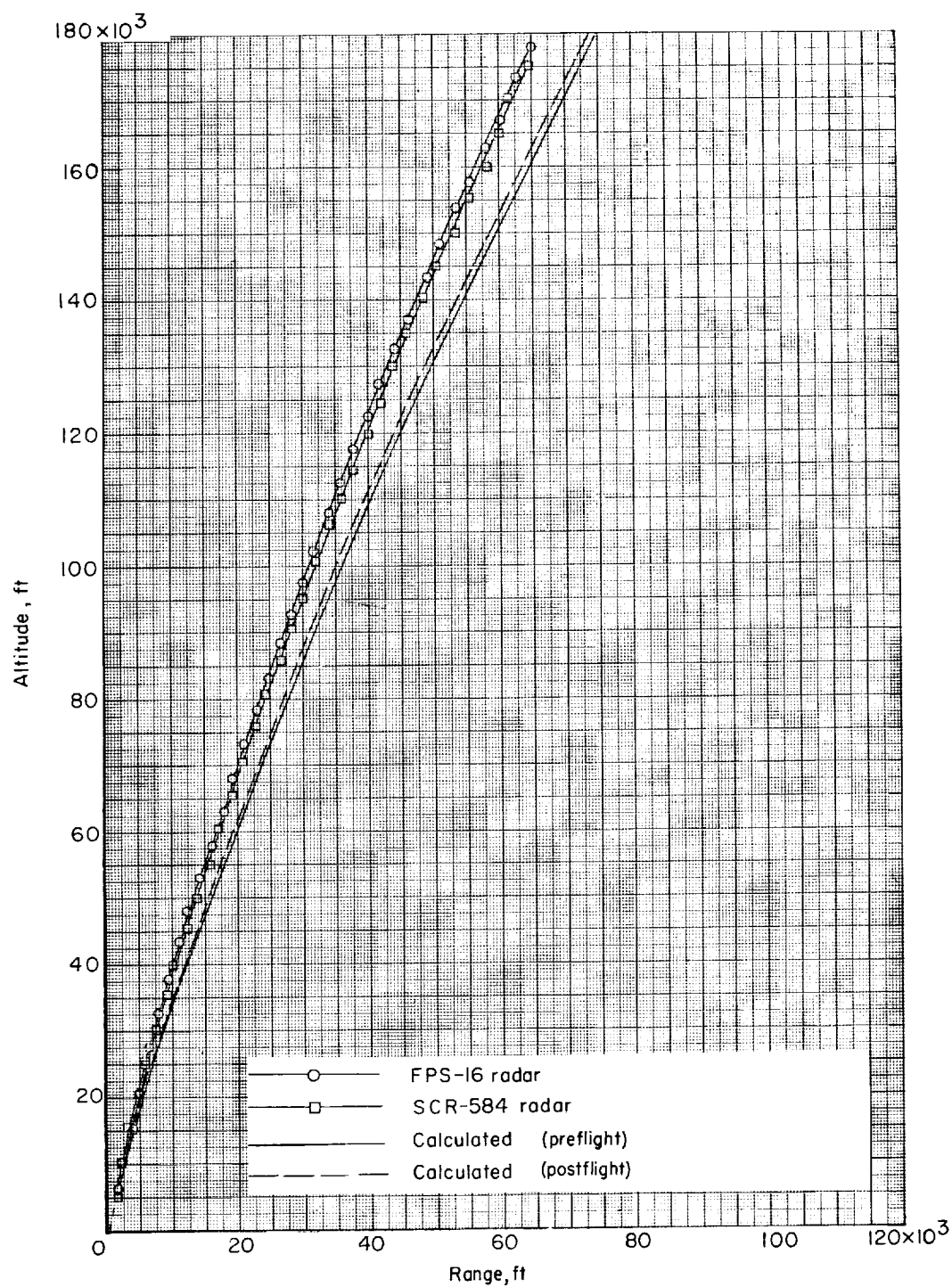
Figure 58.- Variation of altitude with range through first-stage burning phase. Calculated and measured data.
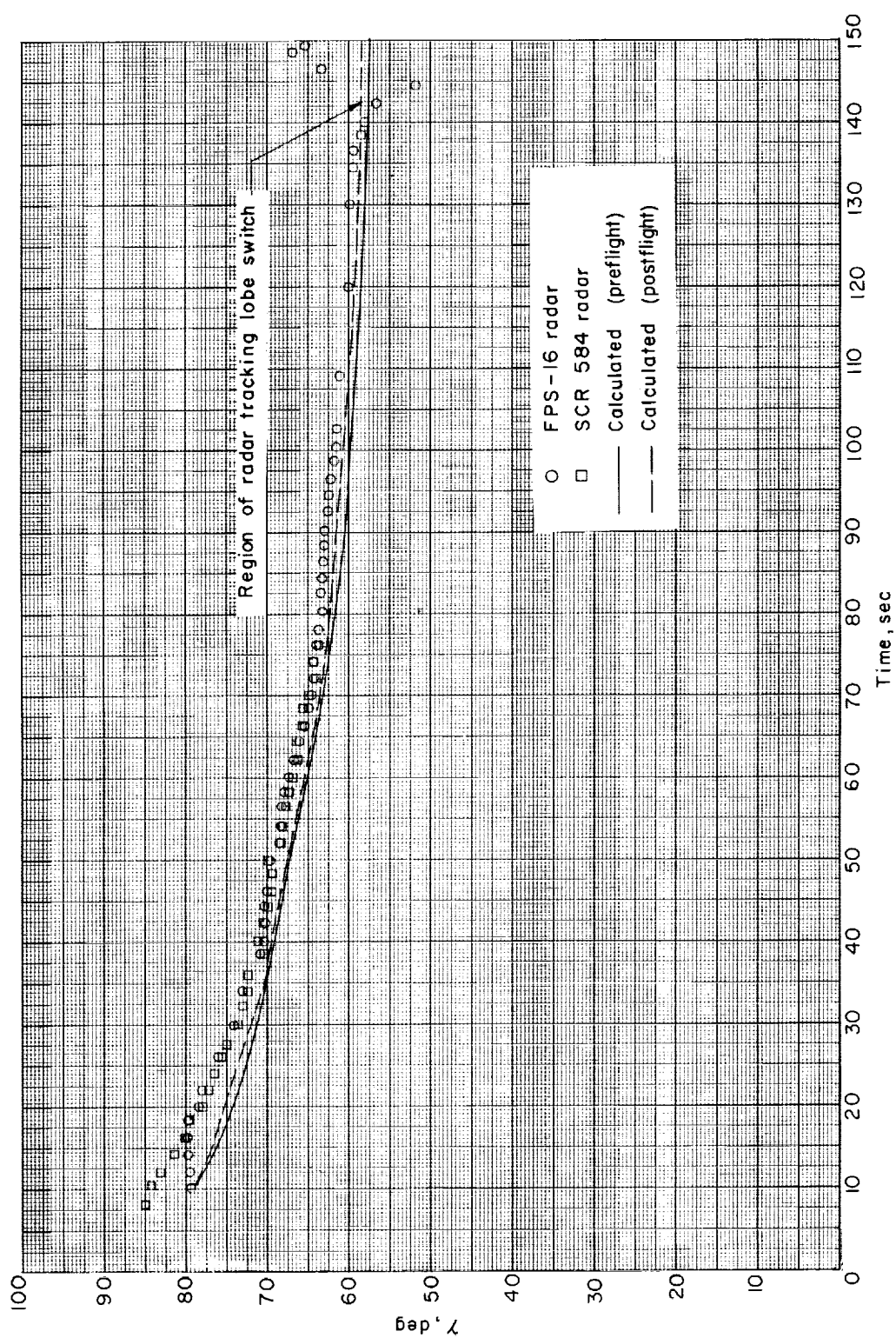
Figure 59.- Variation of flight-path angle with time. Measured and calculated data.
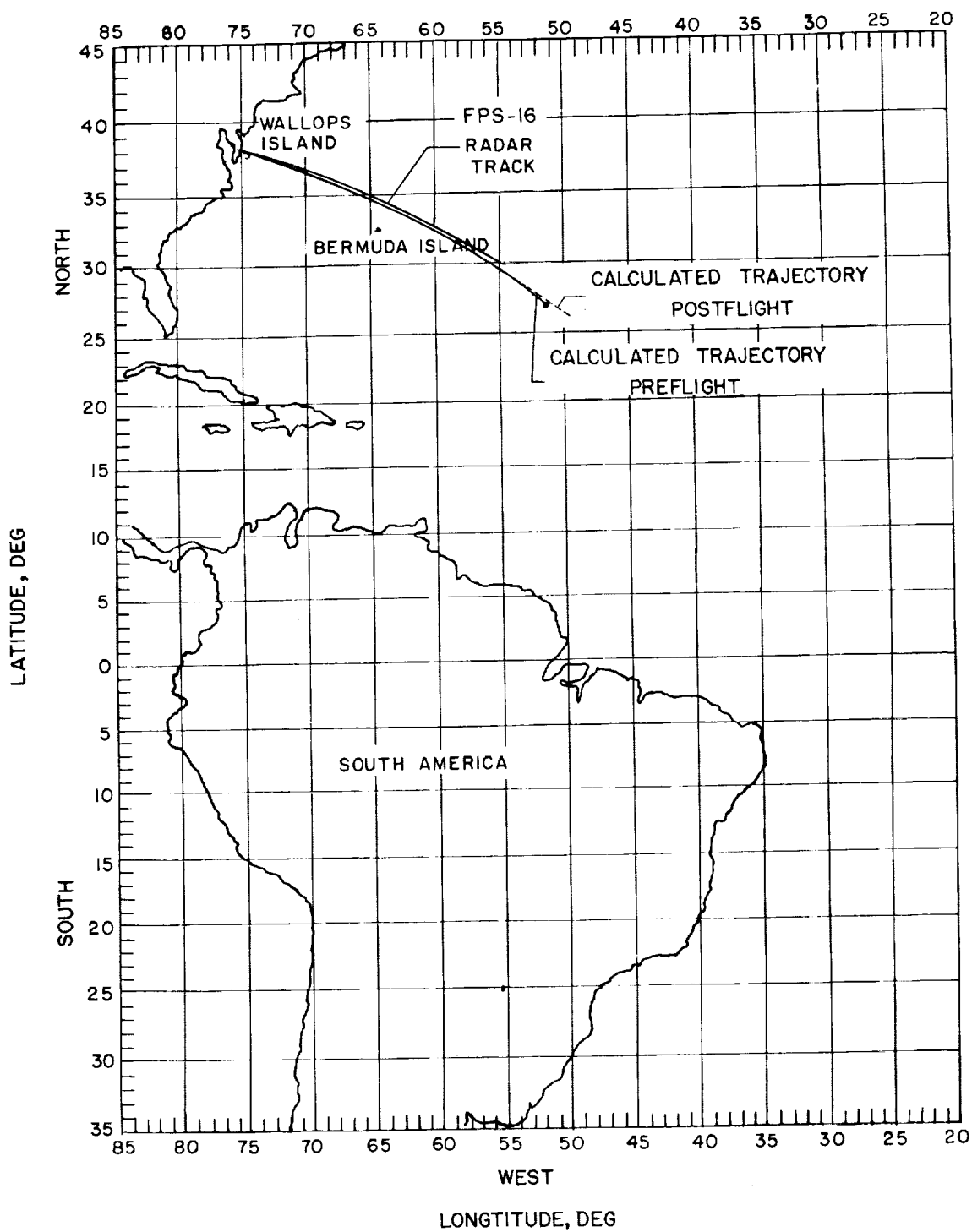
Figure 60.- Measured and calculated ground tracks to splash.
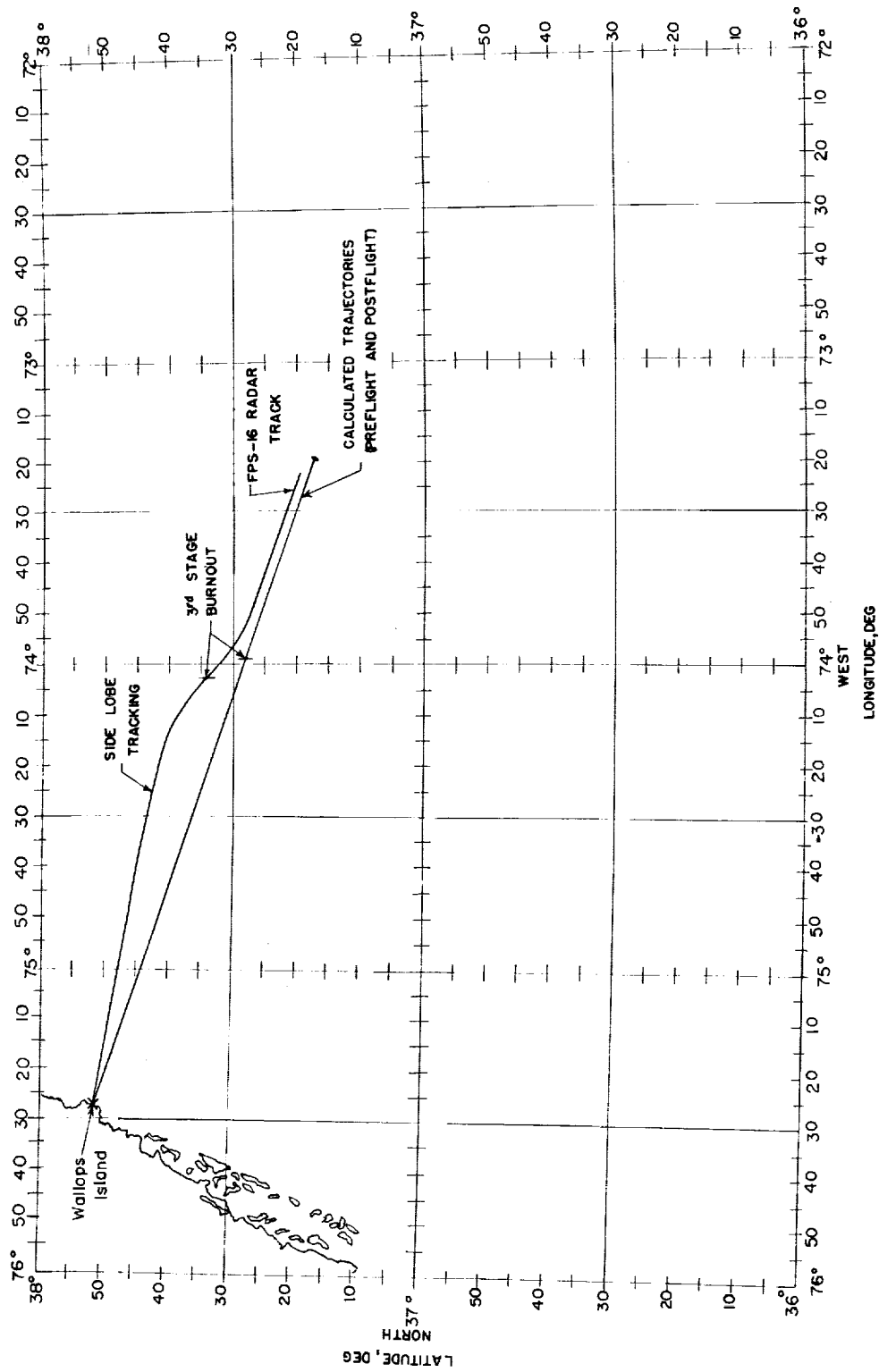
Figure 61.- Measured and calculated ground tracks through third-stage burning.
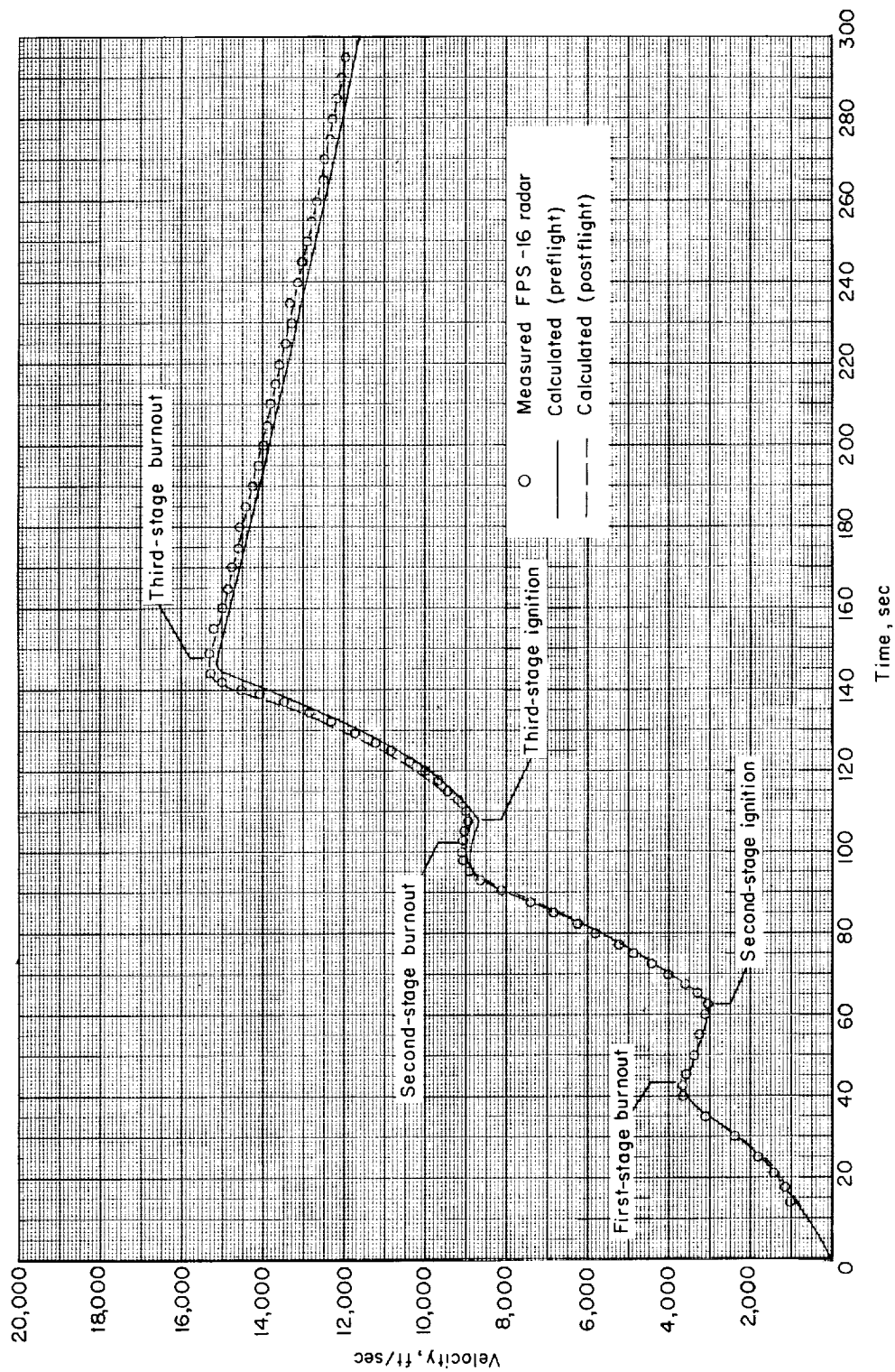
L-1924

L-1924

Figure 62.- Variation of velocity with time through third-stage burnout.
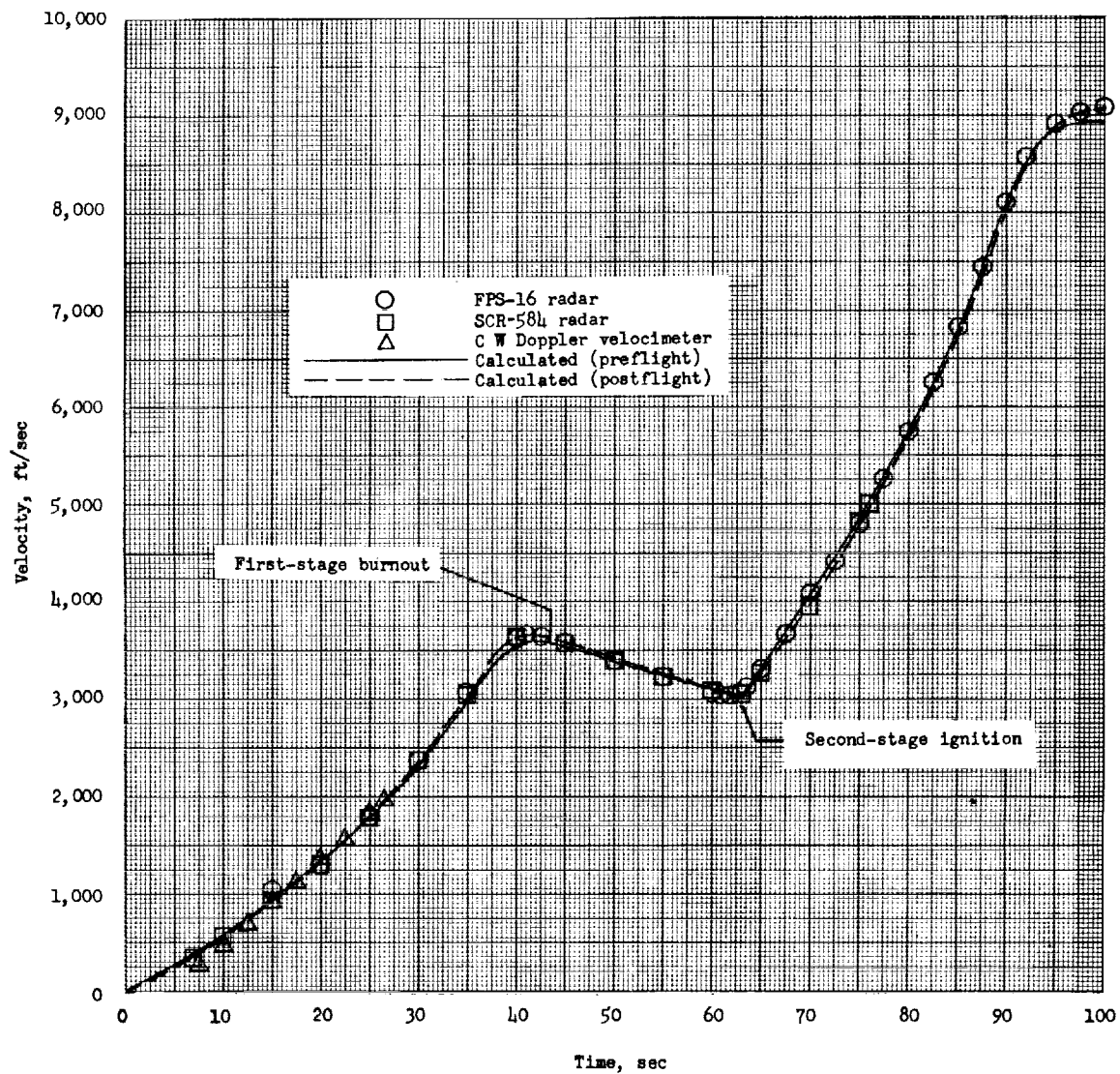
Figure 63.- Variation of velocity with time through second-stage ignition.
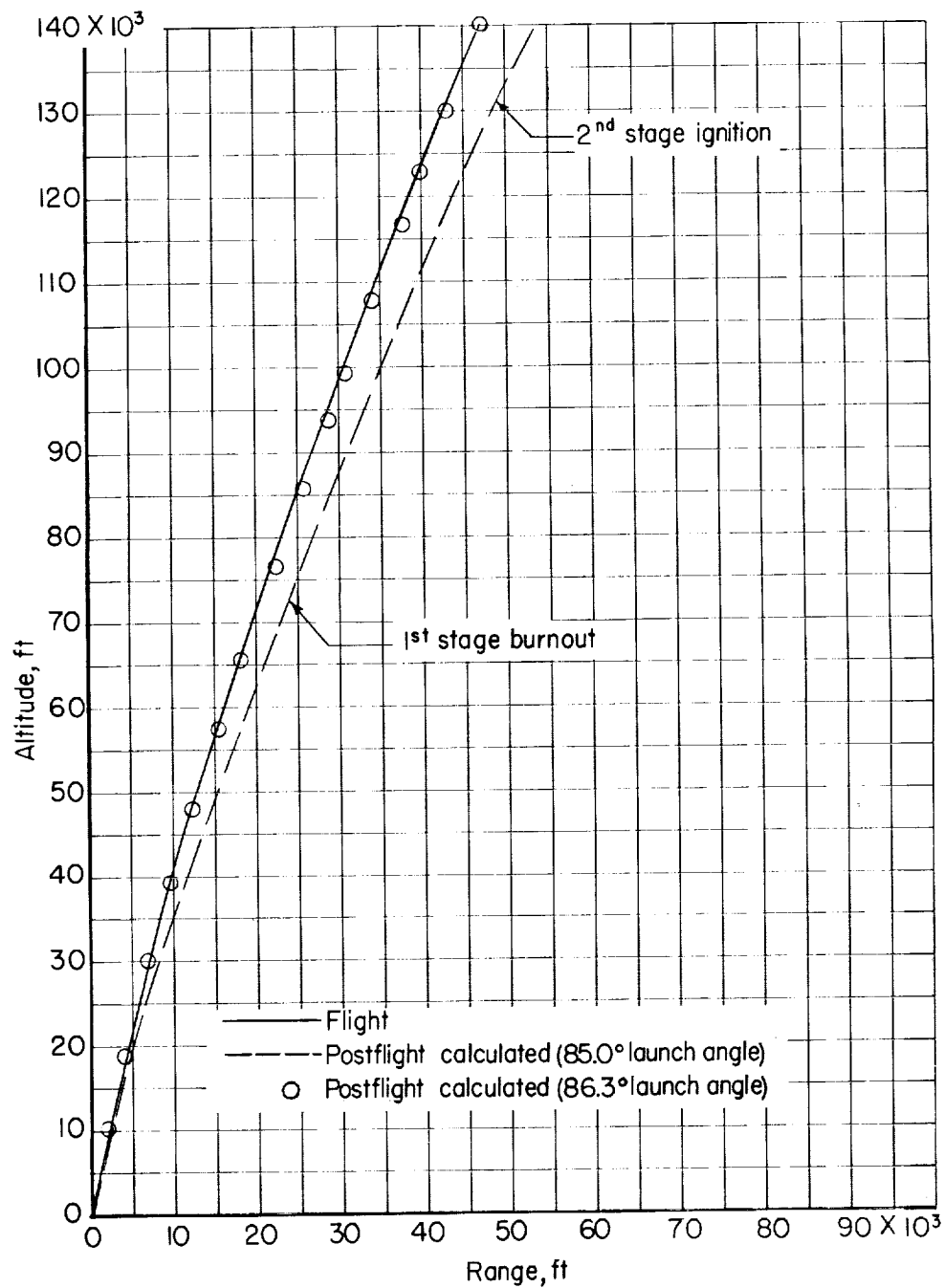
(a) Launch through second-stage ignition.

Figure 64.- Flight and postflight calculated results for variation of altitude with range.
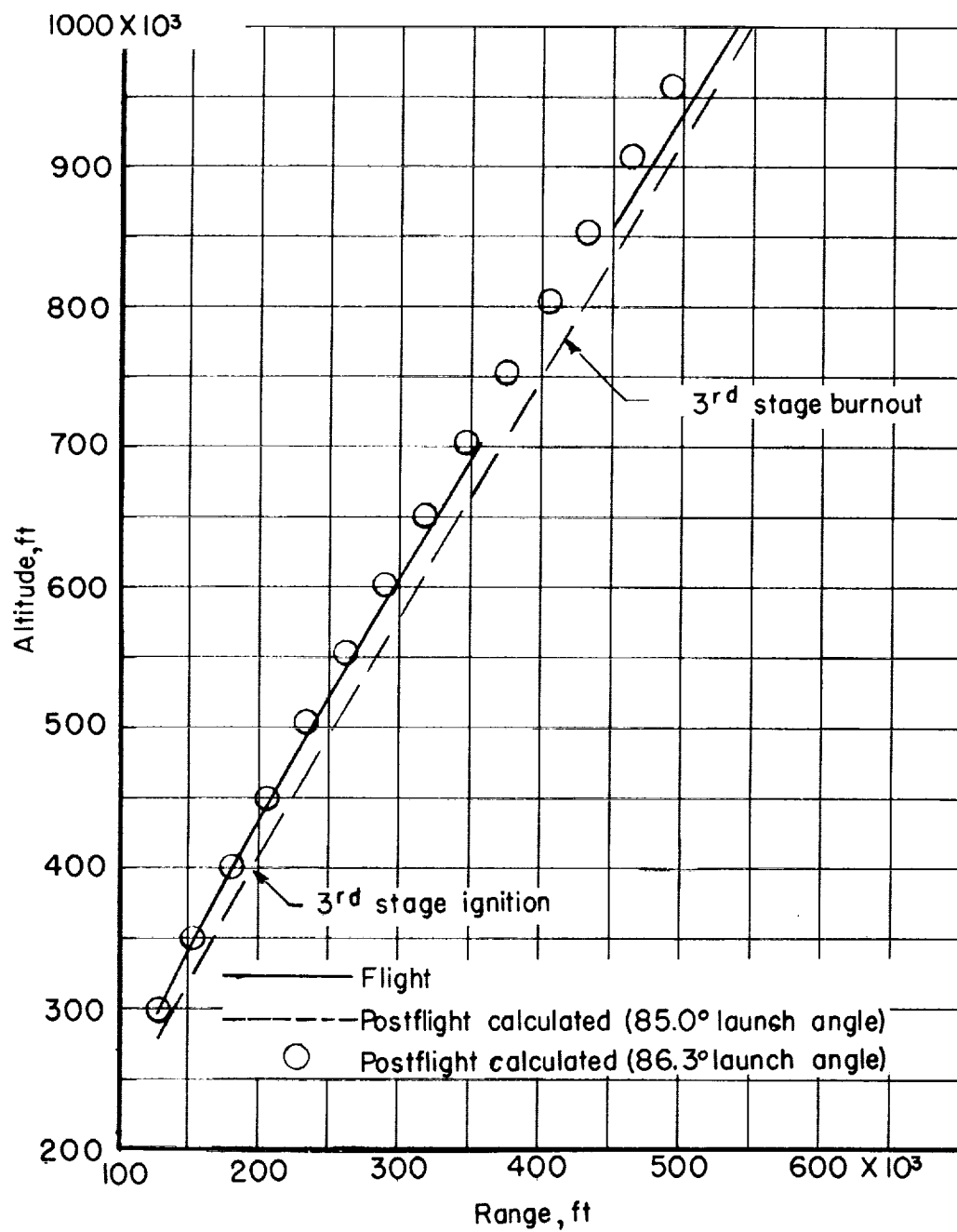
(b) Third-stage ignition to burnout.

Figure 64.- Concluded.

L-1924

Flight

Postflight calculated (85.0° launch angle)

Postflight calculated (86.3° launch angle)

o

Time, sec

γ, deg

Time, sec

Pitch deflection, deg

T.E. down   T.E. up
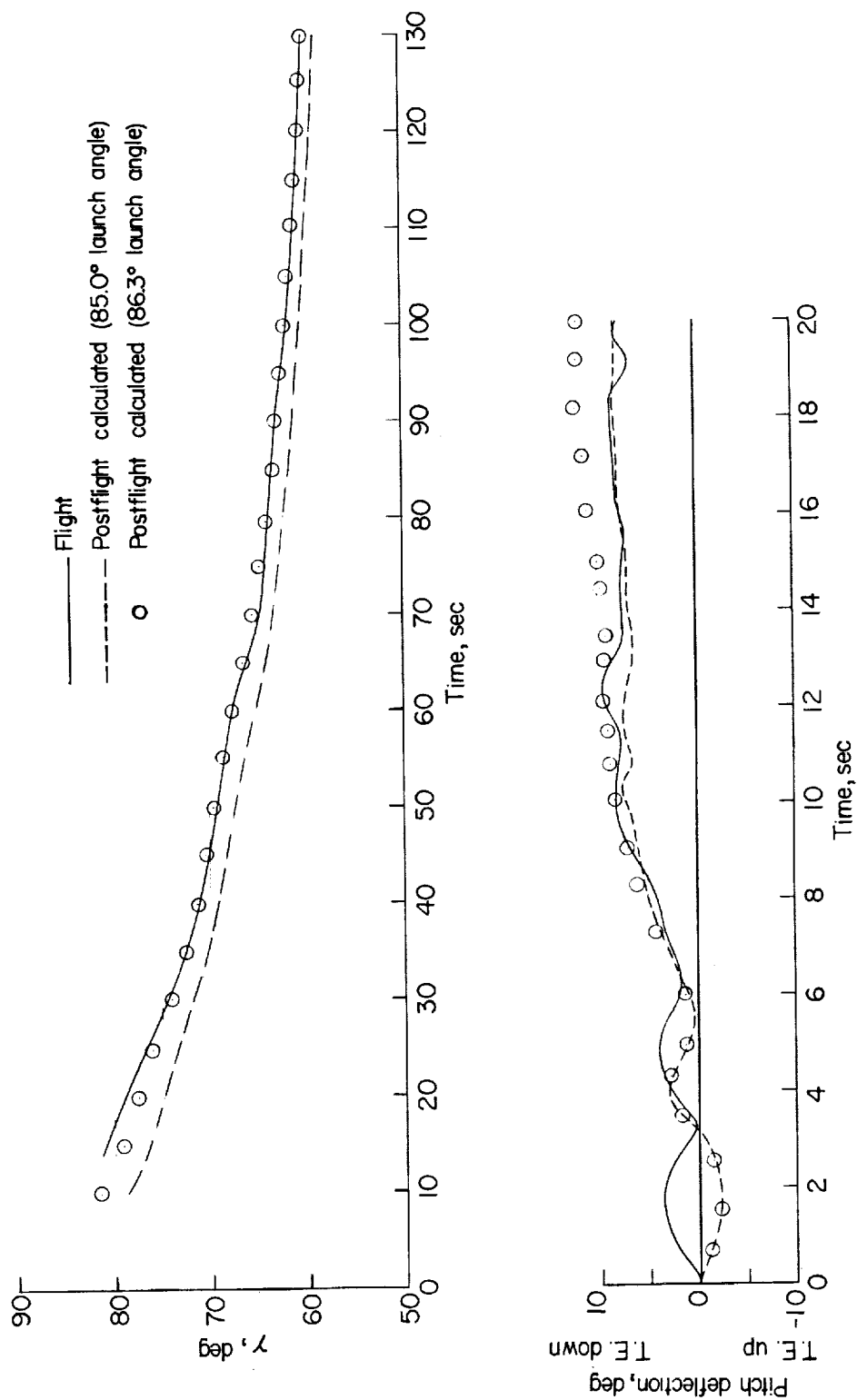
Figure 65.- Flight and calculated results for variations of flight-path angle and pitch control deflection with time.

L-1924
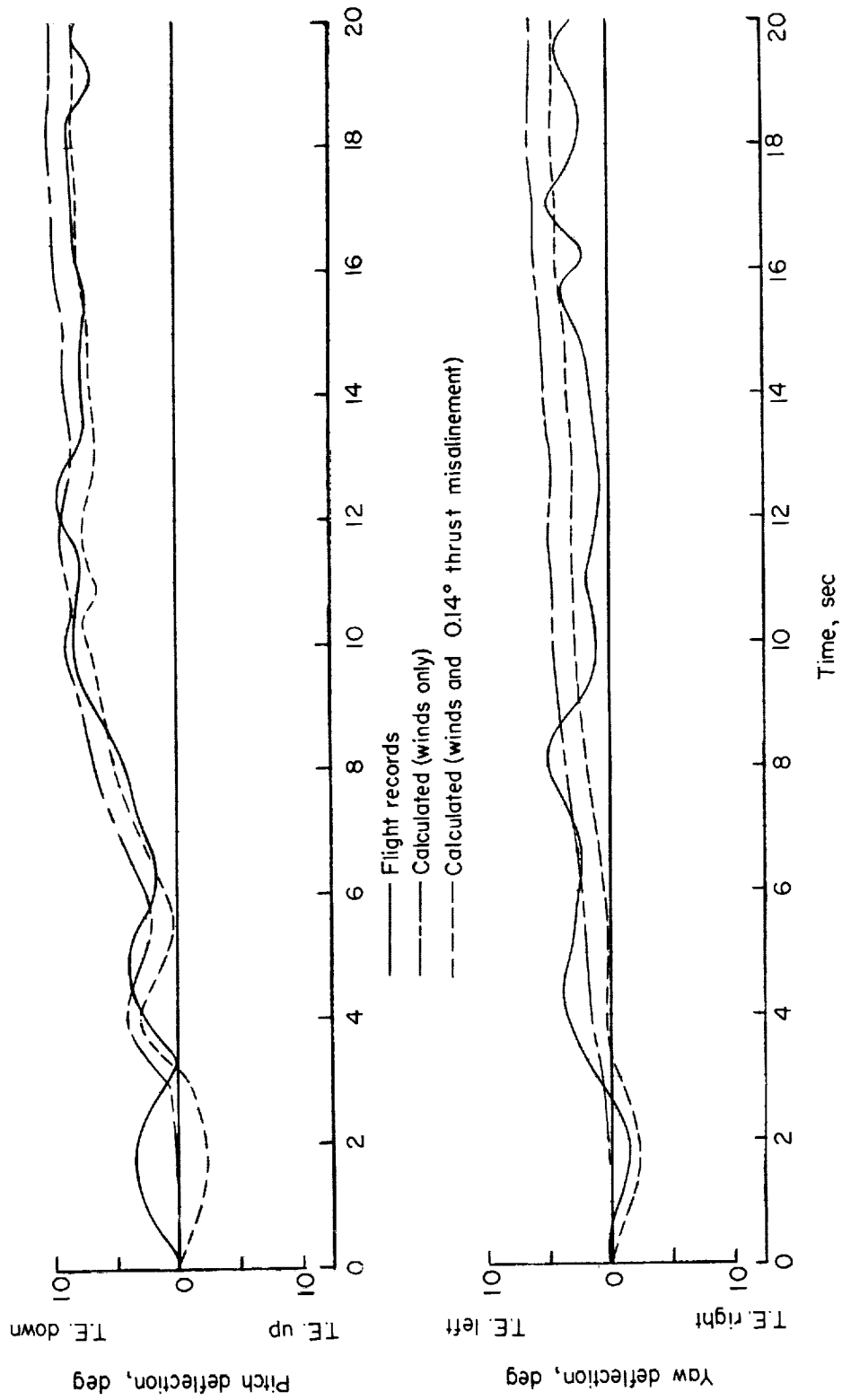
Figure 66.- Time histories of pitch and yaw control-surface deflections for first 20 seconds of flight.

L-1924
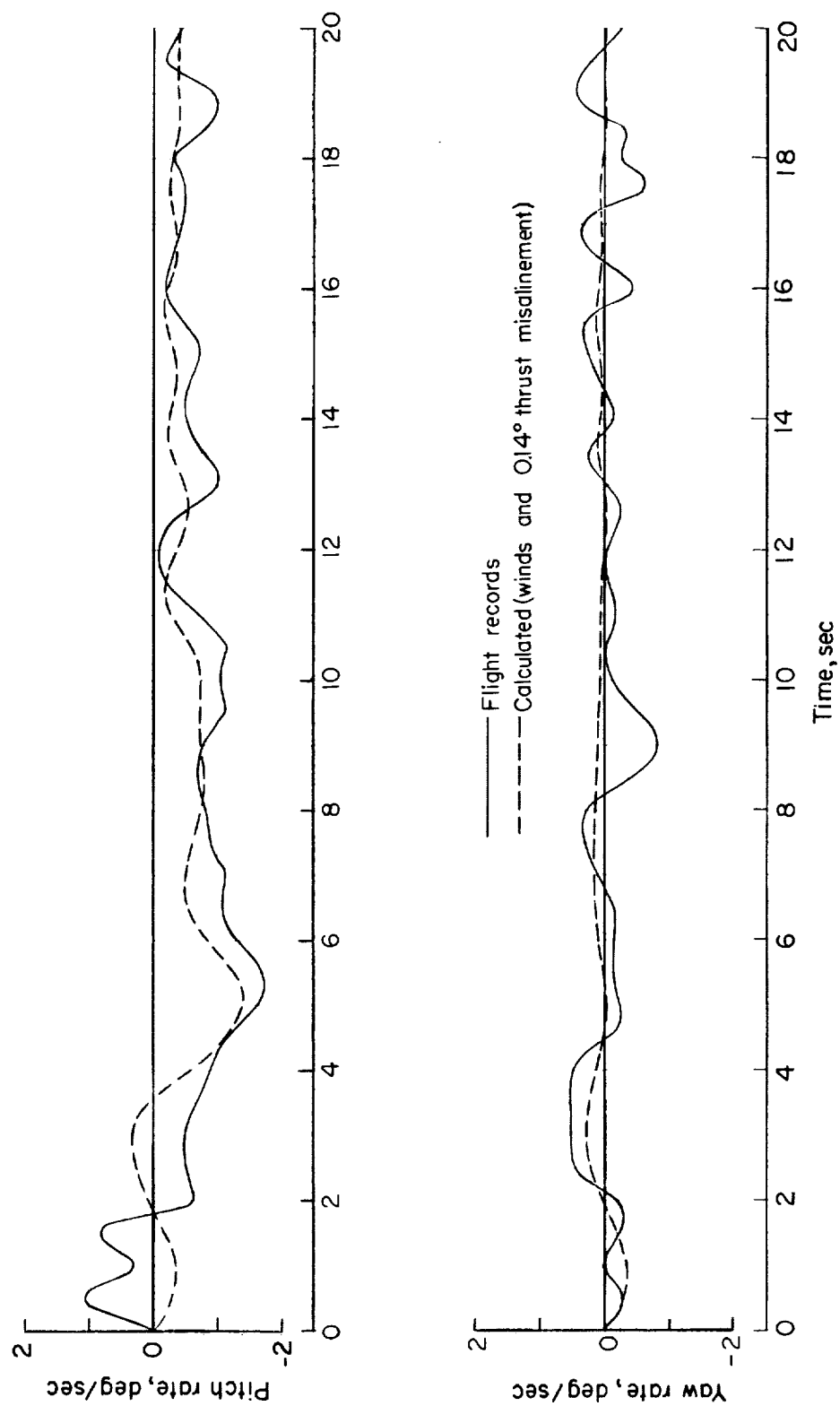
Figure 67.- Time histories of pitch and yaw rates for first 20 seconds of flight.
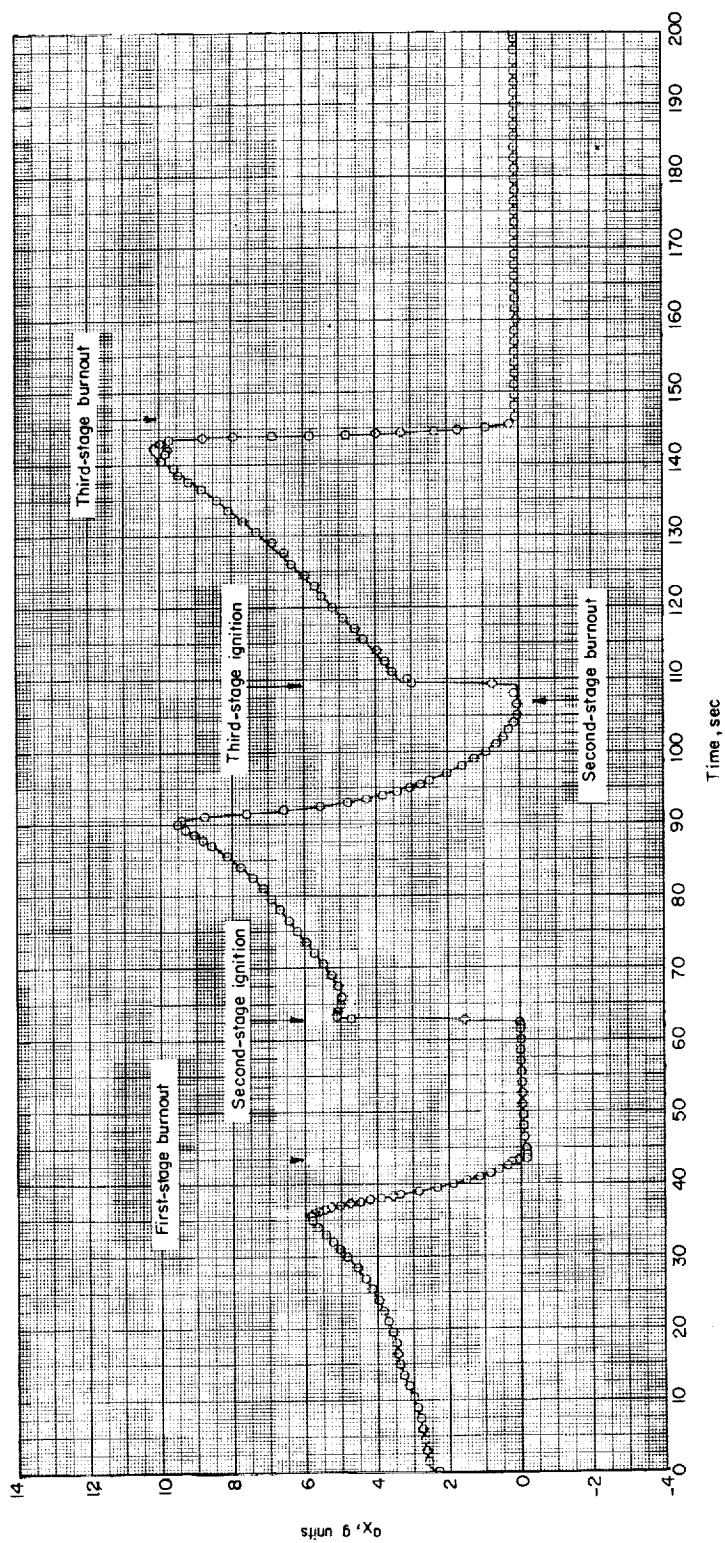
Figure 68.- Time history of payload longitudinal acceleration through third-stage burnout.

L-1924
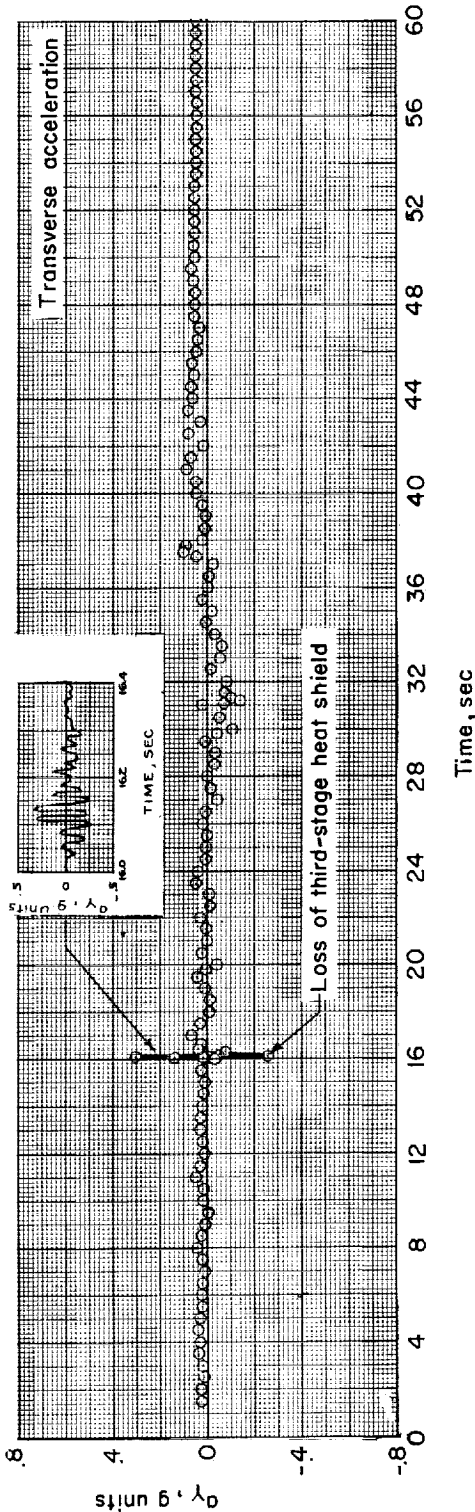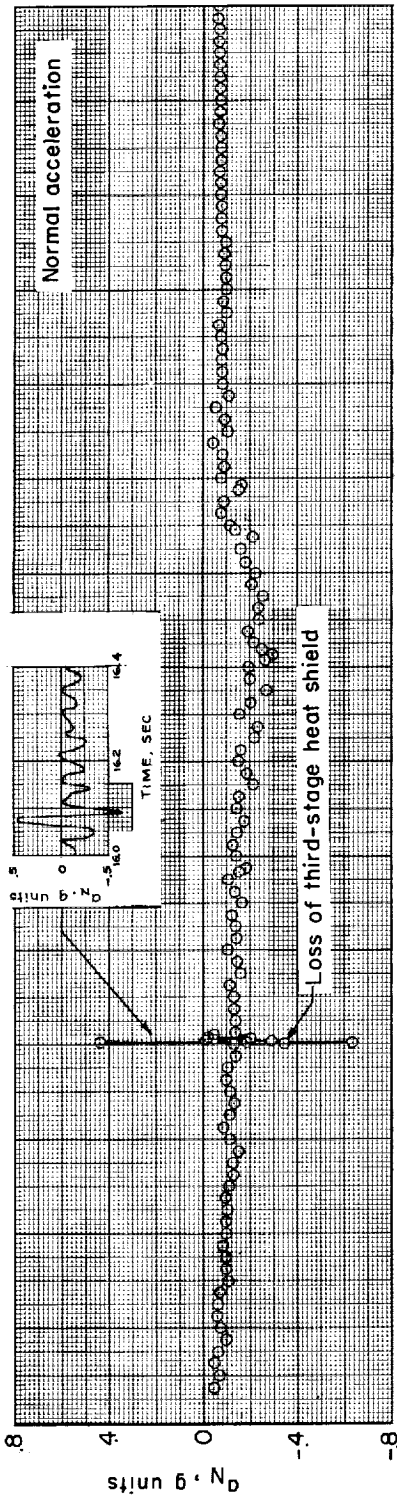
Figure 69.- Time histories of normal and transverse accelerations in base section A.
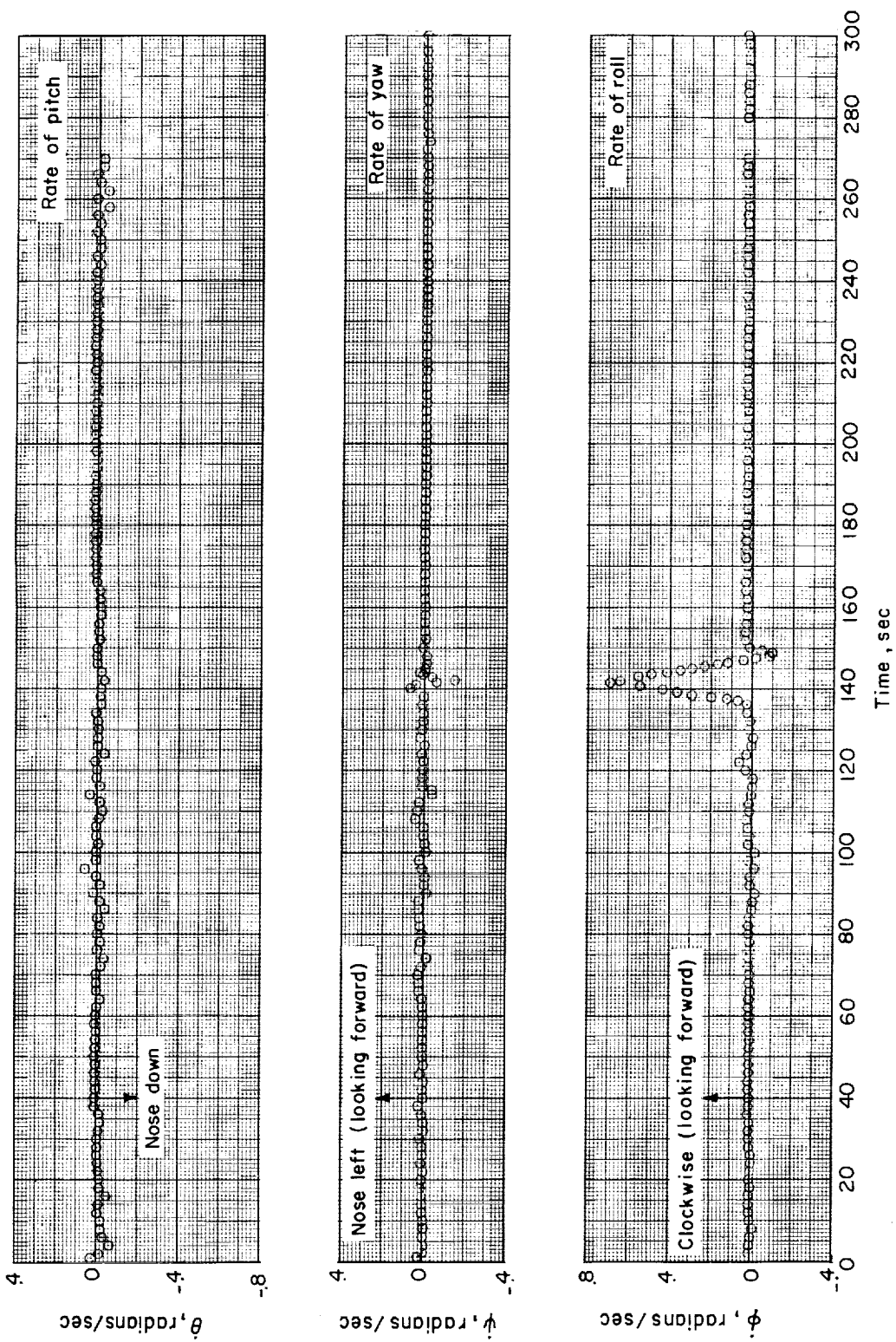
Figure 70.- Time histories of payload angular velocities in pitch, yaw, and roll.

L-1924
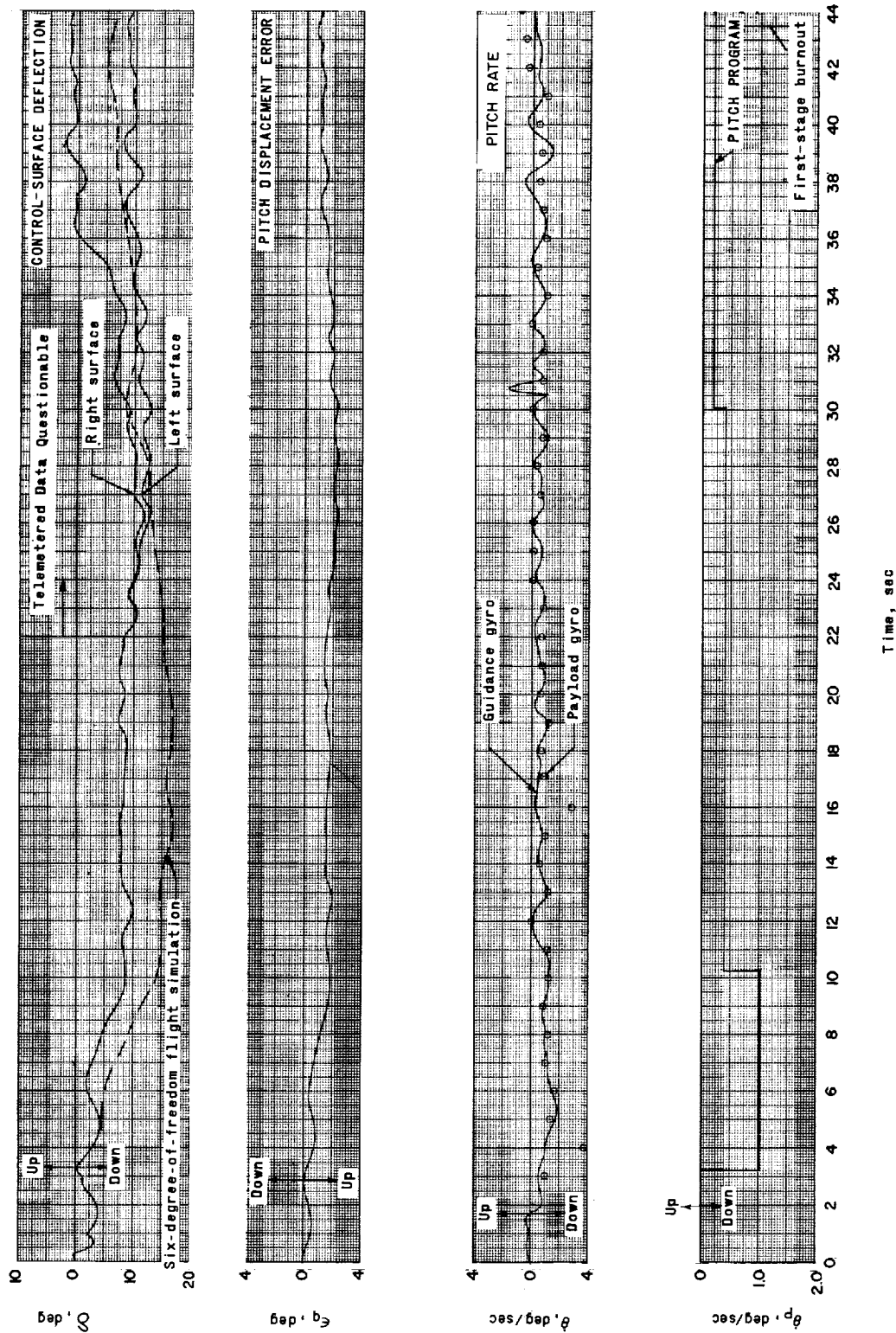
(a) Pitch.

Figure 71.- Time histories of guidance- and control-system performance during first-stage burning.

Time, sec
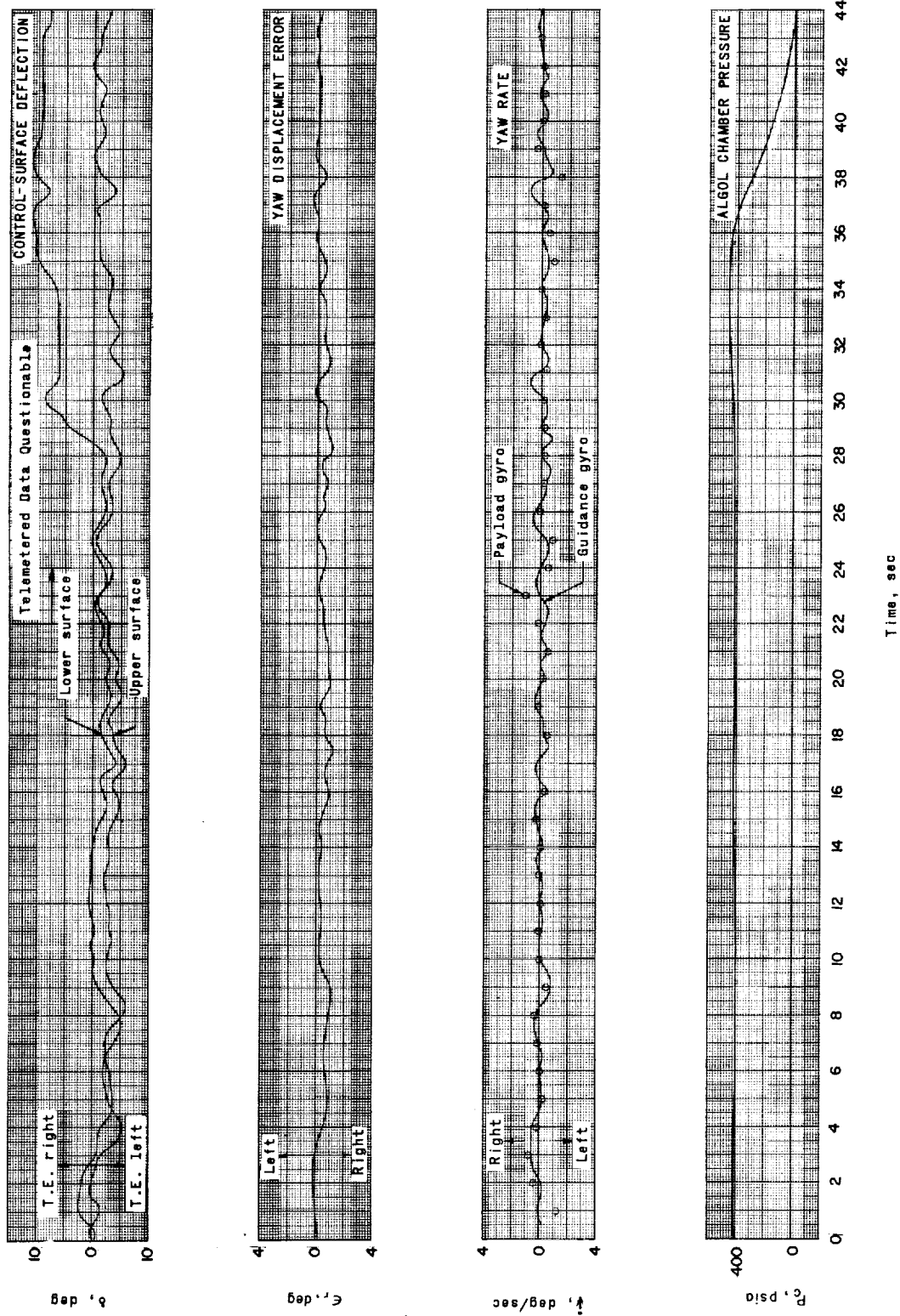
(b) Yaw.

Figure 71.- Continued.

L-1924

L-1924

Time, sec
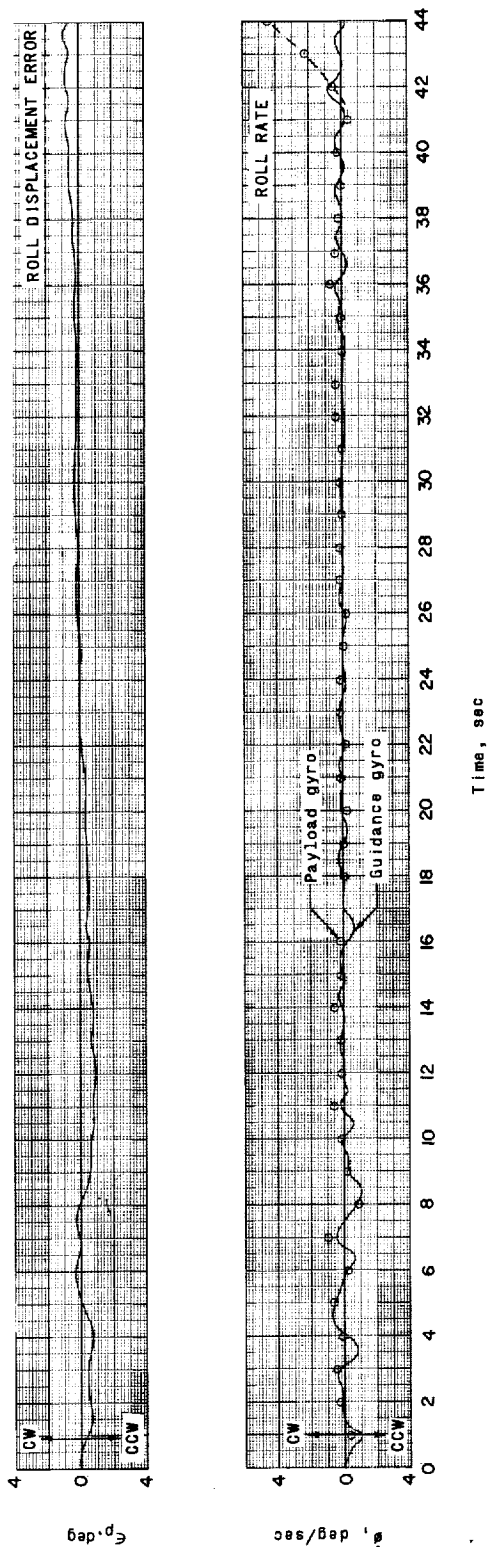
(c) Roll.

Figure 71.- Concluded.
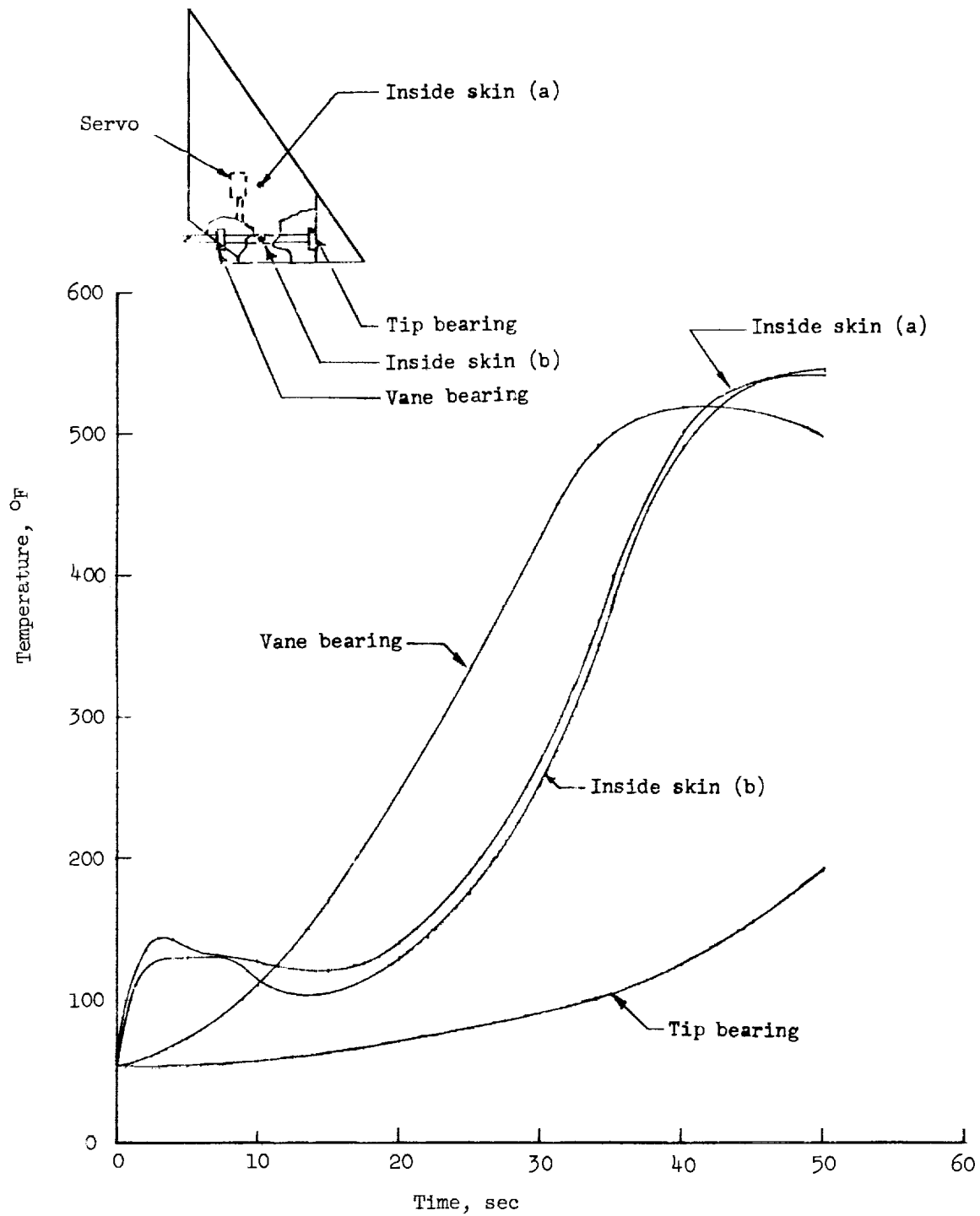
Figure 72.- Time histories of flight environment temperatures measured in vicinity of a vane on base section A.

L-1924
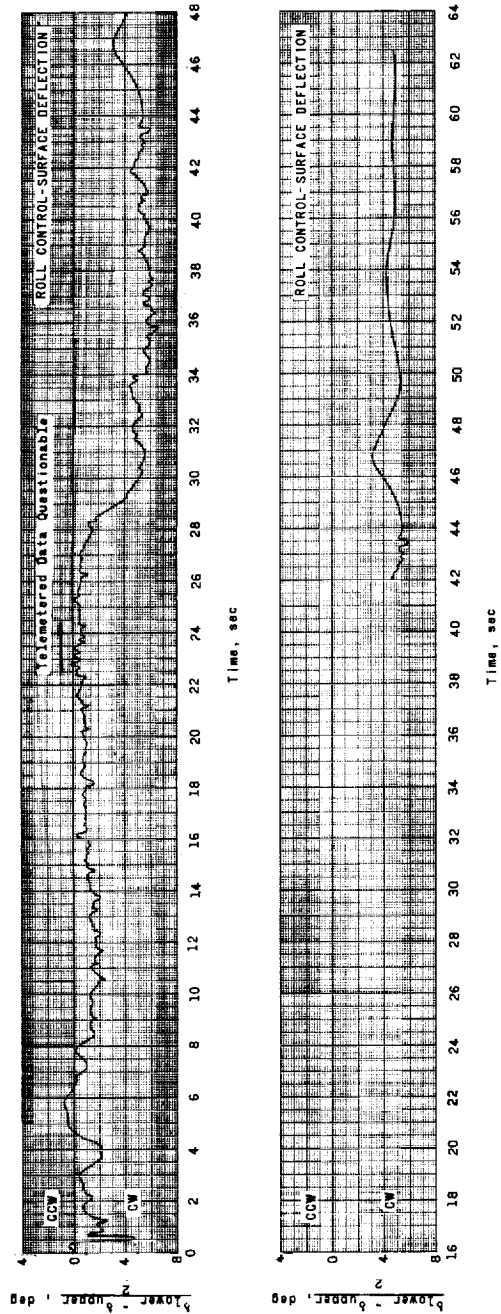
(a) Roll.
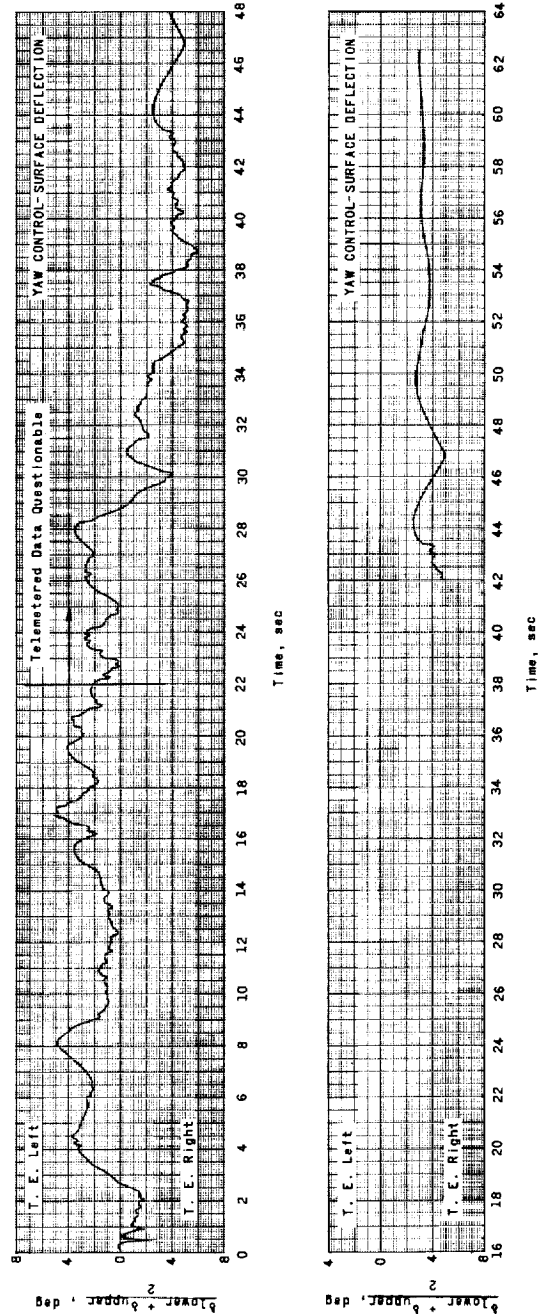
(b) Yaw.

Figure 73.- Time history of combined roll-yaw control-surface deflections reduced to show the contribution of the total deflection to yaw and roll control separately.
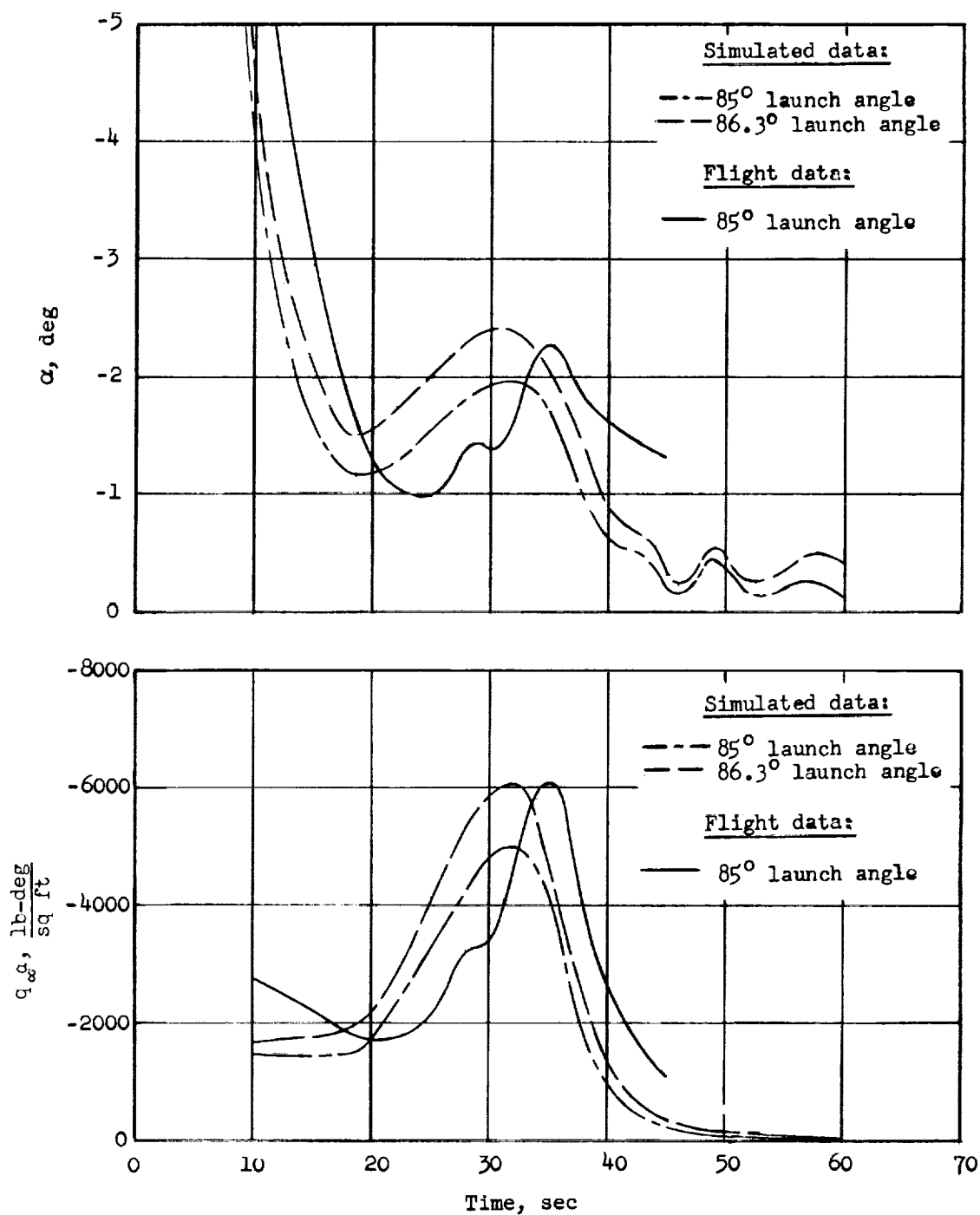
Figure 74.- Comparison of flight and simulated time histories of angle of attack and product of angle of attack and dynamic pressure during first-stage burning and coast.

L-1924

Time, sec
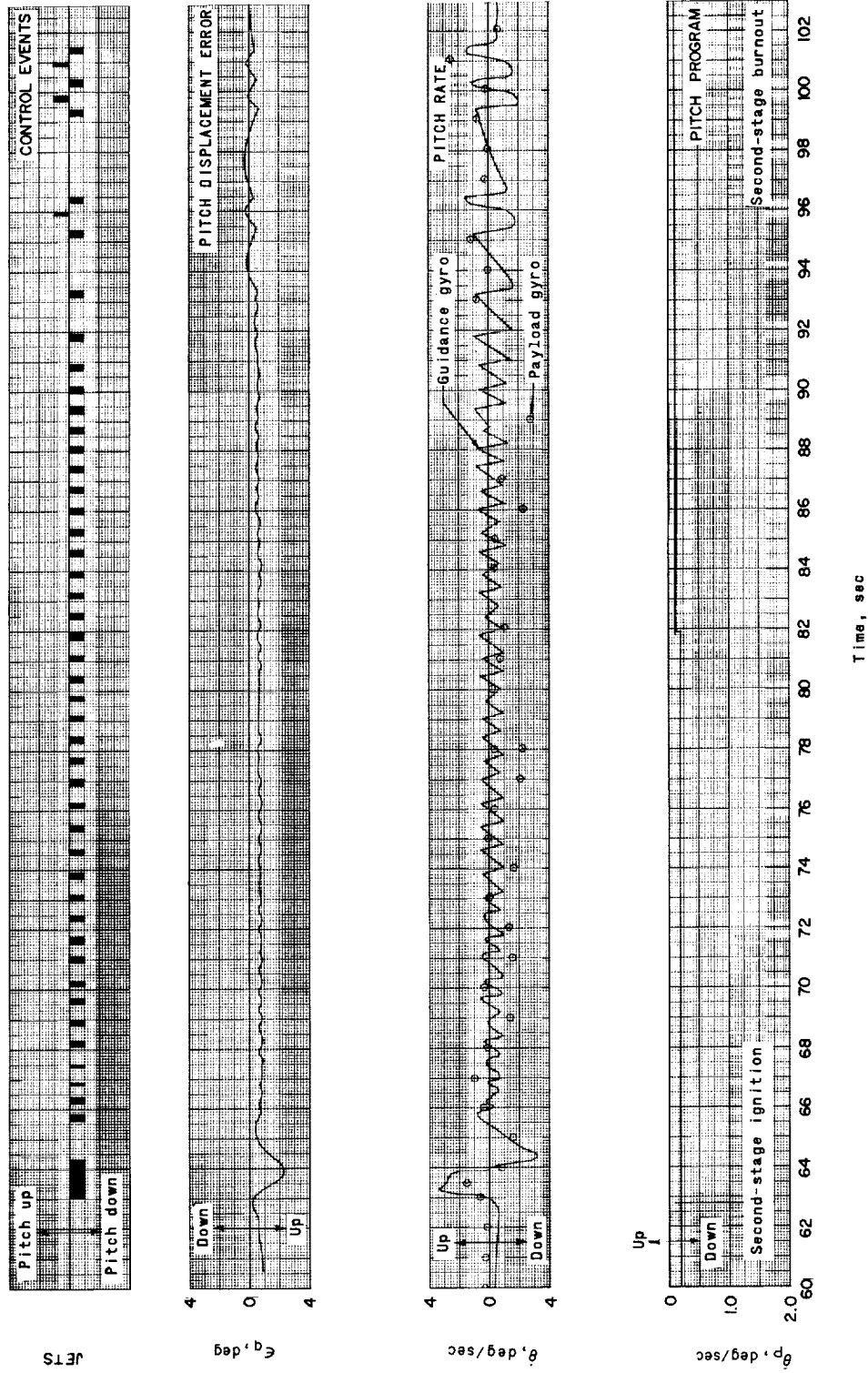
(a) Pitch.

Figure 75.- Time histories of guidance- and control-system performance during second-stage burning.
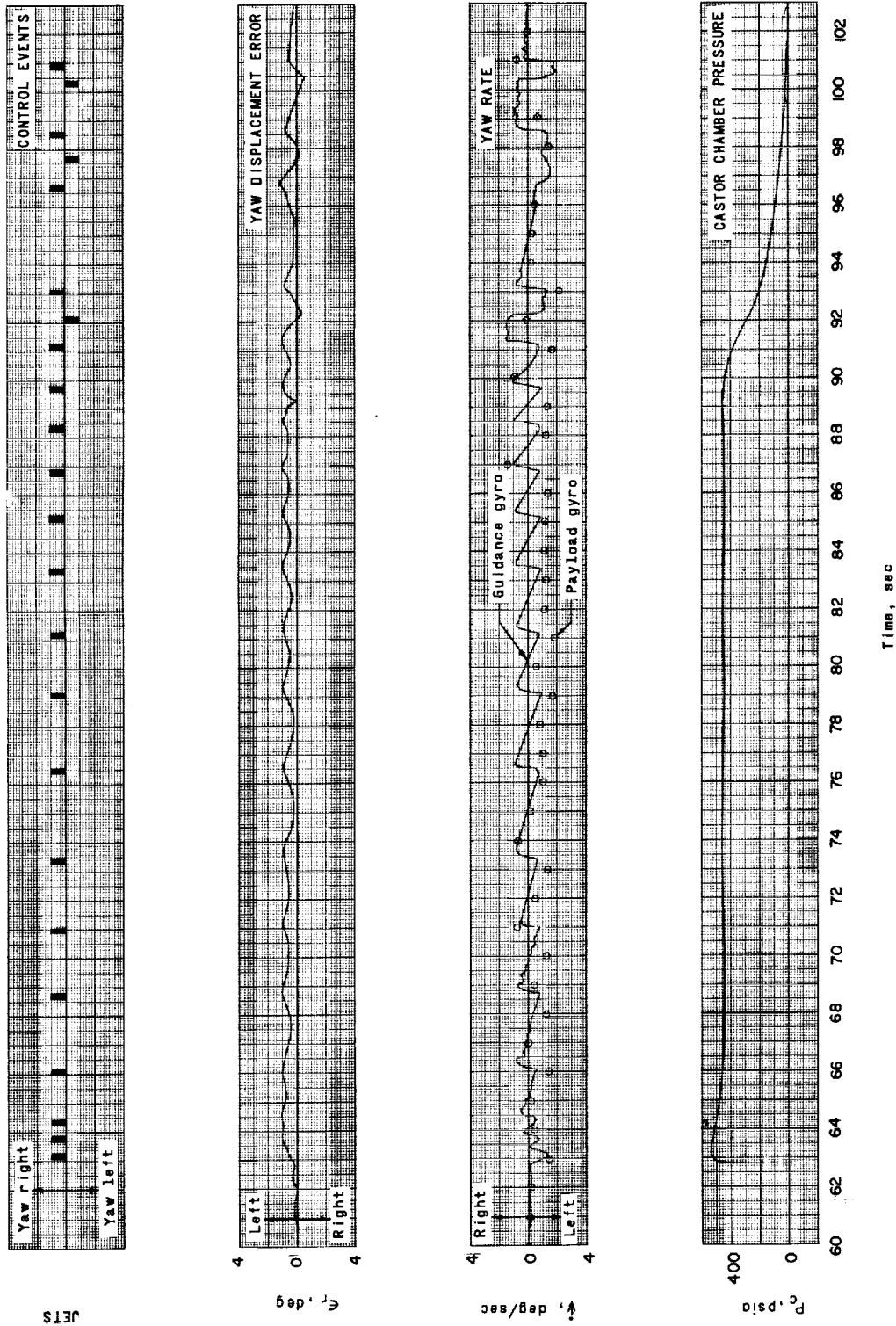
(b) Yaw.

Figure 75.- Continued.

L-1924

L-1924
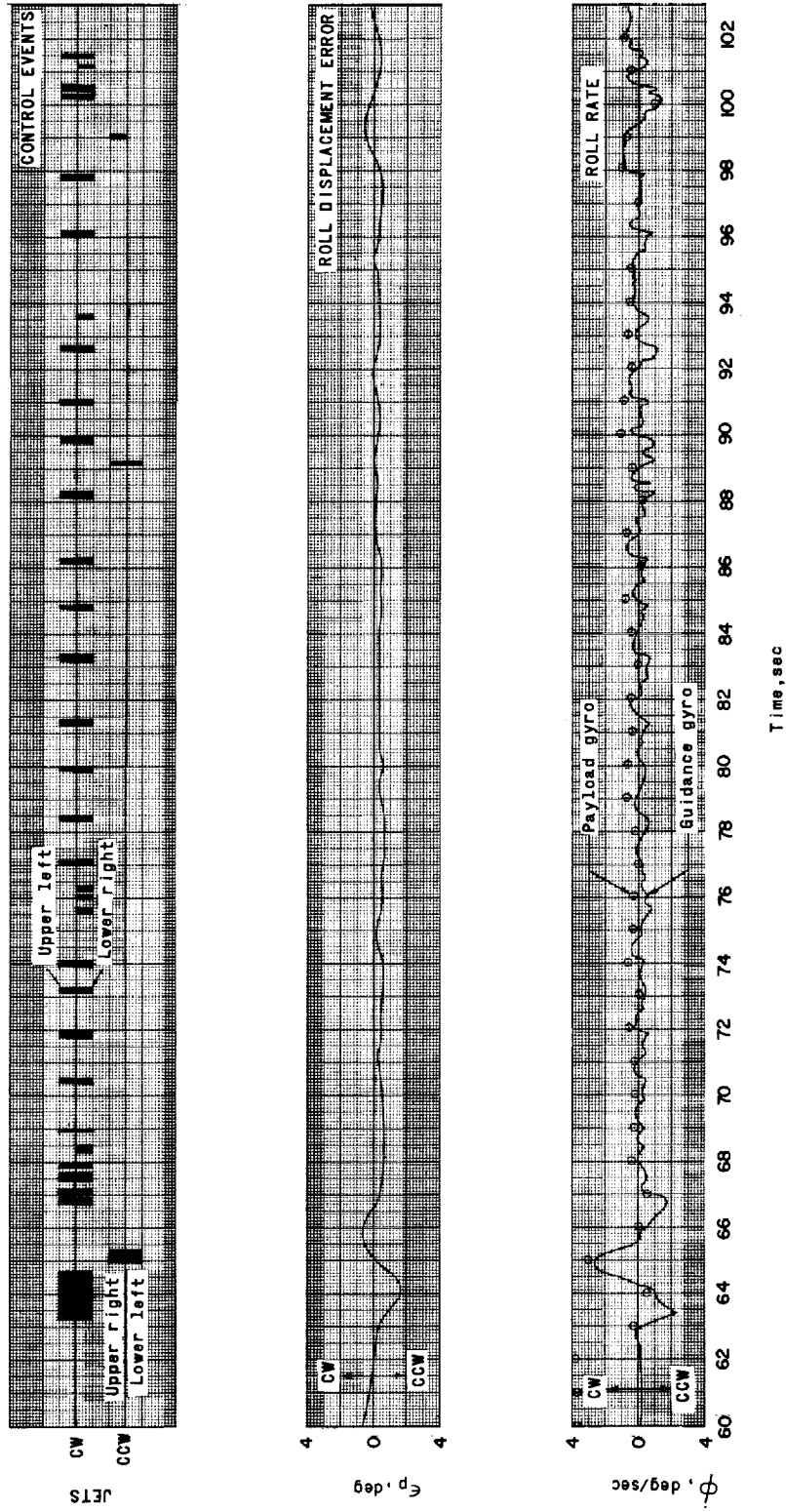
(c) Roll.

Figure 75.- Concluded.
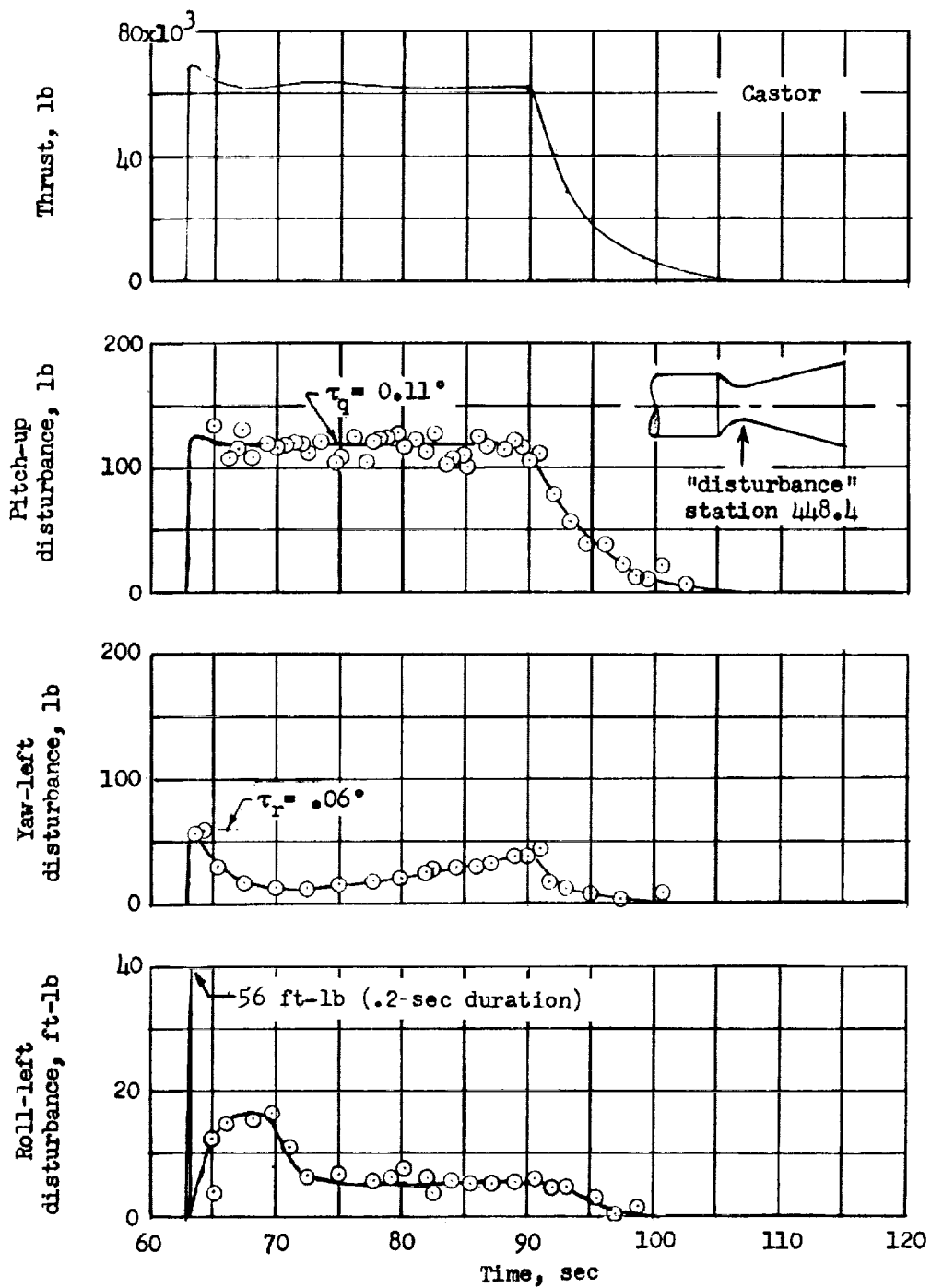
Figure 76.- Time histories of disturbing forces and moments derived from flight data obtained during second-stage thrusting.
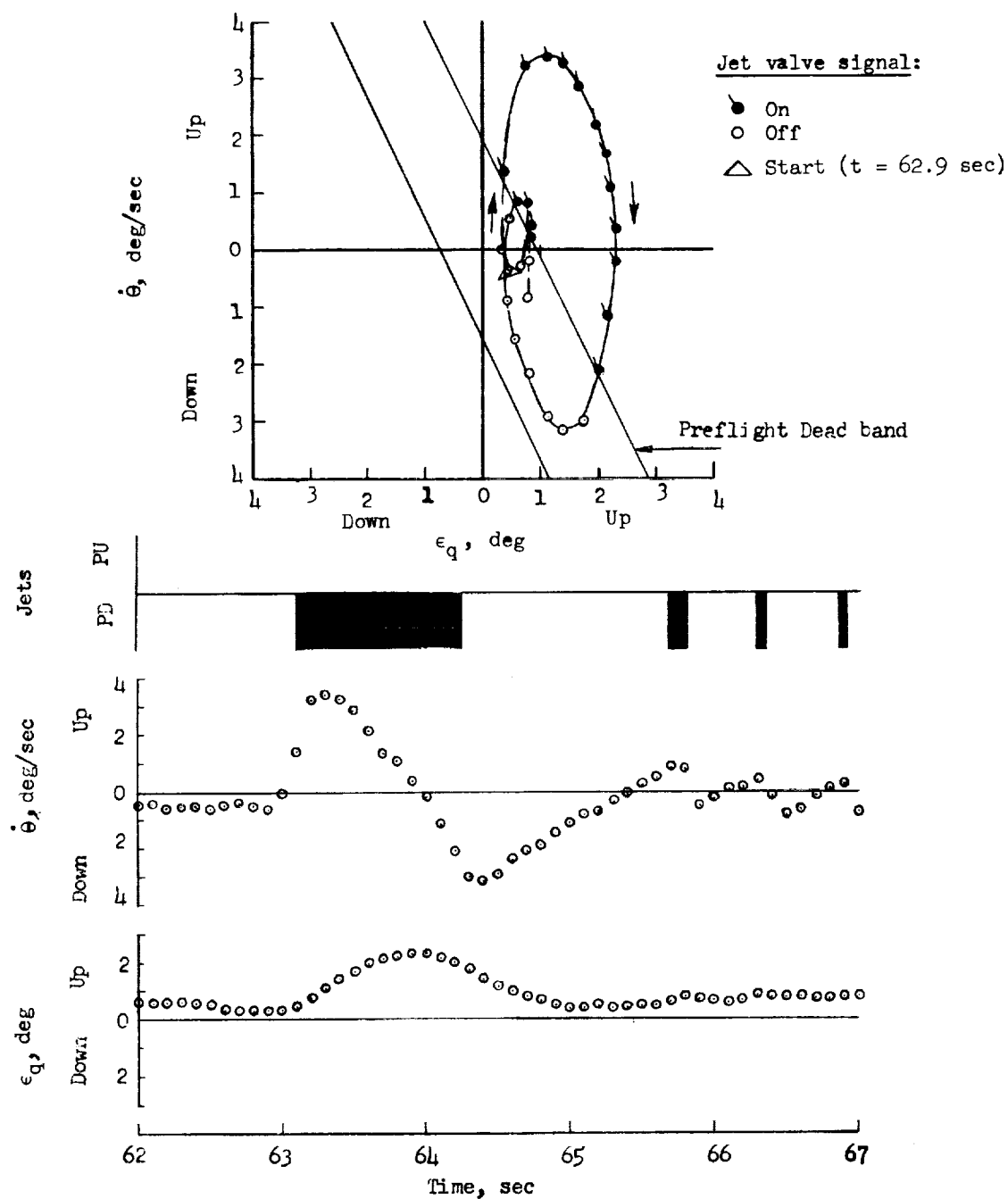
(a) Pitch.

Figure 77.- Phase-plane and time-history response of position errors and rates during second-stage ignition or capture maneuver.
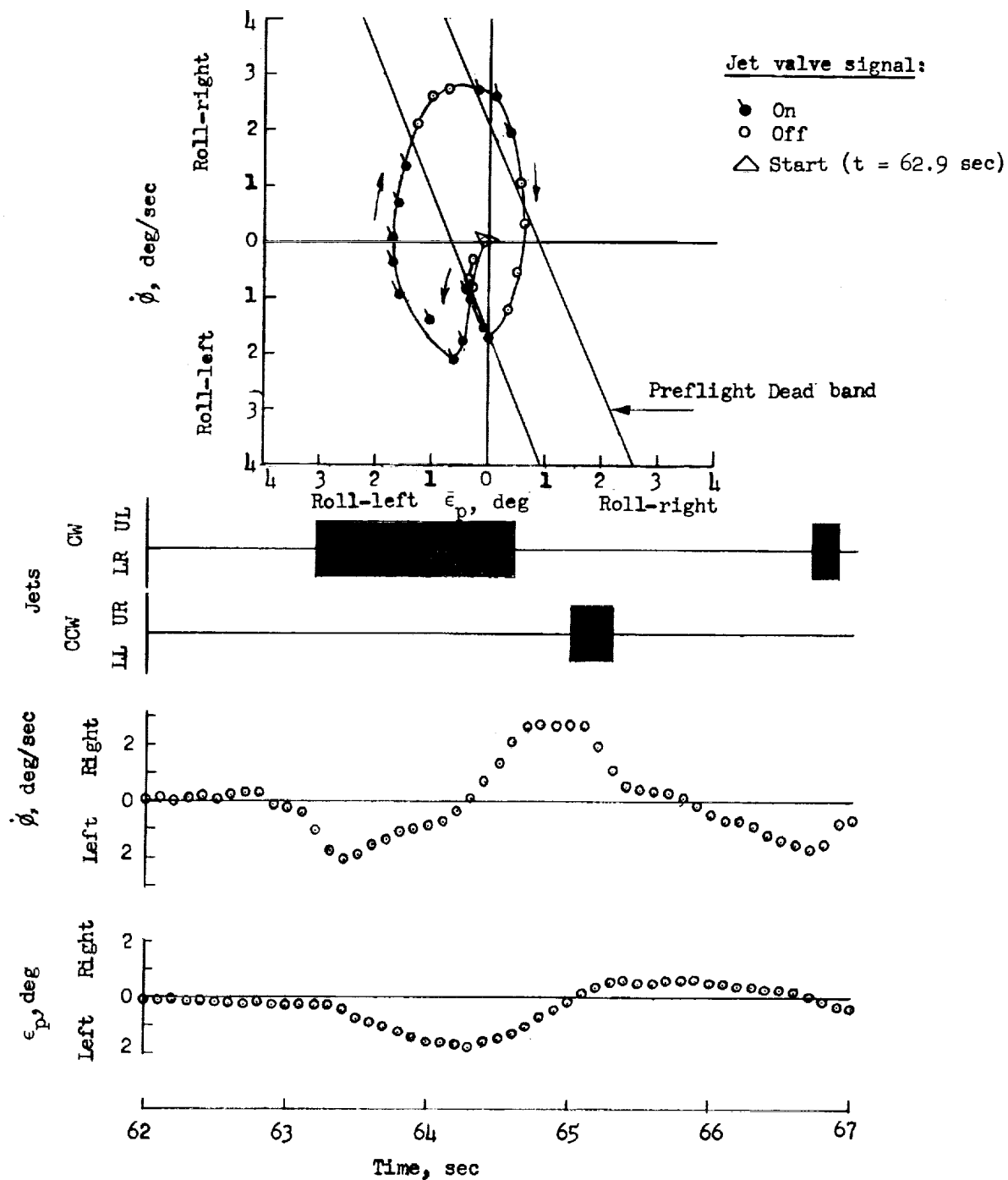
(b) Roll.

Figure 77.- Concluded.
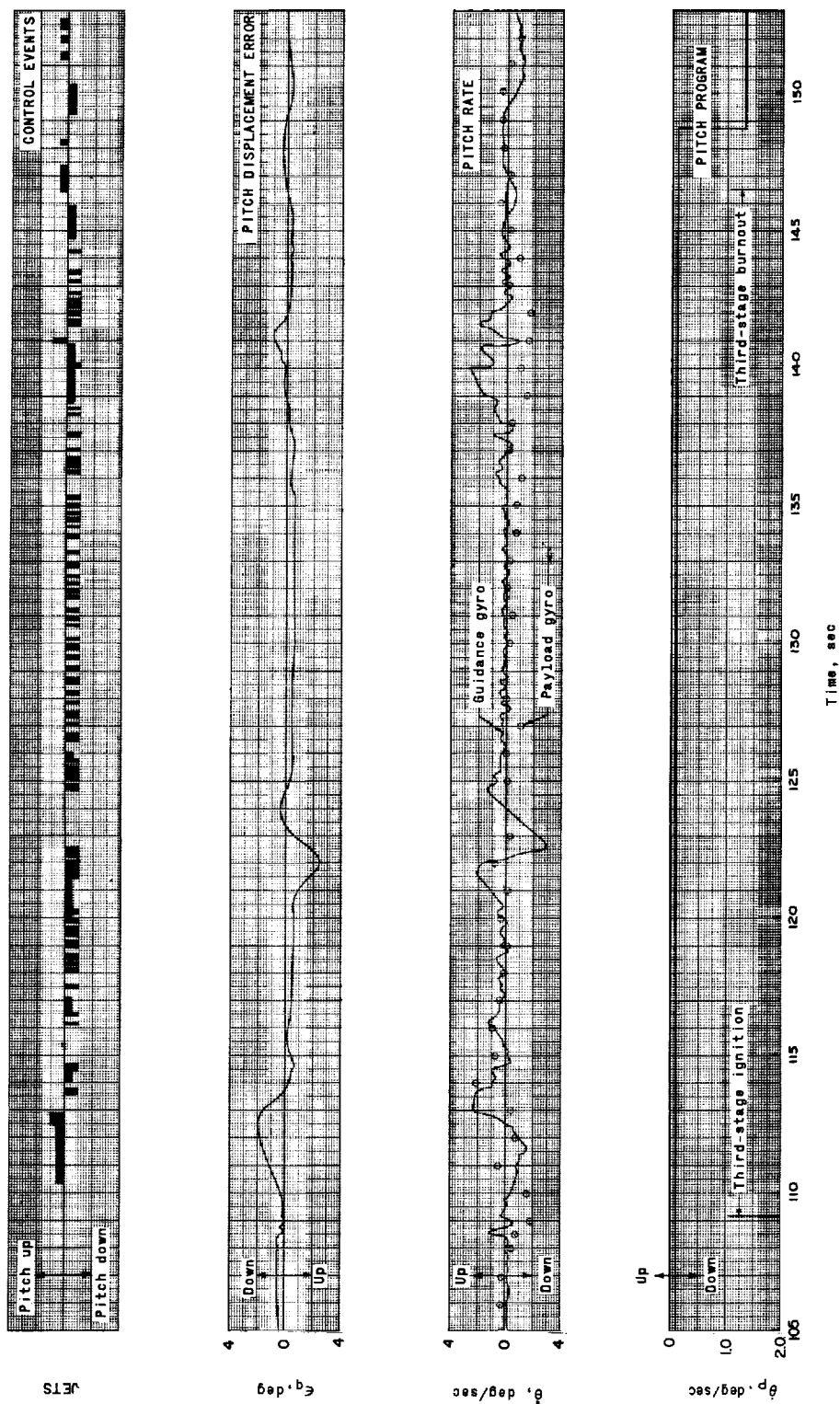
(a) Pitch.

Figure 78.- Time histories of guidance- and control-system performance during third-stage burning.

194
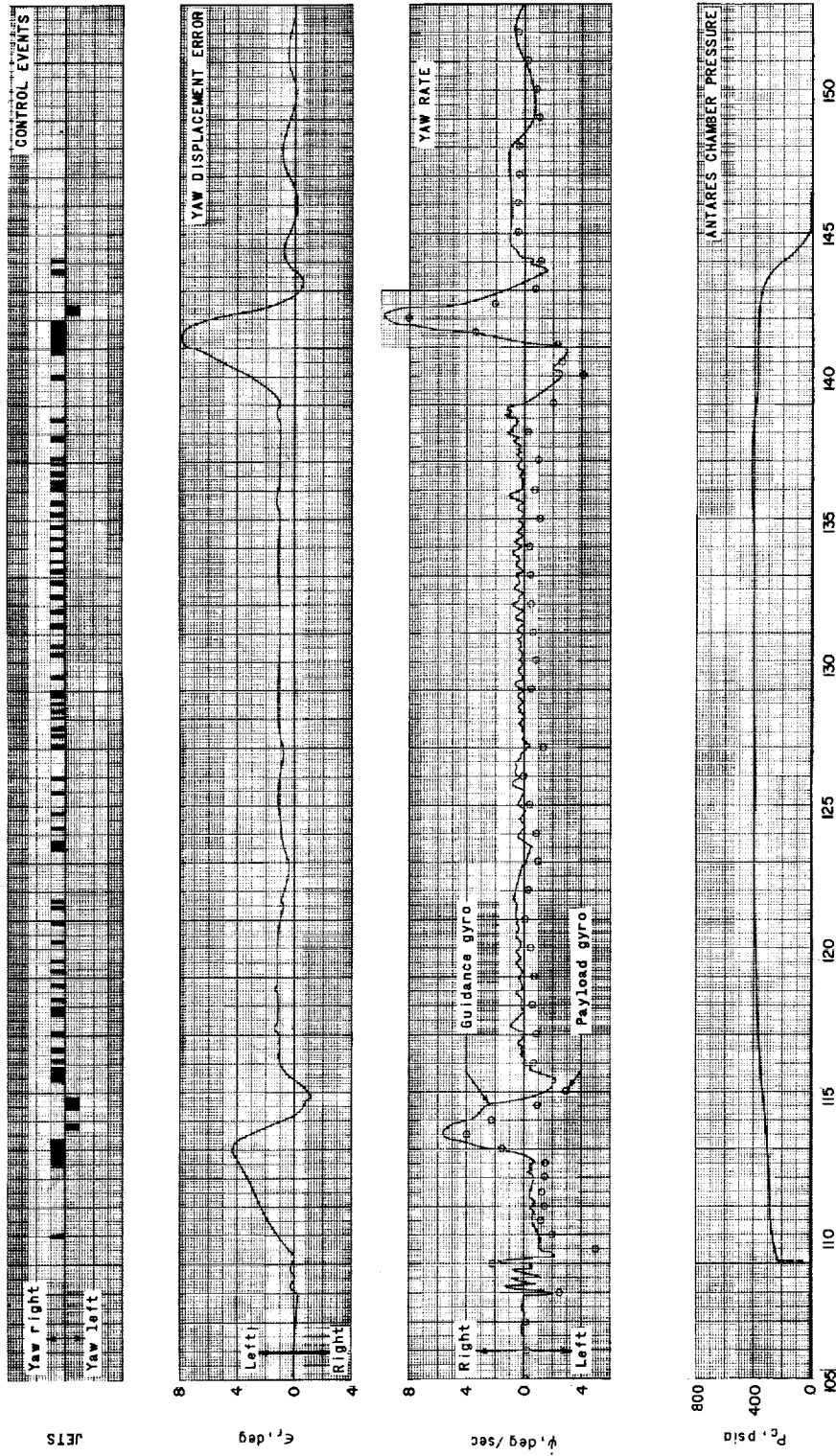
(b) Yaw.

Figure 78.- Continued.

L-1924

L-1924
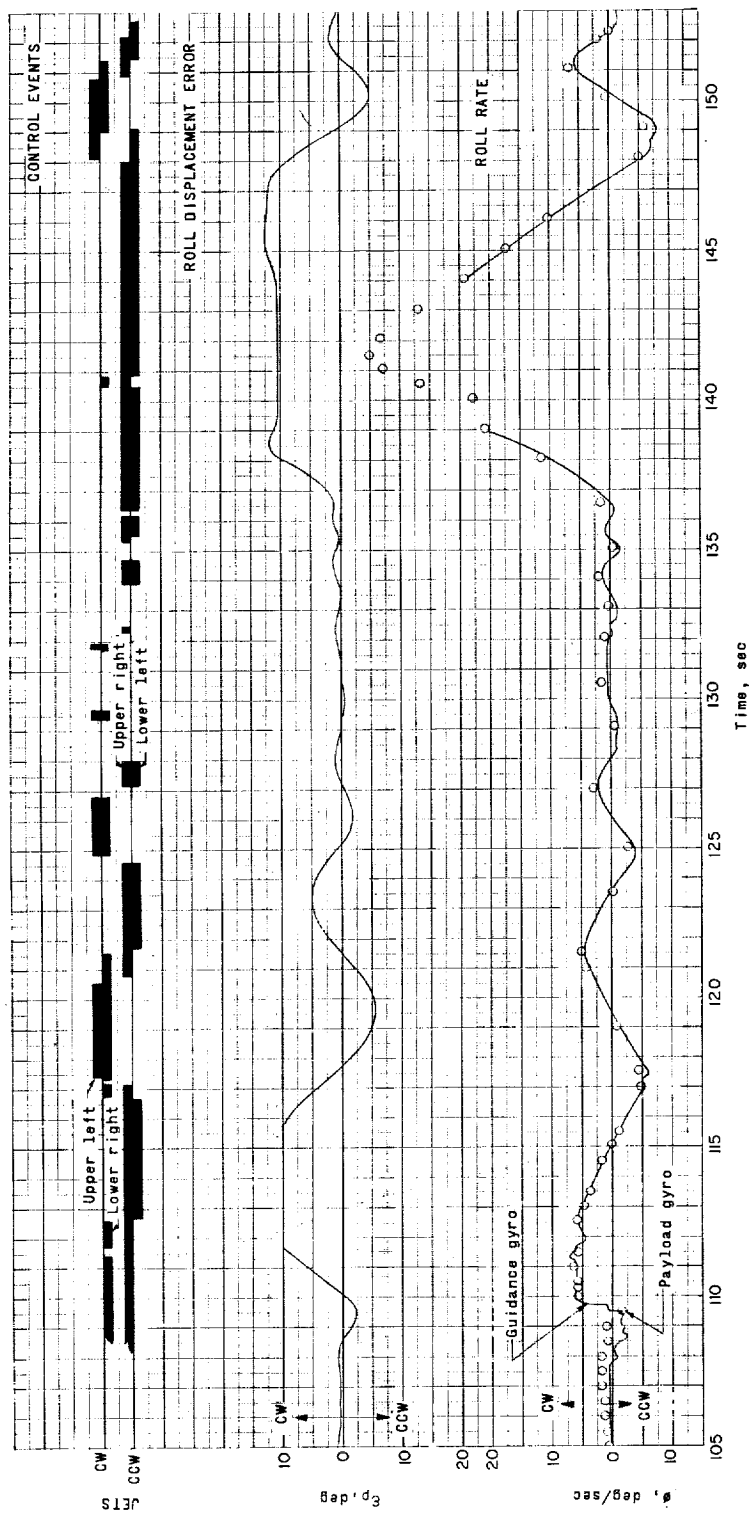
(c) Roll.

Figure 78.- Concluded.

CONTROL EVENTS

Pitch up

Pitch down

JETS

PITCH DISPLACEMENT ERROR

Down

Up

ϵ_q, deg

PITCH RATE

Payload gyro

Guidance gyro

Up

Down

$\dot{\theta}$, deg/sec

PITCH PROGRAM

Third-stage coast

Up

Down

$\dot{\theta}_p$, deg/sec

0

1.0

2.0

145   150   155   160   165   170   175   180   185

Time, sec
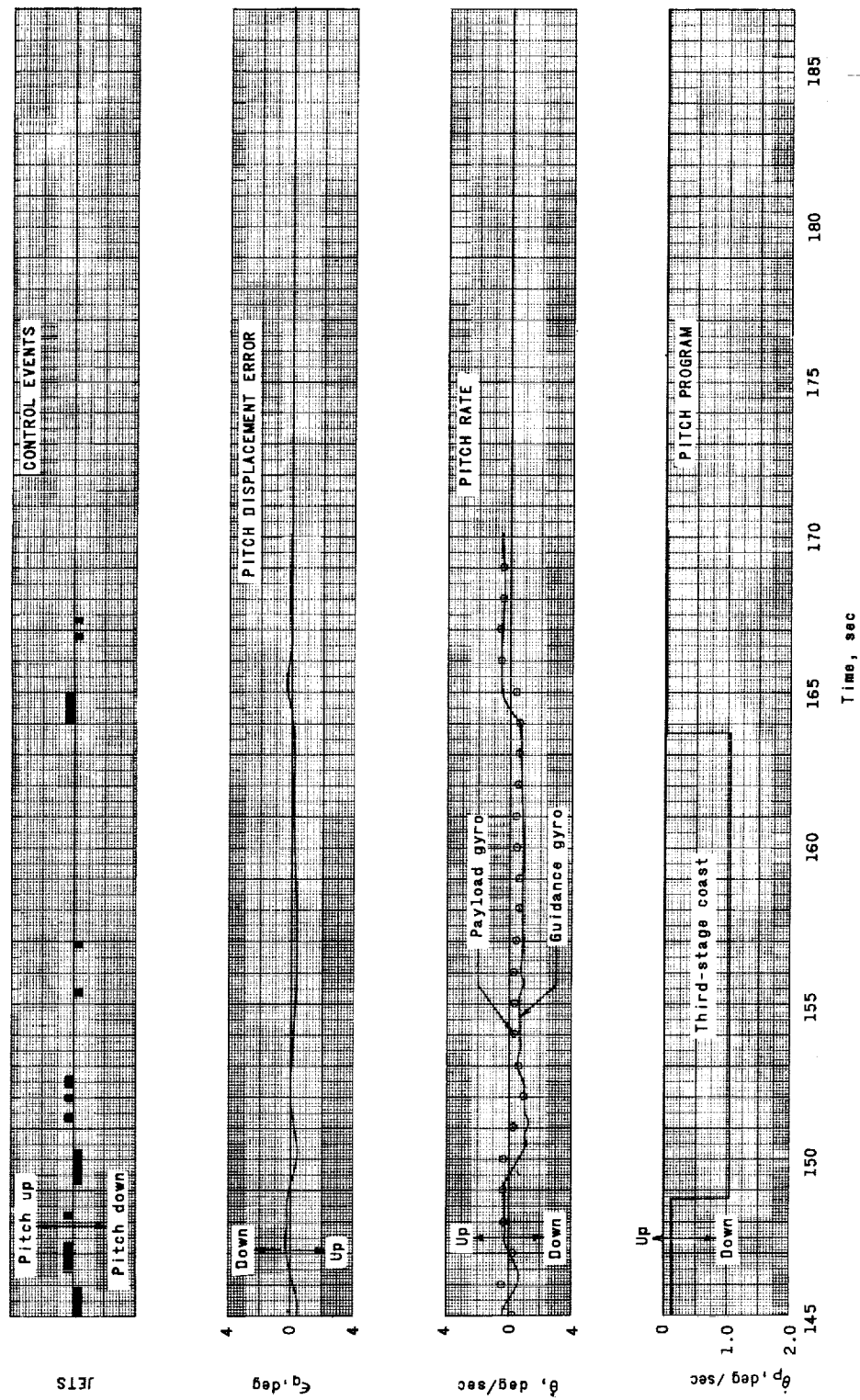
(a) Pitch.

Figure 79.- Time histories of guidance- and control-system performance during third-stage coast.

L-1924
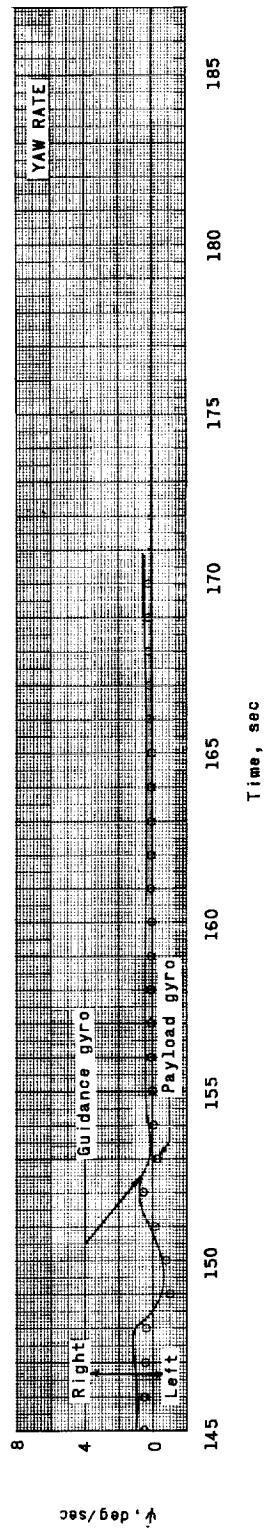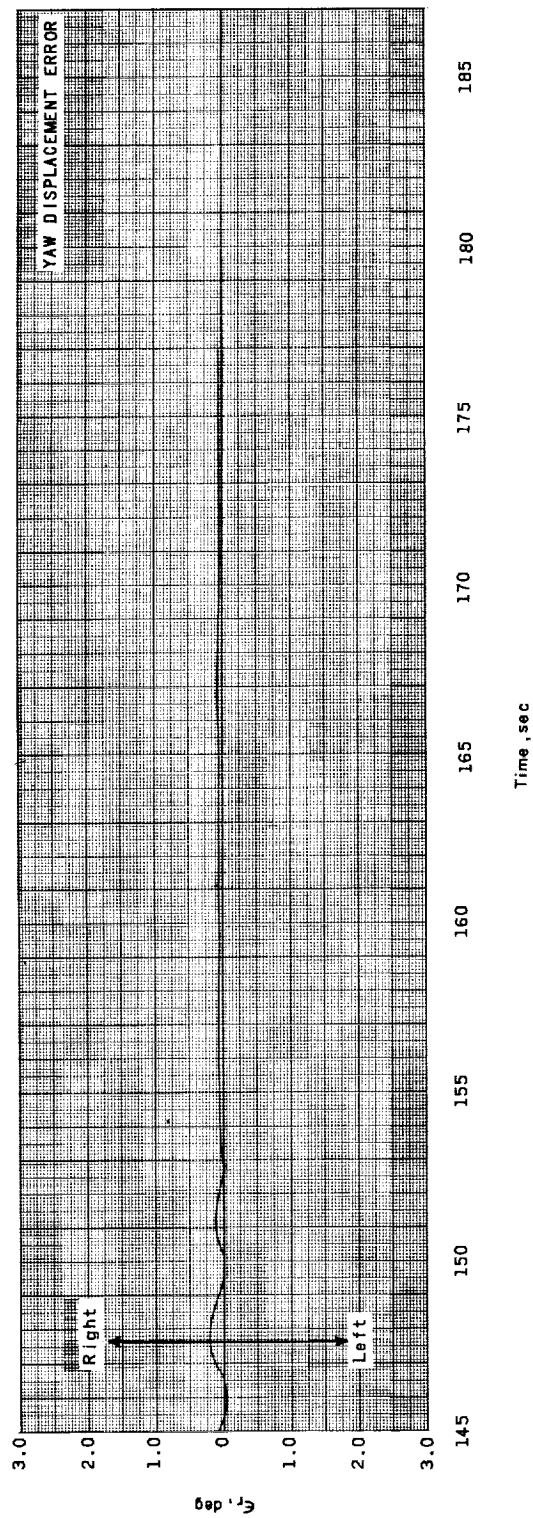
(b) Yaw.

Figure 79.- Continued.

197
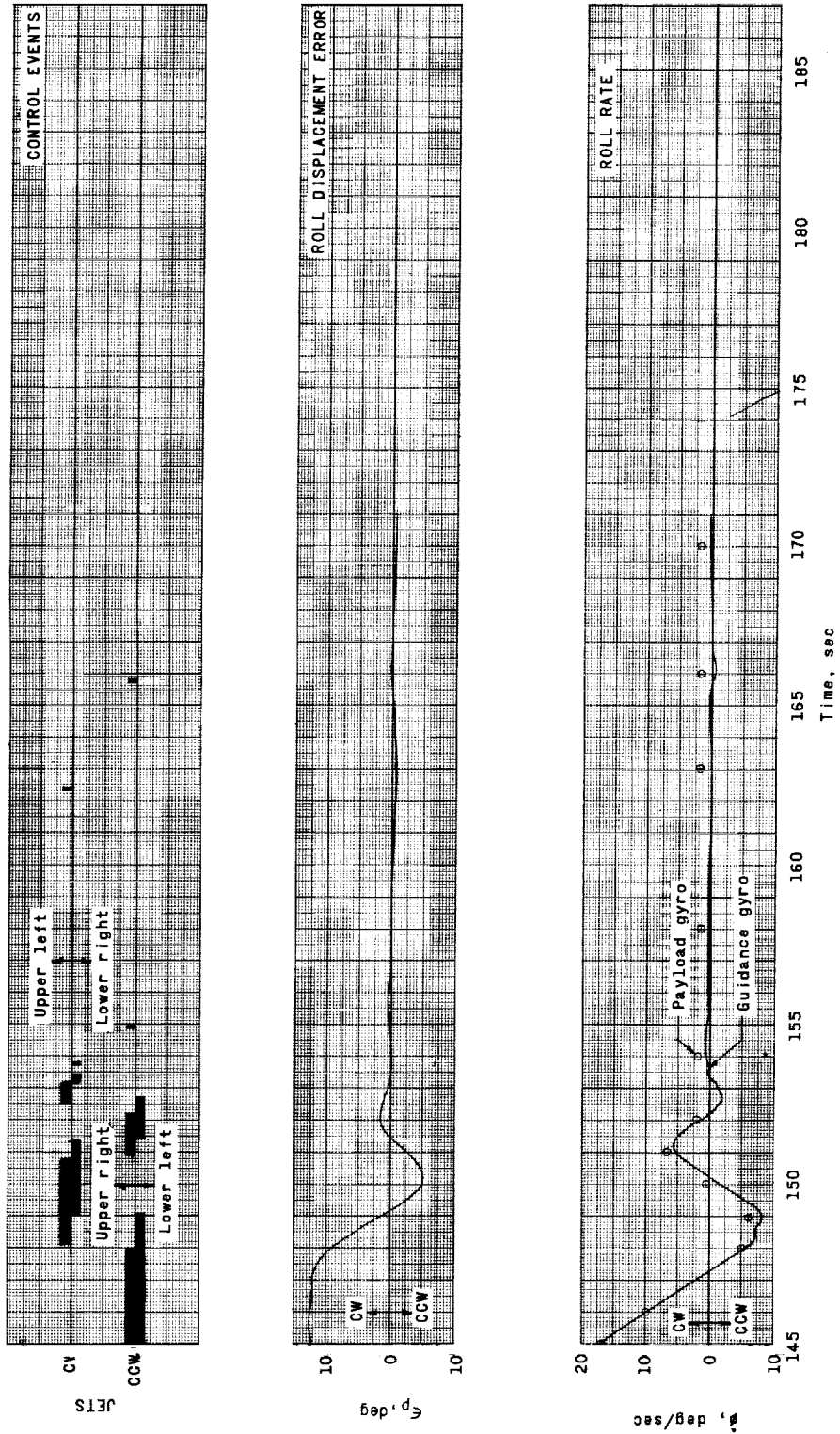
(c) Roll.

Figure 79.- Concluded.

L-1924
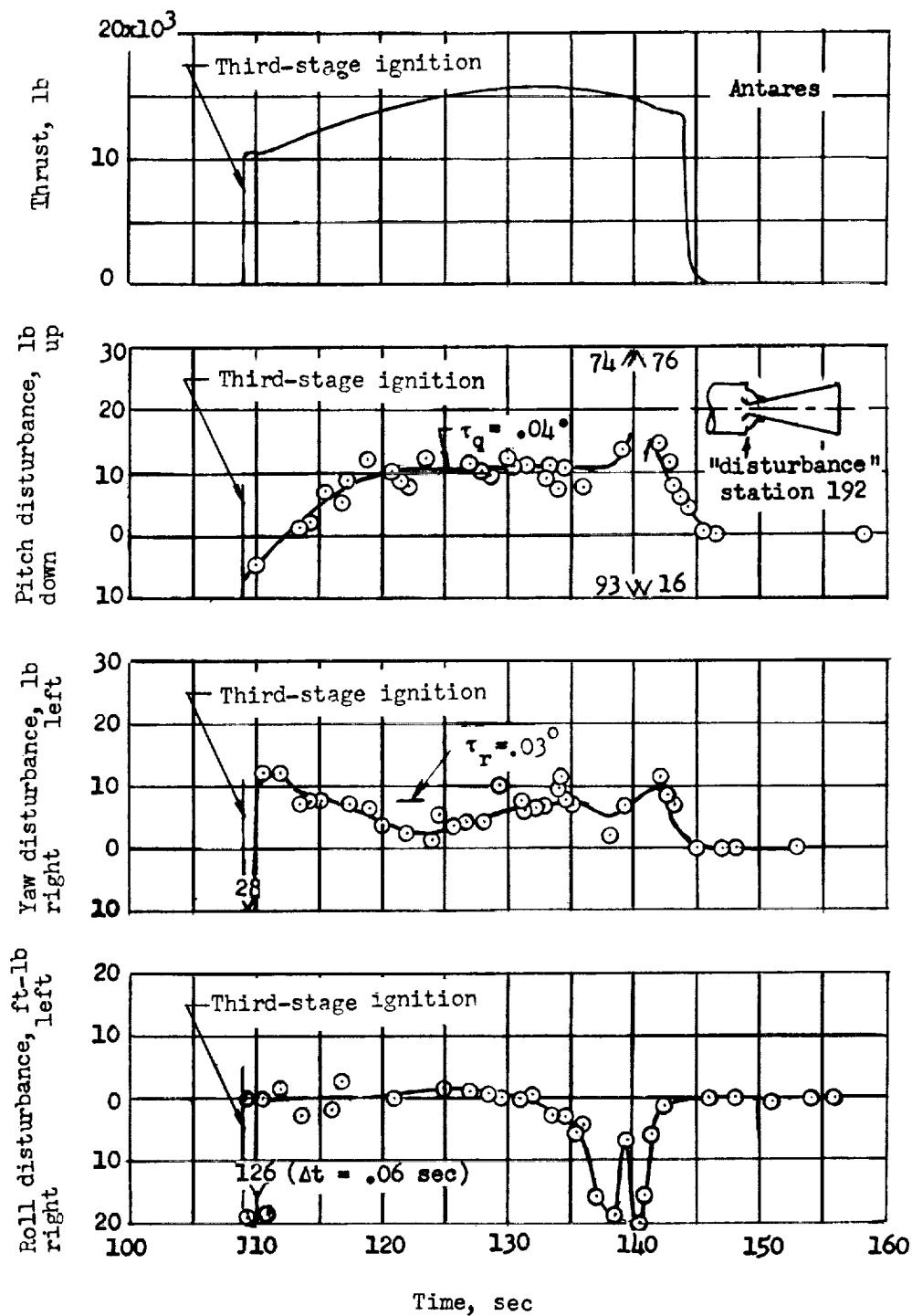
Figure 80.- Time histories of disturbing forces and moments derived from flight data obtained during third-stage thrusting.
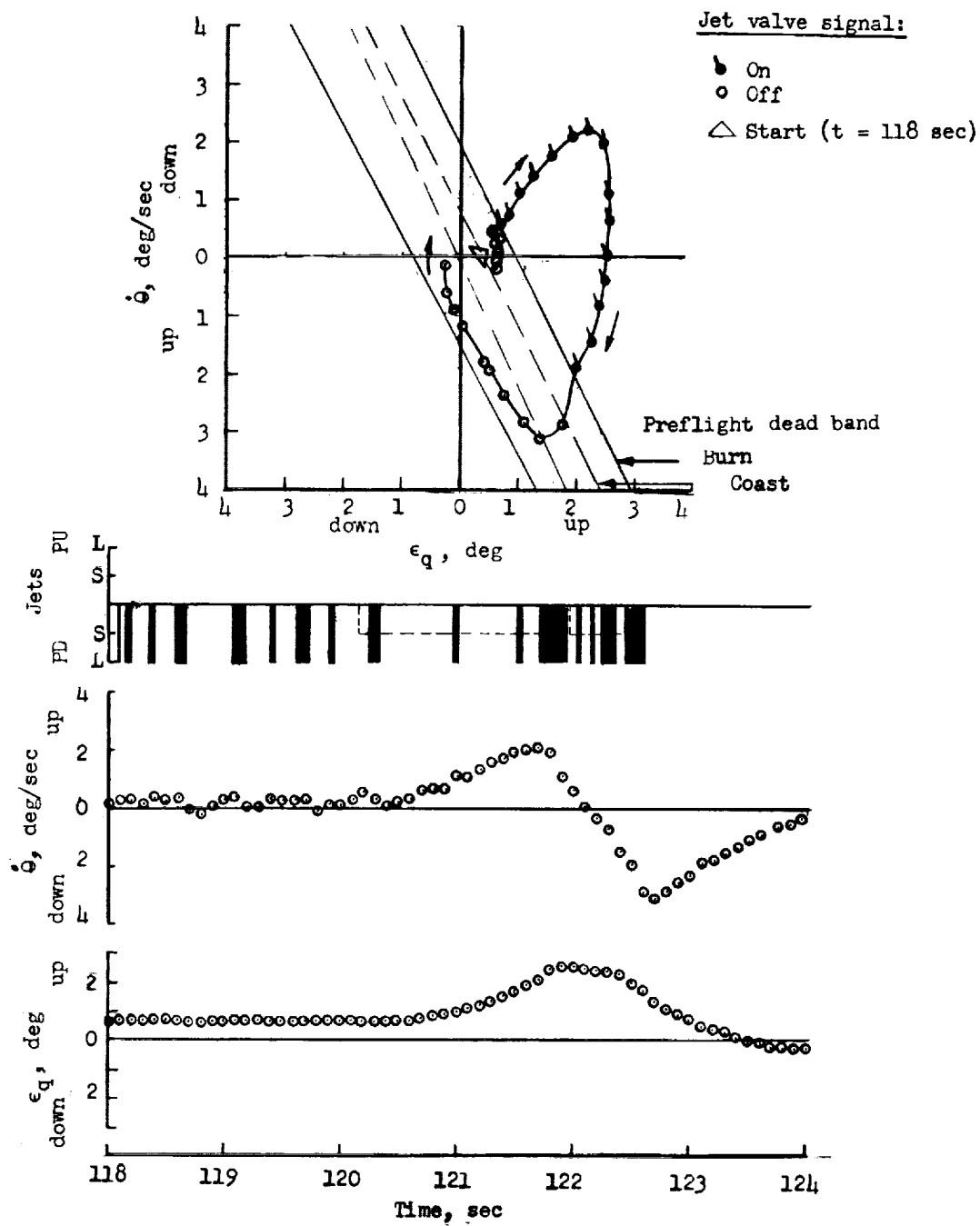
(a) Pitch.

Figure 81.- Phase-plane and time-history response of position errors and rates to disturbances during third-stage burning.
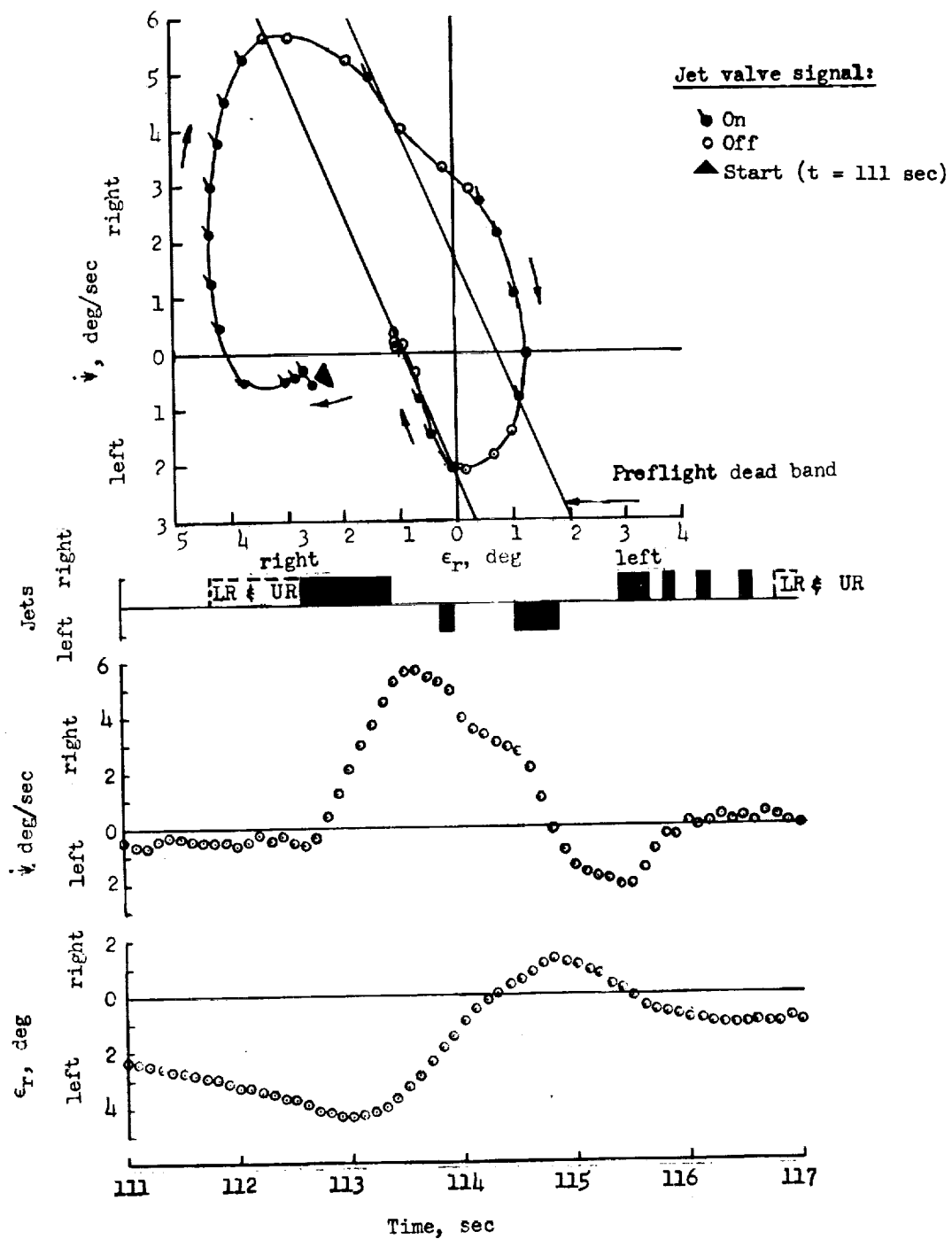
L-1924

(b) Yaw (t = 111 to 117 seconds).

Figure 81.- Continued.
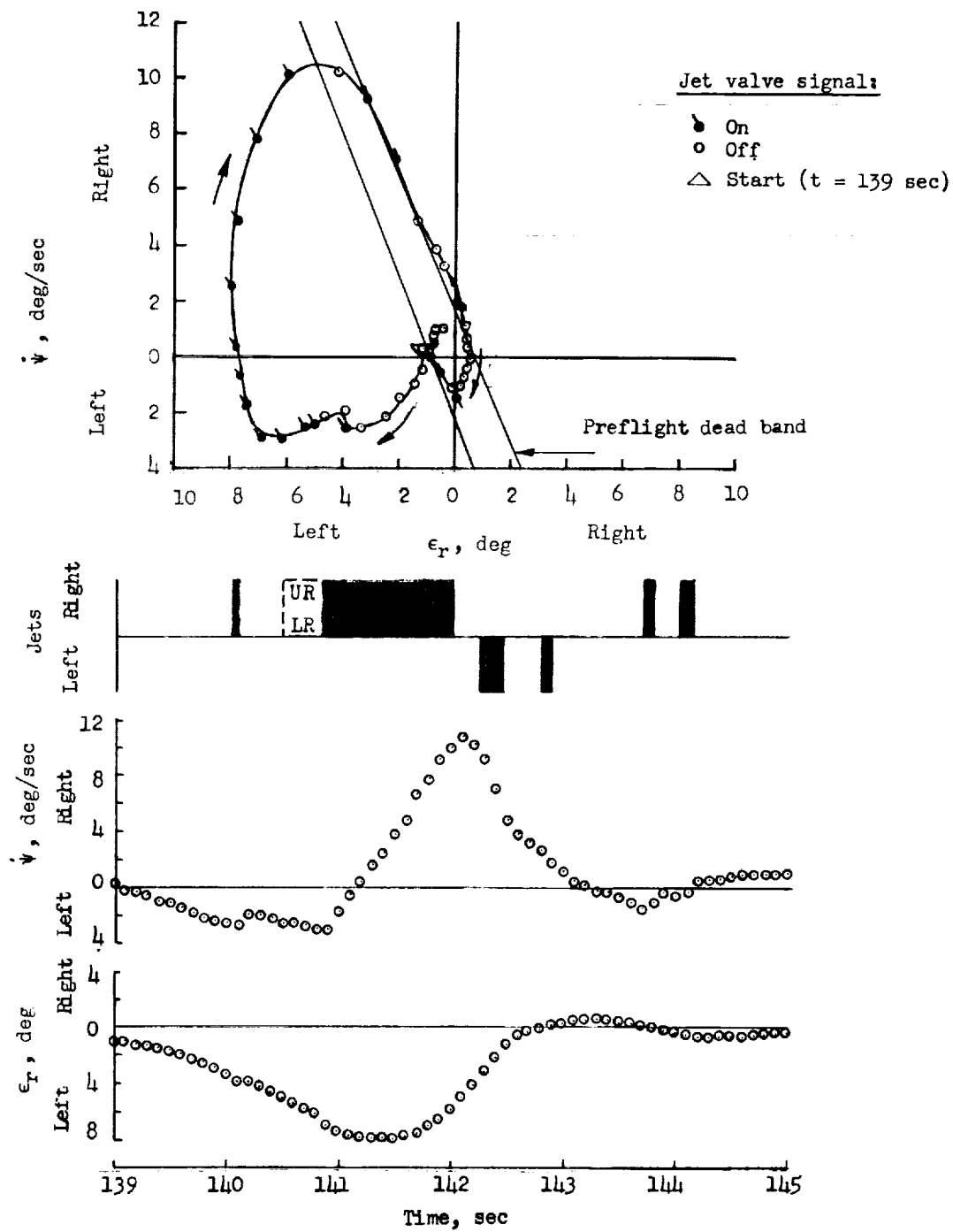
(c) Yaw (t = 139 to 145 seconds).

Figure 81.- Continued.
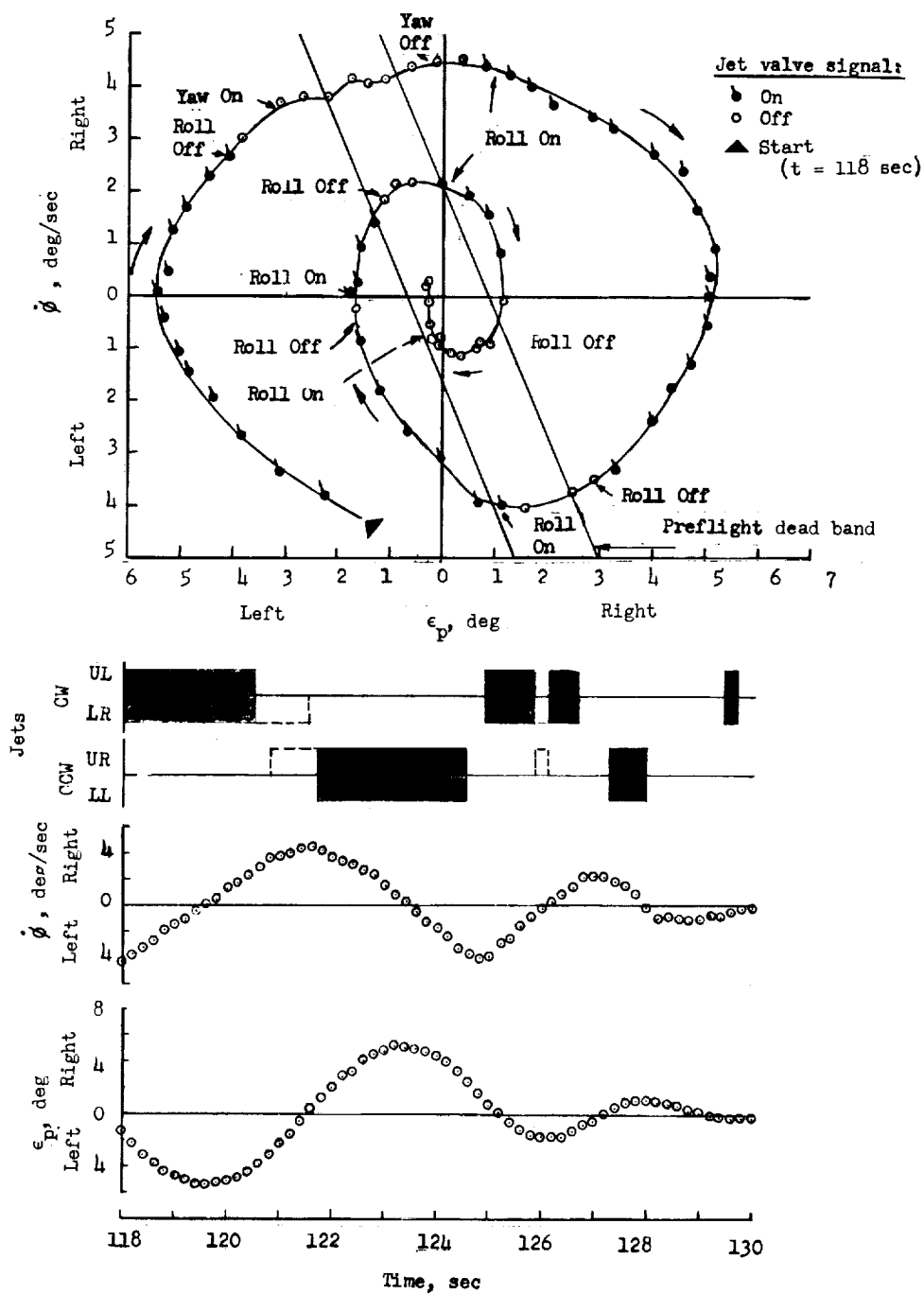
(d) Roll. (Dashed lines indicate control jets operating to produce yaw.)

Figure 81.- Concluded.
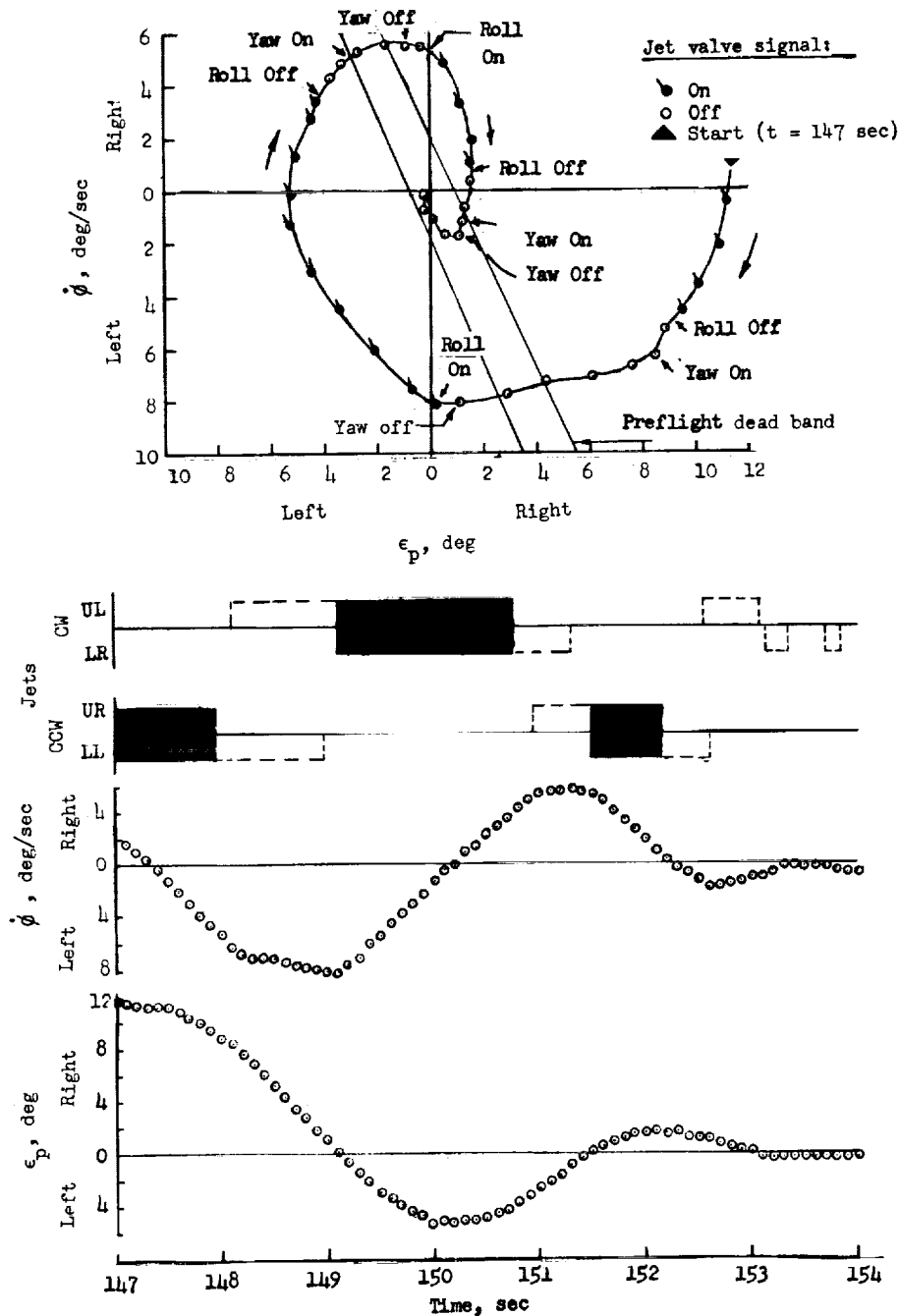
Figure 82.- Phase-plane and time-history response of position errors
and rates during third-stage coast to a roll disturbance originating
during final moments of Antares burning. (Dashed lines indicate
control jets operating to produce yaw.)

L-1924

$$\delta = K_\theta \left(\epsilon_q + \frac{K'_\theta}{K_\theta} \dot\theta \right)$$

where $\epsilon_q = \theta - \theta_P$
and $\theta = \gamma + \alpha$
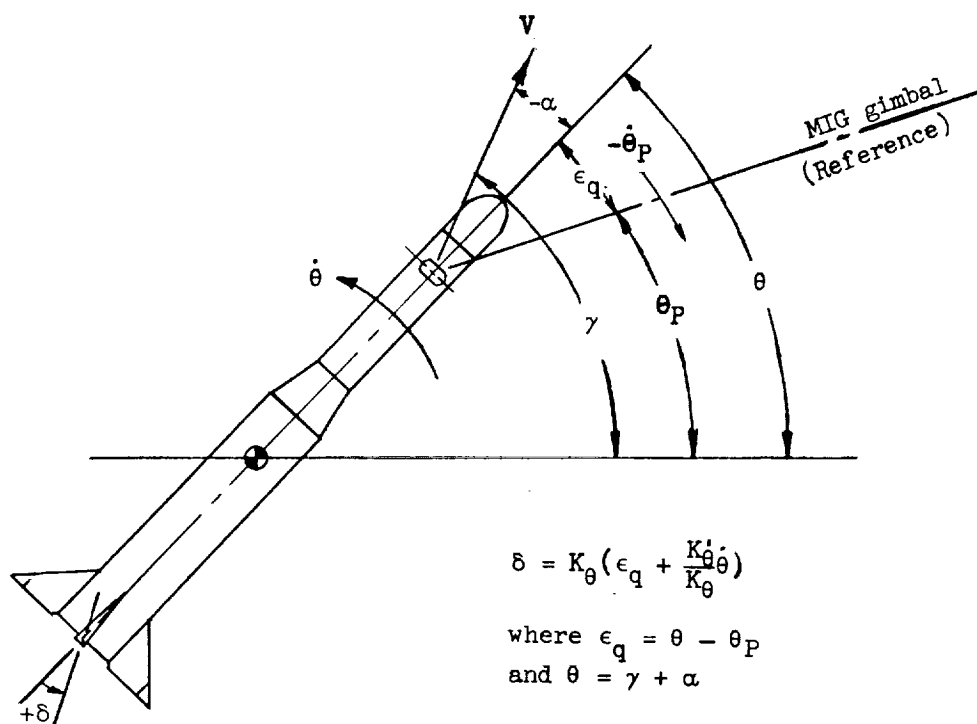
Time, sec	Calculated θ_P, deg	Measured ϵ_q, deg	Calculated θ, deg	Simulated α, deg	Calculated γ, deg	Measured γ, deg
0	85.00	0	85.0	---	---	---
5	83.01	0.6	83.6	-4.5	88.1	85.0
10	78.05	1.8	79.8	-3.9	83.7	84.2
15	76.20	1.7	77.9	-1.6	79.5	81.0
20	74.40	1.6	76.0	-1.2	77.2	78.8
25	72.58	2.0	74.6	-1.6	76.2	76.5
30	70.76	2.0	72.8	-1.9	74.7	74.2
35	69.87	1.6	71.5	-1.7	73.2	72.5
40	68.98	1.2	70.2	-0.6	70.8	71.0
45	68.08	1.4	69.5	-0.3	69.8	70.0
50	67.19	1.0	68.2	-0.4	68.6	69.2
55	66.30	1.2	67.5	-0.1	67.6	68.5
60	65.41	1.0	66.4	-0.2	66.6	67.5

Figure 83.- Comparison of derived values of first-stage flight-path
angle with radar data.
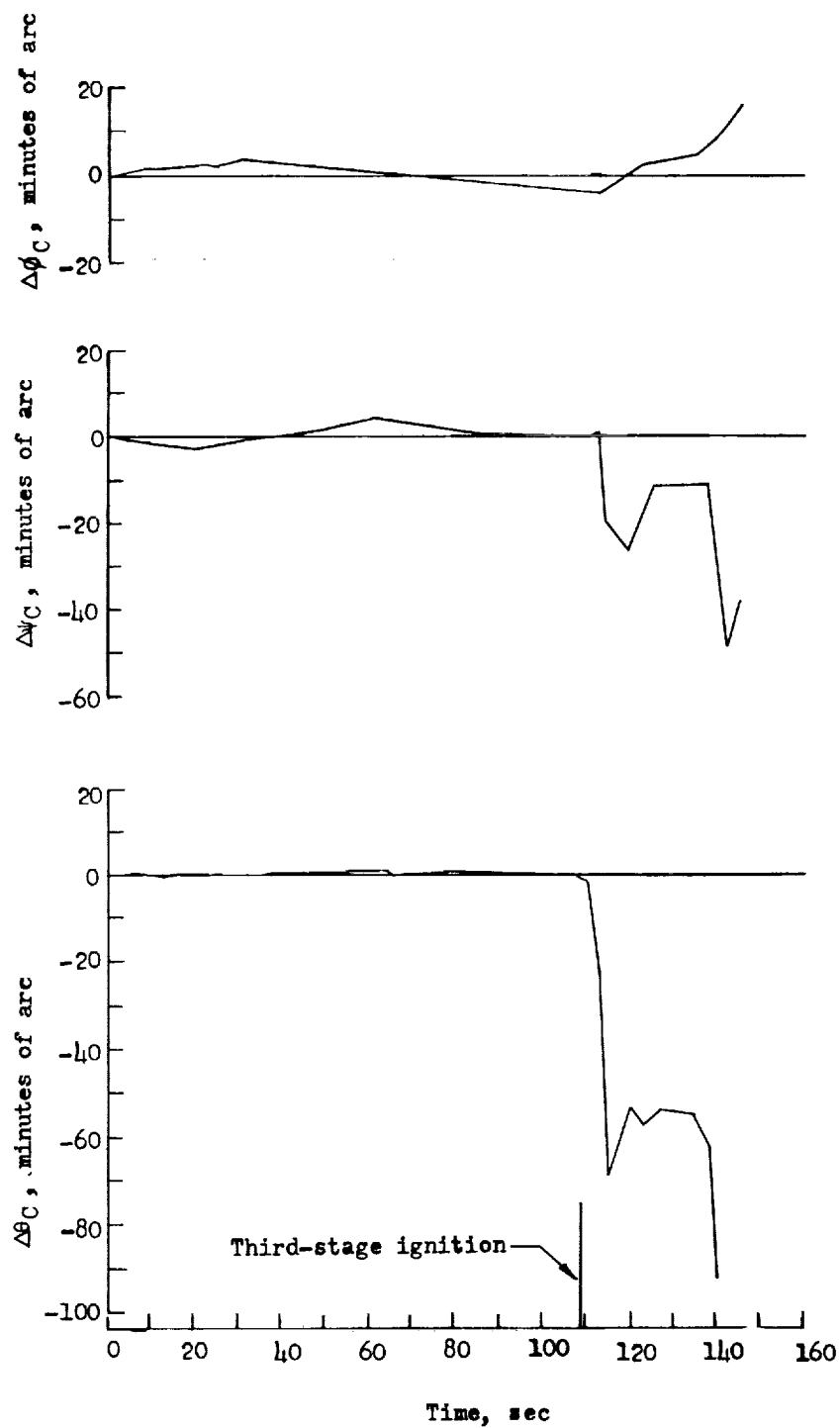
Figure 84.- Time histories of attitude angle errors due to
gyro coning effect.

L-1924
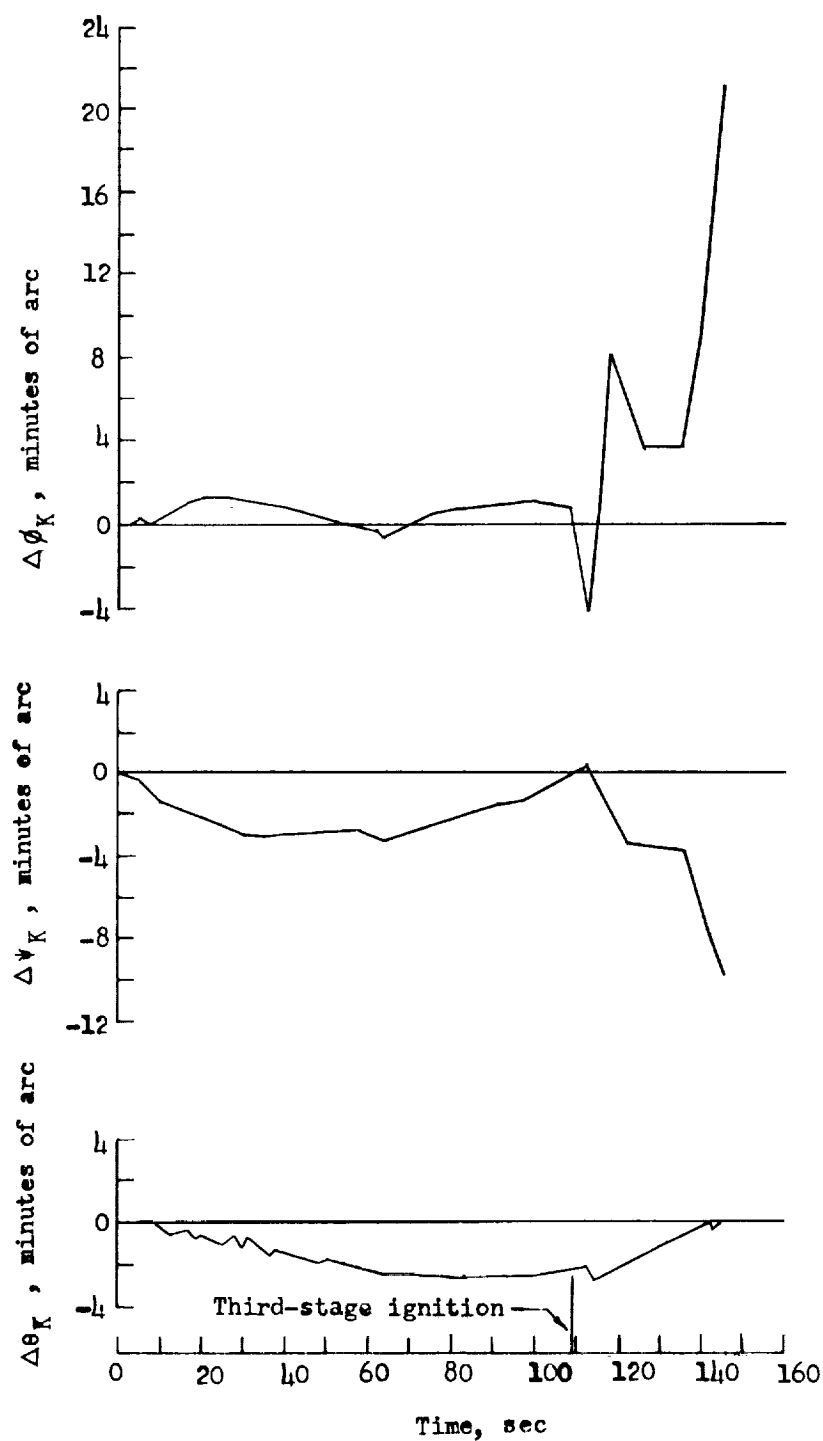
Figure 85.- Time histories of attitude angle errors due to gyro cross-coupling effect.
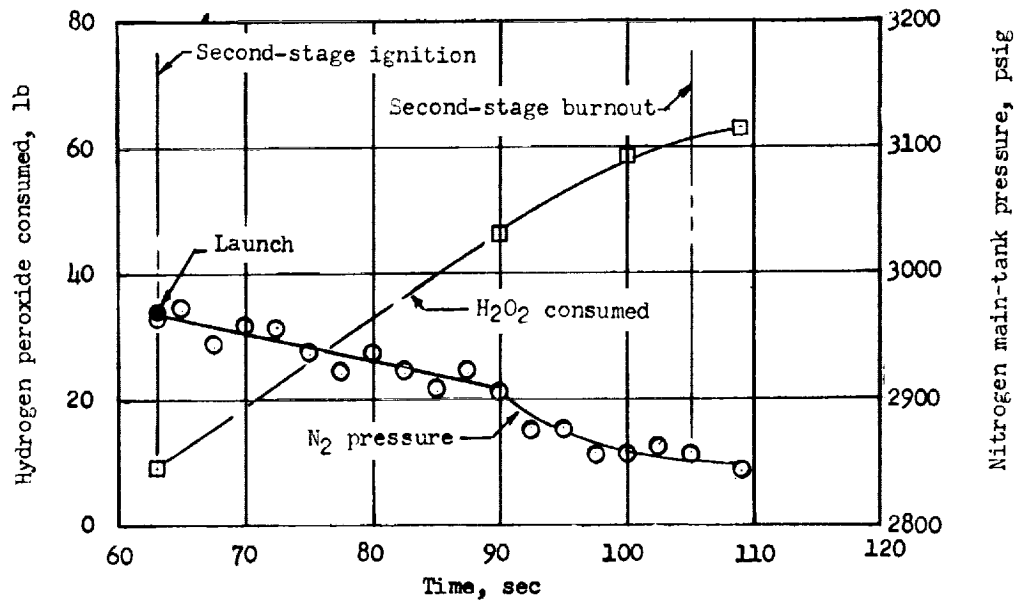
(a) Second stage.
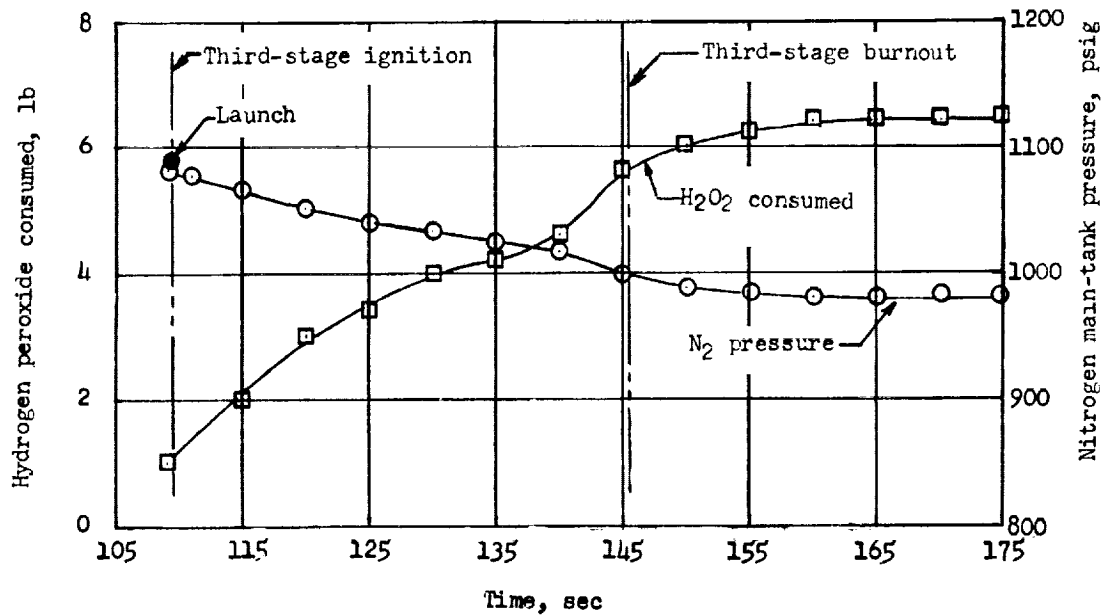
(b) Third stage.

Figure 86.- Time histories of nitrogen main-tank pressure variation and hydrogen peroxide consumed by second- and third-stage control systems.

Jet	Time interval jet on, sec	Impulse from jet during time interval, lb-sec (1)	Impulse from disturbing forces, lb-sec (2)
Pitch	5.95	3,570	3,750
Yaw	2.40	1,440	875
Roll	4.49	216	169
Combined pitch, yaw, and roll	Combined total, 12.84	5,226	4,794

[1]Based on nominal thrust levels.

[2]From measured thrust disturbances.
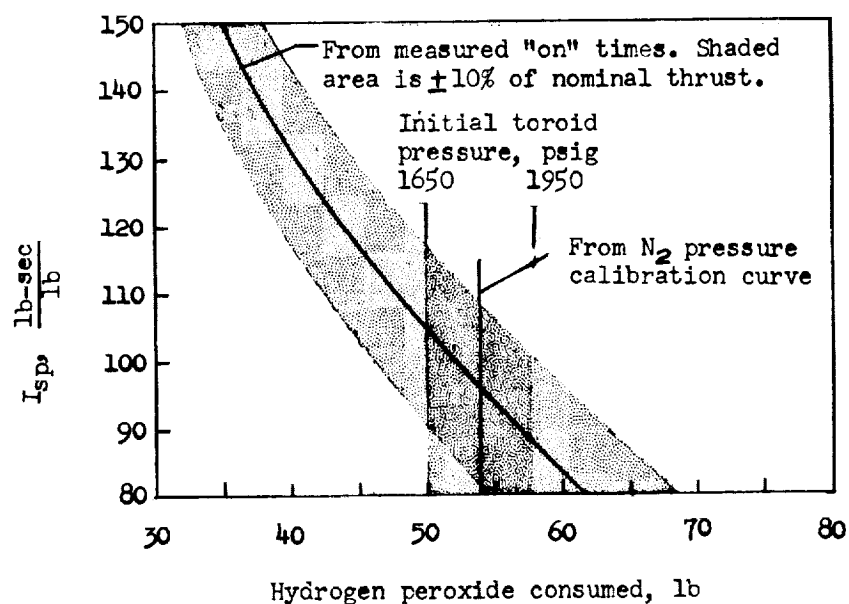
(a) Second stage.

Figure 87.- Hydrogen-peroxide fuel consumption and impulse data obtained for the second- and third-stage control systems from an analysis of flight records.

Jet		Time interval jet on, sec	Impulse from jet during time interval, lb-sec (1)	Impulse from disturbing forces, lb-sec (2)
Pitch	L	5.51	243	300
	S	15.00	33	
Yaw		5.09	224	213
Roll		35.03	154	155
Total			654	668

1
Based on nominal thrust levels.

2
From measured thrust disturbances.
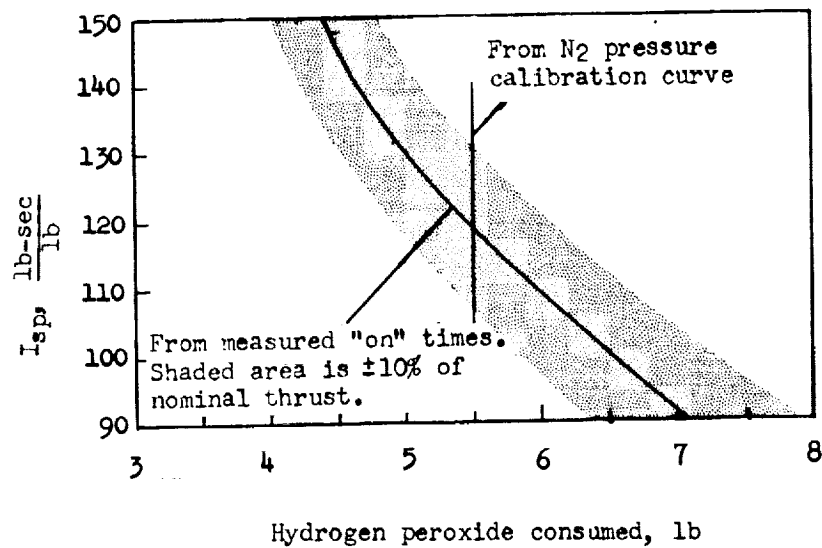
(b) Third stage.

Figure 87.- Concluded.
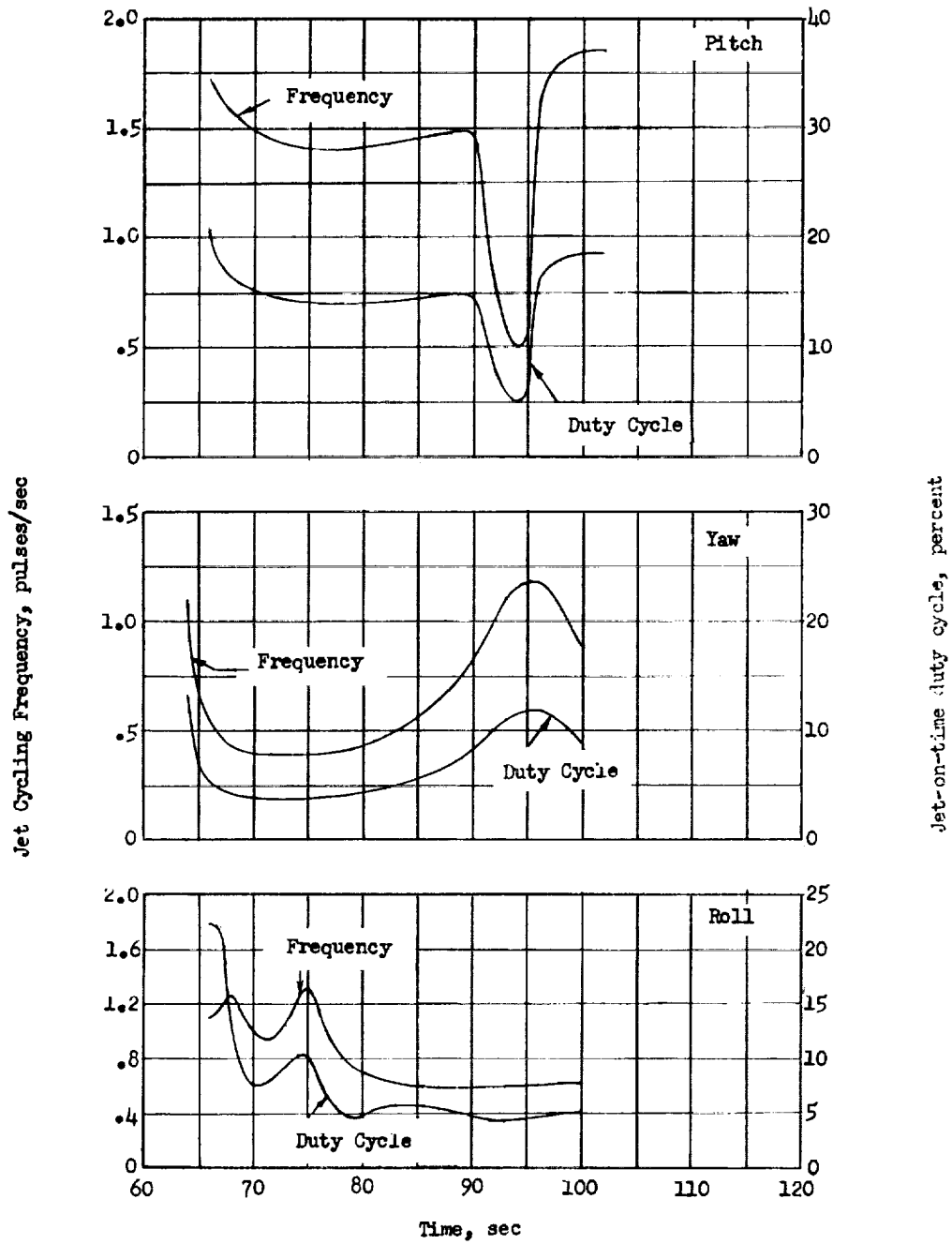
L-1924

(a) Second stage.

Figure 88.- Hydrogen-peroxide reaction-jet frequency and duty cycle
during second- and third-stage thrusting.
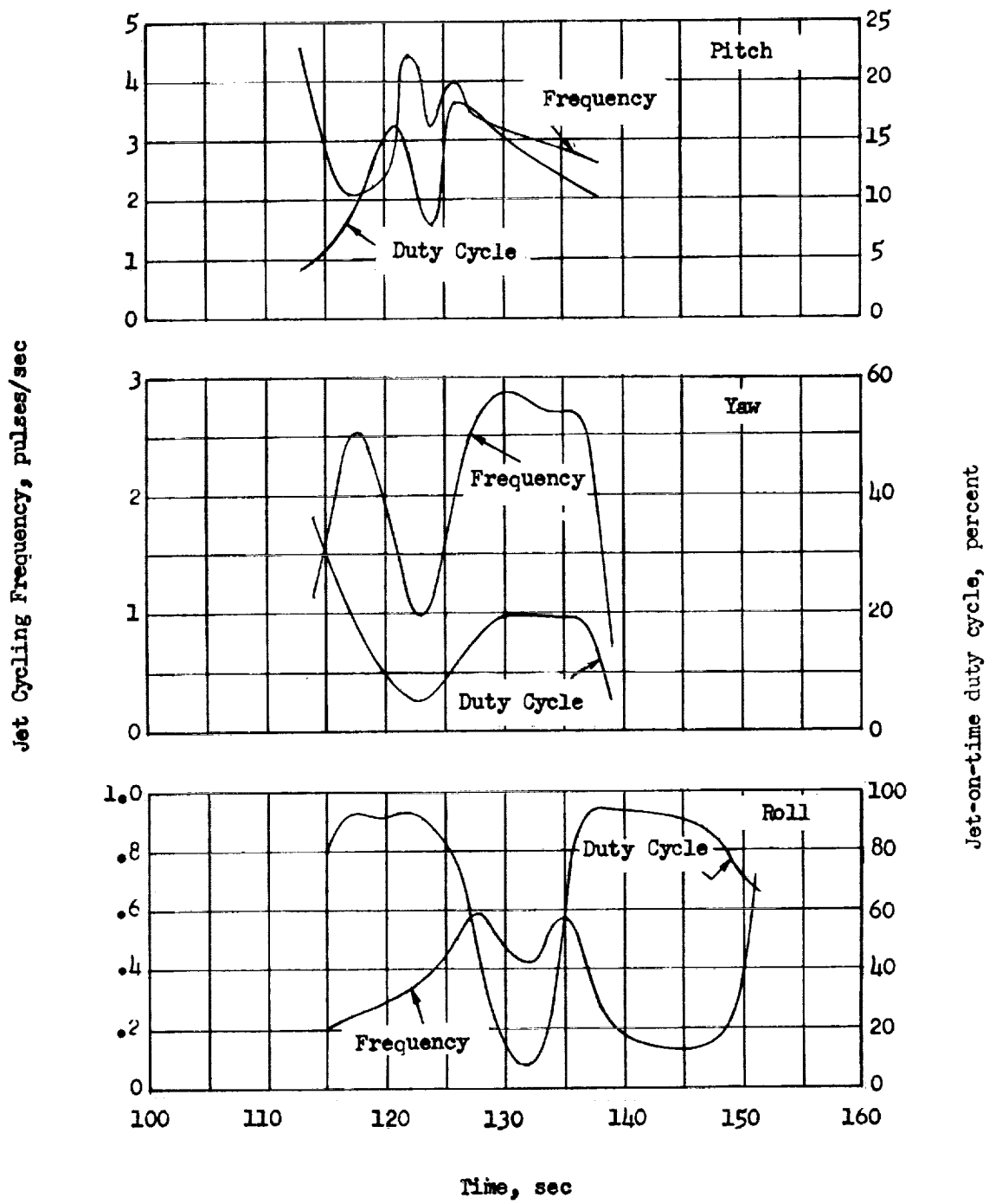
(b) Third stage.

Figure 88.- Concluded.
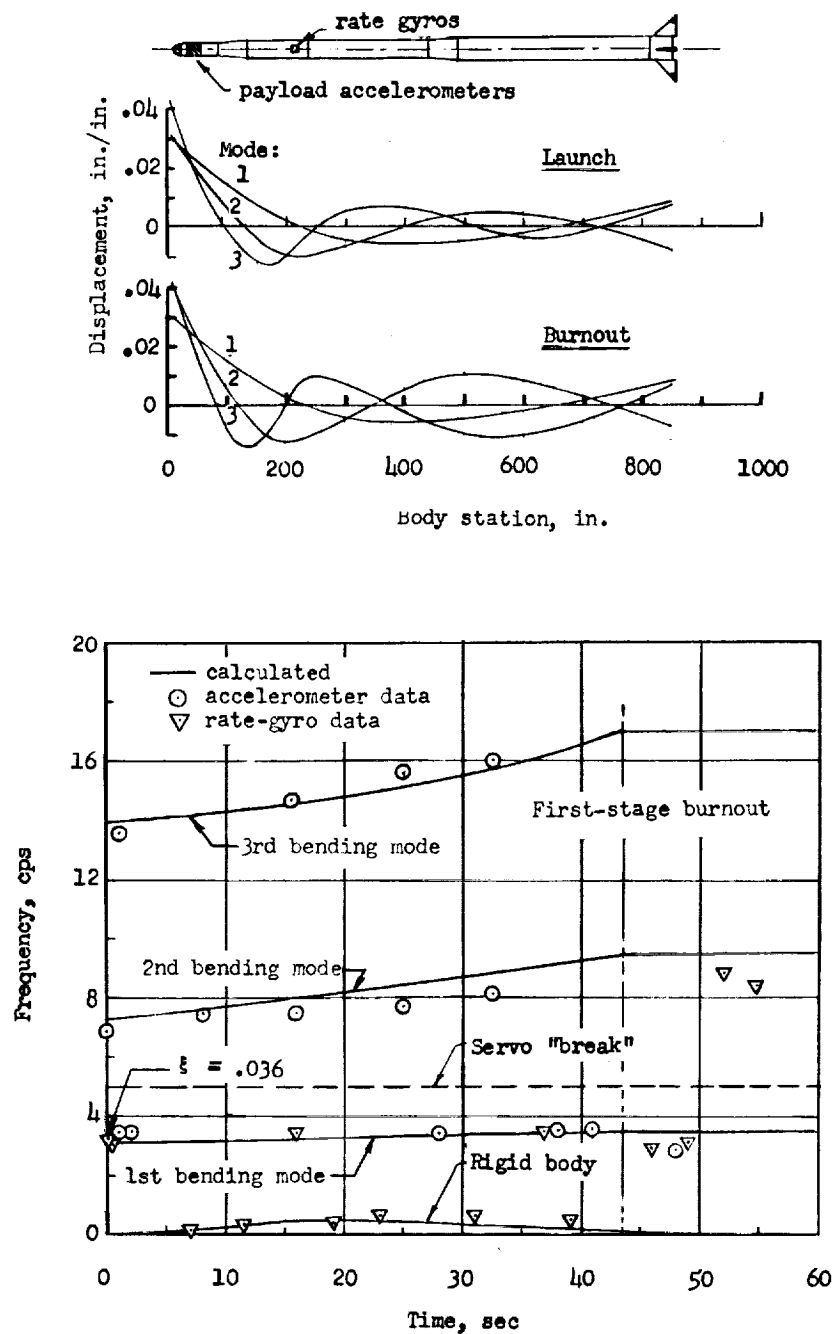
(a) First stage.

Figure 89.- In-flight measured data oscillations and preflight esti-
mates of the significant structural, control, and aerodynamic
frequencies.
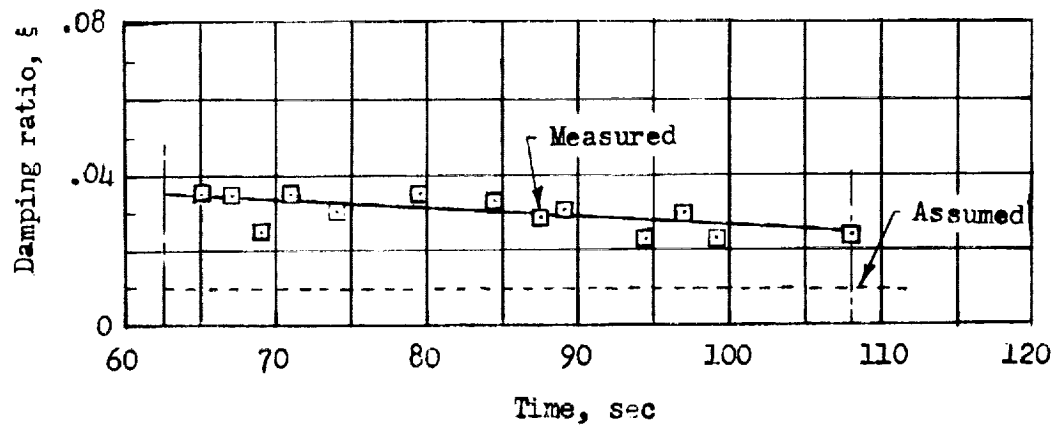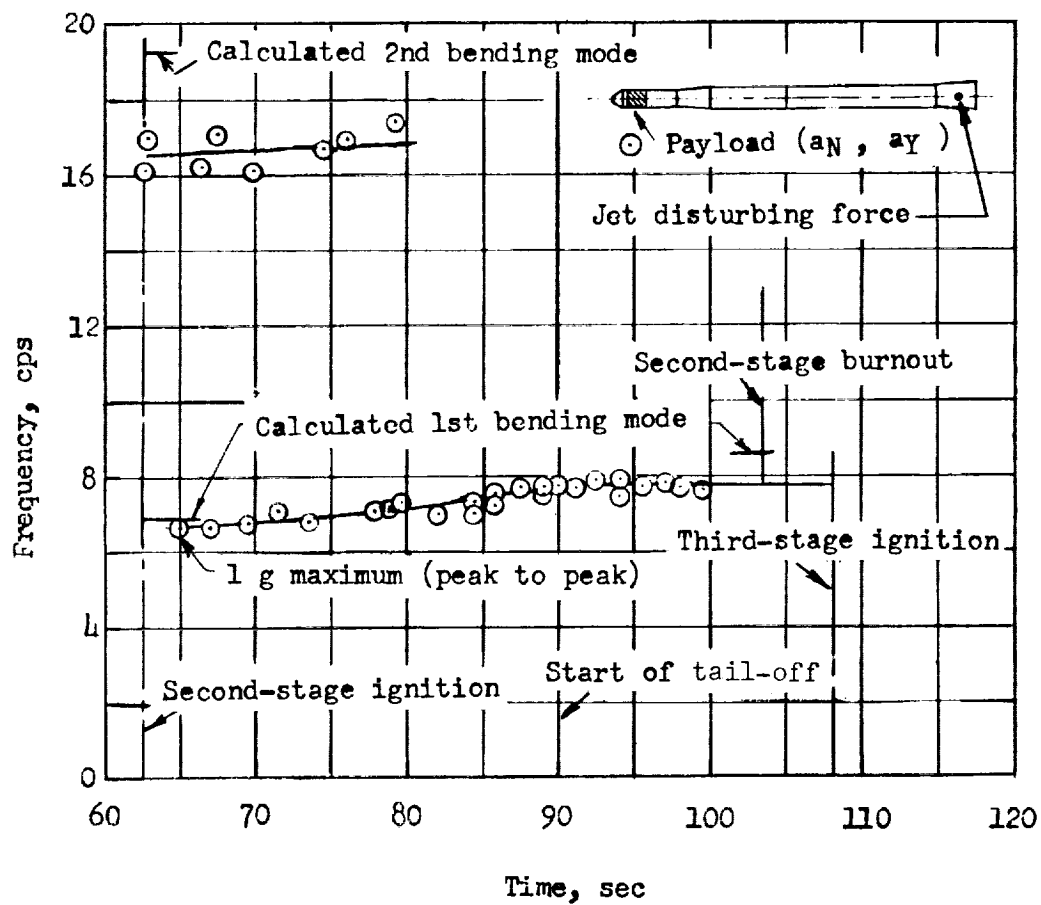
(b) Second stage.

Figure 89.- Continued.
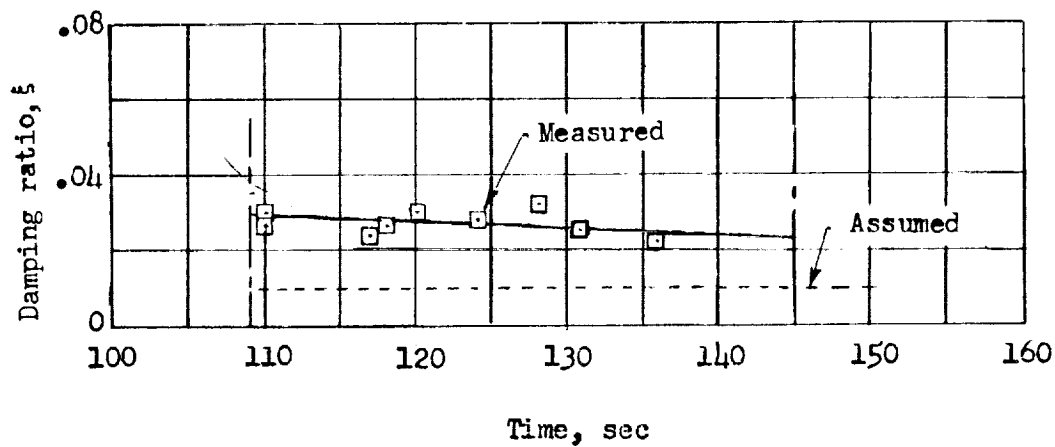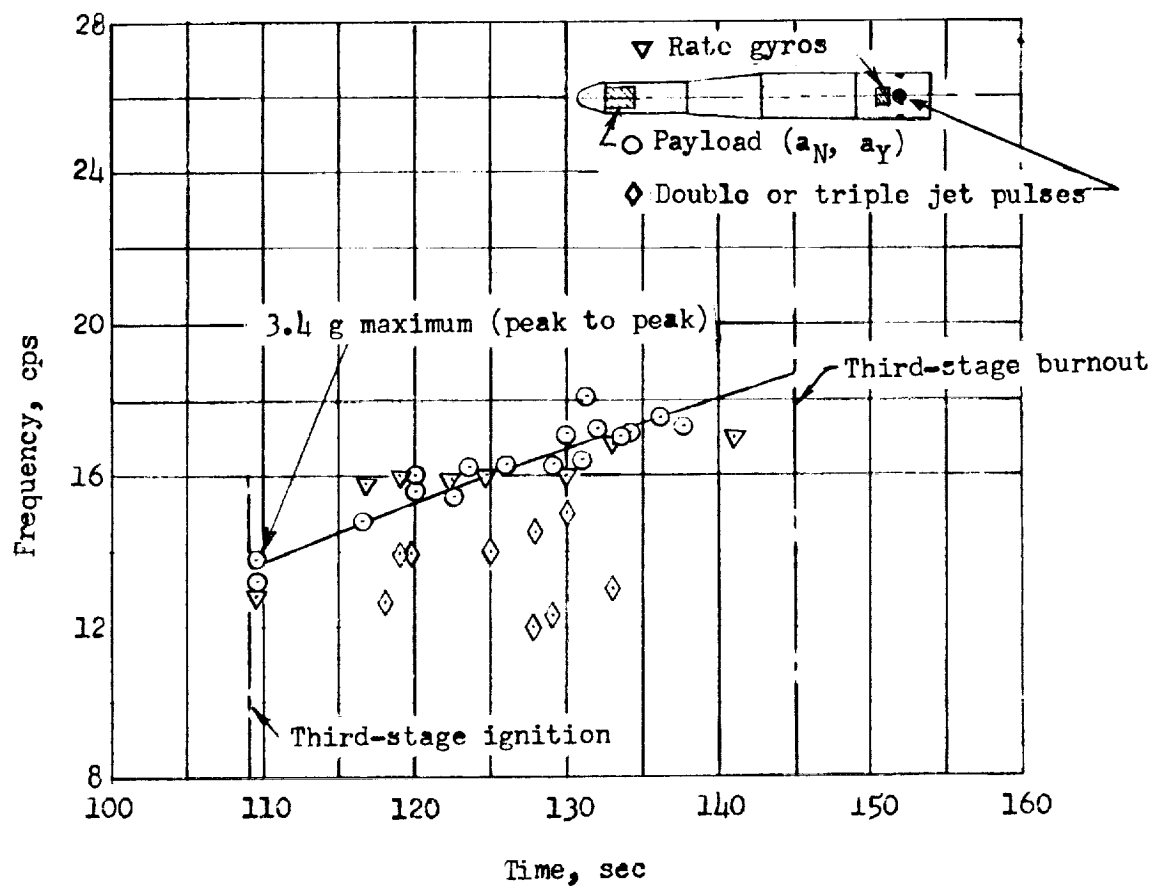
(c) Third stage.

Figure 89.- Concluded.
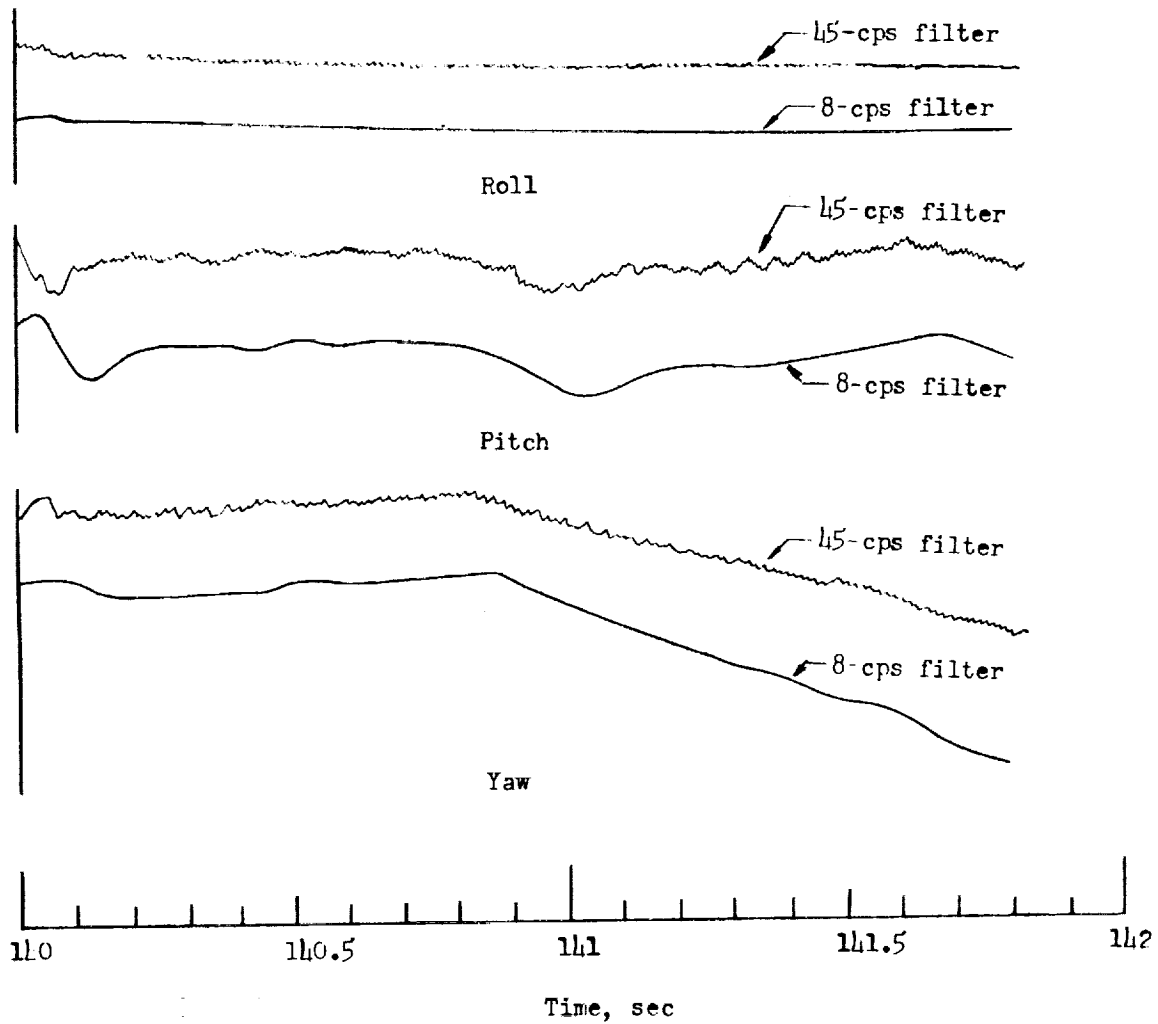
Figure 90.- Partial time histories of guidance rates illustrating the effects of different filters.

L-1924
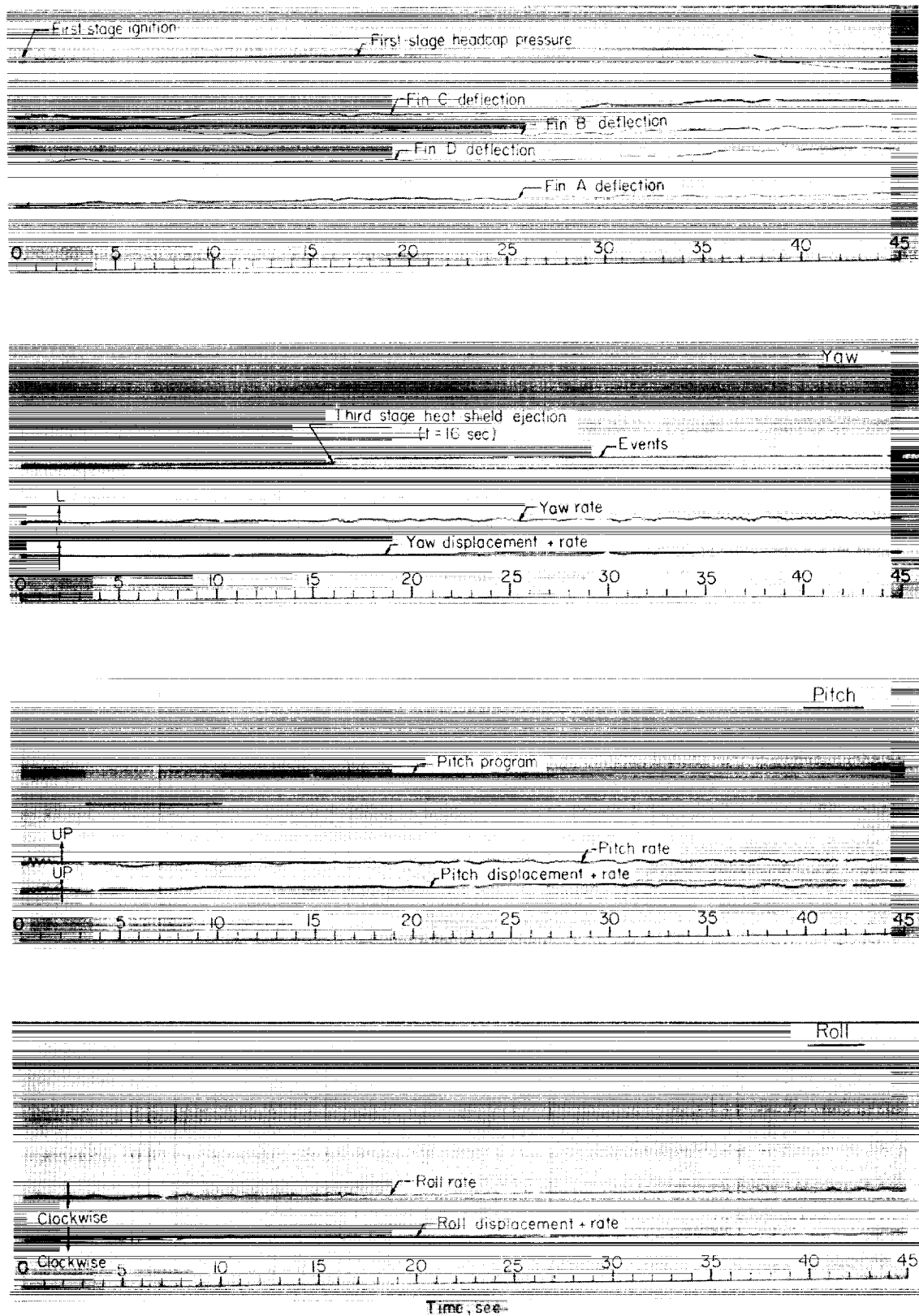
Figure 91.- Sample of guidance telemeter record during first-stage
motor thrusting.

218
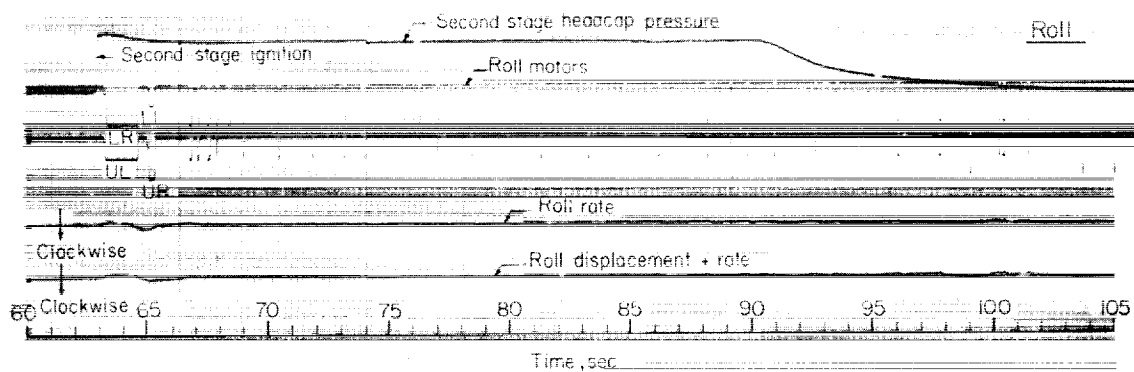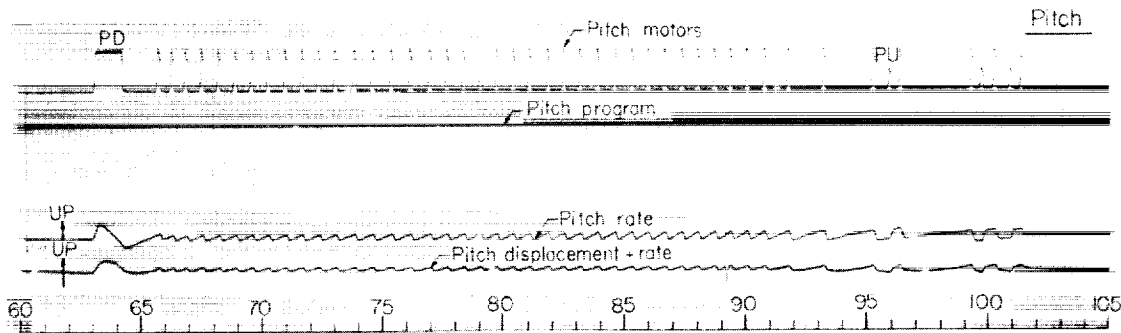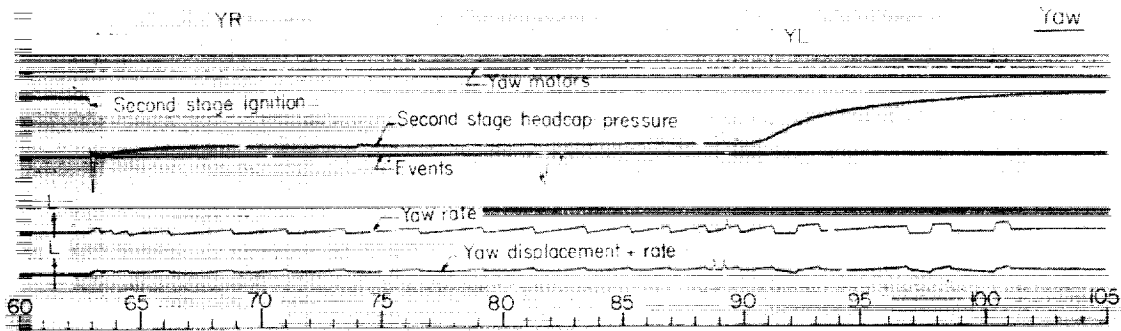
Figure 92.- Sample of guidance telemeter record during second-stage motor thrusting.

L-1924
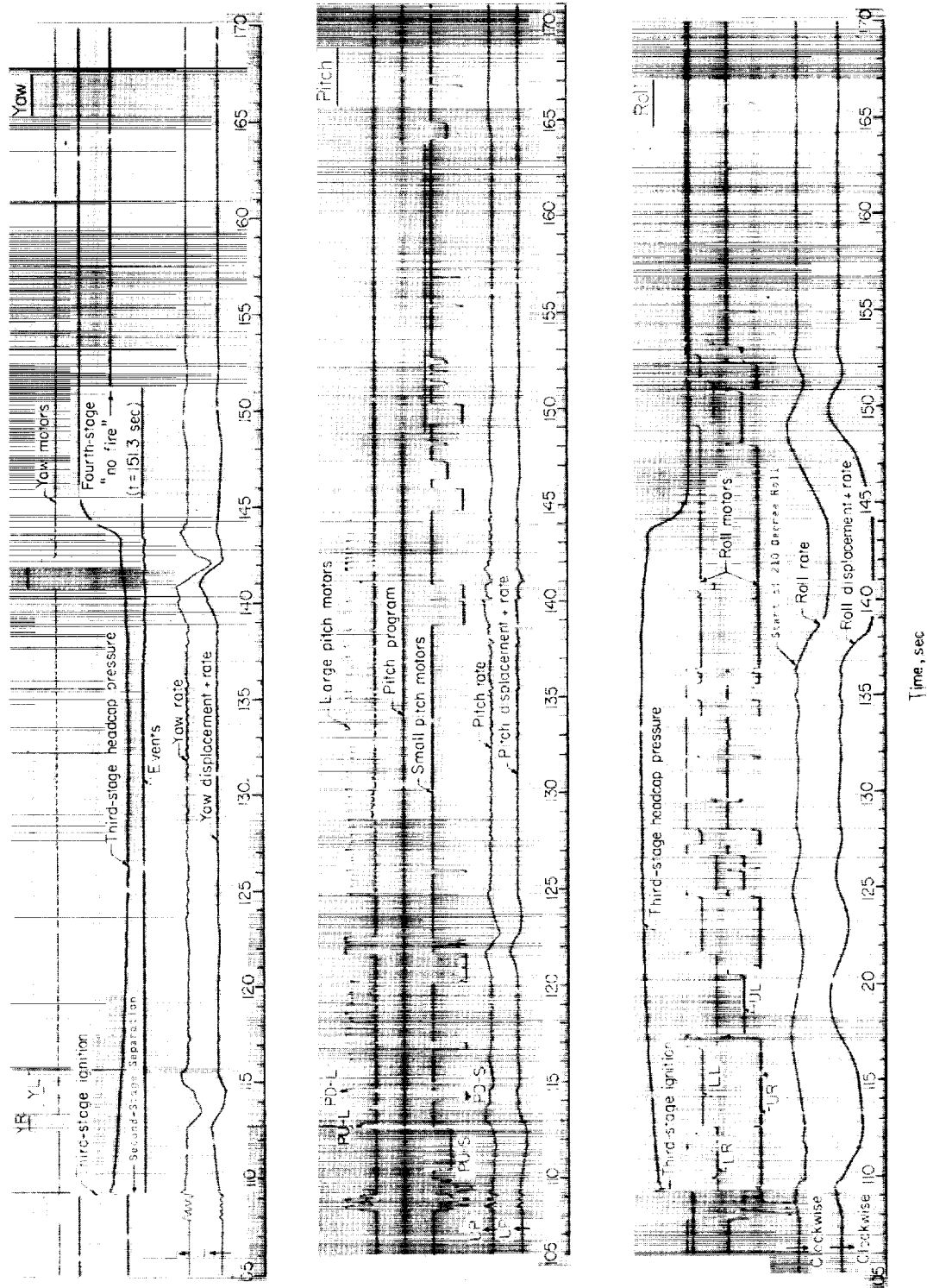
Figure 93.- Sample of guidance telemeter record during third-stage motor thrusting.

220

Second-Stage Headcap Pressure(From Third-Stage Telemeter)

Transverse Acceleration

Accelerations from Yaw Reaction Control Motors

Normal Acceleration

Accelerations from Pitch Reaction Control Motors

Transverse Acceleration

Normal Acceleration

Angular Roll Rates

Angular Pitch Rates

Angular Yaw Rates

Rates From Yaw Reaction Control Motors

Longitudinal Acceleration

65   70   75   80   85   90   95   100

Time,sec

Figure 94.- Sample payload records during second-stage motor burning.

L-1924

L-1924

Third-Stage Headcap Pressure(From Third-Stage Telemeter)

Third-Stage Ignition

Transverse Acceleration

Normal Acceleration

Transverse Acceleration

Accelerations from Yaw Reaction Control Motors

Normal Acceleration

Accelerations from Pitch Reaction Control Motors

Roll Rate during period vehicle rolled approximately 210 degrees and lost guidance roll reference.

Angular Roll Rates

Angular Pitch Rates

Angular Yaw Rates

Longitudinal Acceleration

Third-Stage Ignition

Time, sec

Figure 95.- Sample payload records during third-stage motor burning.

222
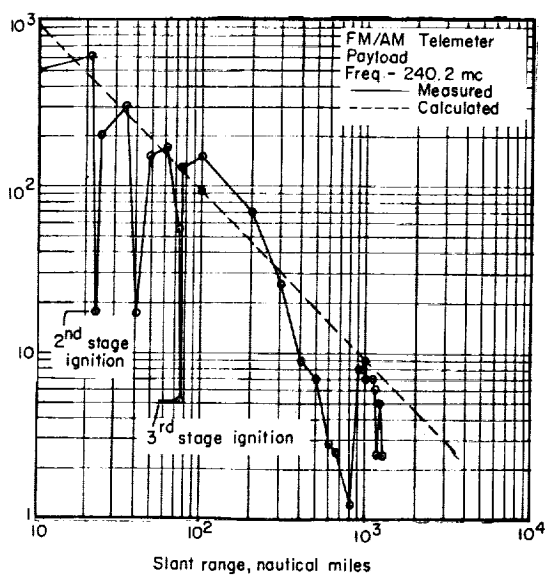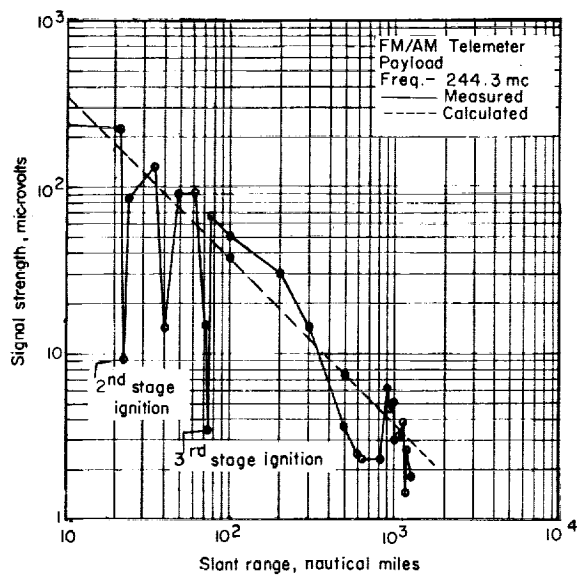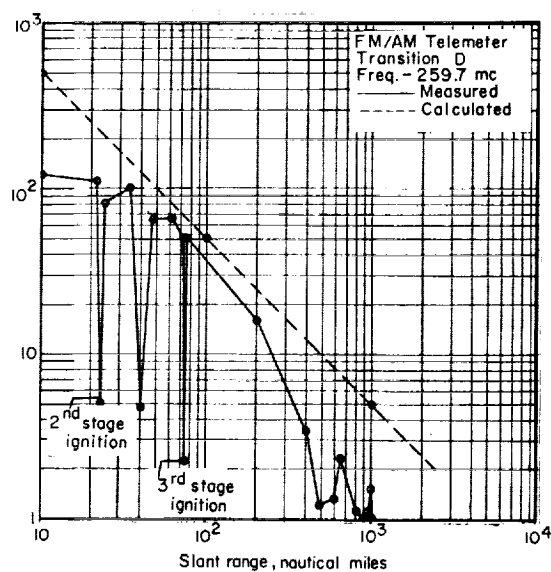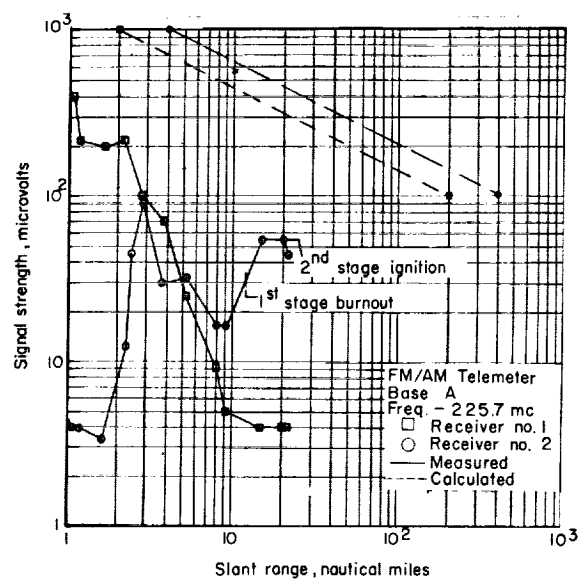
Figure 96.- Variation of telemeter signal strength with slant range.

L-1924
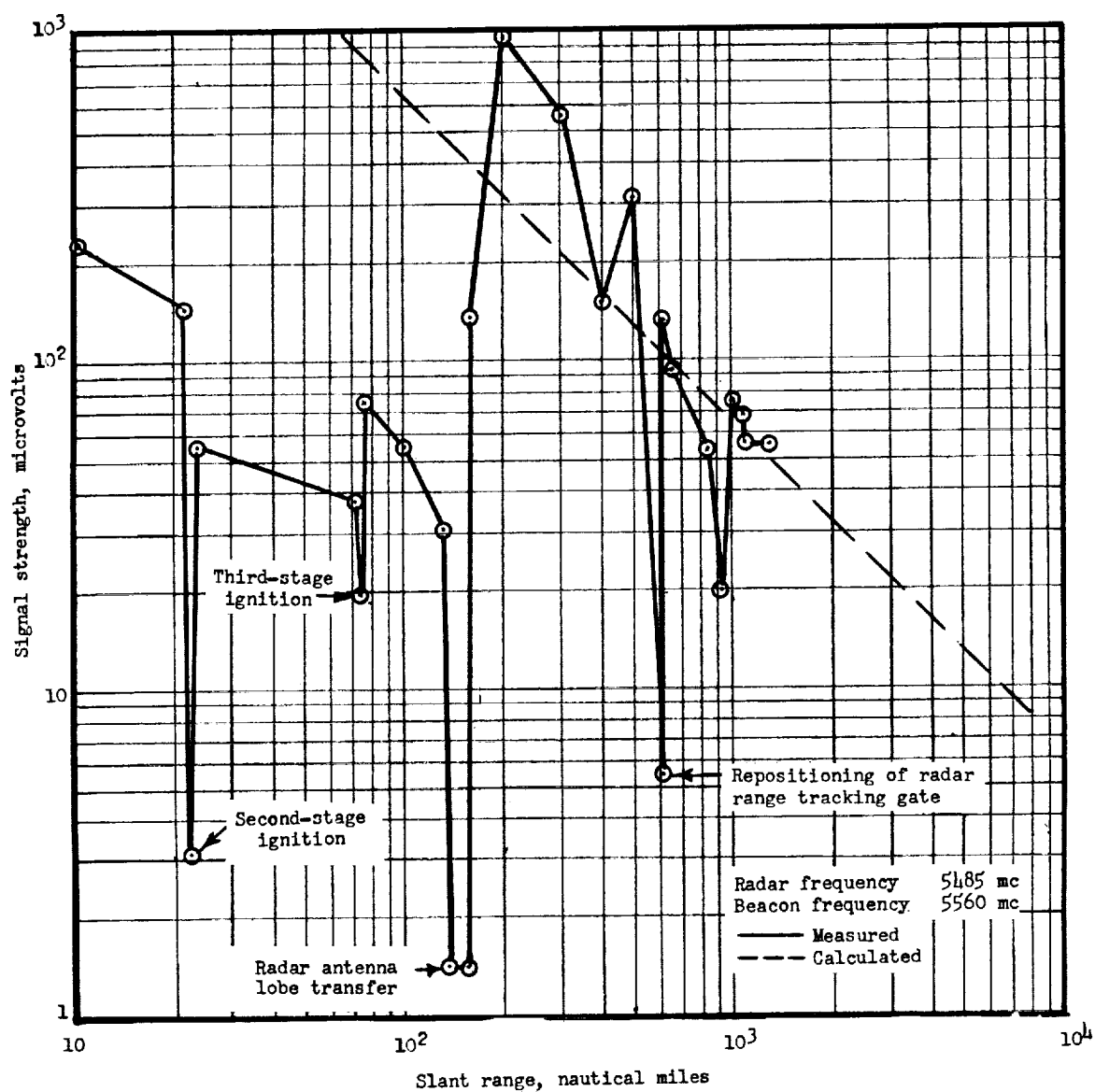
Figure 97.- Variation of FPS-16 C-band radar receiver signal strength with slant range.
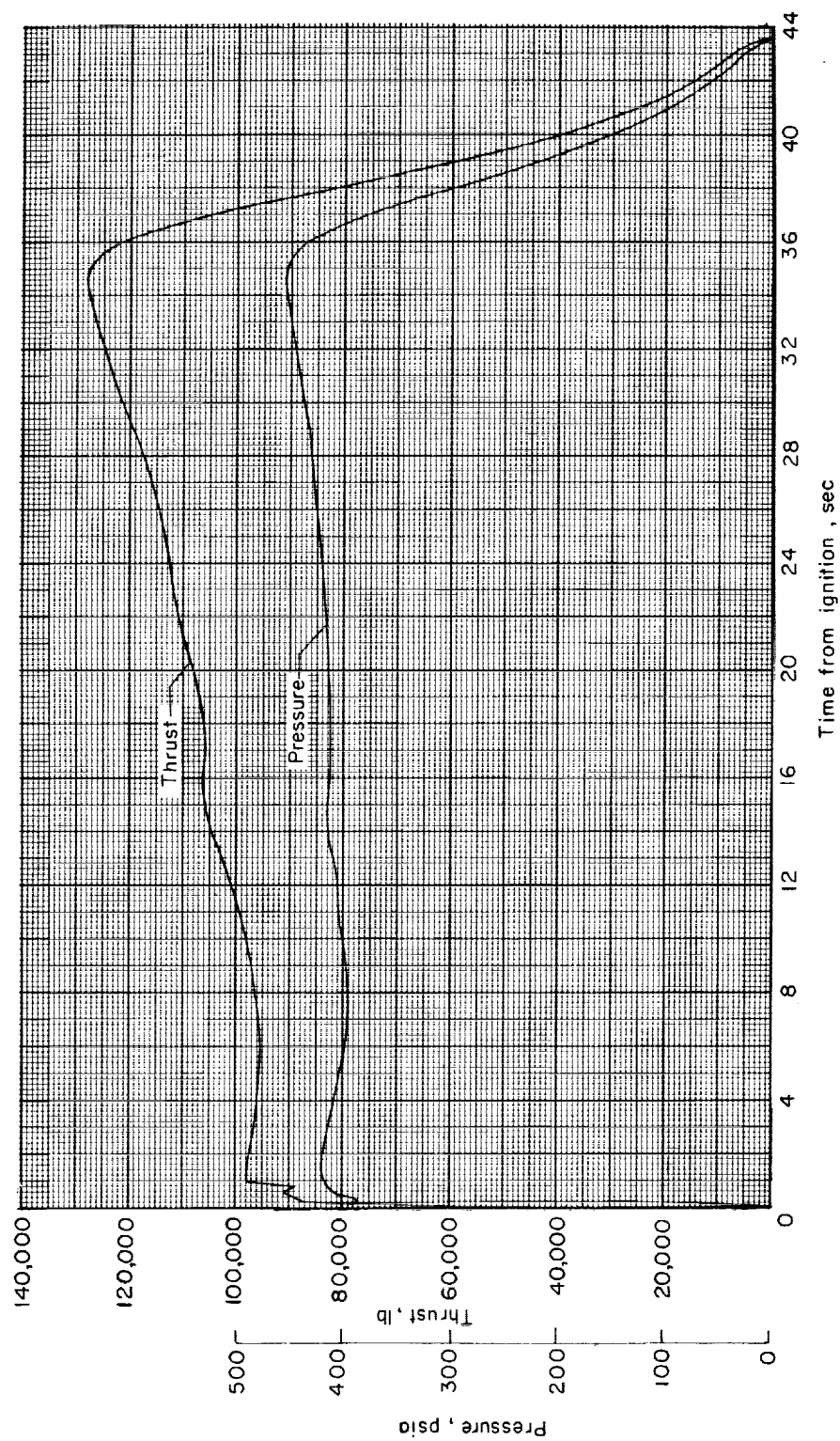
Figure 98.- Time history of Algol chamber pressure and thrust.

L-1924

L-1924
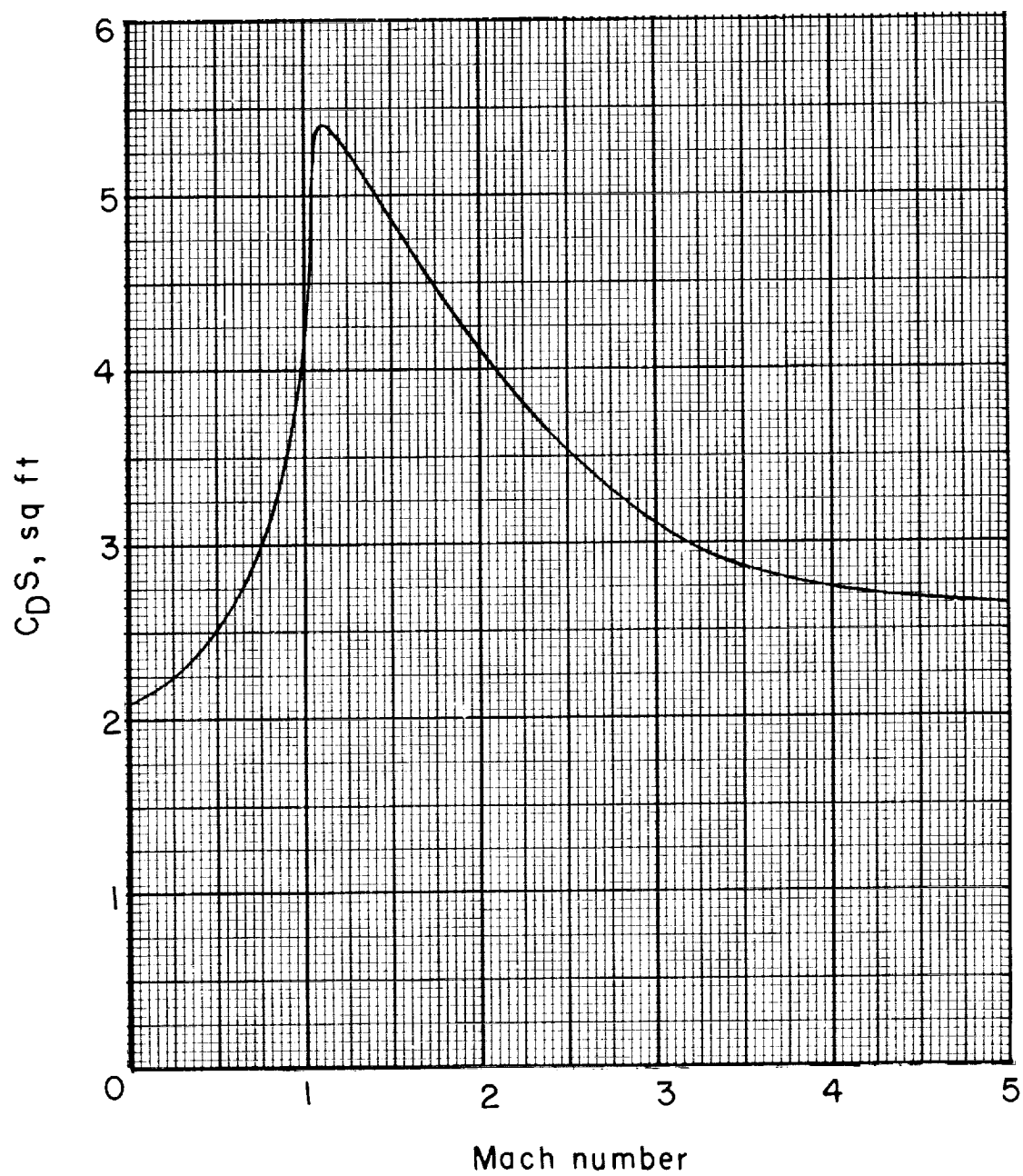
Figure 99.- Variation of the parameter C_DS with Mach number for vehicle during Algol thrusting.
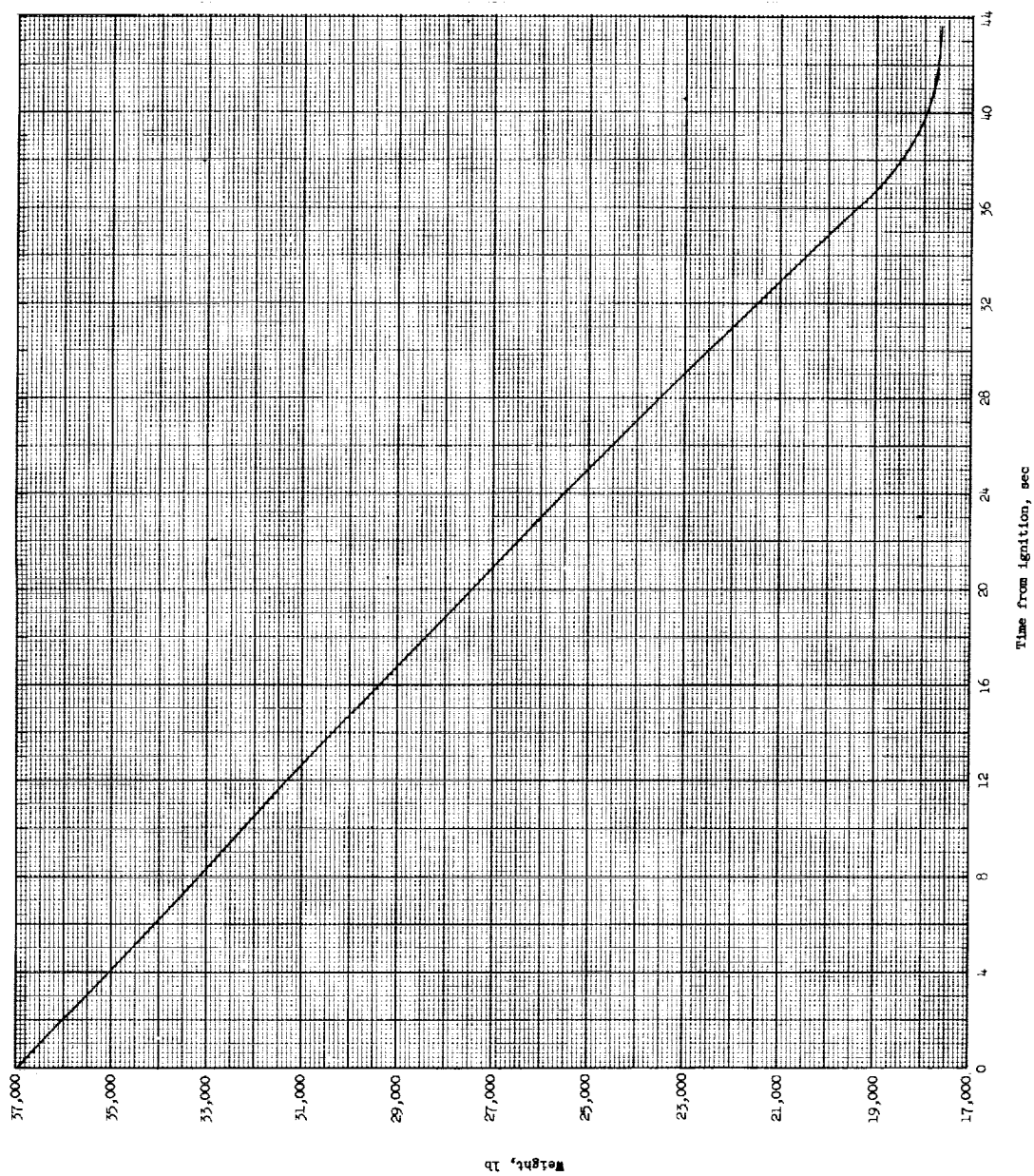
Figure 100.- Time history of calculated vehicle weight during Algol thrusting.

L-1924

L-1924
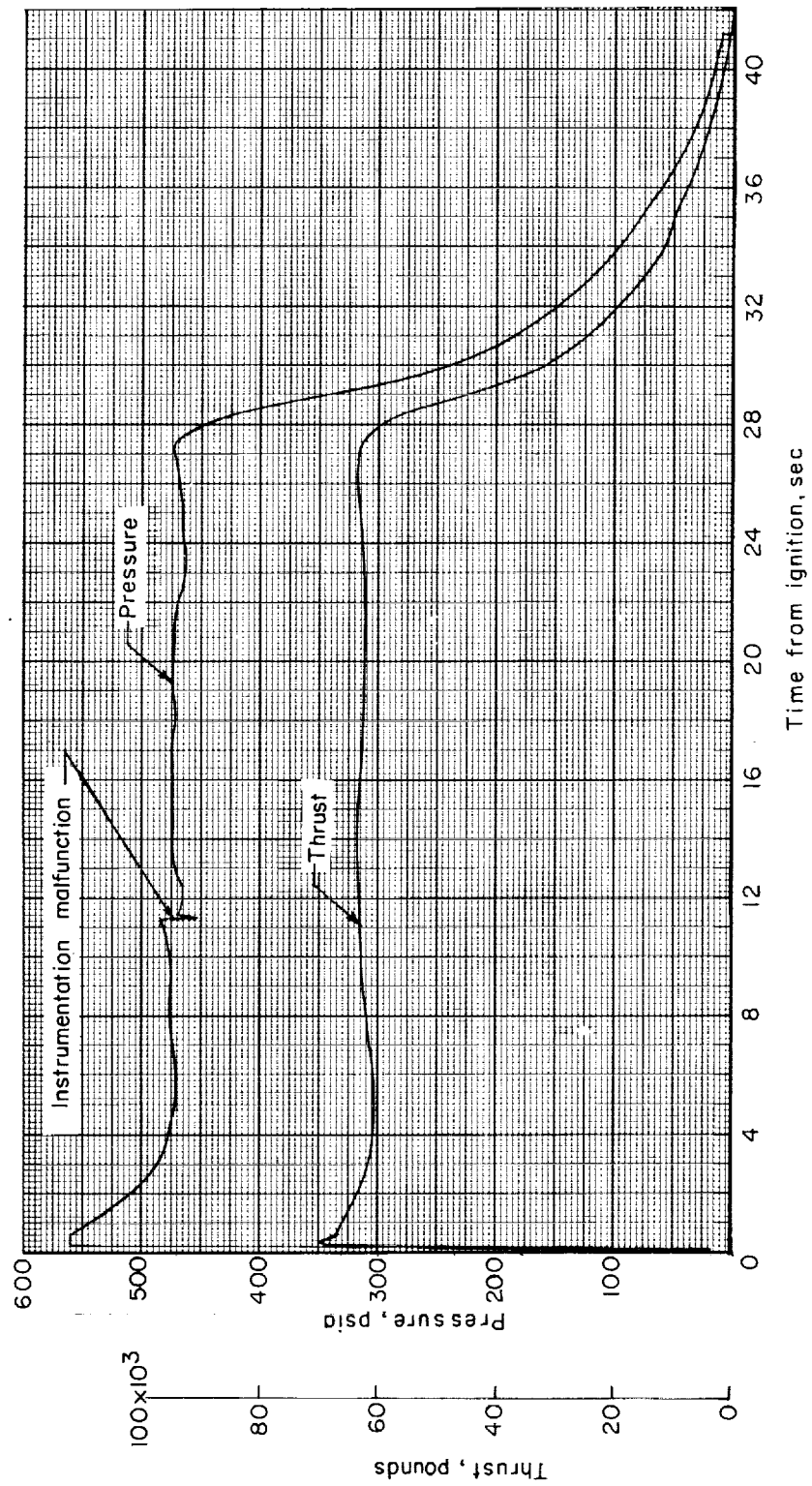
Figure 101.- Time history of chamber pressure and thrust of Castor.
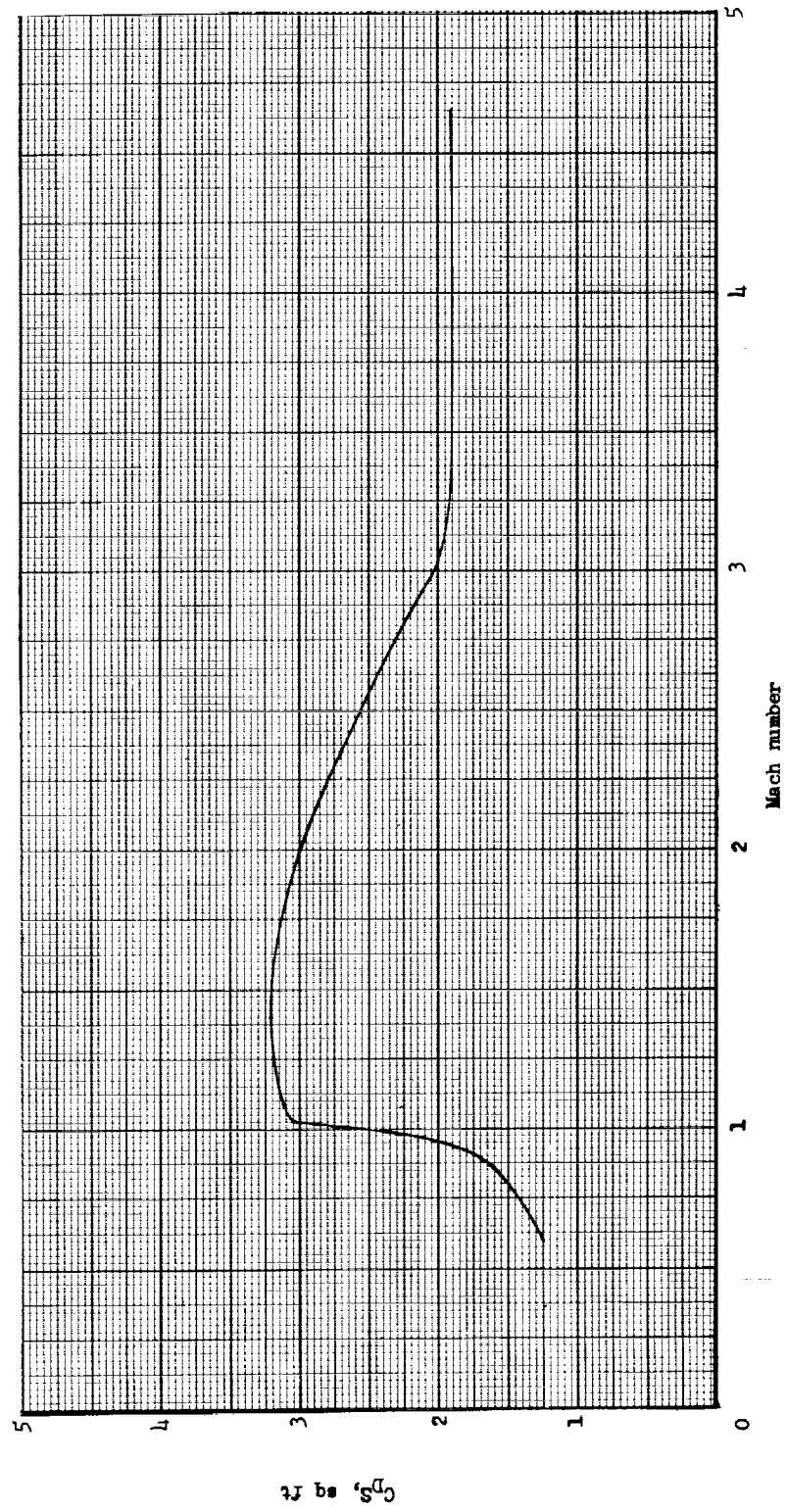
Figure 102.- Variation of the parameter $C_D S$ with Mach number during Castor thrusting.

L-1924

L-1924
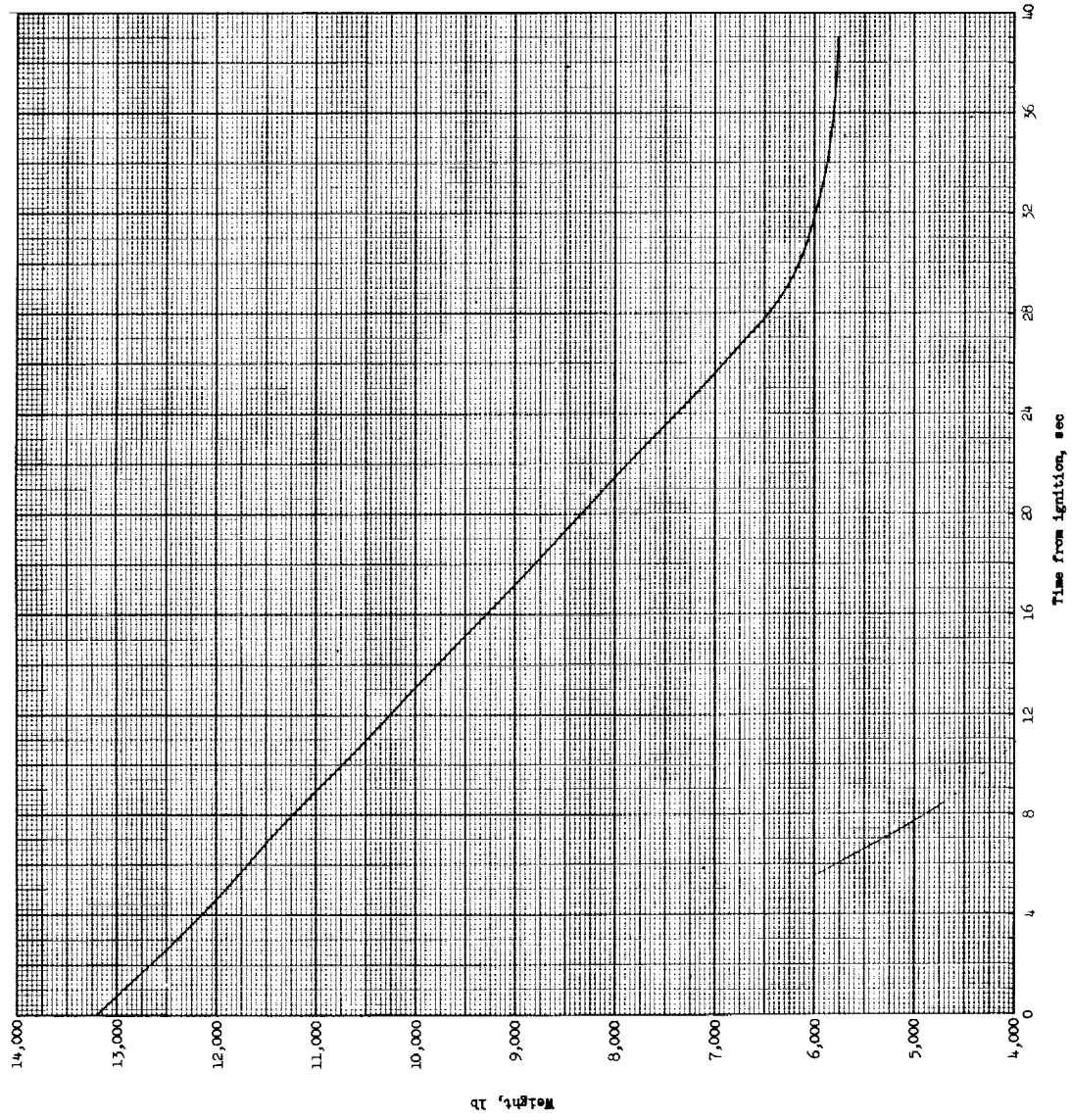
Figure 103.- Time history of calculated vehicle weight during Castor thrusting.

230
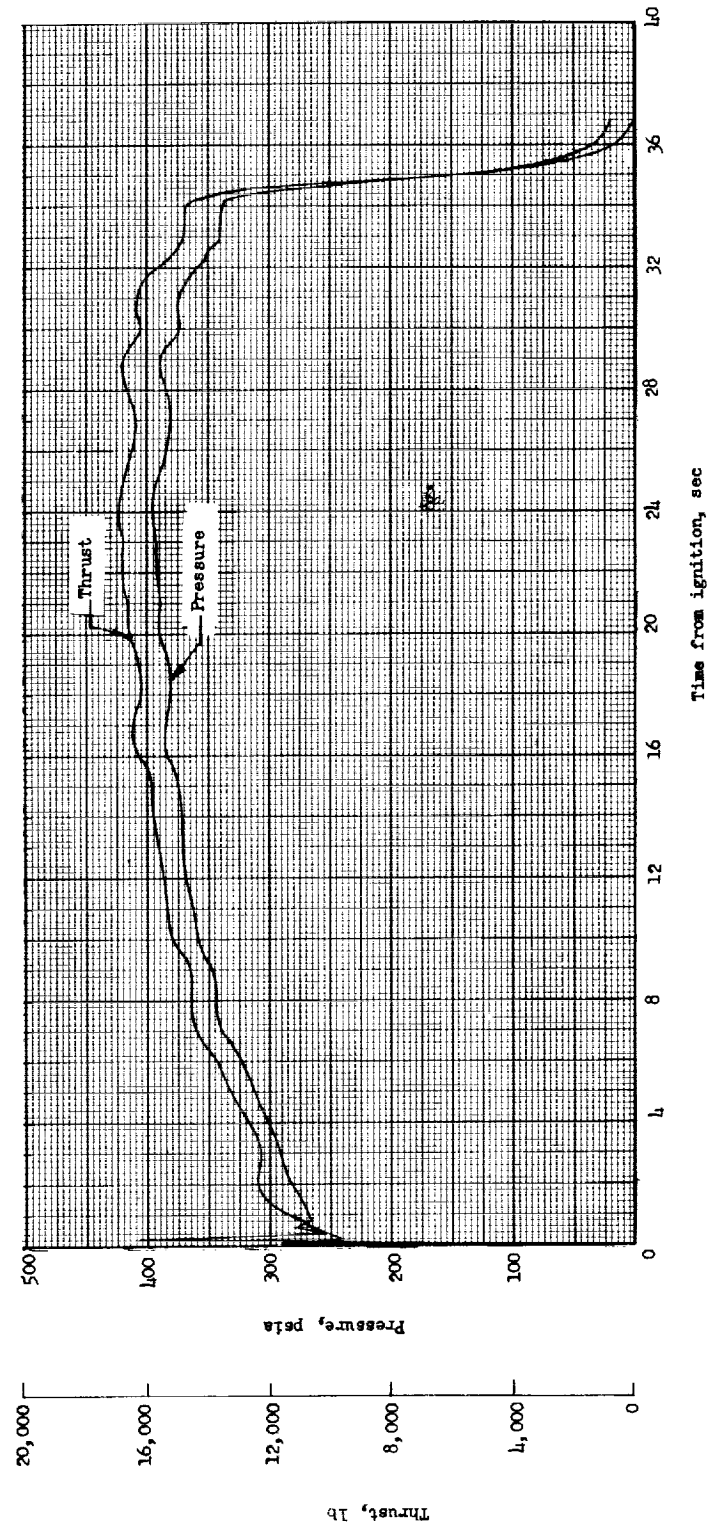
Figure 104.- Time history of chamber pressure and thrust of Antares.

L-1924

L-1924
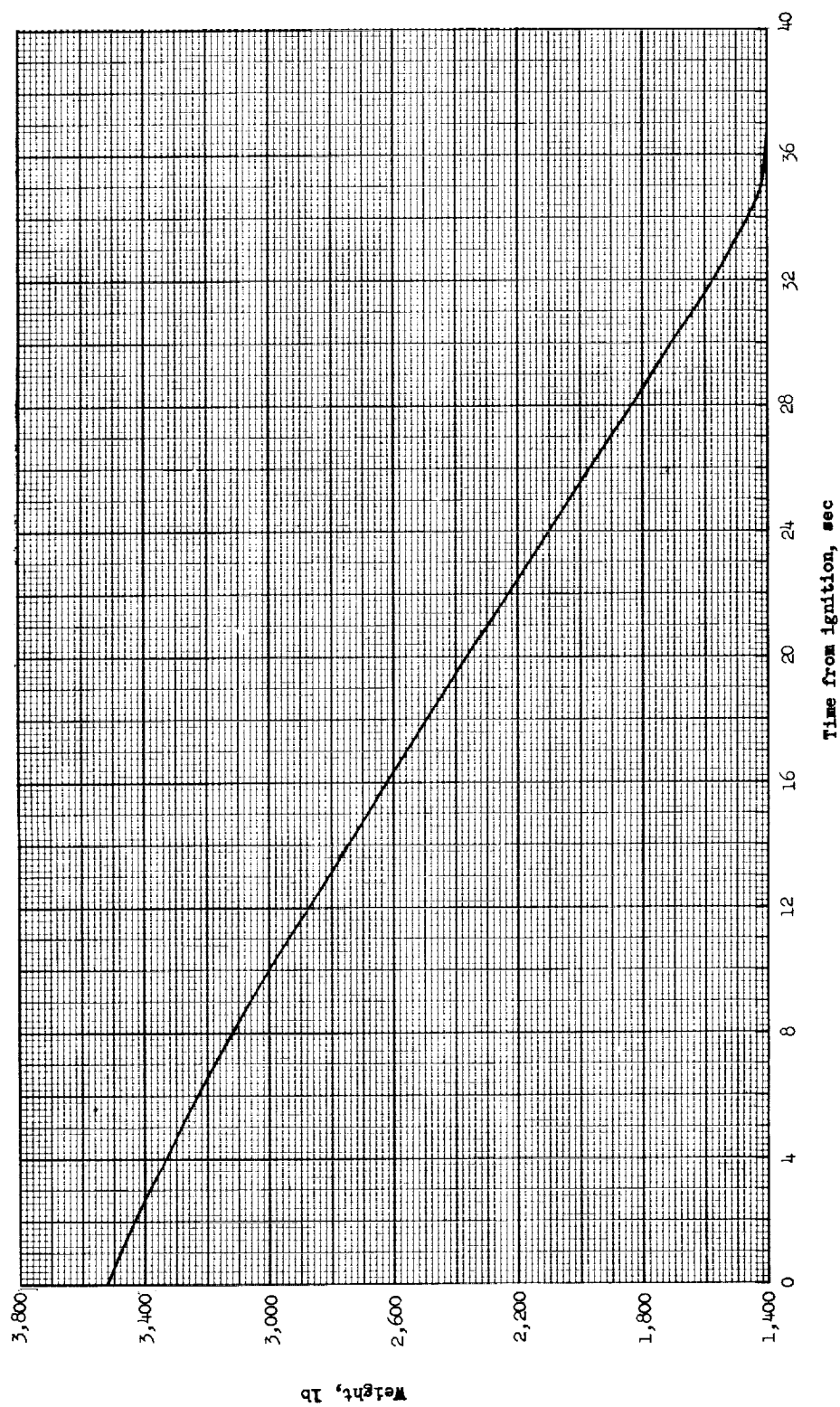
Figure 105.- Calculated vehicle weight during Antares thrusting.
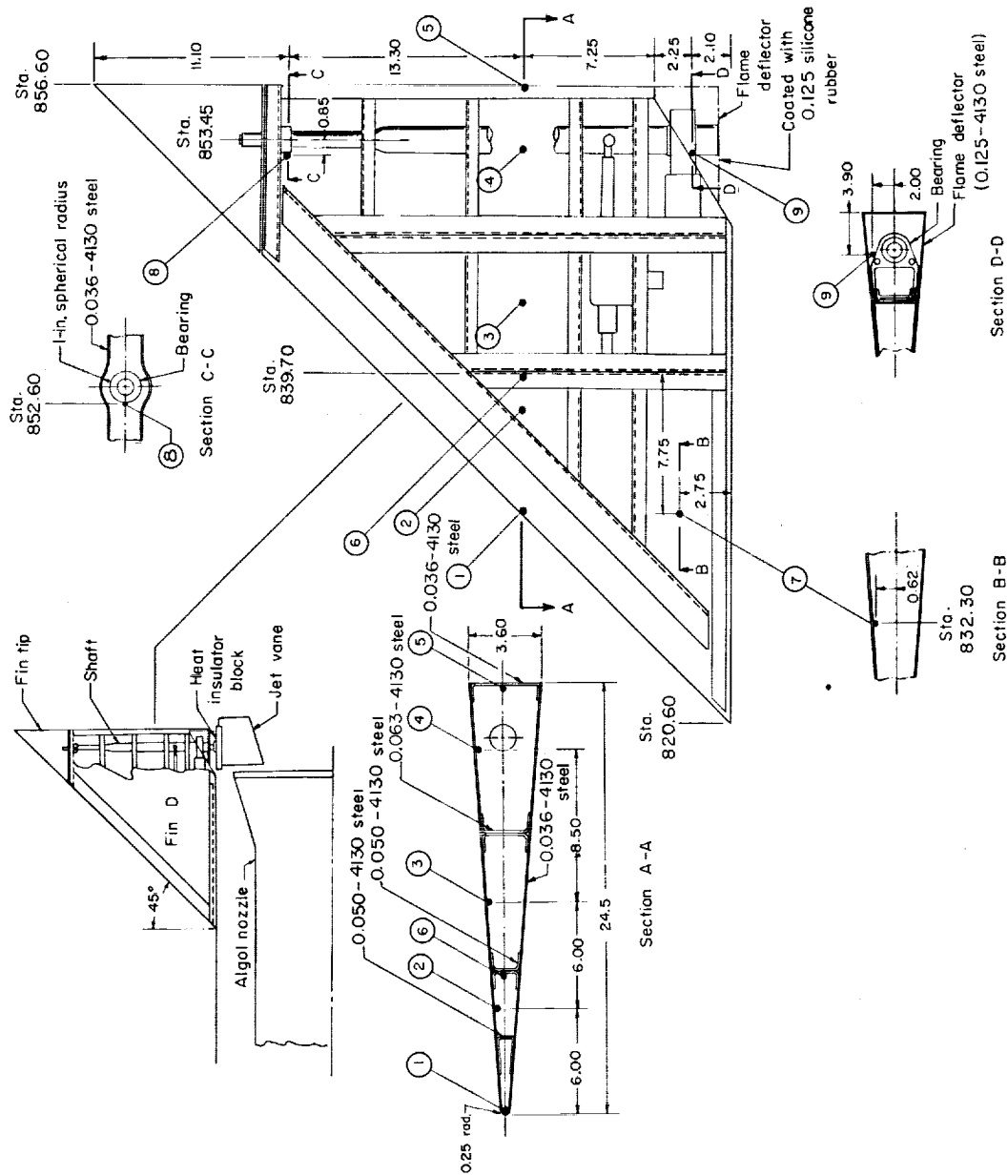
Figure 106.- Drawing of base A fin showing thermocouple locations. Locations are denoted by numbered circles. All dimensions are in inches unless otherwise noted.

L-1924

L-1924
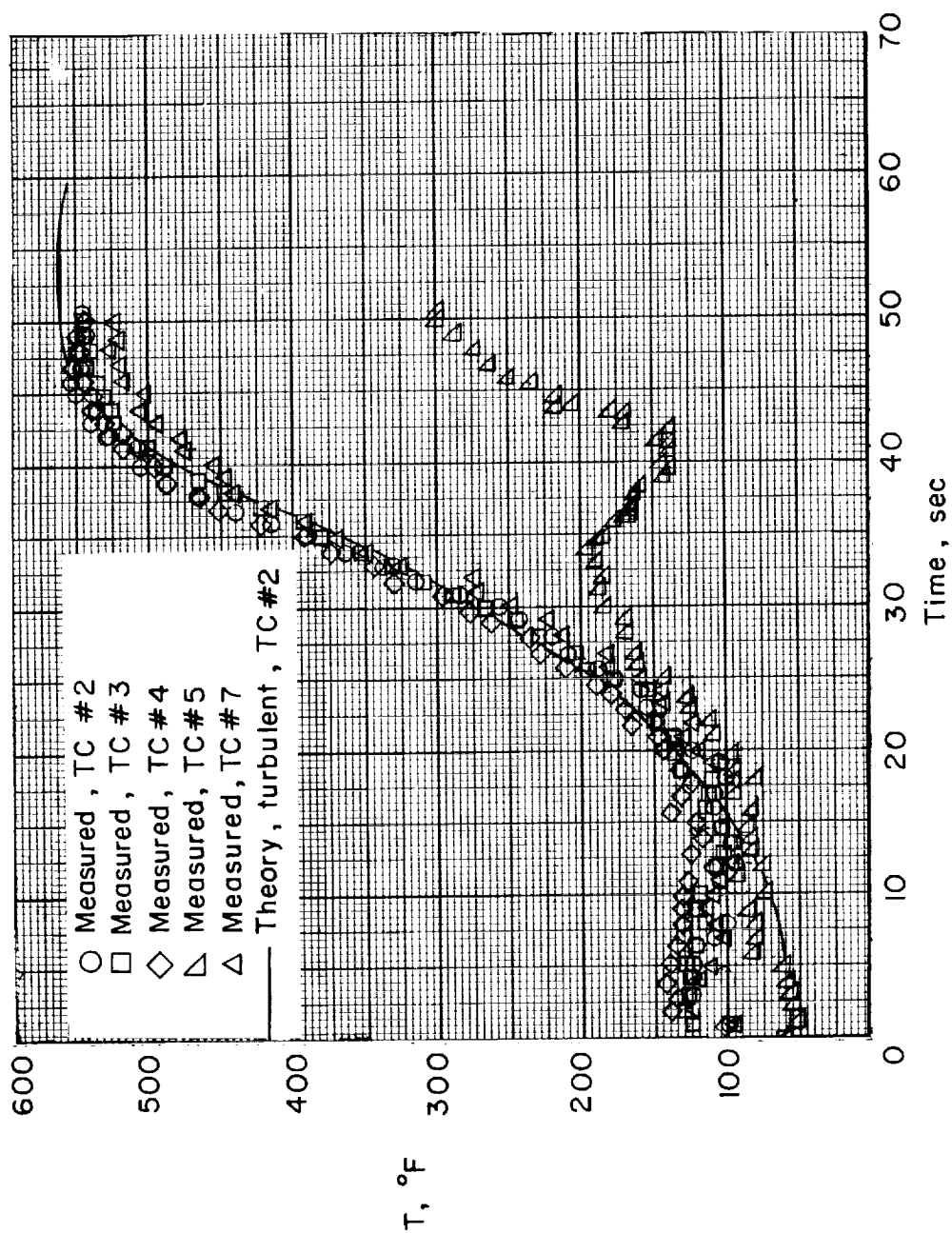
(a) Base A fin, skin.

Figure 107.- Time histories of base A fin temperatures.
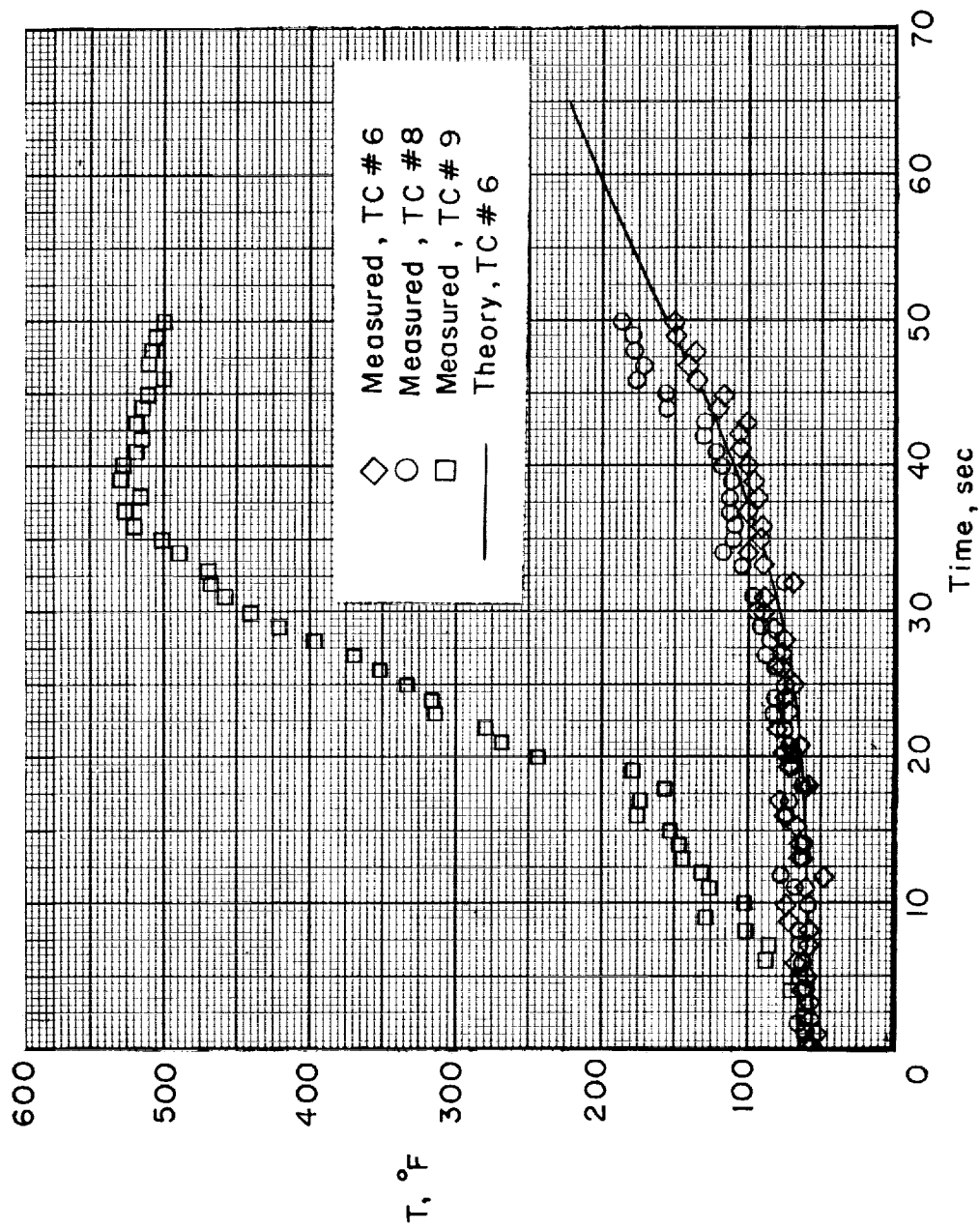
(b) Base A fin, internal.

Figure 107.- Concluded.

L-1924

Figure 108.- Drawing of transition D showing thermocouple locations. Locations are denoted by numbered circles. All dimensions are in inches unless otherwise noted.
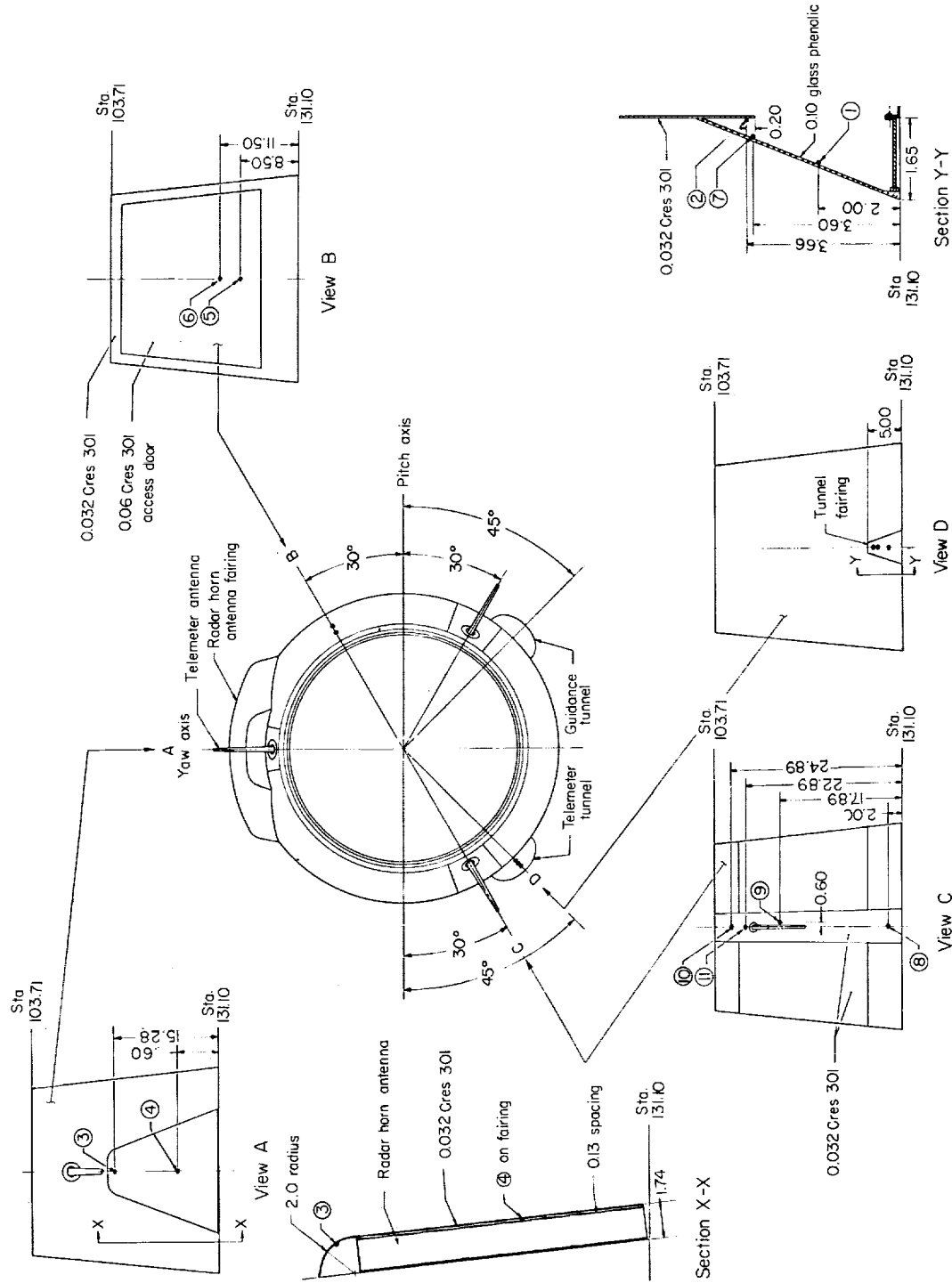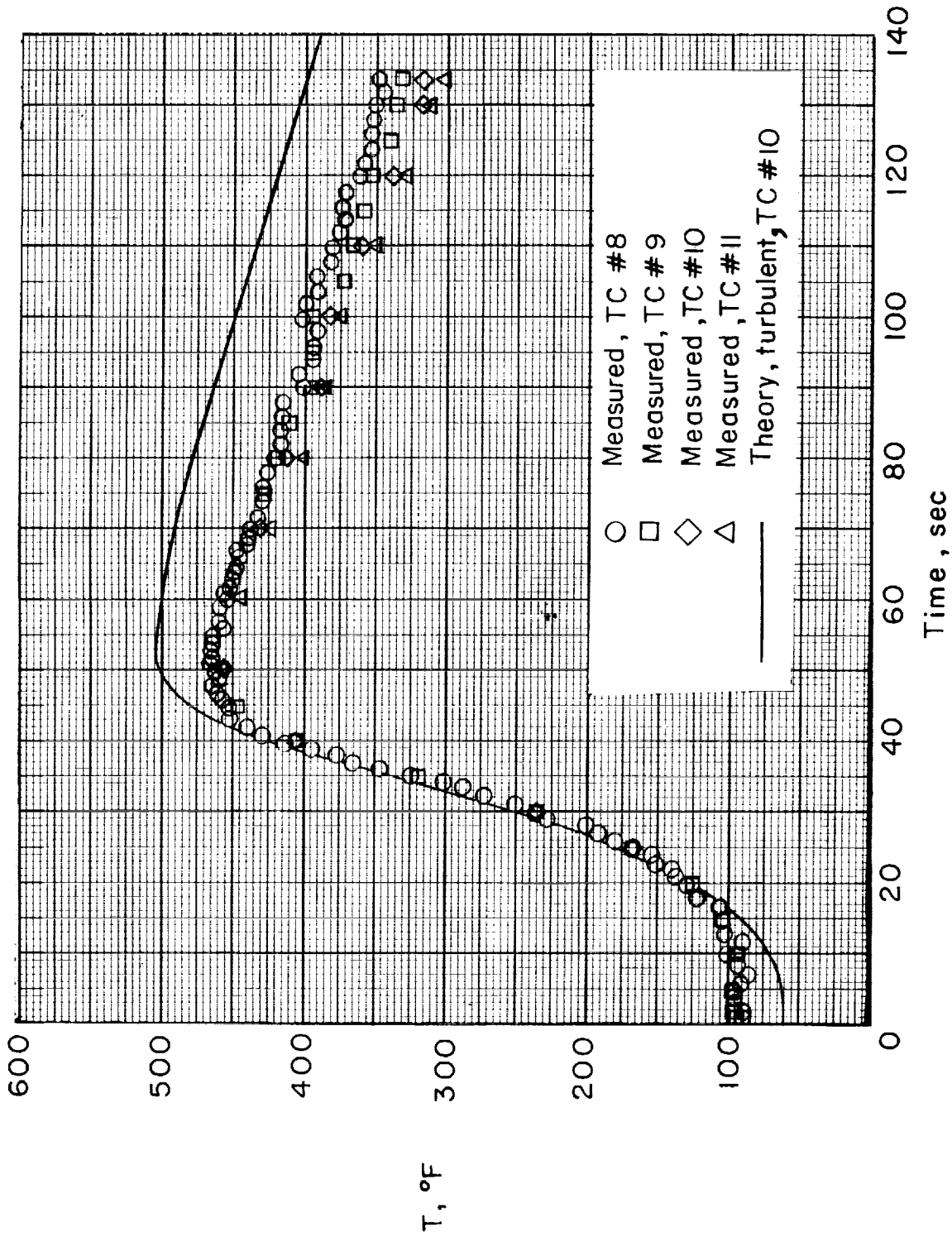
(a) Transition D, skin

Figure 109.- Time histories of transition D temperatures.

L-1924
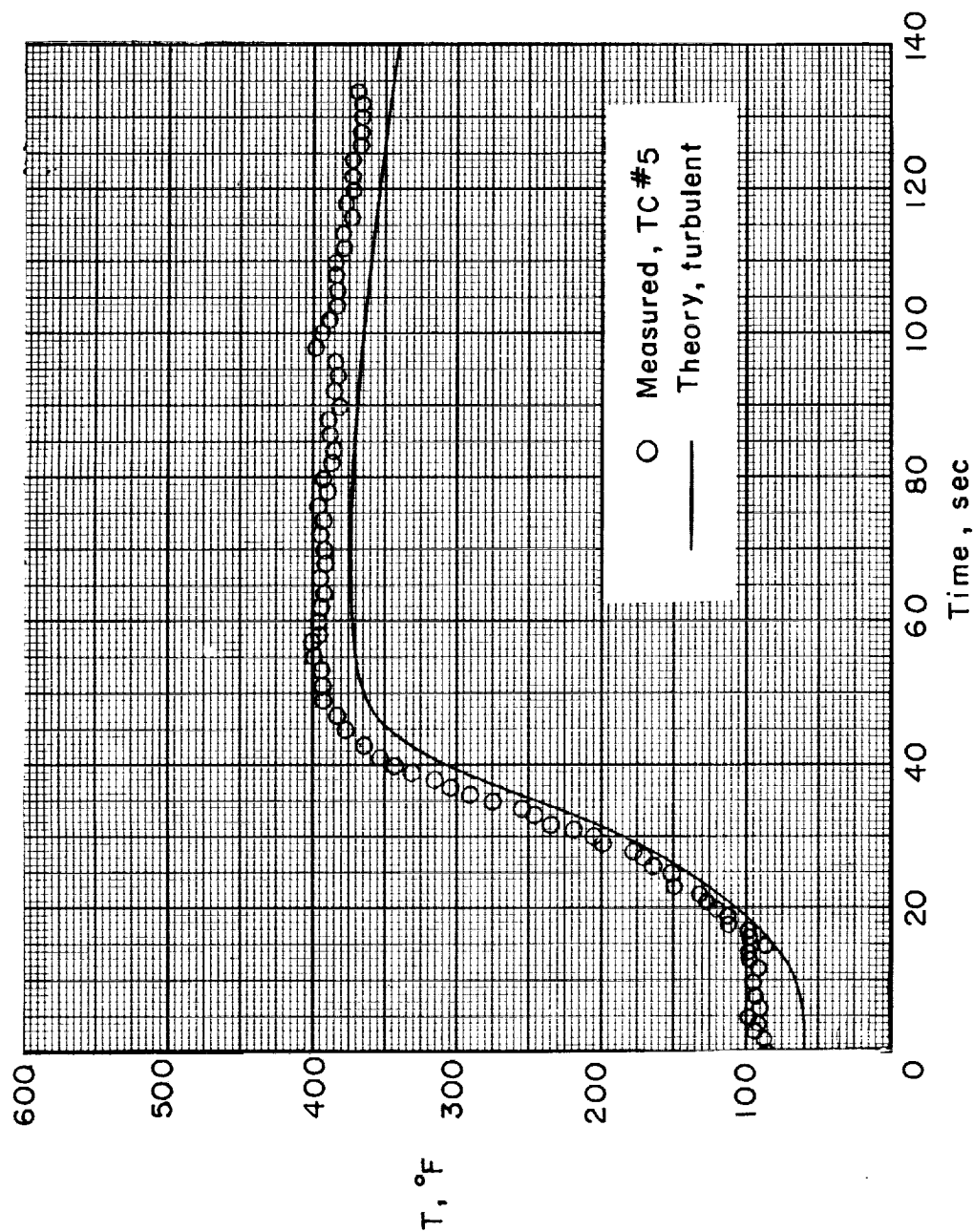
(b) Transition D, access door.

Figure 109.- Continued.
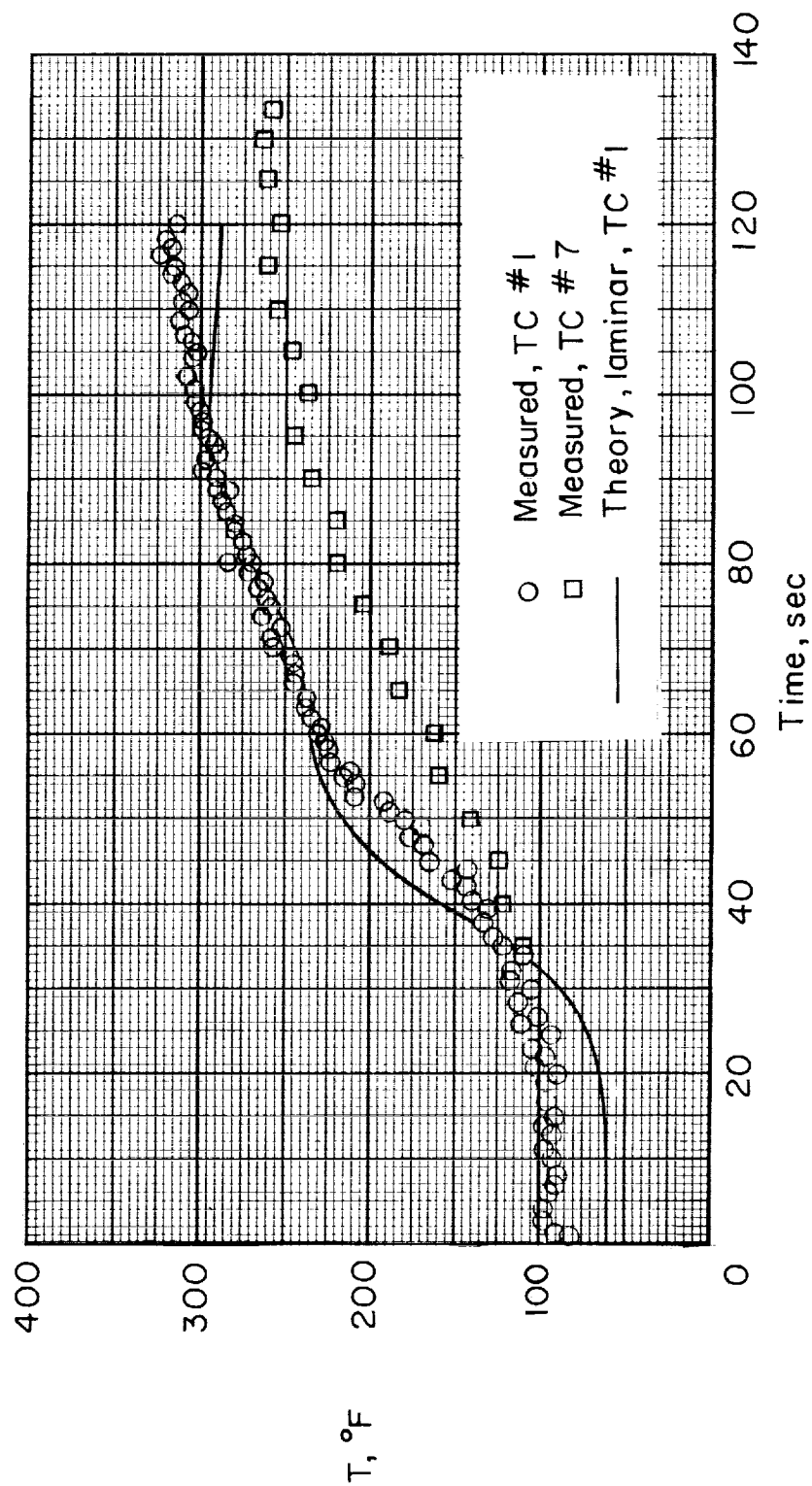
(c) Transition D, electrical conduit fairing.

Figure 109.- Continued.
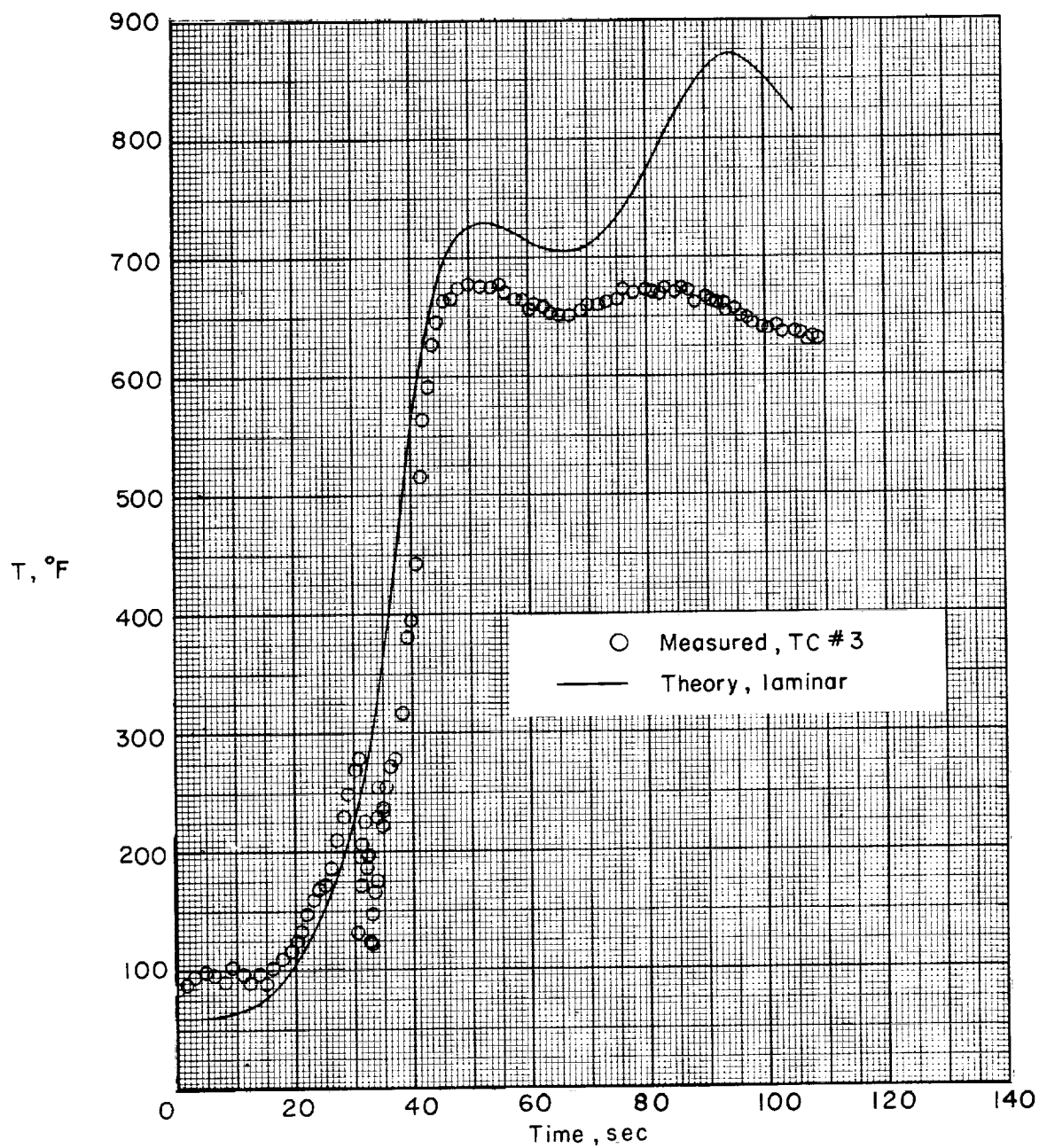
(d) Transition D, horn antenna.

Figure 109.- Concluded.

240
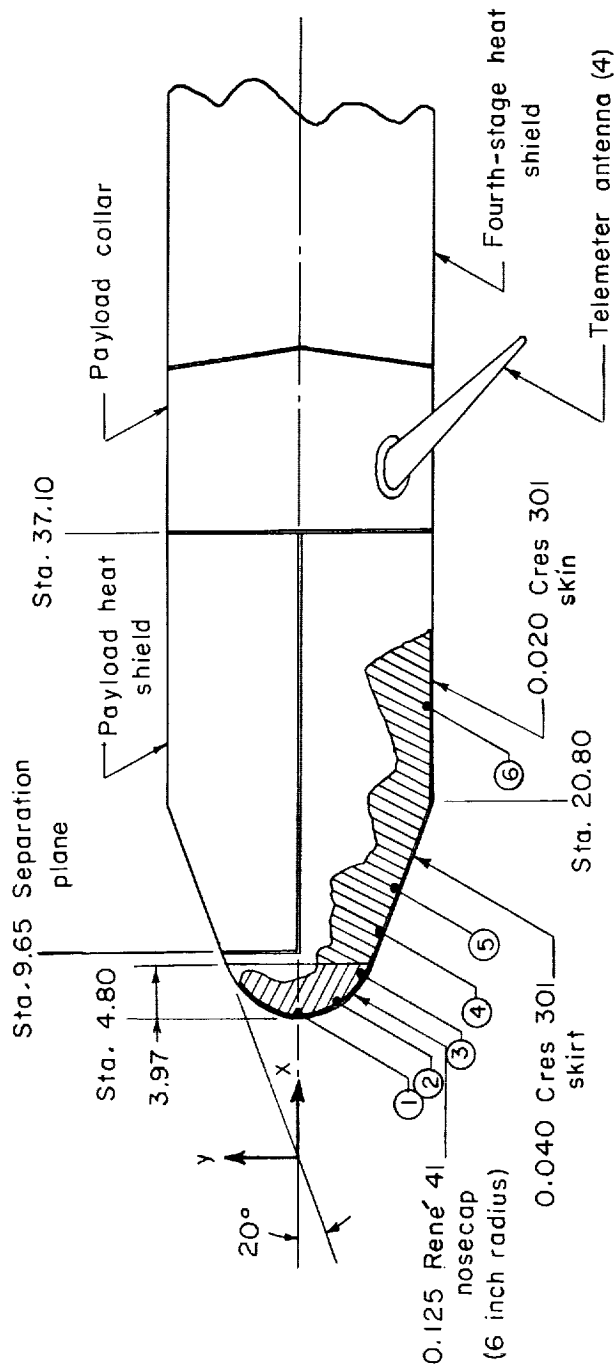
Thermocouple number	Position, in	
	x (sta.)	y
1	4.93	0
2	5.80	-3.20
3	8.00	-5.20
4	11.11	-6.40
5	14.49	-7.40
6	28.36	-10.00

Note :

All thermocouples located in pitch plane.

Skin coated externally with chrome oxide.

Figure 110.- Drawing of payload heat shield showing thermocouple locations. Locations are denoted by numbered circles. All dimensions are in inches unless otherwise noted.

L-1924

L-1924
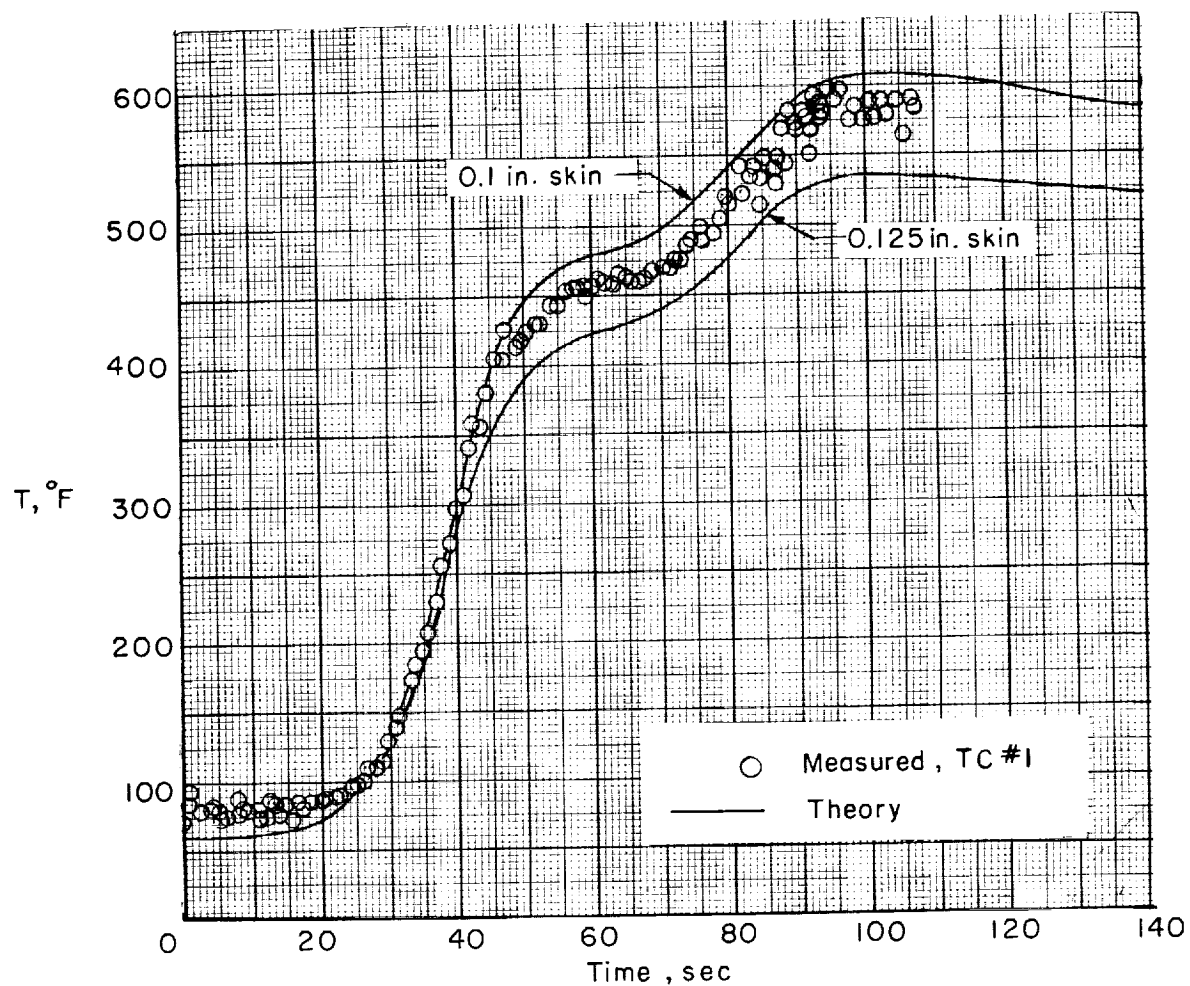
(a) Stagnation point.

Figure 111.- Time histories of calculated and measured payload heat-
shield temperatures. Calculated values are obtained from theory for
uncoated skin.
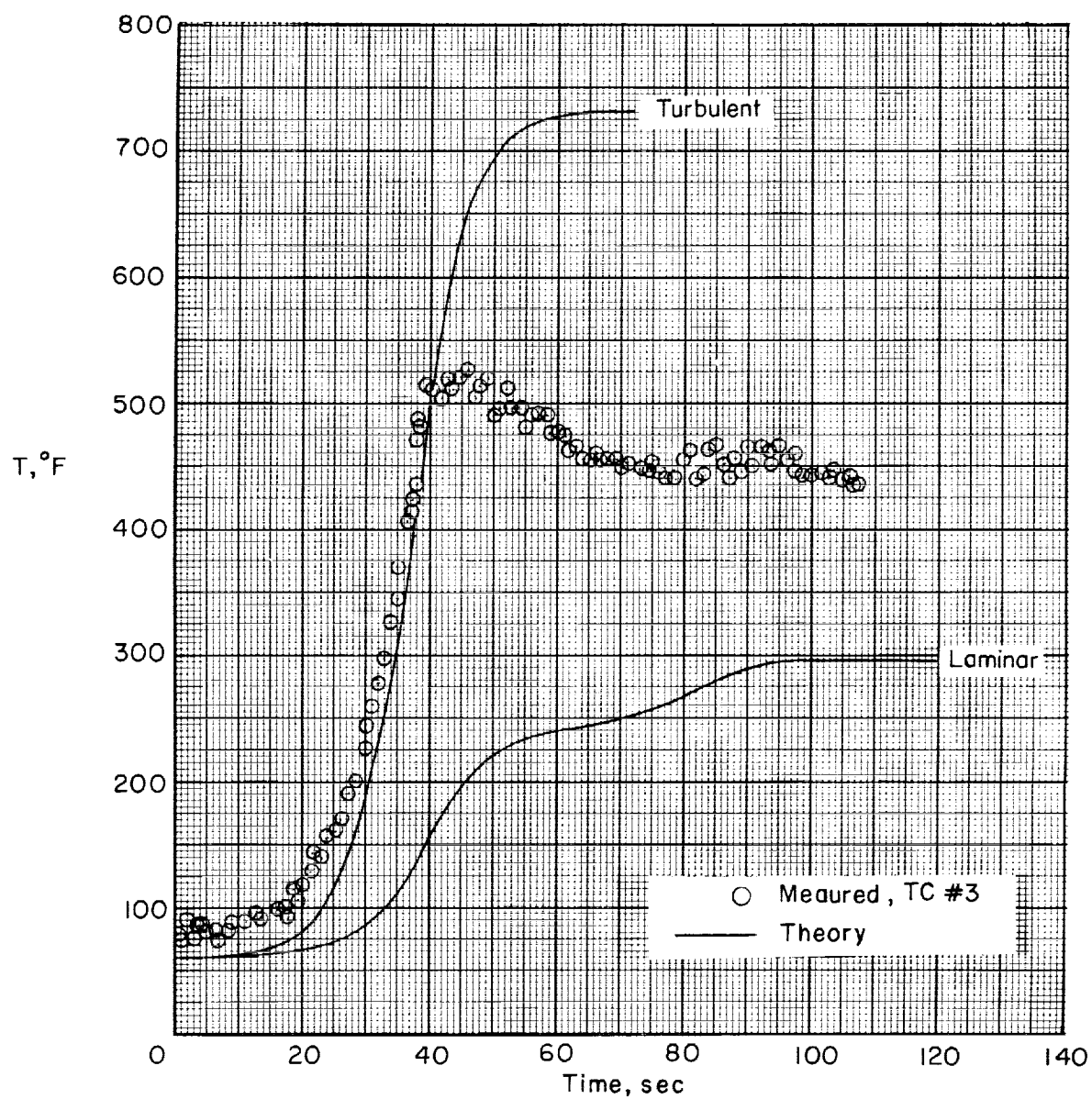
(b) Hemispherical section.

Figure 111.- Continued.
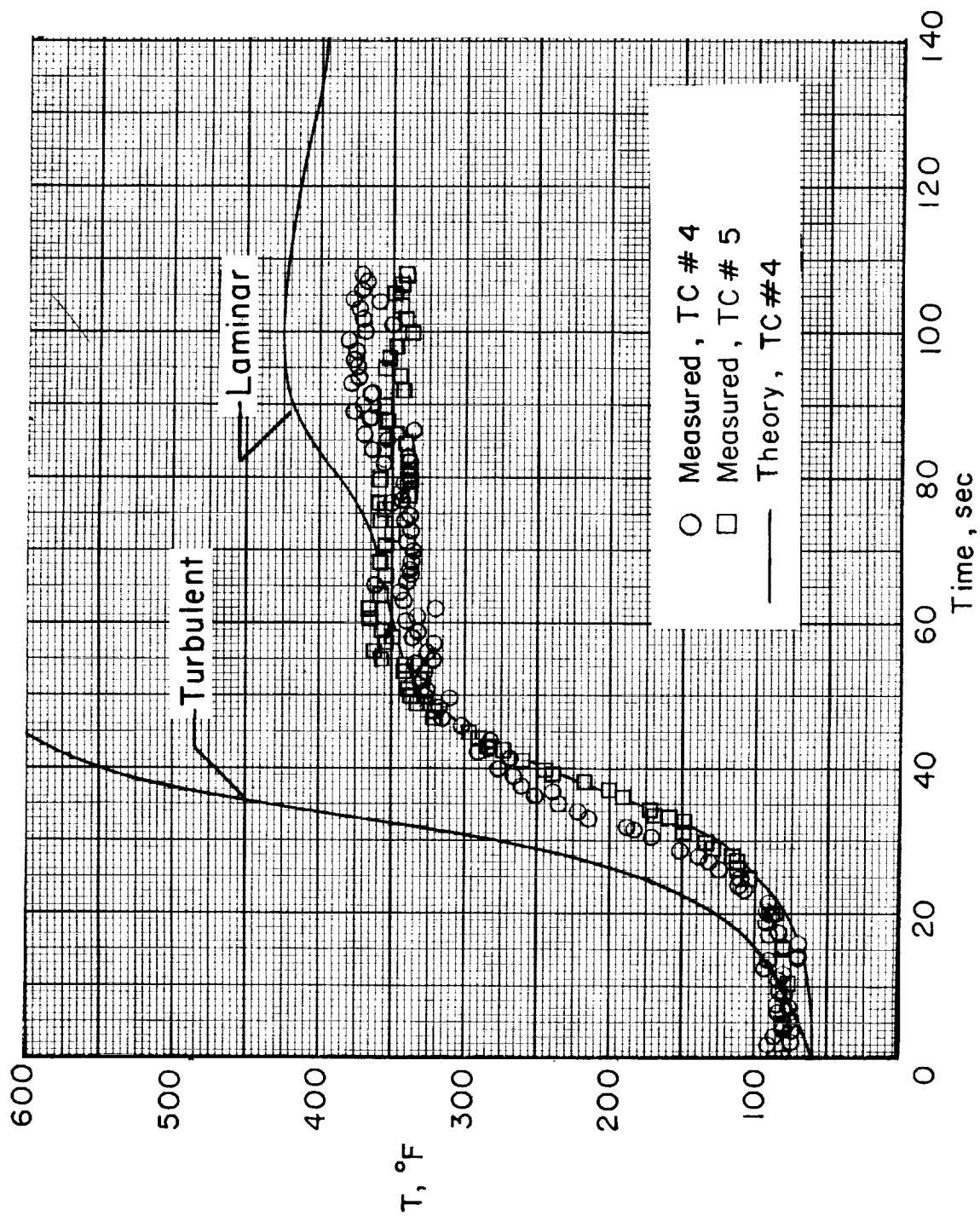
(c) Conical section.

Figure 111.- Continued.
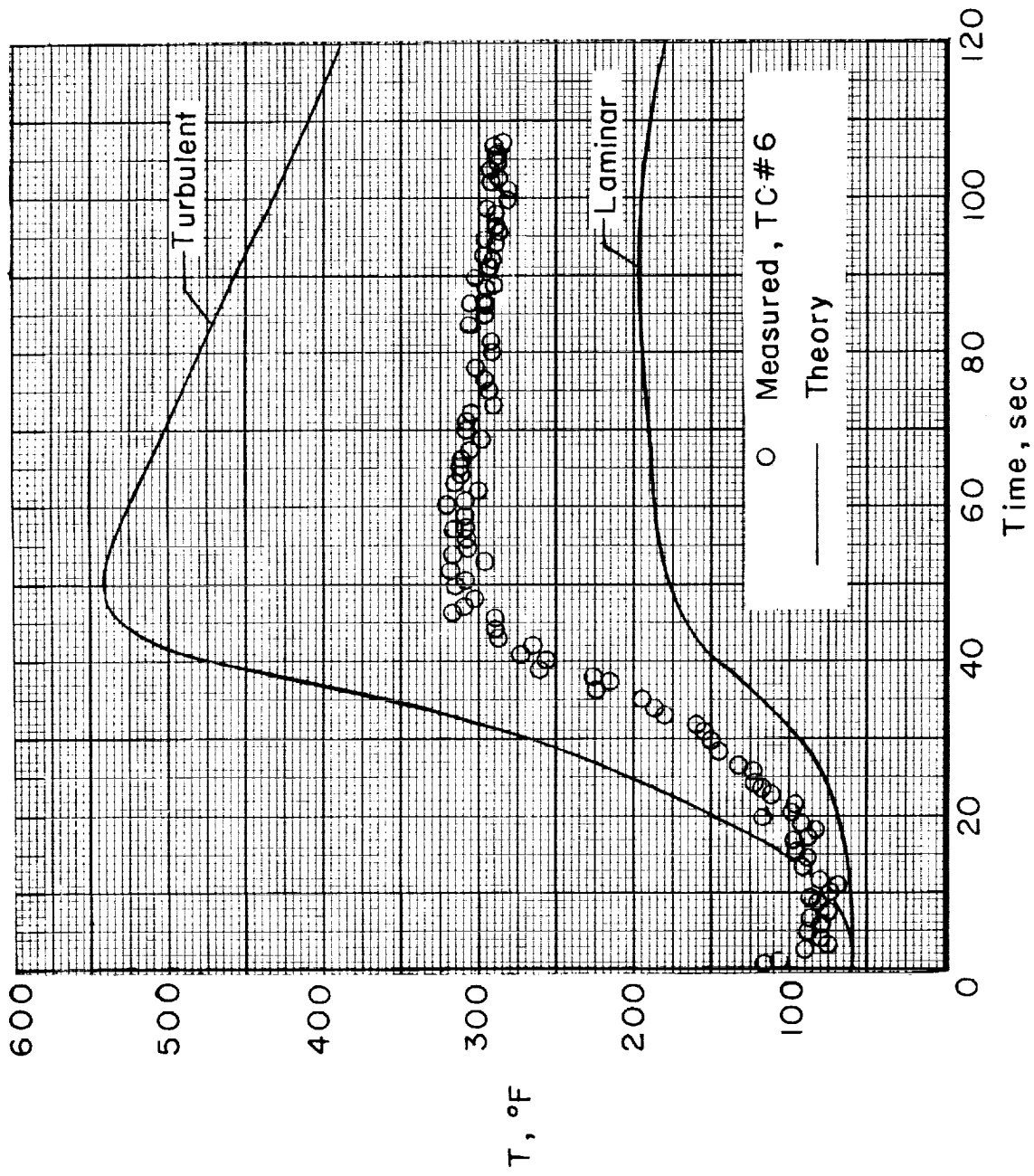
(d) Cylindrical section.

Figure 111.- Concluded.

L-1924
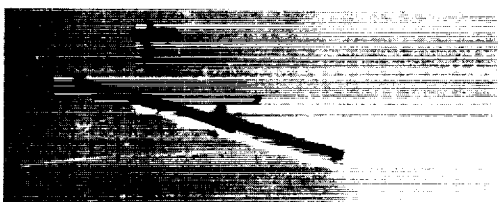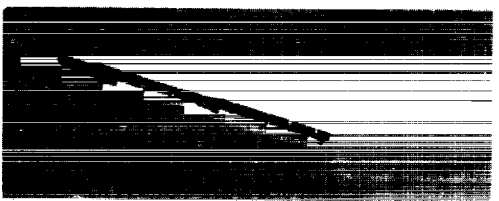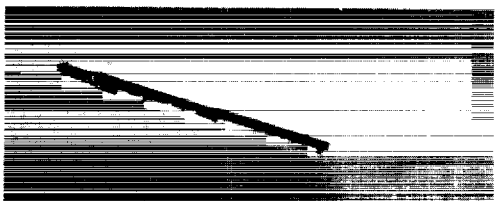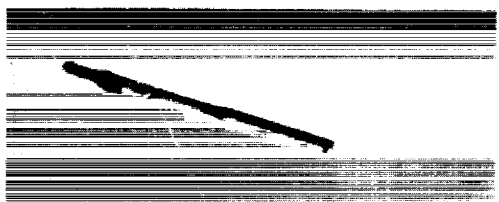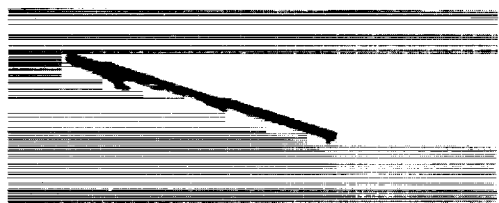
L-61-33

Figure 112.- Photo sequence of breakup of third-stage heat shield.

L-61-34
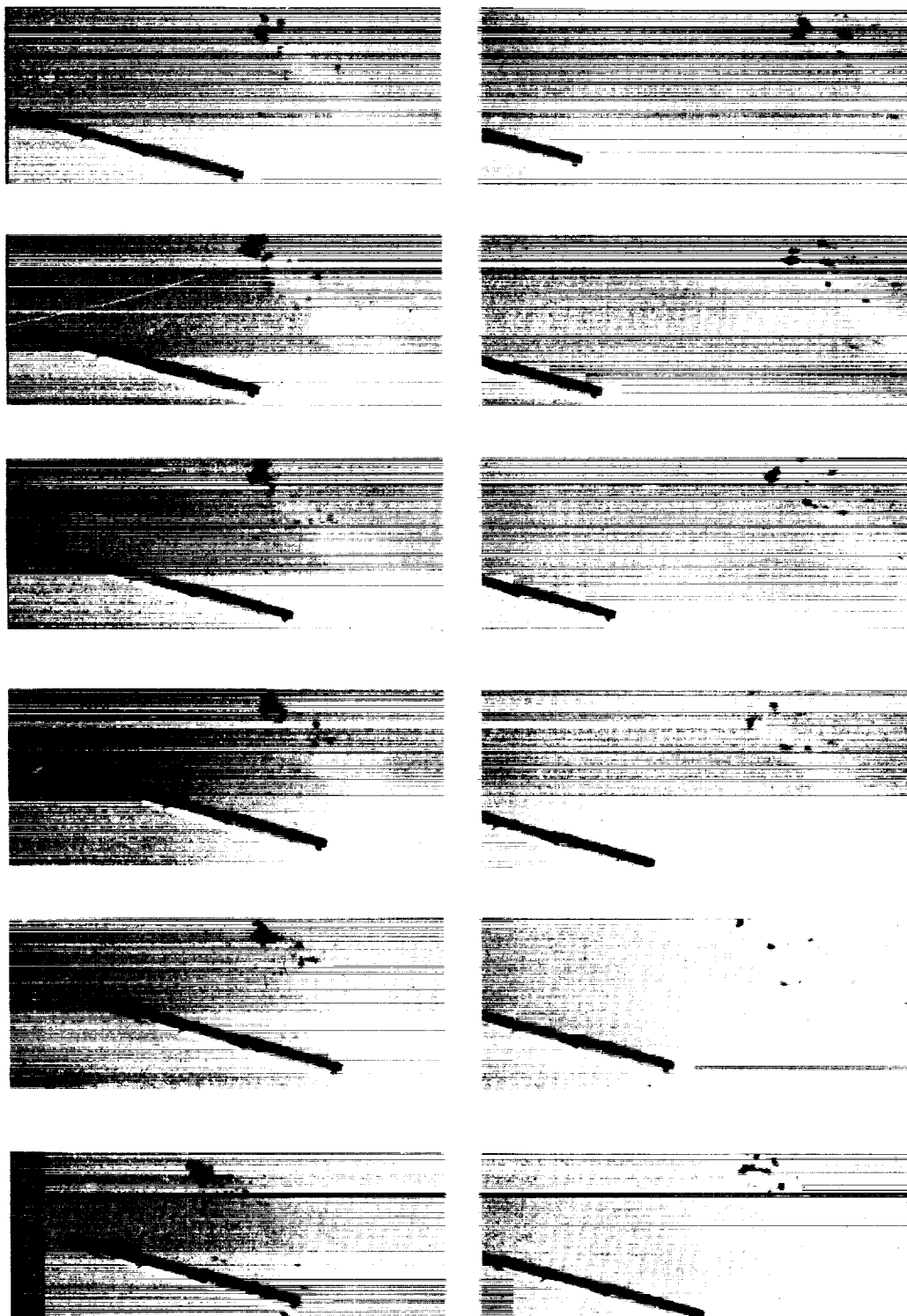
L-1924

Figure 112.- Concluded.

L-1924
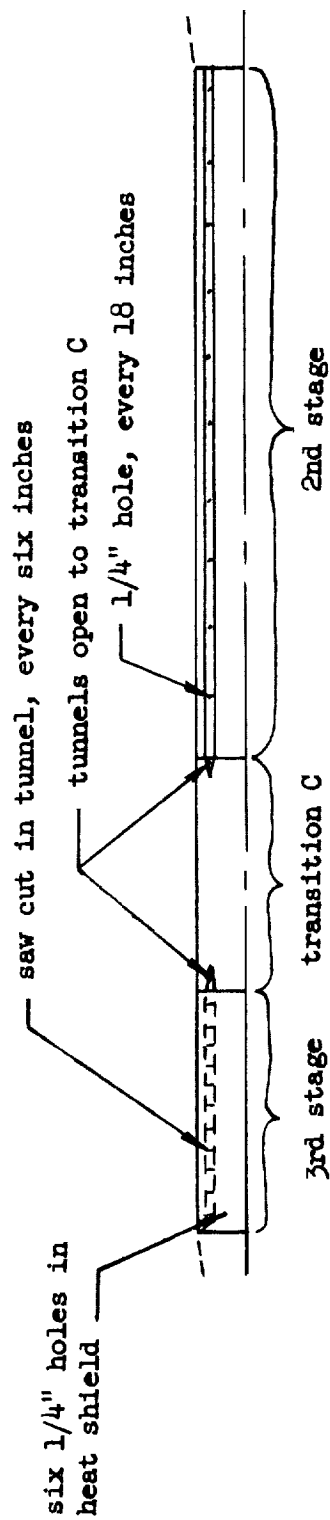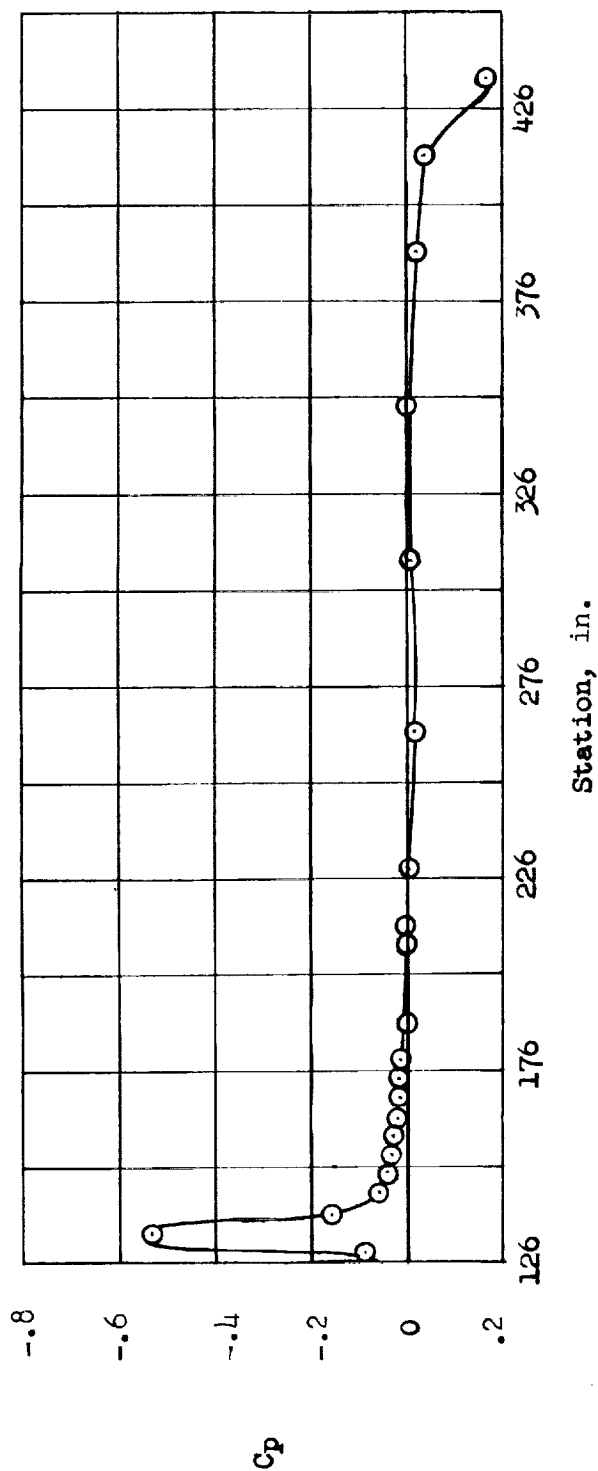
Figure 113.- Sketch showing venting and pressure distribution at a Mach number of 0.9 on second and third stages.
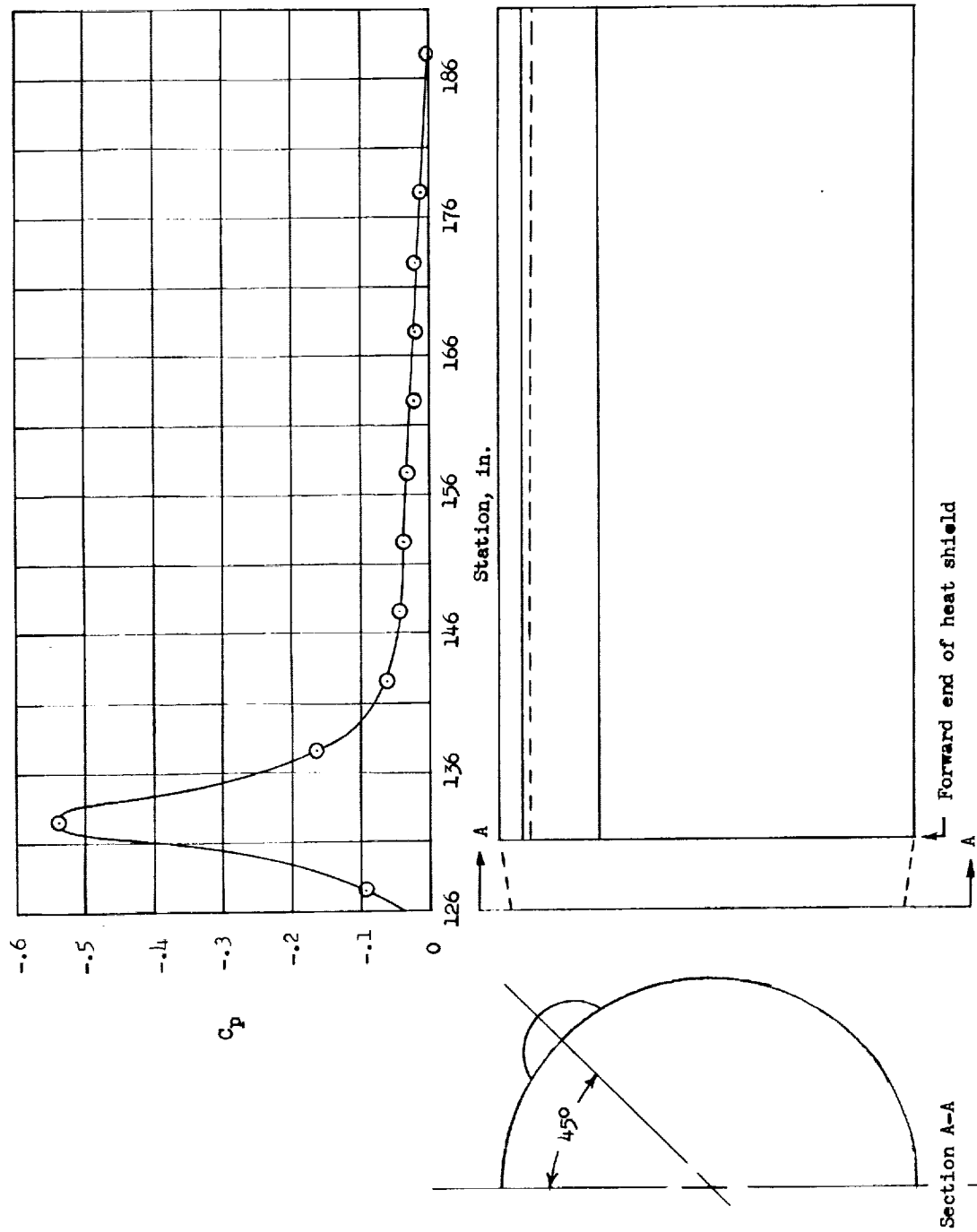
Figure 114.- Sketch of third-stage heat shield and pressure distribution at a Mach number of 0.9.

L-1924
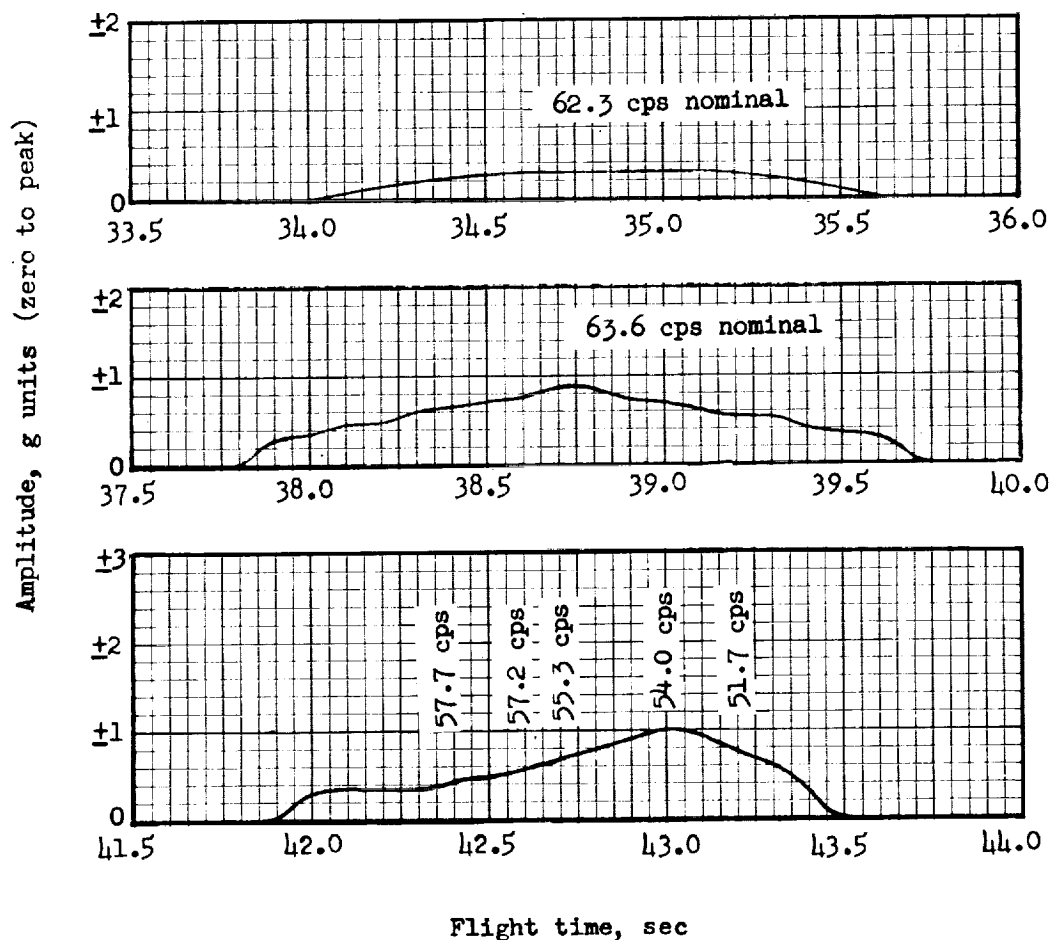
Figure 115.- Time histories of amplitudes of payload longitudinal linear accelerations during first-stage burnout.
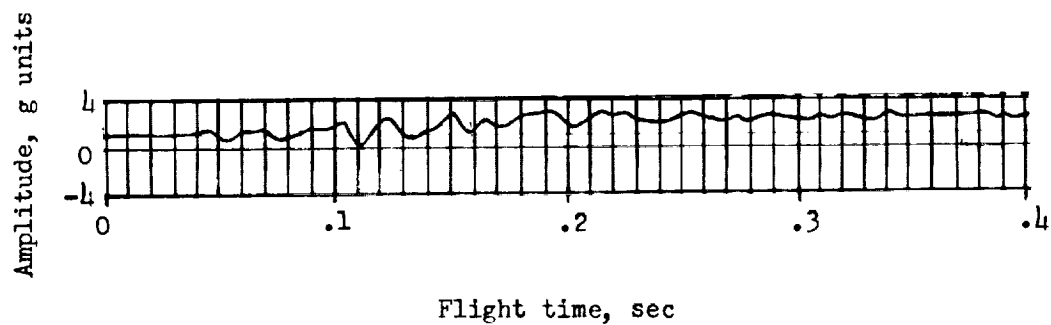
Figure 116.- Time history of the amplitude of payload longitudinal linear acceleration at first-stage ignition.

250
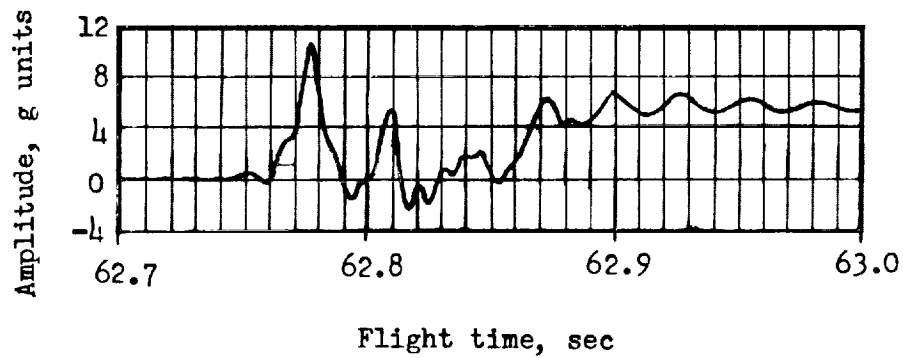
Figure 117.- Time history of the amplitude of payload longitudinal
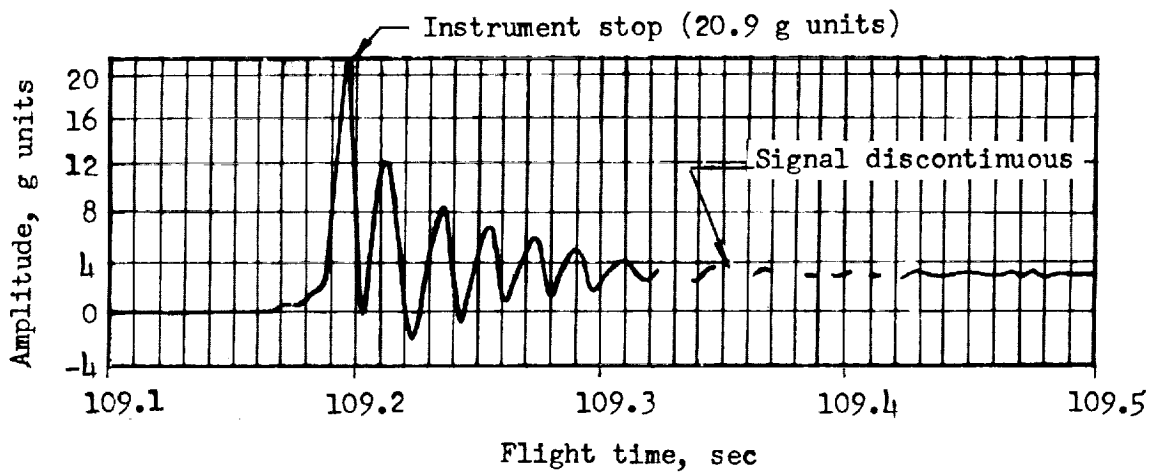linear acceleration at second-stage ignition.

Figure 118.- Time history of the amplitude of payload longitudinal
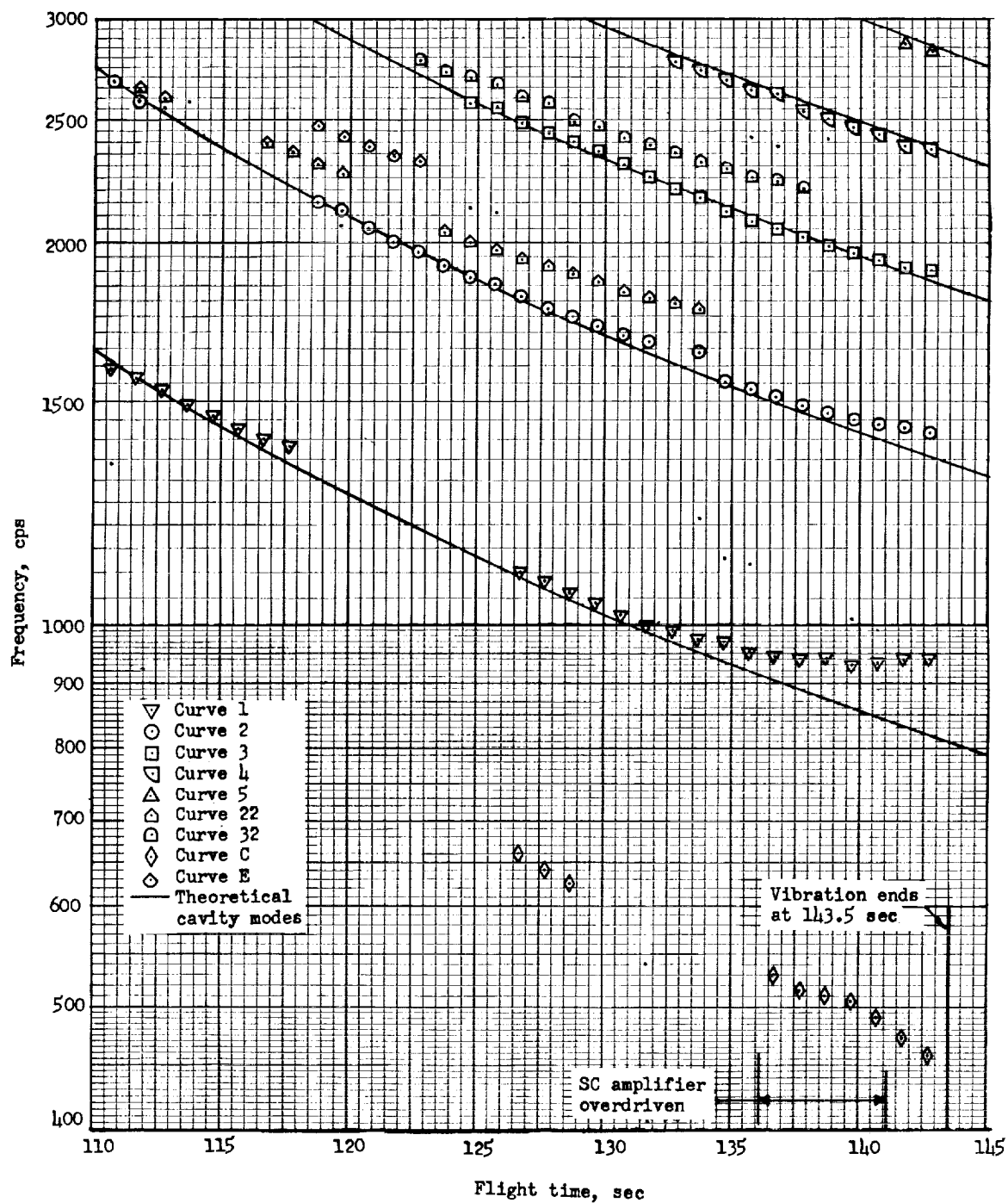linear acceleration at third-stage ignition.

L-1924

Figure 119.- Time histories of frequencies of guidance package
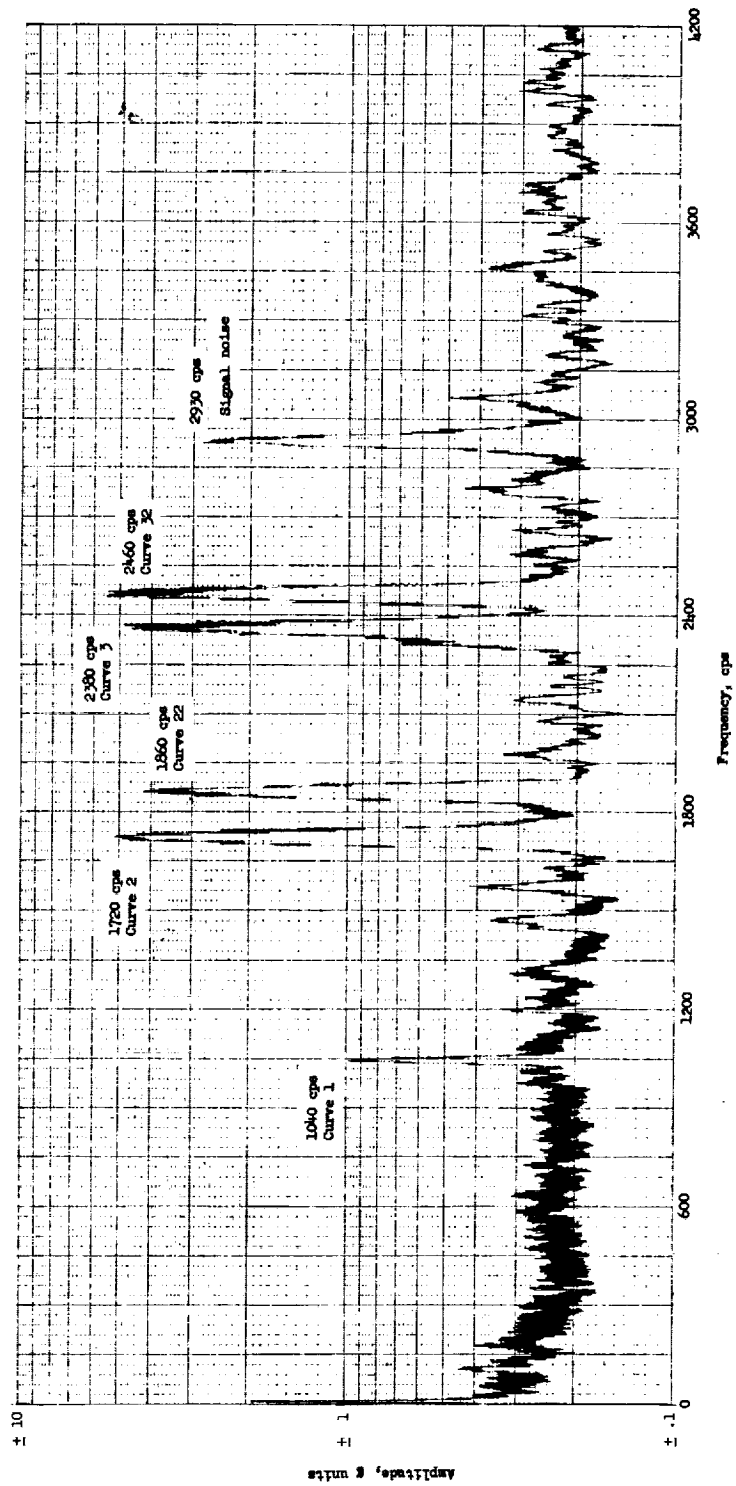transverse vibration accelerations.

252

Figure 120.- Typical wave analyzer output plot showing the variation of amplitude with frequency of the guidance package transverse vibration accelerations from 129.2 to 130.2 seconds.
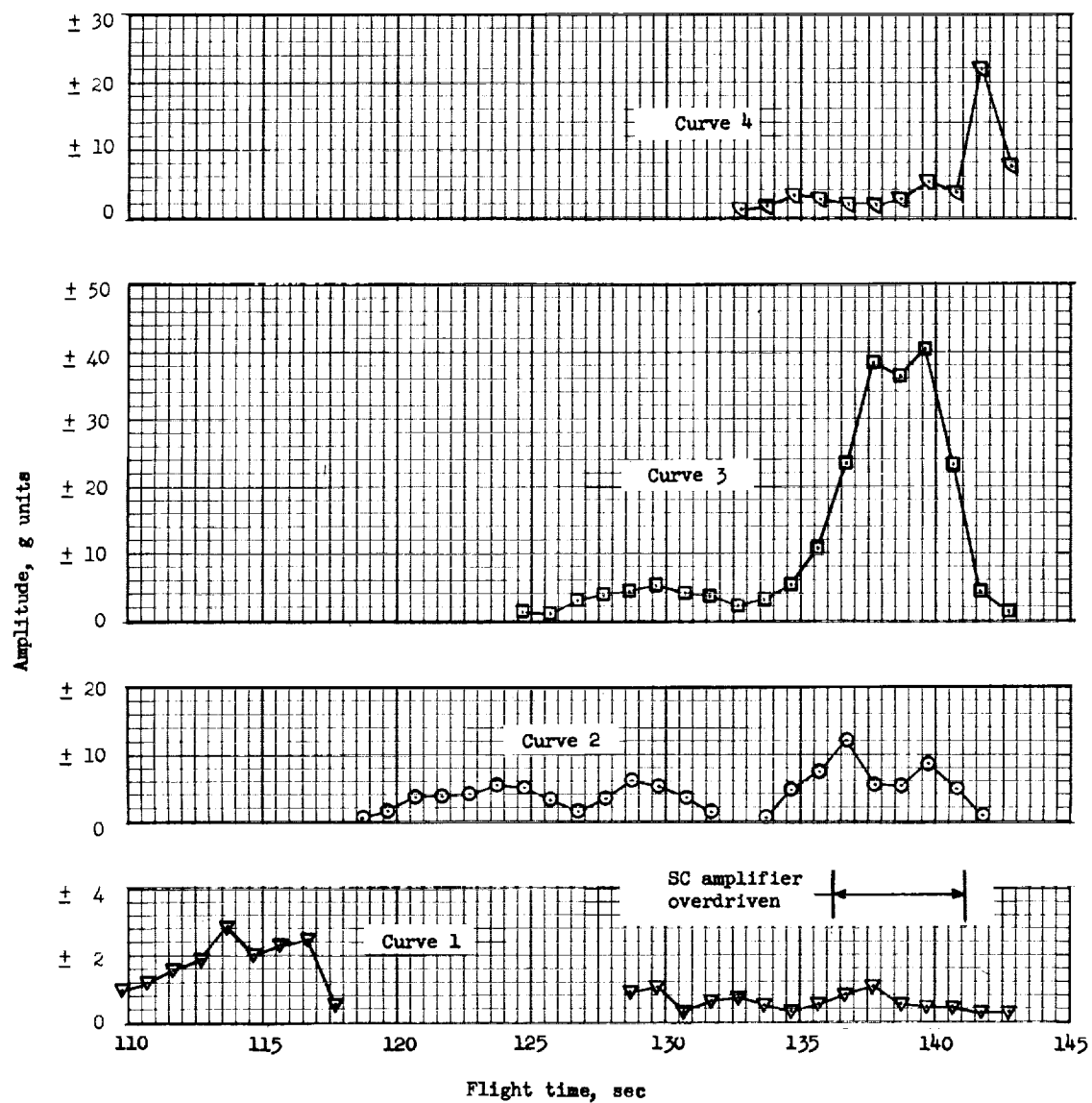
L-1924

L-1924

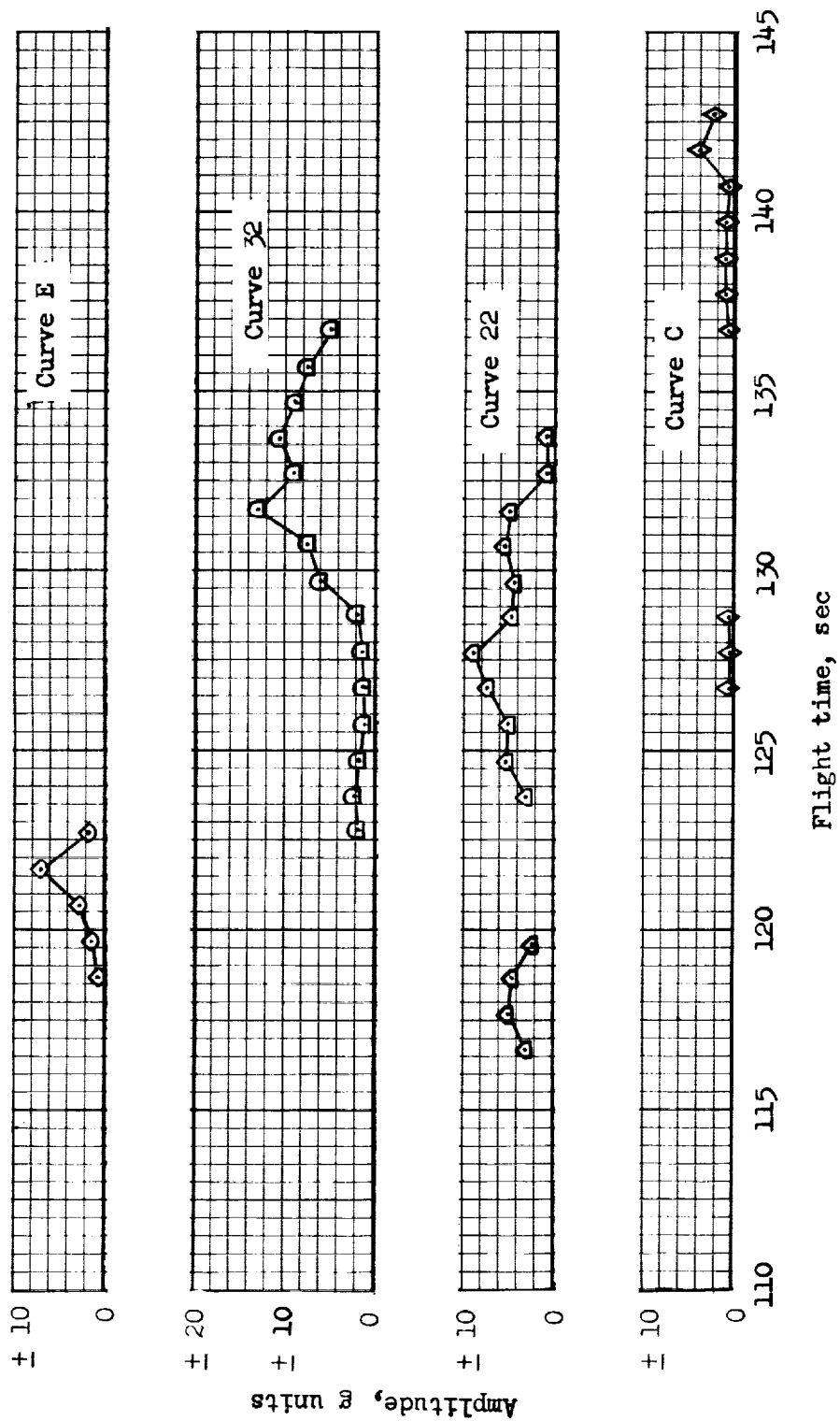Figure 121.- Time histories of the amplitudes of frequency
curves 1, 2, 3, and 4.

Figure 122.- Time histories of the amplitudes of frequency
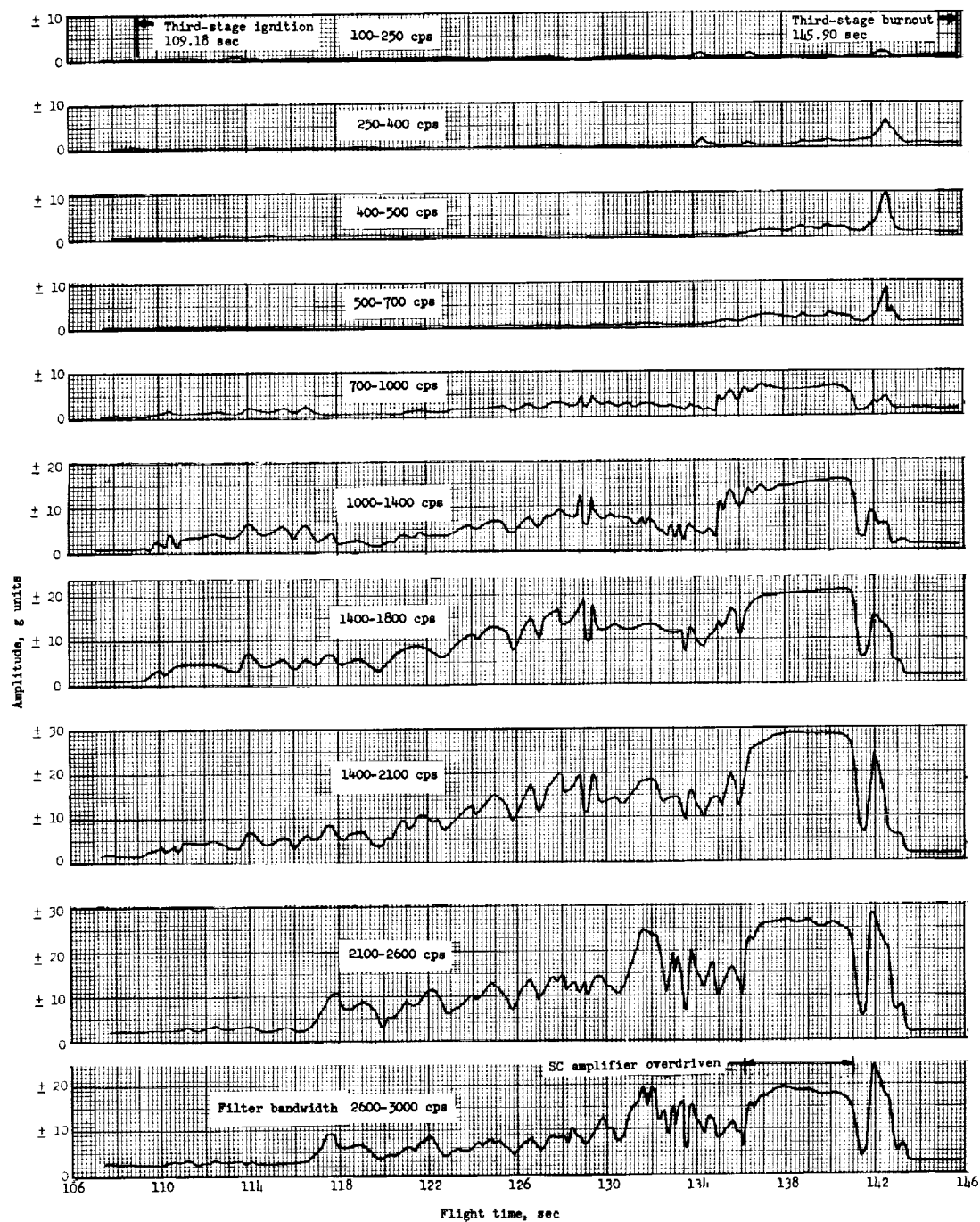curves C, E, 22, and 32.

Figure 123.- Time histories of the wave envelopes of the amplitudes of the guidance package transverse vibration accelerations obtained with bandpass filters.
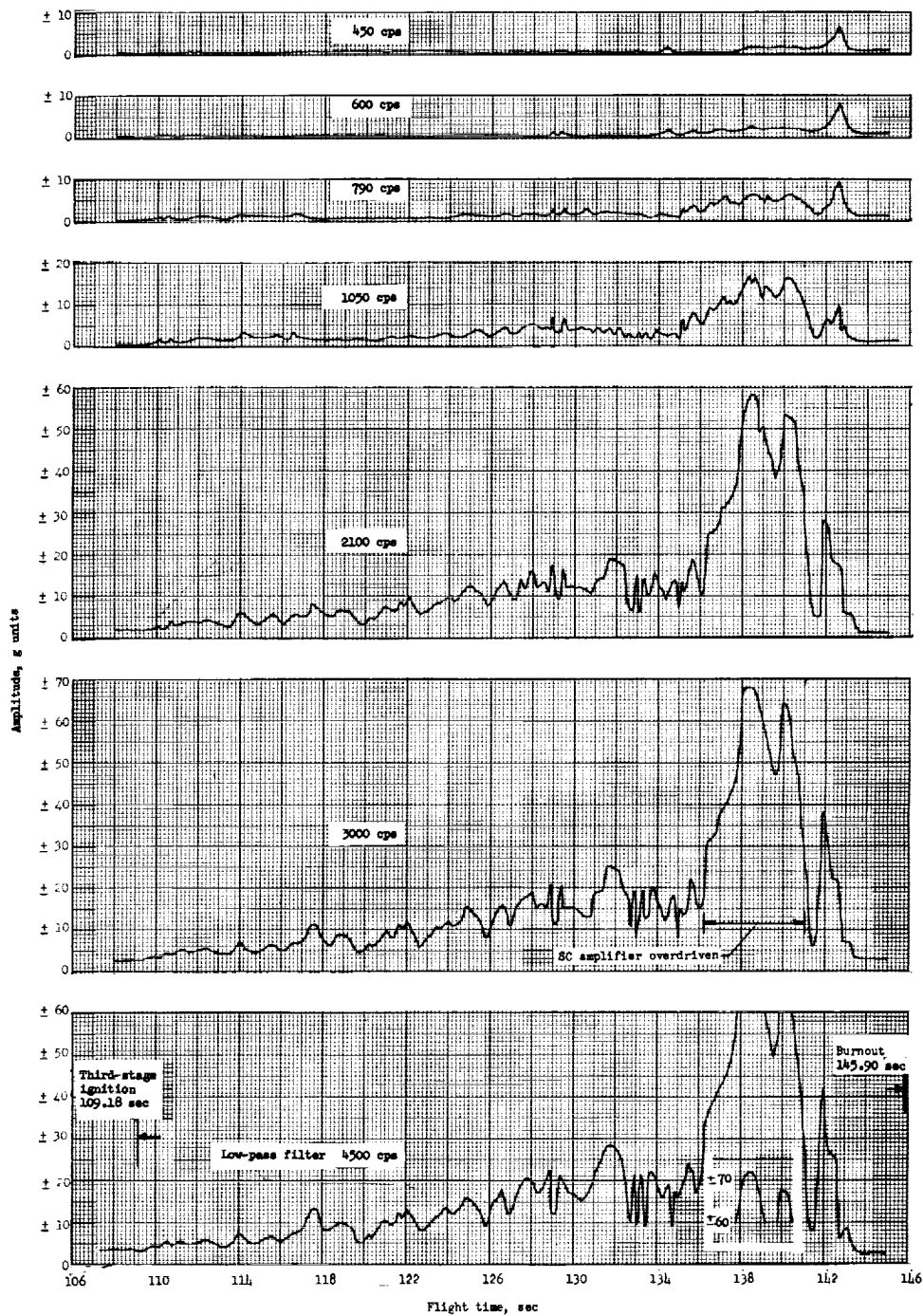
256

Figure 124.- Time histories of the wave envelopes of the amplitudes of the guidance package transverse vibration accelerations obtained with low-pass filters.

NASA TN D-1240
National Aeronautics and Space Administration.
NASA SCOUT ST-1 FLIGHT-TEST RESULTS AND
ANALYSES, LAUNCH OPERATIONS, AND TEST
VEHICLE DESCRIPTION. Robert J. Mayhue, compiler. June 1962. xiii, 256p. OTS price, $4.00.
(NASA TECHNICAL NOTE D-1240)

The test vehicle and launching operations are described, and results obtained during the initial flight test of the vehicle over a high-altitude probe trajectory are presented. Flight data are compared with preflight nominal predictions and with postflight theoretical analyses for evaluation of the performance characteristics of the vehicle and components.

I. Mayhue, Robert J.,
compiler
II. NASA TN D-1240

(Initial NASA distribution:
2, Aerodynamics, missiles
and space vehicles;
18, Communications and
tracking installations,
ground; 23, Launching
facilities and operations;
24, Launching dynamics;
28, Missiles and satellite
carriers; 40, Propulsion
systems, solid-fuel rockets;
48, Space vehicles.)

NASA

NASA TN D-1240
National Aeronautics and Space Administration.
NASA SCOUT ST-1 FLIGHT-TEST RESULTS AND
ANALYSES, LAUNCH OPERATIONS, AND TEST
VEHICLE DESCRIPTION. Robert J. Mayhue, compiler. June 1962. xiii, 256p. OTS price, $4.00.
(NASA TECHNICAL NOTE D-1240)

The test vehicle and launching operations are described, and results obtained during the initial flight test of the vehicle over a high-altitude probe trajectory are presented. Flight data are compared with preflight nominal predictions and with postflight theoretical analyses for evaluation of the performance characteristics of the vehicle and components.

I. Mayhue, Robert J.,
compiler
II. NASA TN D-1240

(Initial NASA distribution:
2, Aerodynamics, missiles
and space vehicles;
18, Communications and
tracking installations,
ground; 23, Launching
facilities and operations;
24, Launching dynamics;
28, Missiles and satellite
carriers; 40, Propulsion
systems, solid-fuel rockets;
48, Space vehicles.)

NASA

NASA TN D-1240
National Aeronautics and Space Administration.
NASA SCOUT ST-1 FLIGHT-TEST RESULTS AND
ANALYSES, LAUNCH OPERATIONS, AND TEST
VEHICLE DESCRIPTION. Robert J. Mayhue, compiler. June 1962. xiii, 256p. OTS price, $4.00.
(NASA TECHNICAL NOTE D-1240)

The test vehicle and launching operations are described, and results obtained during the initial flight test of the vehicle over a high-altitude probe trajectory are presented. Flight data are compared with preflight nominal predictions and with postflight theoretical analyses for evaluation of the performance characteristics of the vehicle and components.

I. Mayhue, Robert J.,
compiler
II. NASA TN D-1240

(Initial NASA distribution:
2, Aerodynamics, missiles
and space vehicles;
18, Communications and
tracking installations,
ground; 23, Launching
facilities and operations;
24, Launching dynamics;
28, Missiles and satellite
carriers; 40, Propulsion
systems, solid-fuel rockets;
48, Space vehicles.)

NASA

NASA TN D-1240
National Aeronautics and Space Administration.
NASA SCOUT ST-1 FLIGHT-TEST RESULTS AND
ANALYSES, LAUNCH OPERATIONS, AND TEST
VEHICLE DESCRIPTION. Robert J. Mayhue, compiler. June 1962. xiii, 256p. OTS price, $4.00.
(NASA TECHNICAL NOTE D-1240)

The test vehicle and launching operations are described, and results obtained during the initial flight test of the vehicle over a high-altitude probe trajectory are presented. Flight data are compared with preflight nominal predictions and with postflight theoretical analyses for evaluation of the performance characteristics of the vehicle and components.

I. Mayhue, Robert J.,
compiler
II. NASA TN D-1240

(Initial NASA distribution:
2, Aerodynamics, missiles
and space vehicles;
18, Communications and
tracking installations,
ground; 23, Launching
facilities and operations;
24, Launching dynamics;
28, Missiles and satellite
carriers; 40, Propulsion
systems, solid-fuel rockets;
48, Space vehicles.)

NASA